Semiconductor Vertical Quantum Structures Self-Formed in Inverted Pyramids

THÈSE N^{O} 4145 (2008)

PRÉSENTÉE LE 18 JUILLET 2008
À LA FACULTE SCIENCES DE BASE
LABORATOIRE DE PHYSIQUE DES NANOSTRUCTURES
PROGRAMME DOCTORAL EN PHYSIQUE

ÉCOLE POLYTECHNIQUE FÉDÉRALE DE LAUSANNE

POUR L'OBTENTION DU GRADE DE DOCTEUR ÈS SCIENCES

PAR

Qing ZHU

B.Sc. in modern applied physics, Tsinghua University, Beijing, Chine
et de nationalité chinoise

acceptée sur proposition du jury:

Prof. R. Schaller, président du jury
Prof. E. Kapon, directeur de thèse
Prof. H. Brune, rapporteur
Prof. J. Faist, rapporteur
Prof. J. Finley, rapporteur

ÉCOLE POLYTECHNIQUE
FÉDÉRALE DE LAUSANNE

Suisse
2008

Contents

Abstract vii

Version abrégée ix

Preface xiii

1 Introduction: Low-Dimensional Quantum Nanostructures 1
- 1.1 Semiconductors . . . 1
  - 1.1.1 Crystal structures . . . 1
  - 1.1.2 Energy bands . . . 3
  - 1.1.3 Heterostructures . . . 6
- 1.2 Excitons and optical properties of QW, QWR, QD . . . 9
  - 1.2.1 Optical absorption and polarization dependence of the interband matrix element . . . 9
  - 1.2.2 Excitons in bulk semiconductors . . . 11
  - 1.2.3 Excitons in QWs and QWRs . . . 12
  - 1.2.4 Excitons in QDs . . . 13
- 1.3 QWRs and QDs: state of the art . . . 15
  - 1.3.1 QWRs fabrication techniques . . . 15
  - 1.3.2 Optical studies of QWRs . . . 18
  - 1.3.3 QD and QD molecule fabrication techniques . . . 21
  - 1.3.4 Optical studies of QDs . . . 24
  - 1.3.5 Optical studies of coupled QDs and QD molecules . . . 26
- 1.4 Summary . . . 28

2 Fabrication and Characterization Techniques 29
- 2.1 Fabrication of vertical quantum structures in inverted pyramids . . . 29
  - 2.1.1 The substrate patterning technology . . . 29
  - 2.1.2 Epitaxial growth . . . 31
  - 2.1.3 Post-growth processing . . . 35
  - 2.1.4 Structural Characterization using AFM, SEM, TEM . . . 37
- 2.2 Optical characterization techniques . . . 40
  - 2.2.1 Photoluminescence spectroscopy . . . 41
  - 2.2.2 Micro-Photoluminescence spectroscopy . . . 41

2.2.3 Linear polarization-resolved photoluminescence spectroscopy . . 42
2.2.4 Time-resolved photoluminescence spectroscopy 43
2.2.5 Photoluminescence excitation spectroscopy 44
2.2.6 Photon correlation spectroscopy 44
2.2.7 Cathodoluminescence 45
2.3 Summary 46

3 Pyramidal Vertical Quantum Wires: a New QWR System 47
3.1 Formation of pyramidal VQWR 48
3.1.1 Structures designed for studying the growth mechanism 49
3.1.2 Microscopy of pyramidal heterostructures 49
3.1.3 Cathodoluminescence spectrosopy for probing the barrier structures 51
3.1.4 Evaluation of Al-Ga segregation effect by optical measurement . 52
3.1.5 Simple model of segregation effect in pyramids 53
3.2 2D quantum confinement 55
3.2.1 Infinitely long QWR modeling 56
3.2.2 Comparison of calculation and measurement 61
3.3 Carrier capture phenomena inside a pyramid 65
3.4 Summary 66

4 Quantum Wires of Controlled Length: from QWR to QD 69
4.1 Transition from 2D to 3D quantum confinement 69
4.1.1 Structures designed for studying 2D to 3D quantum confinement 70
4.1.2 Effect on ground state energies and s-p separation 72
4.1.3 Size dependent polarization properties 79
4.1.4 Effect on exciton radiative lifetime 84
4.1.5 Summary 87
4.2 Optical properties of pyramidal AlGaAs QDs 88
4.2.1 Pyramidal AlGaAs QD: a novel QD system 88
4.2.2 Cathodoluminescence spectroscopy for studying carrier capture within the pyramidal heterostructure 90
4.2.3 The power dependence of X, X^- and 2X peaks 92
4.2.4 Temperature dependence of X, X^- peaks 95
4.2.5 Single photon emission from single AlGaAs QD 96
4.2.6 Correlated photon emission from single QD 97
4.3 Summary 99

5 QD Molecules and QD Superlattices 101
5.1 Hybridized electron and hole states in QD molecules 101
5.1.1 Structure of vertically stacked pyramidal QDs 102
5.1.2 Enhanced QD coupling using QWR barriers 103
5.2 From single QD to multi-QD molecules 107
5.2.1 Structures designed for studying electron and hole hybridazation 107

    - 5.2.2 Calculated wavefunctions of single-, double- and triple-QD molecules 108
    - 5.2.3 Comparison of calculated absorption spectra and measured photoluminescence spectra 110
    - 5.2.4 Correlated photon emission from QD molecules 112
  - 5.3 Tuning the coupling between two QDs in double-QD molecule 114
    - 5.3.1 Systematically changing the barrier in between the QDs 114
    - 5.3.2 Systematically modifying the QDs dissimilarity 115
  - 5.4 Perturbing the wavefunction in QD molecules 122
  - 5.5 Summary 131

6 Conclusions and Future Direction **133**

A QWR and QD formalism **135**

B Epitaxial layer sequences **137**

C Processing run sheets **155**

Bibliography **159**

Publications **173**

Acknowledgements **178**

Curriculum vitae **181**

To my family...

Abstract

Semiconductor quantum wires (QWRs) and quantum dots (QDs) represent important classes of low-dimensional quantum nanostructures, useful for studies and applications of quasi one- and zero-dimensional systems. Recently, considerable efforts have been devoted to developing QWRs and QDs of high optical quality for studying the properties of these low dimensional structures. However, realization of QWRs and QDs in a highly reproducible and controllable manner remains challenging.

The present thesis systematically investigated a novel QWR-QD system self-formed in inverted tetrahedral pyramids due to capillarity induced alloy segregation effect during metallorganic vapor phase epitaxy (MOVPE). Growth of an otherwise homogenous AlGaAs layer inside the pyramid results in formation of a Ga-enriched vertical QWR (VQWR) running through the center of the pyramid, along the growth axis, and three vertical QWs (VQWs) at the three wedges of the pyramid. Since the VQWR forms along the growth direction, the structure and the composition can be adjusted via the growth conditions and parameters, offering possibilities of achieving QWR structures with controlled potential. In particular, the composition and/or structure of these wires can be tailored with monolayer accuracy, opening the way for a new generation of complex low dimensional nanostructures of different functionalities. Moreover, these QWRs are embedded in a semiconductor matrix, so that high quality interface can be achieved. This feature offers opportunities for integrating these QWRs in electronic and optical devices.

As a starting point, we studied the formation mechanisms involved in the pyramid system, particularly the alloy segregation effect. This forms the basis for the entire project, giving useful guidance in structural design for the more complex structures investigated later. The Ga-Al segregation is evidenced by high resolution electron microscopy images and photoluminescence (PL) spectroscopy. A simple diffusion model was developed to interpret the effect qualitatively and quantitatively. Quantum confinement of electrons and holes in these wires is evidenced by peculiar transitions observed in the PL spectra at high excitation levels and confirmed by theoretical modeling of these structures. The wires are also connected to a set of higher bandgap, self-ordered VQWs that promote carrier capture into the wire. The temperature dependence of the PL spectra clearly reveals efficient carrier capture into the VQWR from the surrounding VQWs, particularly at an intermediate temperature range (~ 100 K) where the carrier mobility is enhanced. Cathodoluminescence spectroscopy is applied to identify the individual structures and to investigate the carrier transfer within the structures.

In the next step, we systematically shortened the VQWR to bring the structure into the QD regime, simply by decreasing the grown layer thickness from nearly one micron to several nanometers. Thus, a continuous transition from two-dimensional to three-dimensional quantum confinement was realized in the very same system, revealing the impact of dimensionality on the electronic and optical properties of the nanostructures. Several advanced measurement techniques were employed in this study, including polarization-resolved and time-resolved PL spectroscopy. Three main evidences for the QWR-QD transition were observed experimentally and confirmed theoretically: (i) strongly blue-shifted ground state emission, accompanied by increased separation of ground and excited transition energies; (ii) change in the orientation of the main axis of linear polarization of the PL, from parallel to perpendicular with respect to the growth axis; and (iii) prolonged exciton radiative lifetime. The optical properties of the single QDs were also studied. Single- and correlated photon emission from single QD were demonstrated by photon correlation measurements.

The success in fabrication of QDs with controlled potential inside the pyramids stimulated the development of QD molecules by stacking several QDs on top of each other. In our QD molecule systems, QDs are tunnel-coupled via connected QWRs. The stronger tunnel coupling in this integrated QD-QWR system allows the hybridization of both electron and hole states, yielding direct-real-space excitonic molecules. Evidence for this hybridization was provided by polarization-resolved PL spectroscopy confirming the formation of delocalized hole states, and by photon correlation spectroscopy showing photon bunching for bonding- and anti-bonding QD-molecule transitions. The QD molecule configuration could be modified intentionally for probing local electron/hole probability density, by insertion of very thin barriers as perturbations in the given structure at specified positions.

In conclusion, the controlled growth in inverted pyramids provides considerable freedom in designing complex nanostructures that are difficult to achieve with purely self-assembly approaches. The investigated structures provide new information on low-dimensional systems and hold promise for the development of nano-photonic devices for quantum information processing applications.

Keywords

Semiconductor, AlGaAs, GaAs, MOVPE, epitaxy, nanostructure, heterostructure, quantum wire, quantum dot, quantum dot molecule, optical properties, photoluminescence (PL), polarization-resolved PL, time-resolved PL, photon correlation, Cathodoluminescence, state hybridization, effective mass approximation.

Version abrégée

Les fils quantiques (QWRs) et les boîtes quantiques (QDs) à base de matériaux semiconducteurs représentent une catégorie importante de nanostructures quantiques, utiles pour les études et applications de systèmes un- ou zero-dimensionnels. Récemment, des efforts considérables ont été consacrês au développement de QWRs et QDs de bonne qualité optique pour l'étude des propriétés de ces structures de basse dimensionnalité. La fabrication contrôlée et reproductible de QWRs et de QDs reste toutefois un défi technologique.

Cette thèse présente l'étude systématique d'un nouveau système QWR-QD, formé par croissance épitaxiale à l'intérieur de pyramides tétrahédrales inversées grâce à un phénomène de ségrégation d'alliage induit par capillarité. La croissance d'une couche d'AlGaAs nominalement homogène à l'intérieur de la pyramide débouche sur la formation d'un QWR vertical (VQWR), enrichi en Ga, le long de l'axe de croissance au centre de la pyramide, ainsi que sur trois QWs verticaux (VQW) reliant les arrêtes de la pyramide à son centre. Du fait de la formation du VQWR le long de la direction de croissance, sa composition et sa structure peuvent être ajustés via les paramètres de croissance, permettant de créer des structures ayant un potentiel déterminé. En particulier, la composition et/ou structure de ces fils peut être maîtrisée avec un précision de l'ordre de la mono-couche atomique, et ouvre la voie à la conception de nanostructures complexes, de basse dimensionnalité, et ayant diverses fonctionnalités. De plus, l'inclusion de QWRs dans une matrice de semiconducteur résulte en l'obtention d'une grande qualité des interfaces, offrant la possibilité de les intégrer dans des dispositifs électroniques ou optiques.

Pour commencer, nous avons étudié les mécanismes de formation en jeu lors de la croissance l'intérieur d'une pyramide; en particulier, l'effet de ségrégation d'alliage. Cette étude est la base de l'entier du projet, puisqu'elle donne des indications utiles à la conception des structures complexes investiguées par la suite. La ségrégation de Ga et Al a été mise en évidence par microscopie électronique à haute résolution et par spectroscopie de photoluminescence (PL). Un modèle de diffusion simplifié a été développé pour interpréter qualitativement et quantitativement cet effet. Le confinement quantique des lectrons et des trous dans ces fils est mis en évidence par les transitions spécifiques observées dans les spectres de PL à haute densité d'excitation, et confirmé par la modélisation théorique de ces structures. Les fils sont également connectés à un ensemble de VQWs ayant une bande interdite plus large, qui favorisent la capture des porteurs dans le fil. La dépendance en température des spectres de PL révèle clairement l'efficacité de la capture dans le VQWR à partir des VQWs environnants, en particulier aux températures intermédiaires ($\sim$ 100 K) auxquelles la mobilité des porteurs est supérieure. La technique de spectroscopie de cathodoluminescence a été utilisée pour identifier les diverses structures et pour étudier le transfert des porteurs entre elles.

Dans un second temps, nous avons systématiquement raccourci le VQWR afin de le transposer dans le régime d'un QD, par une simple réduction de l'épaisseur de la couche crue d'environ un micron à quelques nanomètres. De cette manière, une transition continue entre un confinement deux-dimensionnel et trois-dimensionnel est obtenue dans un même système, révélant l'impact de la dimensionnalité sur les propriétés optiques et électroniques des nanostructures. Plusieurs méthodes de mesure sophistiquées ont été utilisées dans cette étude, parmi lesquelles la spectroscopie de PL rsolue en temps ou en polarisation. Principalement, trois indications d'une transition QWR-QD ont été observées et confirmées théoriquement: (i) l'émission de l'état fondamental est fortement décalée vers le bleu, et est accompagnée d'une augmentation de la séparation avec les états excités; (ii) l'orientation de l'axe principal de la polarisation commute de parallèle à perpendiculaire relativement à l'axe de croissance; (iii) le temps de vie radiatif de l'exciton est prolongé. Les proprits optiques de QDs uniques ont également été tudiées. L'émission de photons uniques et corrélés a été démontrée par des mesures de corrélation.

Le succès de la fabrication de QDs ayant un potentiel déterminé a stimulé le développement de molécules de QDs, en empilant plusieurs QDs les uns au dessus des autres. Dans notre système de molécules de QDs, les QDs sont couplés par effet tunnel via les QWRs les reliant. Le fort couplage dans ces systèmes intégrés permet l'hybridisation des états à la fois de la bande de valence et de la bande de conduction, ce qui résulte en molécules excitoniques dans l'espace direct réel. Cette hybridisation est mise en évidence par spectroscopie de PL résolue en polarisation, qui confirme la formation de fonctions d'onde délocalisées pour les trous, et par la spectroscopie de corrélation de photons, qui montre du ”photon-bunching” pour les états liants et antiliants des transitions de la molécule de QDs. La configuration de la molécule peut être modifiée intentionnellement pour sonder la densité de probabilité locale d'électron-trou, en insérant une barrière très étroite en guise de perturbation à des positions spécifiques de la structure.

En conclusion, la croissance contrôlée dans des pyramides inversées offre une liberté considérable dans la conception de nanostructures complexes qui sont difficiles à obtenir à l'aide d'approches basées uniquement sur l'auto-organisation. Les systèmes que nous avons investigués fournissent de nouveaux enseignements sur les systmes de basse dimensionnalité et sont prometteurs pour la fabrication de dispositifs nano-photoniques et pour des applications ayant trait ou traitement des informations quantiques.

Mots-clés

Semiconducteur, AlGaAs, GaAs, MOVPE, épitaxie, nanostructure, hétérostructure, fil quantique, boîte quantique, molécule de boîtes quantiques, propriétés optiques, photoluminescence (PL), PL résolue en polarisation, PL résolue en temps, corrélations de photons, cathodoluminescence, états hybridés, approximation de la masse effective.

Preface

Background

The great success of semiconductor technology during the second half of the 20th century enables the possibility to change the electronic characteristics of the semiconductor effectively by adding impurities (dopants) in a well controlled way. Different electronic components can thus be fabricated by the same material. This led to the invention of the integrated circuit (IC) in the late 1950's, where several electrical components are build in the same piece of material by lithography processing. It was predicted in 1965 by Moore G. E. that the number of transistors in an IC will increase exponentially in time, which is known as Moore's law [1]. This law has been indeed demonstrated by the semiconductor industry more more than four decades.

Today, silicon (Si) is a common semiconductor dominating in memory and logic devices with its highly advanced and ubiquitous technology. However, III-V compound semiconductors such as GaAs, AlAs, InP and their ternary alloy $\mathrm{Al_xGa_{1-x}As}$ are extensively used in many important applications due to their superior optical and electronic properties.

Research on low dimensional electronic heterostructures, also termed quantum nanostructures, was initialed in 1969 by a pioneering proposal of Esaki L. and Tsu R. for an engineered two dimensional semiconductor superlattice (2D-SL) [2], where the carriers are quantum-confined in a small bandgap material sandwiched between large bandgap material layers. It offers another possibility to tailor the electronic properties. For example, by growing $\mathrm{Al_xGa_{1-x}As/GaAs/Al_xGa_{1-x}As}$ layer in a sequence, quantum well (QW) is formed if the GaAs layer thickness is a few nanometers thick. Quantum confinement effect then arises in such QWs. Carrier motions are restricted in the direction perpendicular to the heterostructure interface, which strongly modifies the electronic properties as compared to bulk materials. An extension of the QW concept can be found in quantum wires (QWRs) and quantum dots (QDs), where the carrier motions are restricted even in more directions. It was predicted that the low-dimensional properties of the charge-carriers accommodated in low-dimensional structures will strongly improve the performances of heterostructure laser [3] [4].

Nowadays, high quality 2D quantum wells (QWs) are produced by using advanced material deposition techniques, for example organometallic chemical vapor deposition (OMCVD) and molecular beam epitaxy (MBE), with which one can grow semiconductor crystals layer-by-layer with different bandgap materials. Great success has been achieved in the development of QW lasers utilizing these technologies since 1970. However, it is still challenging to get lower dimensional quantum structures, such as quantum wires (QWRs) (1D) and quantum dots (QDs) (0D), where carrier confinement is also induced perpendicular to the growth direction. A powerful way to obtain high quality QWRs and QDs is epitaxial growth on pre-patterned substrates. This approach has been exploited with various geometries of the nonplanar substrate, using ridges [5], mesa stripe [6], V-grooves [7], pyramid recesses [8] and so on.

Moreover, the on-going exponential miniaturization of electronic devices, will soon result in entire devices exhibiting quantum effects. The properties of such small quantum devices are strongly sensitive to the exact shape, size and composition of the incorporated quantum structures. On one hand, the confinement of the carrier motion introduces another degree of freedom in tailoring the electronic properties. On the other hand, it becomes urgent now to deeply understand the properties related to these lower-dimensional systems and to search for better candidates for near future nano-device applications.

The present thesis deals with these issues. We systematically investigated the optical and electronic properties of novel QWR, QD and QD molecule systems realized in pre-patterned non-planar surface during epitaxial growth. The structures fabricated in this way are fully controllable, extendable and are of outstanding optical quality, suitable for applications in nano-photonic devices.

The thesis is arranged in the following way:

Thesis plan

Chapter 1 introduces the theoretical basis necessary to understand the physics of the investigated quantum structures. A brief review of the QWR, QD and QD molecule fabrication techniques and studies of their optical properties is presented.

Chapter 2 introduces the fabrication process of our pyramidal VQWR/QD structures. Several popular and intensively used structural and optical characterization techniques are summarized as well.

Chapter 3 systematically investigated the alloy segregation effect involved in the formation of AlGaAs pyramidal vertical quantum structures. The optical and electronic properties of pyramidal VQWRs are studied both experimentally and theoretically. The quantum confinement effect in VQWR and carrier capture from surrounding structures into VQWR are evidenced.

Chapter 4 is devoted to studies of transition from two dimensional to three dimensional quantum confinement realized in pyramidal VQWR and QD systems. The optical property of AlGaAs pyramidal QDs is investigated. Single and correlated photon emissions from these QDs are demonstrated.

Chapter 5 demonstrates the hybridization of electron and hole states in our pyramidal QD molecule structures. The presence of coupling between the QDs is evidenced by polarization-resolved PL and photon statistics spectroscopy. The possibilities of tuning the coupling or probing the local carrier probability density in the structures are discussed

Chapter 6 draws some conclusions on the completed project work and presents an outlook on the future research directions of pyramidal VQWR-QD system.

ZHU Qing

Lausanne, March 2008

Chapter 1

Introduction: Low-Dimensional Quantum Nanostructures

This introductory chapter will provide the necessary physical background related to the present thesis. We will start from an introduction of the fundamentals of III-V semiconductors including their crystal structure, energy bands and the heterostructures composed by them in Section 1.1. Then, excitons in low-dimensional quantum nanostructures and their optical properties will be discussed in Section 1.2. Finally, a brief review on quantum wires (QWRs), quantum dots (QDs) and QD molecules fabrication methods and their optical properties will be presented in Section 1.3.

1.1 Semiconductors

1.1.1 Crystal structures

The semiconductor quantum structures studied in the present thesis are composed of elements from the third and the fifth columns in the Periodic Table of Elements. The most common ingredients are AlGaAs alloys made of Aluminium (Al) and Gallium (Ga) from the third and Arsenic (As) from the fifth group. These III-V semiconductors crystallize in the zinc-blende structure. As represented in Fig 1.1 for GaAs, the zinc-blende is constructed from two interpenetrating face-centered cubic (FCC) lattices. By substituting partially the Ga atoms with Al atoms, the ternary alloy AlGaAs is formed. The group III and V elements belong to different FCC lattices, and are displaced relative to each other by one quarter of the main cube diagonal.

In zinc-blende structures, there are several important planes: (001), (110), and (111), as illustrated in Fig 1.2 (a)-(c), respectively. Planes such as the (001), are normal to the principal axes. Each contains one species of atom, which alternate in successive planes of the zinc blende, separated by $\frac{1}{4}\mathbf{a}$. GaAs usually cleaves along a (110)-plane,

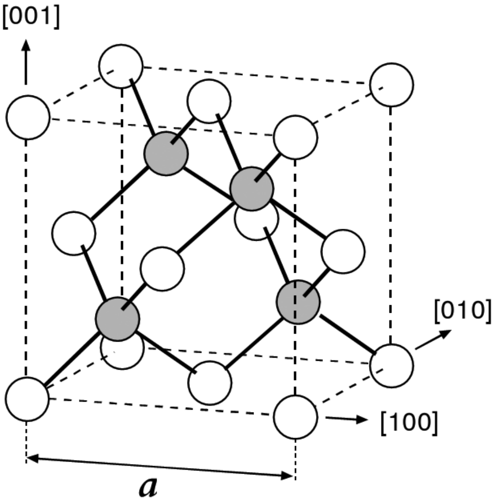

Figure 1.1: Schematic illustration of the atom arrangement in GaAs, with definitions of the lattice constant a and the principal crystallographic direction [100], [010] and [011]. The filled (open) circles represent Ga(As) atoms. [9]

shown in Fig 1.2 (b). These planes are intersect at 45° with the [100]- and [010]- axes. They contain both species of atoms. Note that the figure shows an internal plane; an exposed surface is reconstructed after cleavage, adopting a different structure.

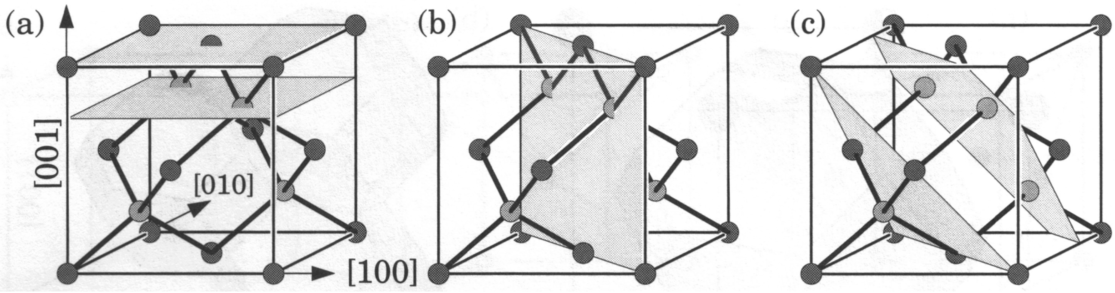

Figure 1.2: Important planes in the zinc-blende structure: (a) (001), (b) (110), and (c) (111). [10]

A third important plane is (111), which is equally inclined to all three principal axes. Each (111) plane contains only one species of atoms as for (100), and a plane of each kind is shown in Fig 1.2 (c). Note that the [111]-direction is polar in a compound semiconductor, because the all bonds point in the same direction from Ga to As. This distinction is not present in an isolated element, which therefore has a higher symmetry. The polar nature of directions such as [111] means that the exposed (111)- and $(\bar{1}\bar{1}\bar{1})$-surfaces have different properties. Fig 1.2 (c) shows that the spacing between successive planes of atoms alternates. Growth proceeds by adding pairs of the more closely spaced planes. Thus, if GaAs is grown on the (111) plane, it is found to terminate in a plane of Ga atoms, which is called a (111)A surface. On the other hand, growth on the $(\bar{1}\bar{1}\bar{1})$

plane terminates in a plane of As atoms known as (111)B. This distinction is important in growth or processing on these surfaces, because growth or chemical etching often proceed on the two surfaces with different rates.

1.1.2 Energy bands

A crystal is made of a large numbers of atoms. The discrete energy levels of individual atoms split up into bonding and antibonding states when the parts of atoms are brought together. The splitting leads to the formation of continuous electronic energy bands, and these bands may be separated by energy gaps. The bands delocalize the accommodated electrons, which no longer belong to specific atoms. The electrons originating from the atoms in the crystal will populate the energy states in the bands. If, at zero temperature, the bands below a band gap are all occupied, and the bands above the band gap are all empty the crystal is called a semiconductor. For most semiconductors the energy gap $\mathrm{E_g} \approx 1$ eV. The energetically highest occupied band is referred to as the valence band (VB), while the lowest empty energy band is defined as the conduction band (CB).

In contrast to free electrons, the crystal electron wave function is modulated by the periodicity of the underlying lattices. This modulation is governed by Bloch's theorem. By assuming that the crystal potential is periodic and identical for all electrons in a band, the electron wave function $\psi(\mathbf{r},\ \mathbf{k})$ depending on the spatial position $\mathbf{r}$ and the wave vector $\mathbf{k}$, limited to the first Brillouin zone (BZ), can be written on the form

$$\psi_{\mathrm{i}}(\mathbf{r},\mathbf{k}) = \chi_{\mathrm{i}}(\mathbf{r},\mathbf{k})\mathrm{u_i}(\mathbf{r},\mathbf{k}) \tag{1.1}$$

where $\chi = \exp(\mathrm{i}\mathbf{k}\cdot\mathbf{r})$ is the plane wave envelope wavefunction, u is the periodic Bloch function and i is a band index.

Semiconductor materials having global CB energy minimum at $|\mathbf{k}| = 0$, which also coincides with the energy maximum of the VB, are called direct-gap semiconductors. This is because only the electron and hole near $|\mathbf{k}| = 0$ can recombine into photon due to the requirements of energy-momentum conservation. All the semiconductors studied in the present thesis are direct-gap. The photon emission efficiency in direct semiconductors is far superior than for indirect semiconductors having the global CB energy minimun at $|\mathbf{k}| \neq 0$, e.g. Si, $\mathrm{Al_xGa_{1-x}As}$ (for $\mathrm{x} > 0.5$).

The Hamiltonian for an electron moving in the periodic crystal potential can be expanded by the complete set of Bloch functions obtained for $|\mathbf{k}| = 0$, and can in principle be solved exactly for any $\mathbf{k}$. A common approximation is to restrict the basis to a number of Bloch functions in the expansion in order to make the mathematical problem practically solvable analytically or numerically. Since the most interesting energy region of the semiconductor is near the band gap, a few Bloch functions related to the bands above and below the band gap are included. The minimal set of Bloch functions to include are those related to CB and the VB, respectively. Such model was developed by Kane [11] [12], where also remote bands where included by perturbation theory. The resulting Hamiltonian includes the spin-orbit coupling and can be expressed in a basis of eigenfunctions $\mathrm{u}_{\mathbf{J},\mathrm{J_z}}$ of the angular momentum operator $\mathbf{J}$, which for the VB is formed by linear combinations of the directed p-like atomic orbitals $|\mathrm{X}\rangle, |\mathrm{Y}\rangle, |\mathrm{Z}\rangle$:

$$\begin{aligned}
\mathrm{u}_{\frac{3}{2},\frac{3}{2}} &= 2^{-1/2}|(\mathrm{X}+\mathrm{iY})\uparrow\rangle,\\
\mathrm{u}_{\frac{3}{2},\frac{1}{2}} &= 6^{-1/2}|(\mathrm{X}+\mathrm{iY})\downarrow\rangle - (2/3)^{1/2}|\mathrm{Z}\uparrow\rangle,\\
\mathrm{u}_{\frac{3}{2},-\frac{1}{2}} &= -6^{-1/2}|(\mathrm{X}-\mathrm{iY})\uparrow\rangle - (2/3)^{1/2}|\mathrm{Z}\downarrow\rangle,\\
\mathrm{u}_{\frac{3}{2},-\frac{3}{2}} &= -2^{-1/2}|(\mathrm{X}-\mathrm{iY})\downarrow\rangle,\\
\mathrm{u}_{\frac{1}{2},\frac{1}{2}} &= 3^{-1/2}|(\mathrm{X}+\mathrm{iY})\downarrow\rangle + 3^{-1/2}|\mathrm{Z}\uparrow\rangle,\\
\mathrm{u}_{\frac{1}{2},-\frac{1}{2}} &= -3^{-1/2}|(\mathrm{X}-\mathrm{iY})\uparrow\rangle + 3^{-1/2}|\mathrm{Z}\downarrow\rangle
\end{aligned} \tag{1.2}$$

The conduction band is simpler, and is constructed from s-like atomic orbitals

$$\begin{aligned}
\mathrm{u}_{\mathrm{c},\frac{1}{2}} &= \mathrm{i}|\mathrm{S}\uparrow\rangle,\\
\mathrm{u}_{\mathrm{c},-\frac{1}{2}} &= \mathrm{i}|\mathrm{S}\downarrow\rangle
\end{aligned} \tag{1.3}$$

In Eq. 1.2 and 1.3, each of the states ($|\mathrm{X}\rangle, |\mathrm{Y}\rangle, |\mathrm{Z}\rangle$ and $|\mathrm{S}\rangle$ are associated with an electron spin, having one of the two possible directions, indicated by $\uparrow$ or $\downarrow$.

The Kane Hamiltonian contains a number of constants which have to be determined experimentally or numerically using an atomistic approach (e.g. pseudopotanital calculations). All parameters are well known for the AlGaAs systems [13].

Figure 1.3 shows the $\mathbf{k}$-dependent eigenvalues $\mathrm{E}(\mathbf{k})$ of the resulting 8×8 Kane Hamiltonian for GaAs. The valence band splits into two bands for $\mathbf{k} \neq 0$, which are referred to as the heavy hole (HH), with $\mathbf{J} = 3/2$, $\mathrm{J_z} = \pm 3/2$, and the light hole (LH), with $\mathbf{J} = 3/2$, $\mathrm{J_z} = \pm 1/2$, bands. In addition, there is a split-off (SO) band corresponding to $\mathbf{J} = 1/2$, $\mathrm{J_z} = \pm 1/2$, which is shifted down in energy as an effect of spin-orbit coupling.

In AlGaAs, the SO and CB parts are relatively well separated from HH and LH for small values of $\mathbf{k}$. The 8×8 Kane Hamiltonian can thus be simplified to include only the HH and LH valence bands, by restricting the basis set to $\mathrm{u}_{\frac{3}{2},\frac{3}{2}}, \mathrm{u}_{\frac{3}{2},\frac{1}{2}}, \mathrm{u}_{\frac{3}{2},-\frac{1}{2}}, \mathrm{u}_{\frac{3}{2},-\frac{1}{2}}$.

The resulting approximate of Schrödinger equation for the valence band is then

$$\mathrm{H_v}\begin{bmatrix} \chi_{\mathrm{v},\frac{3}{2}} \\ \chi_{\mathrm{v},\frac{1}{2}} \\ \chi_{\mathrm{v},-\frac{1}{2}} \\ \chi_{\mathrm{v},-\frac{3}{2}} \end{bmatrix} = \mathrm{E_v}\begin{bmatrix} \chi_{\mathrm{v},\frac{3}{2}} \\ \chi_{\mathrm{v},\frac{1}{2}} \\ \chi_{\mathrm{v},-\frac{1}{2}} \\ \chi_{\mathrm{v},-\frac{3}{2}} \end{bmatrix} \tag{1.4}$$

where $\chi_{\mathrm{v},\mathrm{J_z}}$ are the envelope functions related to the four Bloch functions used as a basis, and $\mathrm{H_v}$ is the 4×4 Luttinger Hamiltonian:

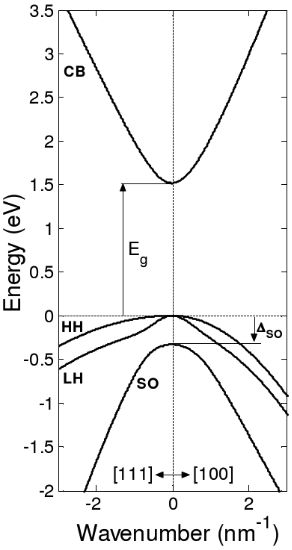

Figure 1.3: Energy band structures of GaAs calculated by 8 × 8 band $\mathbf{k} \cdot \mathbf{p}$ theory near the zone center, for two different cystallorgraphic directions [100] and [111]. Adopted from [9]

$$H_v = E_{VBO} - \frac{\hbar^2}{2m_0} \begin{bmatrix} P+Q & -S & R & 0 \\ -S^* & P-Q & 0 & R \\ R^* & 0 & P-Q & S \\ 0 & R^* & S^* & P+Q \end{bmatrix} \tag{1.5}$$

In Eq.1.5, E_{VBO} is the VB offset at $\mathbf{k}$=0 (we assume arbitrarily $E_{VBO} = 0$ for GaAs). The matrix elements in H_v will depend on which crystallographic directions that are chosen for x, y and z. In our model, the quantization direction is specified by the z direction, for z = [111]. The x direction is in the $(11\bar{2})$ plane, and the y direction in the $(1\bar{1}0)$ plane [14]:

$$\begin{aligned} &P = \gamma_1(k_x + k_y + k_z)^2, \\ &Q = \gamma_3(k_x^2 + k_y^2 - 2k_z^2), \\ &R = -(1/\sqrt{3})(2\gamma_3 + \gamma_2)(k_x - ik_y)^2 - (4/\sqrt{6})(\gamma_3 - \gamma_2)(k_x + ik_y)k_z, \\ &S = (2/\sqrt{3})(\gamma_3 + 2\gamma_2)(k_x - ik_y)k_z + (\sqrt{2/3})(\gamma_3 - \gamma_2)(k_x + ik_y)^2 \end{aligned} \tag{1.6}$$

Where γ_1, γ_2, γ_3 are the so-called Luttinger parameters which are related to the effective masses, and they are functions of their spatial coordinates.

The diagonal elements (P+Q) or (P-Q) describe the dispersion of the heavy- or light- hole bands whereas the off-diagonal elements R and S introduce coupling (mixing) between these two bands.

For $\mathbf{k} \neq 0$ the hole state will not be pure HH or LH. The normalized content of HH and LH for a state is simply given by the following equation:

$$\begin{aligned} \mathrm{HH} &= |\chi_{\frac{3}{2},\frac{3}{2}}|^2 + |\chi_{\frac{3}{2},-\frac{3}{2}}|^2 \\ \mathrm{LH} &= |\chi_{\frac{3}{2},\frac{1}{2}}|^2 + |\chi_{\frac{3}{2},-\frac{1}{2}}|^2 \end{aligned} \tag{1.7}$$

The conduction band is approximated by a single band exhibiting parabolic dispersion, with the CB Schrödinger equation

$$\mathrm{H_c}\chi_\mathrm{c} = \mathrm{E_c}\chi_\mathrm{c} \tag{1.8}$$

Where χ_c is the electron envelope function related to the Bloch functions $\mathrm{u}_{\mathrm{c},\frac{1}{2}}$ and $\mathrm{u}_{\mathrm{c},-\frac{1}{2}}$. $\mathrm{H_c}$ is the CB Hamiltonian

$$\mathrm{H}_\mathbf{c} = \mathrm{E_g} + \mathrm{E_{VBO}} + \gamma_\mathrm{e}\frac{\hbar^2|\mathbf{k}|^2}{2\mathrm{m_0}} \tag{1.9}$$

Here $\mathrm{E_g}$ is the semiconductor band gap. The second term is proportional to the energy dispersion of a free electron in vacuum. The factor γ_e can be interpreted as an effective mass $\mathrm{m_e^*} = \gamma_\mathrm{e}^{-1}\mathrm{m_0}$. Consequently, in this effective mass approximation, the periodic lattice is taken into account simply by modifying the electron mass.

Thus, the above mentioned $\mathrm{H_c}$ and $\mathrm{H_v}$ offer a simplified description of the three most important bands, neglecting possible effects due to the SO band, and mixing between CB and VB. This approach has been used for the band structure calculation in the present work.

1.1.3 Heterostructures

The developments in growth technologies such as molecular beam epitaxy (MBE) and metalorganic vapor phase epitaxy (MOVPE) enable epitaxial crystal growth with a precision of single atomic layers [15] [16]. By changing the alloy composition during the growth, semiconductor heterostructures composed of more than one material can be produced. Variation in composition are used to control the motion of electron and holes through band engineering. Knowledge of the alignment of bands at a heterojunction, where two materials meet, is essential but has proved difficult to determine. In the present thesis, only so called type-I heterostructures are studied, where the same material simultaneously minimizes the effective potential energy for both electrons and holes. For example, an electron in a sandwich of GaAs between wider bandgap $\mathrm{Al_{0.3}Ga_{0.7}As}$ regions (Fig 1.4) can be treated as the elementary problem of a potential well for electrons and for holes.

In principle, it must be possible to join the two materials perfectly in an ideal heterostructure. This requires first that they have the same crystal structure (or at least symmetry). Second, to avoid strain in the final structure, the two materials must have nearly identical lattice constants. The lattice constant of an alloy is usually given

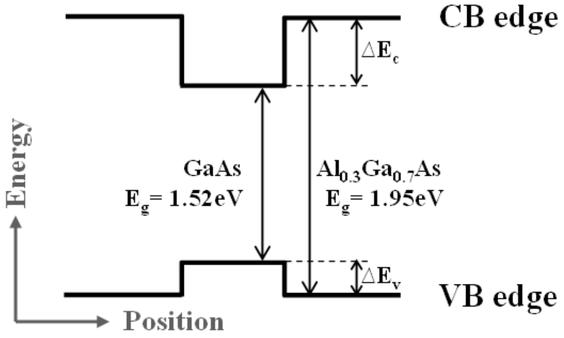

Figure 1.4: Schematic illustration of the conduction and valence band edges of an $Al_{0.3}Ga_{0.7}As/GaAs/Al_{0.3}Ga_{0.7}As$ heterostructures for T = 10 K.

by linear interpolation between its constituents, which is known as Vergard's law. Figure 1.5 is a plot of the lattice constant of various semiconductors against their minimun band gap E_g. Full lines show the cases of a direct bandgap, while dashed lines are for indirect bandgap. This plot shows that the lattice constant changes by less than 0.15% between GaAs and AlAs. Hence, it is possible to grow layers of GaAs and AlAs or any of the intermediate alloys $Al_xGa_{1-x}As$ on top of each other without introducing significant strain.

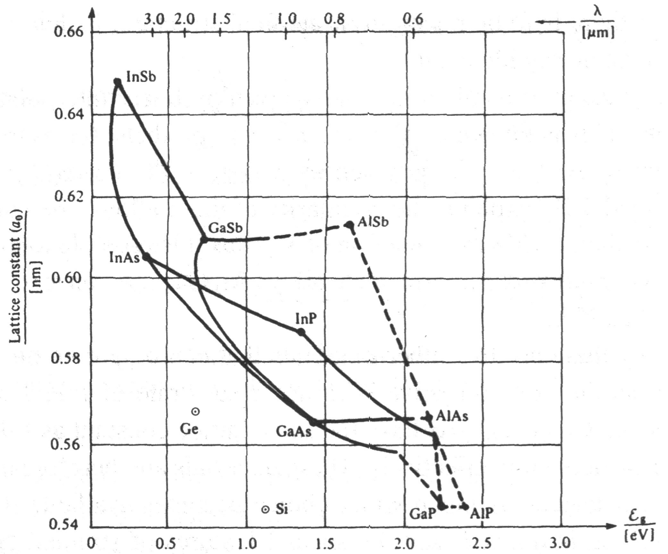

Figure 1.5: Plot of lattice constant of various semiconductors against their minimum bandgap E_g, expressed in eV and in terms of the equivalent photon wavelength. Full lines show direct bandgaps, and dashed lines represent indirect gaps. [17]

For the structure shown in Fig 1.4, if the GaAs layer is thinner than the de Broglie wavelength of the carriers($\sim$ 20 nm for electrons in GaAs), quantum confinement effects arise in the direction perpendicular to the interfaces, splitting the CB and VB states as first demonstrated for QWs [18]. In such QWs, carriers can only move freely along two spatial dimensions parallel to the QW interfaces. By fabricating low-band gap heterostructure confined in two or three directions, quantum wire (QWR) or quantum dot (QD) structures can be realized. The insets in Fig 1.6 schematically illustrate the different families of quantum structures. In QWs, QWRs and QDs, the dispersion is strongly modified as compared to the dispersion for electrons in bulk semiconductors given by Eq. 1.9.

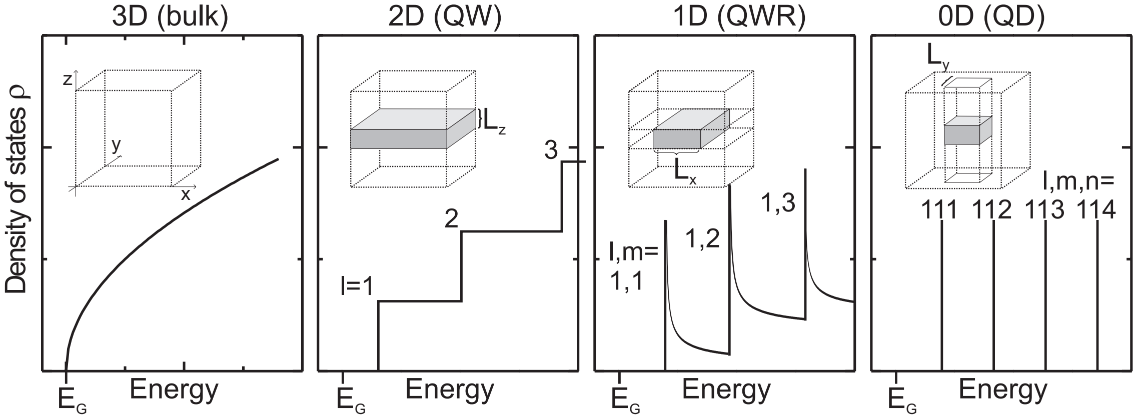

Figure 1.6: Density of states ρ for a bulk semiconductor and for semiconductor heterostructures of decreasing dimensionality. [19]

The reduced carrier dimensionality in ideal quantum structures leads to a dramatic redistribution of the density of energy states (DOS). By assuming that the Bloch functions are identical for the different materials in the heterostructure, the envelope function approximation described in the previous section can be extended to heterostructures. For a heterostructure, the envelope functions in the confined directions will not any more be plane waves. The corresponding **k** vectors in $\mathrm{H_c}$ and $\mathrm{H_v}$ have to be substituted by the momentum operator, $\mathbf{k} \rightarrow -\mathrm{i}\nabla$. Making this substitution in Eq. 1.9, we obtain the following time-independent Schrödinger equation for an electron in the conduction band:

$$[-\frac{\hbar^2}{2\mathrm{m}^*}\nabla^2 + \mathrm{V}(\mathbf{r})]\chi_\mathrm{c}(\mathbf{r}) = \mathrm{E}\chi_\mathrm{c}(\mathbf{r}) \tag{1.10}$$

where m^* is the effective carrier mass, $\mathrm{V}(\mathbf{r}) = \mathrm{E_g}(\mathbf{r}) + \mathrm{E_{VBO}}(\mathbf{r})$ is the heterostructure potential defining the quantum structure, and E is the confinement energy (measured with respect to the bottom of the potential well V). For the simple case of infinitely deep rectangular potential well, this equation can be solved analytically. The solutions for the two-dimensional (2D), 1D and 0D cases are given as a function of the quantum number l, m, n (with V = 0 inside the well).

$$
\begin{aligned}
E_{2D,l}(k_x, k_y) &= \frac{\hbar^2\pi^2 l^2}{2m^* L_z^2} + \frac{\hbar^2(k_x^2 + k_y^2)}{2m^*} \qquad l = 1, 2, ... & (1.11) \\
E_{1D,l,m}(k_y) &= \frac{\hbar^2\pi^2}{2m^*}(\frac{l^2}{L_z^2} + \frac{m^2}{L_x^2}) + \frac{\hbar^2 k_y^2}{2m^*} \qquad l, m = 1, 2, ... & (1.12) \\
E_{0D,l,m,n} &= \frac{\hbar^2\pi^2}{2m^*}(\frac{l^2}{L_z^2} + \frac{m^2}{L_x^2} + \frac{n^2}{L_y^2}) \qquad l, m, n = 1, 2, ... & (1.13)
\end{aligned}
$$

Based on these solutions, we can also calculate the density (per unit volume) of allowed energy states as a function of the electron energy E:

$$
\begin{aligned}
\rho_{3D}(E) &= \frac{(2m^*/\hbar^2)^{3/2}}{2\pi^2} E^{1/2} & (1.14) \\
\rho_{2D}(E) &= \frac{m^*}{\pi\hbar^2 L_z} \sum_{l} \Theta(E - E_{2D,l}(\mathbf{k} = 0)) & (1.15) \\
\rho_{1D}(E) &= \frac{(2m^*)^{1/2}}{\pi\hbar L_z L_x} \sum_{l,m} (E - E_{1D,l,m}(\mathbf{k} = 0))^{-1/2} & (1.16) \\
\rho_{0D}(E) &= \frac{2}{L_z L_x L_y} \sum_{l,m,n} \delta(E - E_{0D,l,m,n}(\mathbf{k} = 0)) & (1.17)
\end{aligned}
$$

where E is measured with respect to the band edge (or state), Θ symbolizes the Heaviside function ($\Theta = 0$ for $x < 0$; $\Theta = 1$ for $x \geq 0$) and δ the Dirac distribution. Figure 1.6 shows these DOS functions for different dimensionality in the case of ideal perfectly uniform quantum structures. For the 0D case, it implies discrete energy levels of electrons. In reality, it is impossible to fabricate a QW or a QWR without statistical fluctuation of the parameters defining the confinement. In order to observe the properties of 1D and 0D carriers, the size and composition fluctuation in the wires and dots should be small enough so that the low-dimensional states remain well resolved.

1.2 Excitons and optical properties of QW, QWR, QD

1.2.1 Optical absorption and polarization dependence of the interband matrix element

Optical transition in the semiconductor can occur via the absorption of a photon, thereby creating an electron-hole pairs. In optical transitions, the description can usually be simplified by neglecting photon momentum and considering vertical transitions across the bands. The rates (O) for optical transitions from a valence band state to a conduction band state due to the absorption of a photon can be estimated by Fermi's golden rule in the electric-dipole approximation, yielding

$$\mathrm{O}(\hbar\omega) \propto \sum_{\mathrm{c,v}} \int_{\mathrm{BZ}} |\mathrm{M}|^2_{\mathrm{c,v}} \delta(\mathrm{E_c}(\mathbf{k}) - \mathrm{E_v}(\mathbf{k}) - \hbar\omega) \mathrm{d}\mathbf{k} \tag{1.18}$$

where c and v designates the conduction and valence bands and $|\mathrm{M}|^2_{\mathrm{c,v}}$ is the optical dipole matrix element involving the light polarization unit vector (**e**) and carrier momentum operator (**p**),

$$|\mathrm{M}|^2_{\mathrm{c,v}} = \sum_{\mathrm{S_z}=\pm\frac{1}{2}} \left| \sum_{\mathrm{J_z}=\pm\frac{1}{2},\pm\frac{3}{2}} \langle \chi_\mathrm{c} | \chi_{\mathrm{v,J_z}} \rangle \langle \mathrm{u_{c,S_z}} | \mathbf{e} \cdot \mathbf{p} | \mathrm{u_{v,J_z}} \rangle \right|^2 \tag{1.19}$$

The atomic-like dipole matrix elements give rise to the dependence on the polarization vector **e** of the light. They are related to the quantum numbers of the initial and final states via overlap integrals $\langle \chi_\mathrm{c} | \chi_{\mathrm{v,J_z}} \rangle$. We express the polarization vector in spherical coordinate $\mathbf{e} = (\cos\varphi \sin\upsilon, \sin\varphi \sin\upsilon, \cos\upsilon)$. For a situation with quantization axis taken along the z-axis (see Fig 1.7), the expression can be written [20]:

$$|\mathrm{M}|^2_{\mathrm{c,v}} \propto \begin{cases} \frac{2}{3}(\mathrm{I}^2_{\frac{1}{2}} + \mathrm{I}^2_{-\frac{1}{2}}), \upsilon = 0 \\ \frac{1}{2}(\mathrm{I}^2_{\frac{3}{2}} + \mathrm{I}^2_{-\frac{3}{2}}) + \frac{1}{6}(\mathrm{I}^2_{\frac{1}{2}} + \mathrm{I}^2_{-\frac{1}{2}}) - \frac{1}{\sqrt{3}}(\mathrm{I}_{\frac{3}{2}}\mathrm{I}_{-\frac{1}{2}} + \mathrm{I}_{\frac{1}{2}}\mathrm{I}_{-\frac{3}{2}})\cos(2\varphi), \upsilon = \frac{\pi}{2} \end{cases} \tag{1.20}$$

where

$$\mathrm{I_{J_z}} = \langle \chi_\mathrm{c} | \chi_{\mathrm{v,J_z}} \rangle \tag{1.21}$$

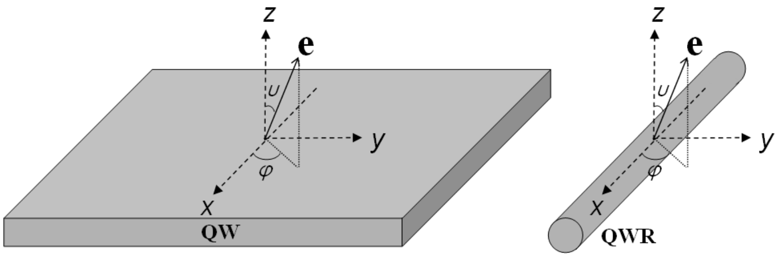

Figure 1.7: Schema of the related orientation of the polarization vector of light with respect to QW and QWR.

In a cubic 3D lattice, the absorption is independent of the polarization direction, if the anisotropy of the lattice unit cell is neglected. In QWs, the summation over the in-plane wave vector eliminates the term proportional to $\cos(2\varphi)$. The absorption depends only on the angle υ. The heavy and light hole levels decouple at the zone center for a QW, and thus exhibit pure heavy or light hole character. From Eq. 1.20, we can conclude that the HH states $\mathrm{J_z} = \pm 3/2$ participates in a transition involving linearly polarized light only if it is polarized parallel to the QW interfaces ($\upsilon = \frac{\pi}{2}$), while LH states $\mathrm{J_z} = \pm 1/2$ participates most efficiently in transitions induced by light polarized perpendicular to the interfaces ($\upsilon = 0$). Defining the degree of linear polarization P as:

$$\mathrm{P} = (\mathrm{O}_{\parallel} - \mathrm{O}_{\perp})/(\mathrm{O}_{\parallel} + \mathrm{O}_{\perp}) \tag{1.22}$$

and using Eq. 1.20, we get $\mathrm{P} = -0.6$ and $\mathrm{P} = 1$ for LH and HH transition respectively. For QWRs, each QWR VB state exhibits a predominantly heavy or light hole character, and hence participates in transitions involving light linearly polarized along or perpendicular to the QWR axis.

1.2.2 Excitons in bulk semiconductors

So far, we gave the physical picture of an optical absorption process in which: an incident radiation field excites an electron from the VB to CB, resulting in the formation of a hole in the VB. We assumed there is no interaction between the resulting electron and hole. However, since the electron and hole are carriers carrying opposite charges, the Coulomb attraction between them should be considered. Actually, an electron and a hole system forming a bound state is referred to as an exciton. Attraction between the electron and hole causes their motion to be correlated. Excitons can be treated in two limiting cases, which depend on the properties of the material. In semiconductors, the dielectric constant is generally large, and as a result, screening tends to reduce the Coulomb interaction between electrons and holes. The result is a Mott-Wannier exciton, which has a radius much larger than the lattice spacing. As a result, the effect of the lattice potential can be incorporated into the effective masses of the electron and hole, and because of the lower masses and the screened Coulomb interaction, the binding energy is usually small, typically on the order of 0.01 eV. In contrast, Frenkel excitons correspond to strong electron-hole attraction, as in ionic crystals. The electron and hole are then tightly bound to each other within the same or nearest-neighbor unit cells.

The attractive potential leads to a reduction in the total energy of the electron-hole system. As the hole mass is generally much greater than the electron mass, then the two-body system resembles a hydrogen atom, with the negatively charged electron orbiting around the positive hole. The exciton is quite stable and can have a relatively long lifetime, of the order of hundreds of ps to ns. Exciton recombination is an important feature of low temperature photoluminescence, although as the binding energies are relatively low in the investigated materials, i.e. a few meV to a few tens of meV, the excitons tend to dissociate at higher temperatures. The binding energy and orbital radius can be represented well by Bohr's theory, with the correction for the mass being the central change [21] [22]. This is implemented by exchanging the orbiting electron's mass with the reduced mass of the two-body system, in this case, the electron-hole pair. The reduced mass is given by:

$$\frac{1}{\mu} = \frac{1}{\mathrm{m_e^*}} + \frac{1}{\mathrm{m_h^*}} \tag{1.23}$$

Hence, the binding energy becomes:

$$\mathrm{E_{X^0}} = -\frac{\mu \mathrm{e}^4}{32\pi^2\hbar^2\epsilon_\mathrm{r}^2\epsilon_0^2} \tag{1.24}$$

and the Bohr radius is:

$$\lambda = \frac{4\pi\epsilon_\mathrm{r}\epsilon_0\hbar^2}{\mu \mathrm{e}^2} \tag{1.25}$$

Taking typical values for bulk GaAs, i.e. the Γ valley electron and the HH effective masses, $\mathrm{m_e^*} = 0.067\mathrm{m_0}$ and $\mathrm{m_{hh}^*} = 0.062\mathrm{m_0}$, we get $\mu = 0.060\mathrm{m_0}$. Using the static dielectric constant $\epsilon_\mathrm{r} = 13.18$ [23], the exciton binding energy and Bohr radius are respectively,

$$\mathrm{E_{x^0}} = -4.7\mathrm{meV} \quad \text{and} \quad \lambda = 115\text{Å} \tag{1.26}$$

which agree well with the low-temperature measured values [23].

1.2.3 Excitons in QWs and QWRs

In bulk, the total energy of the exciton is simply the energy of the free electron-hole pair (i.e. the band gap) plus the exciton binding energy $\mathrm{E_{X^0}}$, whereas if the exciton is in the heterostructure, there are additional components due to the electron and hole confinement energies:

$$\begin{array}{ll} \mathrm{E} = \mathrm{E_g} + \mathrm{E_{x^0}} & \text{(bulk)} \\ \mathrm{E} = \mathrm{E_g} + \mathrm{E_c} + \mathrm{E_v} + \mathrm{E_{x^0}} & \text{(heterostructure)} \end{array} \tag{1.27}$$

The total exciton energy is clearly a function of structure because of the structural dependency of the confinement energies. In addition, it can be expected that $\mathrm{E_{X^0}}$ is also structurally dependent. This is easy to be understand since the electron hole separation can vary considerably between amongst different heterostructures. In another words, the Coulombic potential energy can be very different depending on the electron and hole wavefunction distributions.

The exciton problem is analytically solvable for ideal 2D QW or 1D QWR systems. For any arbitrary dimension α, the ideal exciton problem can be solved analytically within the fractional dimensional theory [24]. The exciton binding energy can be expressed by the following function:

$$\mathrm{E_{X^0}} = \frac{\mathrm{E_{X^0}(bulk)}}{[1 + (\alpha - 3)/2]^2} \tag{1.28}$$

Thus, the binding energy of an exciton confined in an ideal 2D QW is four times of that in bulk. For an ideal 1D QWR, the binding energy approaches infinity. For realistic 2D or 1D structures with finite extensions and potential barriers, the confined exciton should be ascribed as for a fractional dimension [25] [26]: for QW, we can use a value between 3 and 2 to represent its dimensionality whereas for QWR, similarly, a value between 3 and 1 can be applied. The exciton absorption strength is proportional to the probability to find the electron and hole at the same space.

1.2.4 Excitons in QDs

The exciton concept for QDs is slightly different from that for QWRs, QWs or bulk semiconductors, since the Coulomb potential is not responsible primarily for the electron hole binding. Instead, the structural confinement plays more important role for the formation of exciton. The Coulomb interaction merely modifies the existing confinement potential. Since this modification can be either positive or negative, the resulting exciton complexes with positive or negative binding energies can be both achieved in QDs. The radiative decay of QD excitons yields spectrally sharp emission peaks with life-time limited homogeneous broadening for temperature approaching $\mathrm{T} = 0$ K [27]. In the strong confinement regime, where the energy quantization due to confinement is larger than the Coulomb interaction energies, the Coulomb interaction can be treated as a perturbation of the independent particle electron and hole states, $\chi_\mathrm{c}(\mathbf{r}_\mathrm{e})$ and $\chi_\mathrm{v}(\mathbf{r}_\mathrm{h})$ [28]. The Coulomb interaction between the electron and the hole can be given by first order perturbation theory:

$$\mathrm{E}_{\mathrm{X}^0} = -\frac{\mathrm{e}^2}{4\pi\epsilon_0\epsilon_\mathbf{r}}\int\frac{|\chi_\mathrm{c}|^2|\chi_\mathrm{v}|^2}{|\mathbf{r}_\mathrm{e}-\mathbf{r}_\mathrm{h}|}\mathrm{d}\mathbf{r}_\mathrm{e}\mathrm{d}\mathbf{r}_\mathrm{h} \tag{1.29}$$

Another approach is to treat the QD exciton binding energy by using a self-consistent Hartree approximation. It solves the independent particle states in the Coulomb potential produced by the other particle in an iterative way [29]. In that case, a separable exciton wavefunction is assumed and the single electron and hole states, χ_c and χ_v, are determined self-consistently [30] [29]:

$$[\mathrm{H}_\mathrm{v}+\mathrm{V}_\mathrm{e}]\chi_\mathrm{v} = \widetilde{\mathrm{E}}_\mathrm{v}\chi_\mathrm{v}, \quad [\mathrm{H}_\mathrm{v}+\mathrm{V}_\mathrm{h}]\chi_\mathrm{c} = \widetilde{\mathrm{E}}_\mathrm{c}\chi_\mathrm{c} \tag{1.30}$$

where $\mathrm{H}_{\mathrm{v,c}}$ is the empty dot Hamiltonian of Eq. 1.4 and 1.8. The associated Coulomb potential $\mathrm{V}_{\mathrm{e,h}}(\mathbf{r})$ is obtained by solving the Poisson equation:

$$-\mathrm{e}|\chi_\mathrm{c}|^2 = \epsilon_0\nabla(\epsilon_\mathrm{r}\nabla\mathrm{V}_\mathrm{e}), \quad \mathrm{e}|\chi_\mathrm{v}|^2 = \epsilon_0\nabla(\epsilon_\mathrm{r}\nabla\mathrm{V}_\mathrm{h}) \tag{1.31}$$

Here, ϵ_r is the static dielectric constant of the respective material as a function of the position. If E_c and E_v denote the respective eigenvalues of H, then the exciton binding energy is

$$\mathrm{E}_{\mathrm{X}^0} = (\mathrm{E}_\mathrm{c}-\mathrm{E}_\mathrm{v}) - (\widetilde{\mathrm{E}}_\mathrm{c}-\widetilde{\mathrm{E}}_\mathrm{v}) - (\langle\chi_\mathrm{v}|\mathrm{V}_\mathrm{e}|\chi_\mathrm{v}\rangle - \langle\chi_\mathrm{c}|\mathrm{V}_\mathrm{h}|\chi_\mathrm{c}\rangle)/2 \tag{1.32}$$

A QD can accommodate exciton complexes consisting of more than one electron and one hole. If the numbers of electrons and holes are not equal, the exciton is charged. There are several typical QD excitons, referred as neutral (or single) exciton (X), negatively charged exciton (X^-), positively charged exciton (X^+) and biexciton (2X). X^+ and X^- are sometimes referred as trions. Figure 1.8 illustrates the population of electrons and holes for these four kinds of excitons. The X^- exciton has an extra electron that can interact with the other electron and hole. This Coulomb interaction will eventually modify the energy of the system. Reflecting on the photon energy, a shift of X^-

transition with respect to X will be observed in the luminescence spectra. Depending on whether the electron-electron repulsion or the electron-hole attraction wins, the shift can be negative or positive as determined by the total energy of the QD system before and after the recombination. Typically, in the pyramidal GaAs(InGaAs)/AlGaAs QD system, the energy of the X^- transition is 3-5 meV lower than that of X [19]. Similarly, the X^+ and 2X also shift in energy as compare to X. For the 2X, this shift is about 2 meV to the low energy side, while for X^+, it can be either blue or red shift ∼1 meV or even less, sensitive to the actual structure. [19]

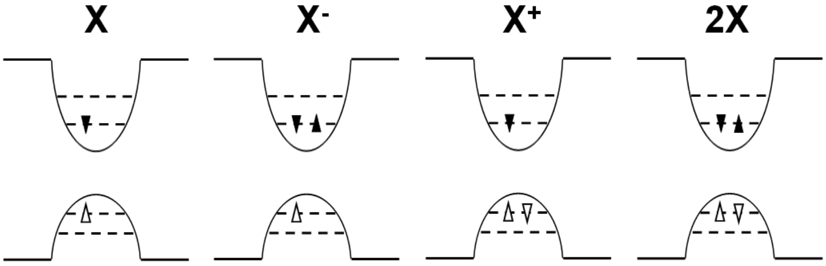

Figure 1.8: Scheme of a QD occupied with X, X^-, X^+, 2X

More complicated exciton complexes also exist, e.g. X^{--}, 3X, as shown in Fig 1.9 (a) and (b) respectively. The X^{--} is obtained when a QD is populated with two extra electrons in addition to the exciton yielding a double negatively charged exciton. Here, due to the Pauli's exclusion principle, one of the extra electrons must be accommodated in the excited level (”p-shell”). After recombination, two electrons remaining in the QD can have either parallel or anti-parallel spins, resulting in a fine split of the final state (Fig 1.9 (a)). Therefore, the optical decay of X^{--} can be distributed in two photon energies.

Multiexciton complexes can be formed when a QD is populated with more than one exciton. 2X is the simplest multiexciton. The 3X is the second simplest. Again, one pair of electron and hole has to be accommodated in the p-shell. Thus, the 3X exciton can radiatively decay over both a p to p transition and an s to s transition, emitting photons of different energies.

The distinct separation of photon energies resulting from the decay of the different excitonic complexes is the key optical property of QDs different from other higher dimensional structures. This makes semiconductor QDs usable as single and correlated photon emitters, promising for future quantum information processing application.

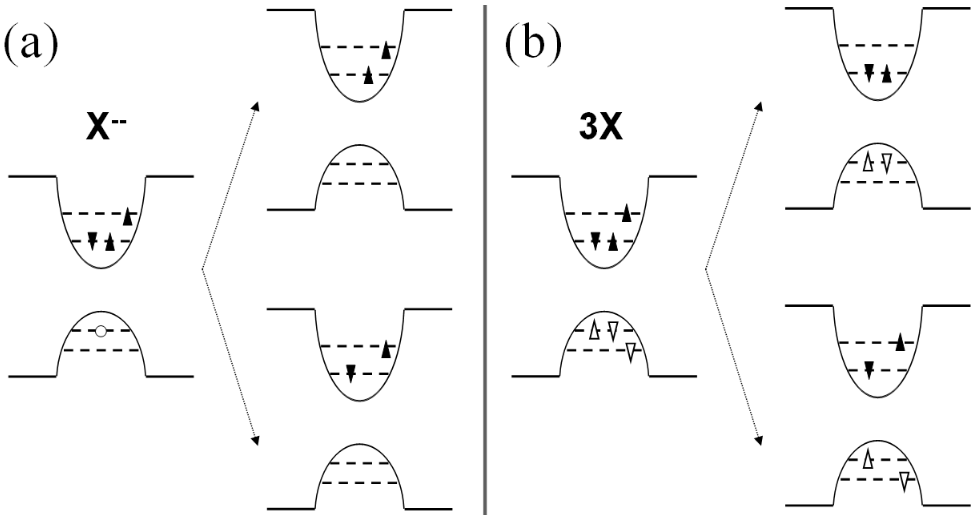

Figure 1.9: Schematic illustration of radiative decays of (a) X^{--}, (b) 3X

1.3 QWRs and QDs: state of the art

1.3.1 QWRs fabrication techniques

Nowadays, high quality 2D QWs are achieved by using material deposition techniques on planar substrates, for example organometallic chemical vapor deposition (OMCVD) and molecular beam epitaxy (MBE), where one can grow semiconductors layer-by-layer with different bandgap materials. These techniques are already quite mature. Some remaining questions are how to get purer materials, control of chemical composition, smoother interfaces between the layers and so on. However it is still challenging to get lower dimensional quantum structures, such as QWRs (1D) and QDs (0D), with high quality and controllability.

QWRs of different potential shapes can be realized, depending on the fabrication technique. The corresponding fabrication technology plays a crucial role in tailoring the desired electronic and optical properties. Below we will give a review on the important QWR fabrication techniques.

QWRs on patterned substrates This technology is based on lithography and wet chemical etching to reveal crystalline facets, creating nonplanar patterned substrates. Then, due to crystallographic orientation dependent growth rate, the subsequent MOVPE or MBE growth results in enhanced thickness at specific portions of the patterned substrate, forming QWRs if their lateral dimensions could be controlled in quantum size regime (less than a few tens of nanometers) [31]. Representative structures fabricated by this technique are V-groove QWRs [32] [33], Ridge-type QWRs [34] [35] and QWRs made on sidewalls [36] [6].

V-groove QWRs were developed by Kapon et al [32], utilizing the growth rate enhancement around the bottom of ”V-shaped” groove etched into a flat substrate. The fabrication processes are illustrated in Fig 1.10 (left panel): (a) preparation of line-and-space photoresist pattern using lithography; (b) formation of V-grooves by wet chemical etching; (c) growth of GaAs/AlGaAs heterostructures to realize QWRs at the bottom of the V-groove.

Ridge-type QWR is a wire formed at the top of a sharp ridge structure. It is very similar to V-groove QWR in the sense that a ridge structure can be viewed as an inverted V-groove. Figure 1.10 (right panel) illustrates the MBE growth of GaAs/AlGaAs QWRs on [100]-oriented ridges:(a) formation of sharp ridges with a self-limited ridge top width (W) on a GaAs ridge substrate aligned along the [110] direction by MBE growth of GaAs. The thick solid and dashed lines represent ridge substrates fabricated by dry and wet chemical etchings, respectively; (b) the variation of surface chemical potential around the ridge top. (c) formation of GaAs/Al(Ga)As QWRs on the sharp ridge top.

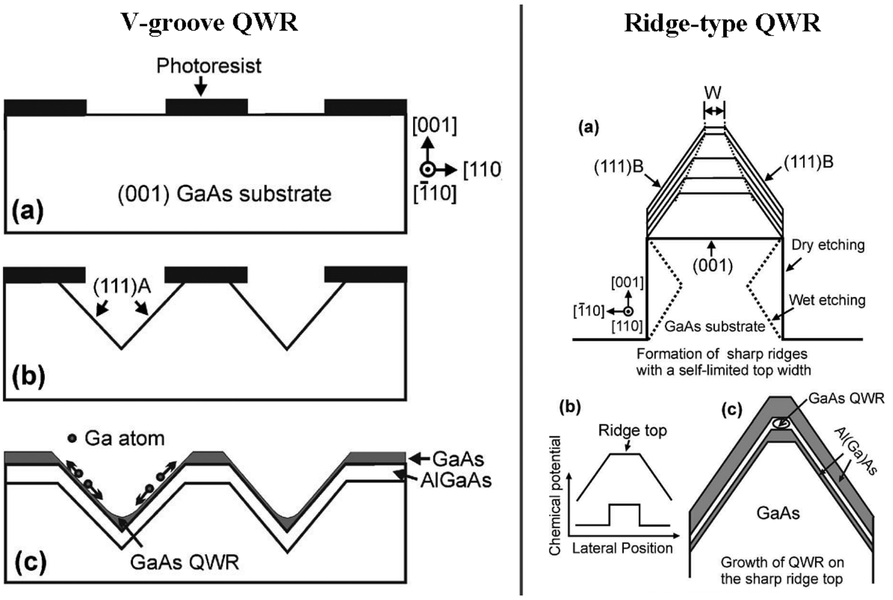

Figure 1.10: (Left)Schematic illustration for the fabrication processes of V-shaped GaAs/AlGaAs QWRs; (Right)Schematic illustration of MBE growth of GaAs/AlGaAs QWRs on [100]-oriented ridges. Adopted from [37]

As illustrated in Fig 1.11 (a), the sidewalls of a shallow mesa structure with height in the quantum-size regime could serve as a template for QWR growth, providing that group-III adatoms on both the mesa top and mesa bottom migrate towards the sidewalls. The advantage of this kind of QWR is that its quasi-planar surface can be easily incorporated into device structures. But unfortunately, in most cases, the sidewall represents a slow-growing facet; group-III adatoms arriving on the sidewall facets tend to migrate away from the sidewalls towards the mesa top and bottom. This brings difficulties to the formation of QWR. One successful case is demonstrated by Nötzel et al [36] [6]. They found the sidewalls of the mesa stripes aligned along the [01$\bar{1}$] direction on (311)A substrate with a (311)A-like facet could act as a local fast-growing facet for

GaAs, therefore could be applied to the growth of sidewall QWRs (Fig 1.11 (b)). This is due to the absence of any slower-growing facets near this specific sidewall due to the low symmetry of the (311)A surface [36] [6]. Growth of sidewall GaAs QWRs in parallel grooves along $(01\bar{1})$ orientation etched on 6° off (100) GaAs substrate was reported even earlier by Colas et al in 1990 [38] [39].

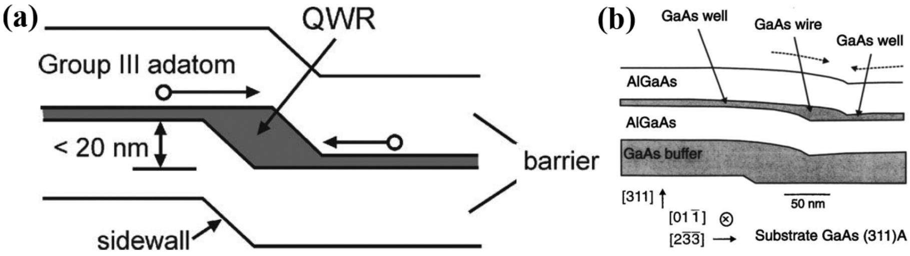

Figure 1.11: Schematic illustration of the formation of sidewall QWRs. Adopted from [37]

T-shaped QWs on cleaved edges This kind of QWR is formed at the intersection of two QWs using cleaved-edge overgrowth technique [40] [41]. As illustrated in Fig 1.12, the fabrication processes are the following: (a) growth of GaAs/AlGaAs single or multiple QWs on (001) GaAs substrate; (b)cleaving of the sample in the ultrahigh vacuum chamber of a MBE machine to expose a (100) surface; (c-d) a second MBE growth on the exposed (100) surface. The second growth can be either of a modulation-doped AlGaAs layer (c) or a GaAs well layer followed by an AlGaAs barrier layer (d) for electron transport or optical studies respectively. One weak point of this technique is that it is quite difficult to obtain a strong 1D confinement since the depth of the effective 1D confinement potential is only of the order of $30 - 40$ meV even when the GaAs/AlAs, InGaAs/AlGaAs material combinations are used [42].

Others There are several other well known technique for fabrication of QWRs. For example, QWs on vicinal substrates (including QWRs based on control of monoatomic steps [43] [44] and QWRs based on multiatomic steps [45] [46] [47] [48], QWs on corrugated high-index substrates [49] [50] [51], and QWs based on stain-induced self-organization [52] [53].

Besides, the synthesis of semiconductor nanowires (or nano whiskers) grown "under" metal particles are also studied intensively worldwide for a wide spectrum of materials [54]. This idea was demonstrated as early as the 1960s by Wagner et al [55]. A corresponding theory was developed based on the "vapor-liquid-solid" mechanism. The main growth process can be divided into two steps as illustrated in Fig 1.13 (a) and (b): 1) formation of small droplets; and 2) the alloying, nucleation and growth of nanowire. Moreover, heterostructural nanowires can be also formed by adding one or more layers of a second semiconductor compound material horizontally (Fig 1.13 (c)) or radially (Fig 1.13 (d)) to the first one by changing the type of the precursor used [54].

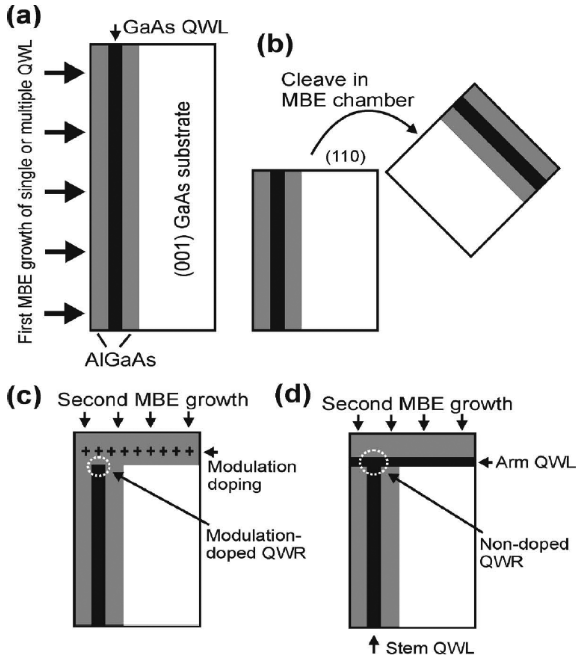

Figure 1.12: Schematic illustration of the fabrication processes of T-shaped QWRs. Adopted from [37]

1.3.2 Optical studies of QWRs

Among the above mentioned varies QWR fabrication techniques, T-shaped QWRs and V-groove QWRs are most intensively investigated since these QWRs offer the highest structural and optical qualities. Here, we will discuss the optical properties of these two sorts of QWRs mainly in relation to two aspects: disorder effect and exciton recombination.

Disorder in quantum wires

Due to increased interface-to-volume ratio in QWRs as compare to two-dimensional QWs, some intrinsic quantum effects in QWRs are masked by structural fluctuations. For example, it has been shown that excitons in a QWR are completely localized in monolayer step-induced island at low temperature [56] [57].

Different imaging techniques were developed for visualizing the structural disorder. A very powerful tool for imaging the localization effect is scanning micro-PL, in which the excitation beam can be moved along the QWR by piezoelectric actuators in order to obtain mapping of the emission along the wire axis. Fig 1.14 shows examples of the scanning micro-PL images of single V-groove QWRs at 10K. Such images shown were measured on two different generations of QWRs formed in V-groove based on different growth conditions [56] [58]. In Fig 1.14(a) and (b), the QWR has quite rough interfaces, containing numerous localized islands. These types of QWRs are often regarded as QWRs in the 0D-regime. The QWRs of the new generation have much better quality,

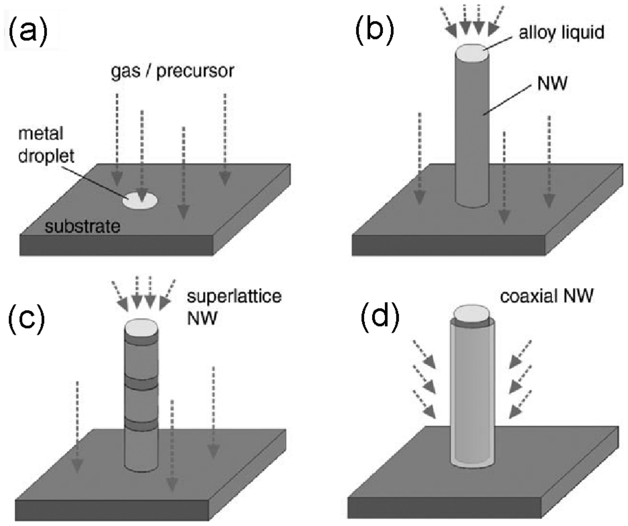

Figure 1.13: Nanowires of different structures based on the "bottom up" growth mode: (a) Exposure of a metal-droplet-coated substrate to reactant precursors; (b) a monophase nanowire grown outwards, with the metal droplet acting as catalyst; (c) a superlattice nanowire grown by consecutively alternating the reactant precursors; (d) a coaxial nanowire formed by conformal coating of the preformed nanowire in (b) with a different material. Adopted from [54]

in the sense that the localized islands are much longer on the order of a few microns. This generation is referred as QWRs in the 1D-regime.

The localization of excitons occurs mainly due to fluctuations of the interfaces of the QWR, translating into potential fluctuation equivalent to of about 10 meV on the central (001) facet, and 3 meV for the lateral (113)A facets. For QWRs in the 1D regime, this fluctuation energy can be identified from Fig 1.14(b), in which the 3 meV fluctuations are the most common ones. In the same time, the exciton localization length (L_{loc}) is also derived from the same image yielding $1 \sim 2\mu$m. The same method can not be applied to QWRs in the 0D-regime due to the limitation in the spatial resolution of the scanning μPL image system. This problem can be solved by performing μPLE spectroscopy. Detecting at certain chosen photon energies that are associated with a given localized quantum box, one can find the corresponding excited state in μPLE spectra. Then, for a given ground to excited state separation, the exciton localization length can be determined by model calculations.

High quality T-shaped QWRs fabricated by cleaved-edge overgrowth with MBE on the interface improved by a growth-interrupt high-temperature anneal reveal high uniformity, sharp spectral width and small Stokes shift of 1D excitons [60]. Figure 1.15 (a) showing scanning micro-PL spectra by 1 μm steps over 30 μm along the T-shaped wires at 5K [60]. Well-resolved sharp peaks are observed for the T-shaped wires (1.578 eV), giving FWHM of only 1.5 meV [60]. Figure 1.15 (b) shows scaning micro-PL spectra by 10 μm steps over 500 μm along the same T-shape wires in (a), showing

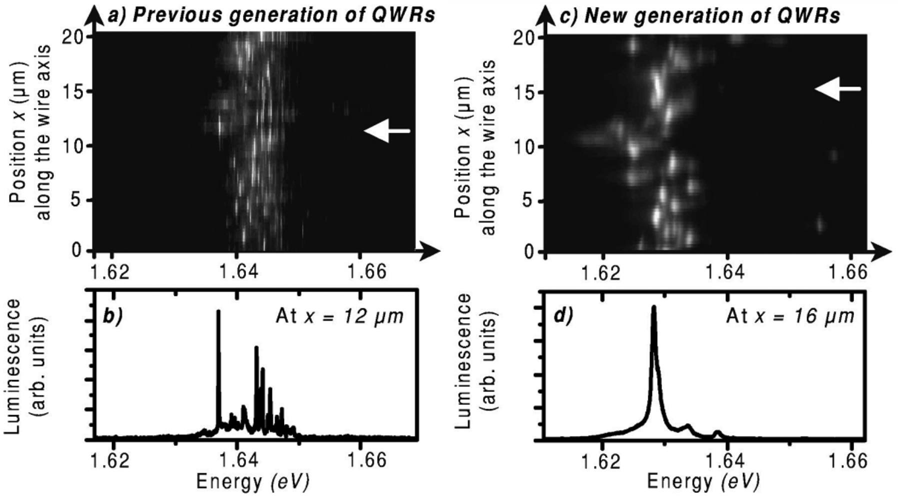

Figure 1.14: Scanning optical images of a single wire of the previous (a) and new (c) generation of QWR's. The μPL intensity is represented by gray levels. Typical μPL spectra, extracted from these images at the positions indicated by white arrows, are presented in (b) and (d). Adopted from [59].

uniform PL over 500 μm.

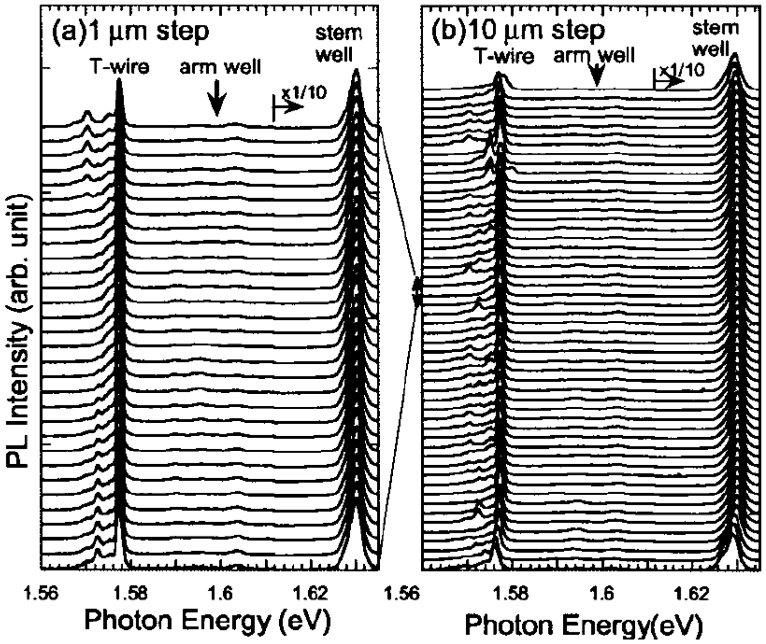

Figure 1.15: Scanning PL spectra measured in (a) 1 μm steps for 30 μm and (b) 10 μm steps for 500 μm along T wires at 5 K. The measured 20 μm region of (a) is indicated by side arrows in (b). Adopted from [60].

Exciton dynamics

The difference in the density-of-states (DOS) of QWs and QWRs is reflected in different temperature dependencies of exciton radiative lifetime ($\tau_{\rm rad}$). This effect directly reveals the dimensionality of the exciton system. Free excitons limited to near zero center-of-mass wave number can recombine radiatively, due to conservation of momentum. In quantum structures, the confinement spreads the exciton wavefunction in **k**-space to cover states that are not optically active, in which prolongs the radiative lifetime. The intrinsic radiative lifetime for excitons in ideal QWs is predicted to be $\sim$ 10 ps theoretically, while for ideal QWRs, this value should be about 150 ps [61]. In reality, excitons are thermally populated over the available states, only a faction occupies the optically active states. In 2D QWs, $\tau_{\rm rad}$ has a linear dependence of T, while in 1D QWRs, $\tau_{\rm rad}$ scales as $\sqrt{\rm T}$ [61]. For QD, the situation is more special, as long as $\rm k_B T$ is smaller than the energy separation between the first two levels of the QD, $\tau_{\rm rad}$ is not dependent of temperature. The measured radiative lifetime of InGaAs/GaAs QDs at low temperature ($\sim$10 K) is about 1 ns [62].

The QWR in the 0D-regime is composed of many localized segment with a localization length $\rm L_{loc}$, acting as weakly confined QDs. Time-resolved PL studies on radiative lifetime of excitons in such segments reveals that $\tau_{\rm rad}$ is inversely proportional to its length $\rm L_{loc}$ [63]. At very low temperature ($<$ 20 K), it is even temperature independent. Since the confinement energy of these segments is only about a few meV, the relaxation can be assisted by emission of longitudinal acoustic (LA) phonons. For QWR in the 1D-regime, $\tau_{\rm rad}$ of excitons is proportional to $\sqrt{\rm T}$ as predicted theoretically [59] [61] [64].

1.3.3 QD and QD molecule fabrication techniques

Various techniques were employed to fabricate QDs or QD molecules, which consist of several closely spaced QDs. Most of these techniques are classified into two classes: the top-down approach and the bottom-up approach. The previous approach mostly relies on lithography to define the resulting nanostructures. Several methods following this approach were investigated, including etching and regrowth [65], and electrostatic gating [66] [67], stain-induced potential wells [68] [69] [70], laser-induced interdiffusion between barrier and well materials [71]. The advantages of using lithographic techniques are the flexibility in the pattern design and compatibility with very large scale integrated semiconductor technology. But, the constrains are also obvious: these techniques usually produce QDs in the weak confinement regime and have limited resolution and imperfections induced by the lithography.

The bottom-up approach has achieved more success. It relies on nature to fabricate nanostructures based on atomic or molecular species and results in higher QD quality (almost defect-free interfaces). Nanostructures can nucleate at random sites, or grow at the positions defined by pre-patterning. Below, we will introduce three most intensively investigated QD fabrication techniques.

Strain-induced Stranski-Krastanow (SK) growth. This growth mechanism was first proposed by I. Stranski and L. Von Krastanow in 1939. It is now the most commonly used self-organization growth method for QD fabrication. The process is rather simple and does not require substrate processing. Deposition of layers with lattice constant different from that of the substrate results in the the formation of 2D strained epitaxial layers after growth of a few monolayers. Then, the strain is released due to the spontaneous nucleation of nanometer-sized islands at random sites [72] [73] [74]. These islands, resting on a so-called 2D wetting layer, act as QDs, confining electron and holes in 3D. Fig 1.16(a) is a schematic illustration of the SK growth mode [75]. It produces high density QDs, interesting for device applications. Drawbacks of this technique are the large QD size nonconformity and lack of position control. QD molecules can be also fabricated by vertical stacking layers containing QDs [76], as upper islands tend to stack on lower islands due to the strain field induced by the bottom islands. Fig 1.16(b) is a cross-sectional TEM images of stacked QDs grown in SK growth mode [76].

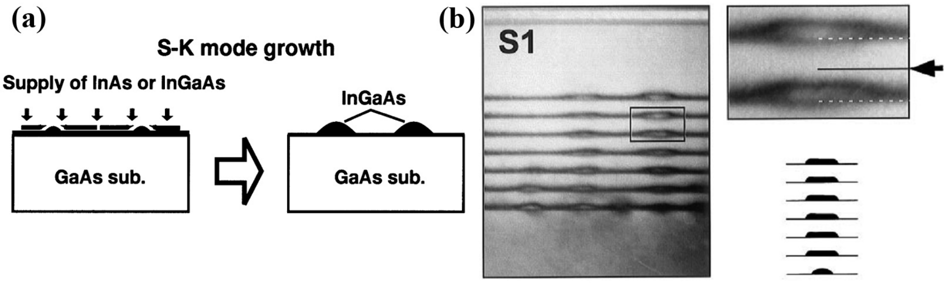

Figure 1.16: (a)Schematic illustration of SK growth mode. Adopted from [75]. (b)Cross-sectional TEM images of stacked SK QDs [76].

Twofold cleaved edge overgrowth. In Subsection 1.3.1, we have introduced the cleaved edge overgrowth technique for fabricating T-shaped QWRs. Furthermore, Grundmann et al predicted theoretically that electronic QDs form at the juncture of three orthogonal QWs, which could be fabricated with twofold cleaved edge overgrowth [77]. This kind of T-shaped QDs was realized by W. Wegscheider et al in 1997 [78]. Coupled QDs can be also achieved in this way [79], as shown in Fig 1.17.

This method allows precise control over the QD size but only very limited number of QDs can be produced at one time. Another drawback of this method is that the confinement strength is usually quite weak.

Selective area MOVPE growth method. Some groups reported the fabrication of an array of mesas on an As-terminated GaAs (111)B substrate. An array of resist patterns aligned in the [110] direction was defined by lithography, followed by wet chemical etching. Growth stopped when each mesa consisted of a truncated triangular pyramid. The mesa top is a (111)B facet, whose size ranges between the initial pattern-defined size and zero. Figure 1.18 illustrates schematically the formation of QDs using this method [80]. Similar GaAs pyramids can be fabricated on (100) substrates with square openings by MOVPE [81]. This method was also combined with the SK growth mechanism, resulting area-controlled growth of self-assembled QDs with improved QD density and size distribution [82].

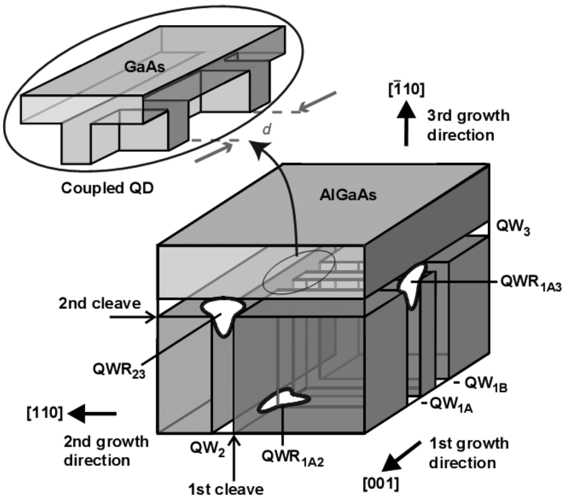

Figure 1.17: Schematic illustration of a T-shaped coupled QD structure. Adopted from [79].

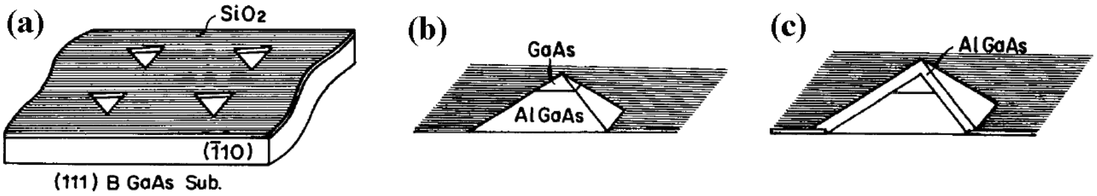

Figure 1.18: Schematic illustration of fabrication procedure for truncated tetrahedral QDs. Adopted from [80].

Seeded growth on nonplanar substrates. One representative structure formed with this approach is the QDs self-formed in inverted tetrahedral pyramids (this thesis work, and also in ref. [83] [19]). The mechanism of QD formation will be discussed in detail in Chapter 2.

H. Lee et al. proposed an approach to control the formation of InAs self-assembled islands on (001) GaAs substrate [84]. The process consists three main steps: 1. Defining the mesa lattices (checkerboard array of square mesas, resembled truncated pyramids); 2. Regrowth of the GaAs buffer layer on patterned GaAs surfaces; 3. Growth of InAs island on patterned substrates. Depending on the growth procedure, two types of sample structures can be fabricated, as shown in Fig 1.19. For type I islands, the InAs QDs are formed between mesas due to capillarity. Type II islands are achieved by introducing strain into regrowth. The majority of InAs QDs were formed in this case on top of mesas (Fig 1.19 (b)).

More recently, laterally QD molecules were produced on GaAs (011) substrates by a unique combination of MBE and in situ atomic layer precise etching [85] [86]. Initially an array of homogeneously sized nanoholes is created by locally strain-enhanced etching of a GaAs cap layer above InAs QDs. Deposition of InAs onto the nanoholes results in a preferential formation of InAs QD molecules around the holes (marked by dashed

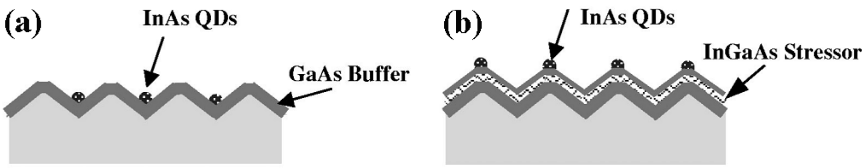

Figure 1.19: Sample structure for two types of regrowth. Sketches of (a) type I islands and (b) type II islands. Adopted from [84].

circles). The number of QDs per QD molecule ranges from 2 to 6, depending on the InAs growth conditions (Fig 1.20) [86].

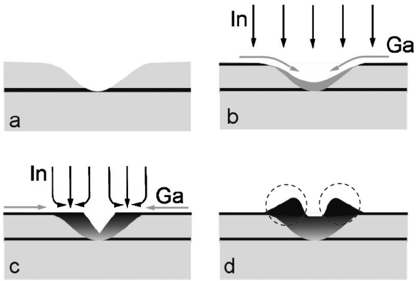

Figure 1.20: Schematic illustration of the molecule formation (a) initial nano-hole, (b) early stage of filling hole process, (c) preferential InAs growth at the hole edge, and (d) QD bimolecule formation. Dashed circles indicate where the dots are formed. [86]

1.3.4 Optical studies of QDs

Recent success in fabrication of high-quality QD structures triggered new interest in study of nonclassical light. Atomic-like properties of QDs result in discrete energy states and sharp lines in PL spectra. Moreover, the QDs can be used as sources for generating nonclassical light with tunable photon statistics, which is promising for novel quantum device application in quantum communication and computation. Intense effort has been directed towards the understanding of the optical properties of these systems. Here, we will focus our attention on the recent progress in studies of single and correlated photon emission from semiconductor QDs.

Experimentally, the statistics of photon emission from single QDs is normally investigated by using a combination of a normal micro-PL setup and two single photon detectors in a Hanbury Brown and Twiss (HBT) configuration (details of such kind of setup will be introduced in Subsection 2.2.6 later). The incoming flux of photons are split by a beamsplitter towards two single photon detector with a 50/50 ratio. The outputs of the two detectors serve as start- and stop-signals for a correlation unit, producing histograms displaying the cumulative number of recorded time delays between start- and stop-signals. In principle, these histograms are proportional to the second order correlation functions, which is defined as [87] [88].

$$g^{(2)}(\tau) = \frac{\langle : I(t)I(t+\tau) : \rangle}{\langle I(t) \rangle^2} \tag{1.33}$$

where::indicates normal ordering and I(t) is the measured intensity. $g^{(2)}(\tau)$ describes the probability for detecting a photon at time τ provided that a first photon has been detected at time $\tau = 0$.

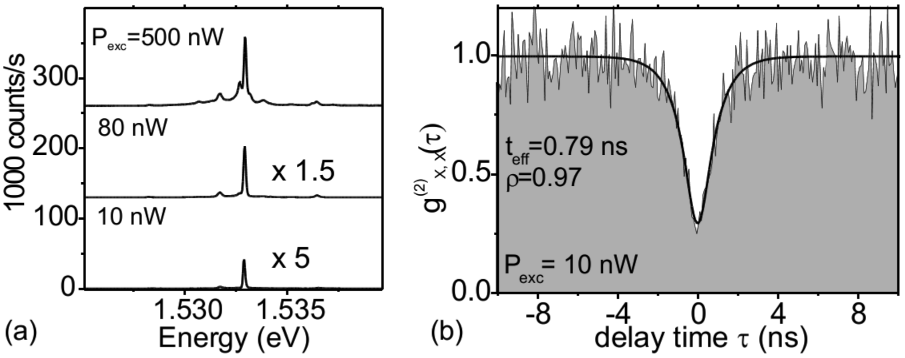

Figure 1.21: (a)Power dependent X emission peak under non-resonant excitation. T = 10 K (b)Measured second order correlation function $g^{(2)}_{X,X}(\tau)$ for photons emitted by the same QD. [19]

Continuous wave(CW) single photon emission and triggered (excited by a pulsed laser) single photon emission were demonstrated by several groups using SK QDs [89] [90] [91] [92] and pyramidal InGaAs (GaAs) QD systems [19]. The autocorrelation curves show pronounced antibunching dips around $\tau = 0$ (Fig 1.21(b)). Under CW excitation, a narrowing of the antibunching dip was also observed for increasing excitation power, in agreement with theoretical prediction of the $g^{(2)}(\tau)$curves [19]. This closing of the dip is due to the decreased characteristic time for electron hole pair capture into QD [19]. Improvement of single photon emission properties by making use of the Purcell effect [93] in micropost microcavities was also reported in Ref. [94] [95] [96].

Cross-correlation measurements provide a powerful tool for investigating the QD multiexciton features. The second-order cross-correlation function is expressed as

$$g^{(2)}_{i,j}(\tau) = \frac{\langle I_j(t)I_i(t+\tau) \rangle}{\langle I_i(t)I_j(t) \rangle} \tag{1.34}$$

where $I_i(t)(I_j(t))$ is the measured intensity of the ith(jth) multiexciton transition. $g^{(2)}_{i,j}(\tau)$ describes the probability for detecting a photon at time τ from the ith multiexciton on the condition that a first photon from the jth multiexciton has been detected at time $\tau = 0$.

Experimentally, studies of correlated photon emission from single QDs were mainly focused on biexciton-exciton, trion-exciton, and trion-biexciton transitions. Kiraz et

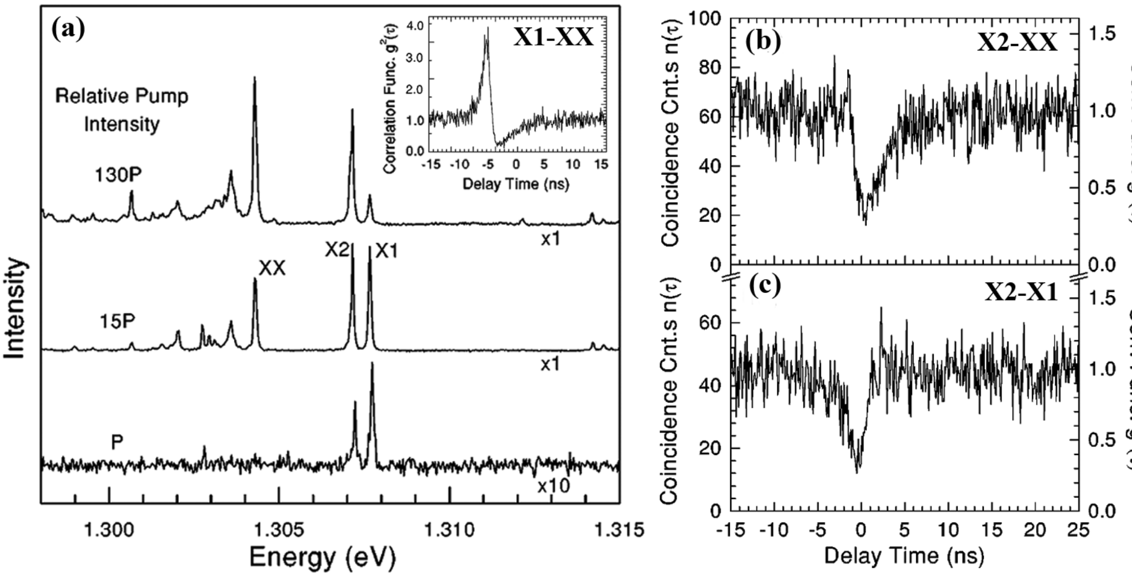

Figure 1.22: (a)Power dependent PL spectra of a single self-assembled InAs QD. Inset: measured cross-correlation between X1 and XX, showing strong bunching. Cross-correlation between (b) X2 and XX; (c)X2 and X1. [97]

al systematically studied these systems [97]. Figure 1.22(a) shows the power dependent PL spectra of a single, self-assembled InAs QD [97]. X1, X2, XX were identified as neutral exciton, charged exciton and biexciton transitions, respectively [97]. The cross-correlation measurement between X1(start)-XX(stop) reveals strong bunching for small negative delay time, whereas cross-correlations between X2(start)-XX(stop) or X2(start)-X1(stop) show asymmetric antibunching behaviors [97]. The observation on different QD systems can differ slightly from each other [19]. Baier et al presented a comprehensive evaluation of the formation and recombination dynamics of neutral and charged excitons in optically excited single QDs using photon correlation spectroscopy and rate equation analysis [98]. The extracted dynamics parameters from his analysis should be useful for design semiconductor QD structure for future quantum information processing applications.

1.3.5 Optical studies of coupled QDs and QD molecules

Semiconductor QDs have attracted attention as a medium for quantum computing due to their long carrier coherence time [99] [100]. However, for single isolated dot, this time is limited to one or two qubit operations [101], with no prospects for further scalability. Thus, the recent interest has been shifted to quantum dot molecules that consist of several coupled QDs. These QD molecules are electrically tunable, promising for application in scalable quantum computing [102] [103] [104] as basic building blocks.

We have introduced several current techniques for fabricating QD molecules in Subsection 1.3.3. Now, we focus on the optical studies of these QD molecule structures that were reported by several groups for verifying the presence of coupling between the composed QDs of the QD molecule.

Krenner et al [105] reported the direct observation of quantum coupling in individual QD molecules made by self-assembled growth. They demonstrated controlled electronic coupling of excitonic states via observation of an electric field induced anticrossing of spatially direct and indirect excitons [105].

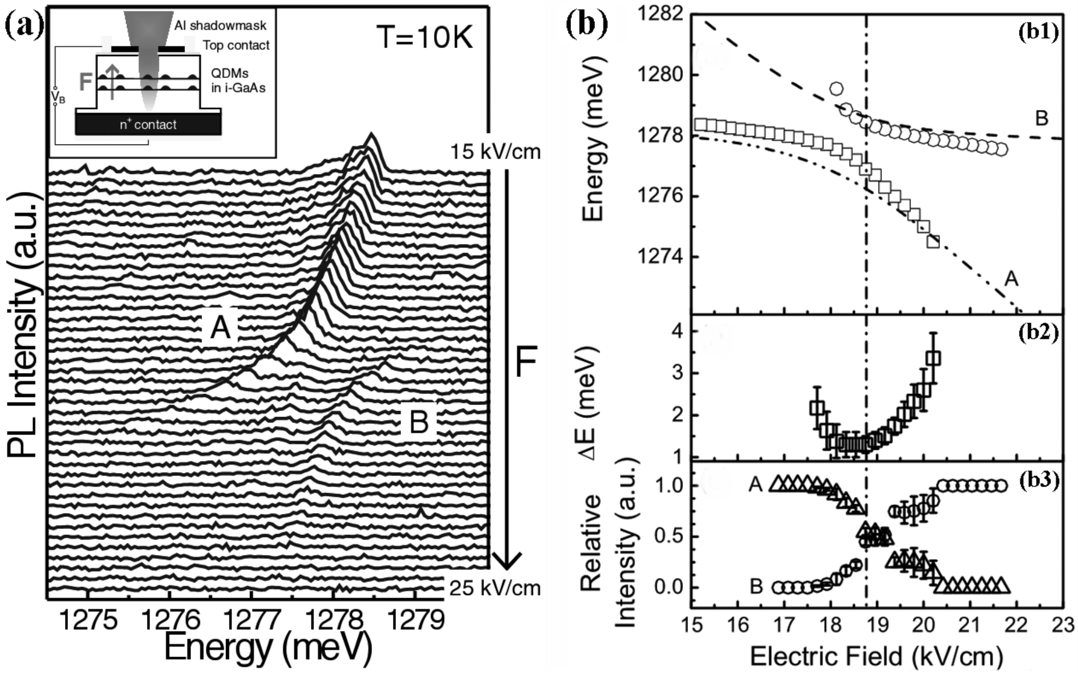

Figure 1.23: (a)Main: PL of single QD molecule as a function of applied electric field ranging from 15 to 25 kV/cm. Inset: Schematic of the investigated n − i Schottky diodes. (b)b1: Calculated and experimentally obtained exciton energies of state A and B as a function of the electric field. b2: Energy splitting between A and B. b3: Relative intensities of $I_{A/B}/(I_A + I_B)$. [105]

Figure 1.23 (a) shows the PL spectra evolution of single QD molecule as a function of applied electric field ranging from 15 to 25 kV/cm. The two excitons, A and B, show a clear anticrossing with a minimum splitting of $\Delta E = 1.4$meV at ~ 18.8 kV/cm. Schematic of the investigated n − i Schottky diodes is illustrated in the inset. The QD molecues are embedded in the intrinsic GaAs layer with the electrical field (F) oriented along the stack axis, parallel to the growth direction. Figure 1.23 (b1) shows the measured and calculated exciton energies of state A and B as a function of electric field. The relative intensities are found to be anticorrelated as shown in Fig 1.23 (b3). The overall reduction in the absolute PL intensity arises from field induced suppression of carrier capture and the transition of the ground state to an optically inactive state [105]. These figures demonstrate that A and B anticross as they are tuned into resonance, which is a clear signature of a tunable, coupled quantum system.

Stinaff et al [106] applied similar approach on asymmetric coupled InAs QD molecules. By applying an electric field, the hole level of the QD molecule is tuned into resonance, while the electron remains localized. The optical spectra show rich pattern of level anticrossings and crossings that can be understood as a superposition of charge and spin configurations of the two QDs [106]. Scheibner et al followed the same path and further studied the spin fine structure of optically excited QD molecules [107]. They explained these observed fine structures in the optical spectra of QD molecules in terms of the interplay between spin exchange, Pauli principle, and tunneling in the limit of wide barriers and negligible direct interdot exchange [107].

Light emission from two laterally coupled (In,Ga)As/GaAs QDs was studied by Beirne et al [108]. There, they performed photon statistics measurements between the various excitonic and biexcitonic transitions of these QD molecules [108]. Strong antibunching behavior was observed confirming the presence of coupling. Again, the tunnel coupling between the QDs was controlled by applying a static field along the QD molecule axis [108].

So far, it has been proven that either electron or hole (not both) levels of the QD molecules can be tuned into resonance by assistance of external fields [105] [106] [108]. However, to form the basis of quantum computation, one needs to have maximally entangled (Bell) states that allow quantum algorithms to outperform classical algorithms [109] [110] [111]. The atomistic pseudopotential calculations of self-assembled QD molecules predict that for self-assembled QD molecules, the hole states remain localized in one of the QDs even at short interdot distance due to strain and the lack of inversion symmetry between the QDs [112]. Simultaneous hybridizations of both electrons and holes are not possible to occur in such self-assembled QD molecules, resulting in excitons with low degree of entanglement [112]. This drawback might be overcome using our approach of self-organized QD molecules structures formed in inverted pyramid. The details of our experiments will be discussed in Chapter 5 of the present thesis.

1.4 Summary

In this chapter, we have discussed the relevant physical background of semiconductors and low dimensional quantum nanostructures. The electronic properties of semiconductors can be tailored by the quantum confinement effect using heterostructures, introducing the concepts of QW, QWR and QD structures. The optical properties of QWs, QWRs and QDs were discussed. Moreover, we reviewed the state of the art of QWRs, QDs and QD molecules fabrication techniques. Some issues on the optical properties of these structures that are related to this present thesis work: disorder, exciton dynamics in quantum wires, single- and correlated photon emission from QD, tuning of the coupling in QD molecules by applying electric field are also discussed.

Chapter 2

Fabrication and Characterization Techniques

The preparation of the QWR and QD structures described in this thesis required the development of new epitaxial growth and fabrication processes related to OMCVD on nonplanar substrates. Their features were studied using a variety of structural and optical characterization methods. In this chapter, we will introduce the techniques for the fabrication and characterization of our AlGaAs VQWR/QD systems in inverted tetrahedral pyramids in Section 2.1. Section 2.2 summarizes the optical characterization techniques we used in our study.

2.1 Fabrication of vertical quantum structures in inverted pyramids

This section describes the details involved in the sample fabrication procedure, including the preparation of patterned substrate in Subsection 2.1.1; epitaxial growth in Subsection 2.1.2 and some post-growth processing in Subsection 2.1.3. Most of these techniques were created and established during previous works of our group [83]. Minor improvement was introduced during this thesis work. In working with such complex nanostructures, different microscopy techniques serve as a necessary tool for characterizing the features of the structures. Therefore, some discussion of atomic force microscopy (AFM), scanning electron microscopy (SEM) and transmission electron microscopy (TEM) are introduced and briefly discussed in Subsection 2.1.4.

2.1.1 The substrate patterning technology

The fabrication of pyramidal heterostructures is a multi-step, time consuming procedure. The key to the inherent site control is the very first step: substrate patterning. It consists of a lithographic process, which creates periodic arrays of holes in a SiO_2 mask deposited on a (111)B GaAs substrate and a pattern transferring process onto the substrate by wet chemical etching. Depending on the dimensions of pyramids (in another words, the density of QWR or QD grown in pyramids) required, optical lithography or electron beam lithography can be used. Optical lithography is a fast and rather easy method, hence it was used for most samples studied in this thesis work. With this method, one can only achieve a pyramid density of less than $1/\mu m^2$. For higher densities, electron beam lithography will be needed. Another advantage of electron beam lithography is the flexibility of the modification of the designed pattern. For example, one can introduce ”defect” intentionally in the array for studying adatom diffusion on the surface of the substrate [113].

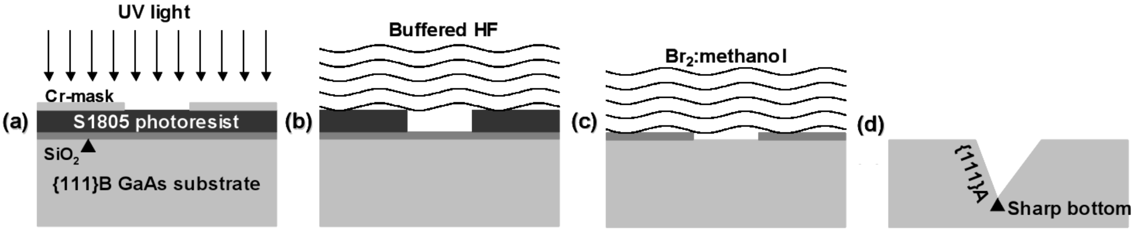

Figure 2.1: Schematic illustration of the preparation of the patterned substrates.

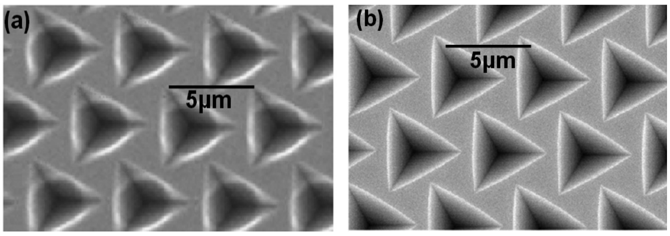

Figure 2.2: Topview SEM images of a patterned (111)B GaAs substrate with (a) and without (b) the SiO_2 mask.

Here, we will concentrate on the patterning process using optical lithography. Usually, we prepared sixths of one 2-inch wafer at a time. First, a thick SiO_2 film is deposited at 300°C using a plasma enhanced chemical vapor deposition (PECVD) unit. Then, a thick layer of positive S1805 photoresist is spun. In between the photoresist and SiO_2 layers, a thin film of primer (HMDS) is introduced to improve the adhesion of the photoresist. Subsequently, the substrate is introduced into a mask aligner, where the regular matrix of hexagonal opening is transfered onto the substrate from the Cr-written mask by shining UV light from a Hg lamp (Fig. 2.1(a)). The illuminated parts of the resist are removed by developing in MF319 solvent (Fig. 2.1(b)). The next step is to transfer the patterning from the resist to the SiO_2 film by performing buffered hydrofluoric acid (BHF) etching. After that, the photoresist is removed with aceton so that the SiO_2 film is now ready to be used as a mask for the following chemical etching of the GaAs substrate(Fig. 2.1(c)). Here, a 1% Br_2:Methanol solution is employed. The anisotropy of the chemical etching exposes three sidewalls in the (111)A orientation, thus forming an array of inverted tetrahedral pyramids. Etching efficiently stops after the (111)A-oriented pyramid sidewalls are formed and a sharp bottom (less than 20nm radius of curvature [83]) is reached (Fig. 2.1(d)). After removing the SiO_2 mask by BHF, the substrate is ready for MOVPE growth. Figure 2.2 (a) and (b) are topview SEM images of a patterned substrate (5 μm pitch) with and without SiO_2 covered. The parameters used for making patterned substrates used in this thesis can be found in Appendix C.

2.1.2 Epitaxial growth

After fabrication of the patterned nonplanar substrates, the next step is to apply the epitaxial deposition of III-V semiconductor layers by metallorganic vapor phase epitaxy (MOVPE). MOVPE is the only specific technique available as it has been shown to provide strong growth rate anisotropy between (111)A and (111)B crystal planes (with growth rate being higher on (111)A planes compared to (111)B) which are essentials to the nanostructures formation mechanism, and cannot be obtained by molecular beam epitaxy (MBE). Crystal growth was performed in a commercial Aixtron 200 horizontal reactor with a rotating susceptor plate. The working principle of an MOVPE unit is based on using a carrier gas to transport the growth species to the substrate in the form of constituents of volatile precursor molecules. Our system uses N_2 as a carrier gas and $Al(CH_3)_3$ (trimethyl-aluminium, TMAl), $Ga(CH_3)_3$ (trimethyl-gallium, TMGa) are the employed precursors for the group III atoms and AsH_3 (Arsine) for the group V. Stoichiometrically, the formation of crystalline GaAs in the MOVPE reactor can be summarized by the reaction

$$[Ga(CH_3)_3]_{gas} + [AsH_3]_{gas} \rightarrow [GaAs]_{solid} + [3CH_4]_{gas} \tag{2.1}$$

For the epitaxial growth of $Al_xGa_{1-x}As$ alloys the same precursor mechanisms and stoichiometry apply, under the condition of statistically replacing Ga atoms by Al atoms. The detailed intermediate steps involved in this reaction depend on a complex interplay between a variety of growth parameters, e.g. carrier gas velocity and the partial pressures ratio between the group V and group III precursors (V/III ratio), growth temperature, etc. Overall, metallorganic precursor migration, their decomposition into adatoms, and diffusion of adatoms on the surface play a key role in determining the VQWR/QD growth rate and composition. For the samples studied in this thesis work, the growth was carried out in N_2 carrier gas with V/III ratio of 500, growth pressure 20 mbar, and estimated substrate temperature of 680°C. The resulting nominal growth rate (measured on (100) orientated substrates) is about 0.13 nm/s.

The formation of interconnected complex nanostructures inside the pyramidal recess is an analog of growth in V-groove wire but with an additional dimension of the diffusion effect. Therefore, we will discuss the growth mechanism governing in the V-groove QWR system and then generalize to pyramidal QWR/QD case. V-groove QWRs are

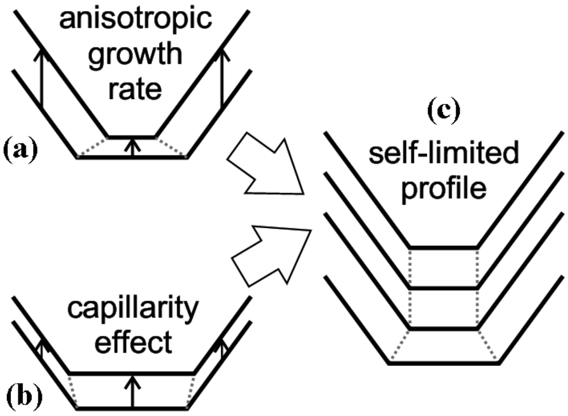

Figure 2.3: Illustrations of (a) anisotropy growth rate; (b) capillarity effect; (c) formation of the self-limiting profile. Adopted from [19].

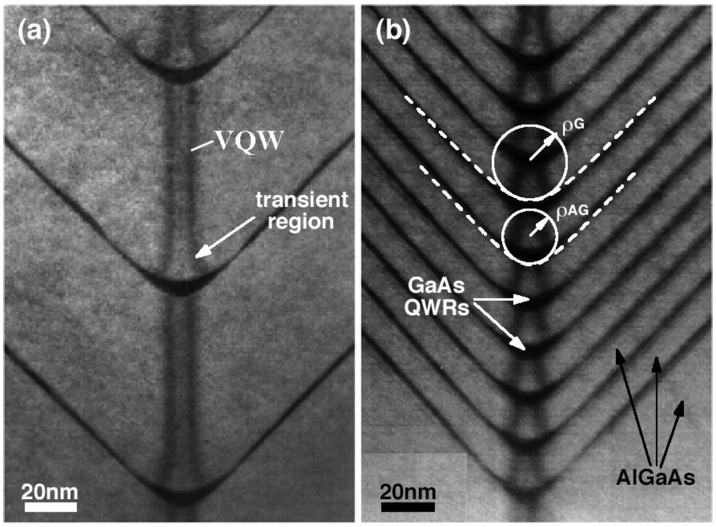

Figure 2.4: TEM cross sections of (a) multiple GaAs / $Al_{0.45}Ga_{0.55}As$ V-groove QWR structure (1.8 nm /60 nm), and (b)140 nm thick GaAs / $Al_{0.45}Ga_{0.55}As$ QWR superlattices with 1.8 nm thick GaAs layers and 11.6 nm thick AlGaAs layers. Adopted from [114].

grown on (100) substrates patterned with parallel V-grooves exposing (111)A facets. During the formation of the QWR, two effects play the important roles. First is an intrinsic growth rate (more accurately, should be "decomposition rate" here) anisotropy between the substrate surfaces with different crystallographic orientation. The precursor decomposition rate is influenced because at different crystal surfaces, different chemical bonds are exposed to the surface [115]. The growth rate on original (100) surface is slower than that on the (111)A oriented sidewalls. This results in a sidewall angle smaller than the one given by the original substrate with respect to the (111)A surface, which is regarded as vicinal (111)A surfaces. On the other hand, capillarity effect gives rise to a preferential diffusion of growth species towards the bottom of the

V-groove (Fig 2.3 (a)). Therefore, it results in an enhanced growth rate there, while the first effect yields higher growth rate at the sidewalls (Fig 2.3 (b)). The two effects can compensate each other, reaching a self-limited growth profile after certain layer thickness (grown under constant growth parameters), as illustrated in Fig 2.3 (c).

Moreover, the Ga adatoms has higher mobility and hence longer diffusion length on (111)A surface than that of the Al adatoms. This will results in two main effects. First, the self-limited profile of GaAs layer will have thinner sidewalls and thicker bottom layer as compared to $\mathrm{Al_xGa_{1-x}As}$. Fig 2.4 clearly demonstrated this effect, in which the radius of curvature of the AlGaAs self-limiting profile (ρ_{AG}) is much smaller than that of the GaAs (ρ_{G}). Second, for the AlGaAs layer, the differences between Al and Ga adatom diffusion coefficient also leads to a Ga-enriched vertical plane in V-groove, typically around 20nm named as VQW (Fig 2.4). This phenomena is often regarded as an alloy segregation effect.

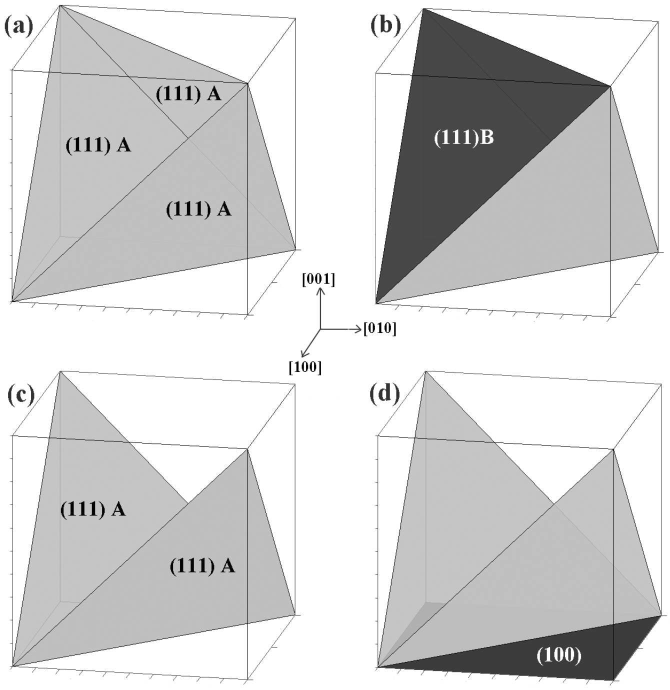

Figure 2.5: Schematic illustrations of geometric configurations between three (111)A facets forming pyramid (a) and (111)B substrate (b), between two (111)A facets forming V-groove (c) and (100) substrate (d).

We now turn our attention to the growth of the pyramidal VQWR/QD heterostructures. Fig 2.5 reveals the similarity between the pyramid corner (constructed by two (111)A facets) and the V-groove. It illustrates the geometric configurations between three (111)A facets forming the pyramid and the original (111)B substrate (Fig 2.5 (a, b)). In parallel, the relation between two (111)A facets forming the V-groove and the (100) substrate in a standard cubic crystal configuration are demonstrated in (Fig 2.5 (c, d)). The growth rate anisotropy is more significant in the pyramid case. The

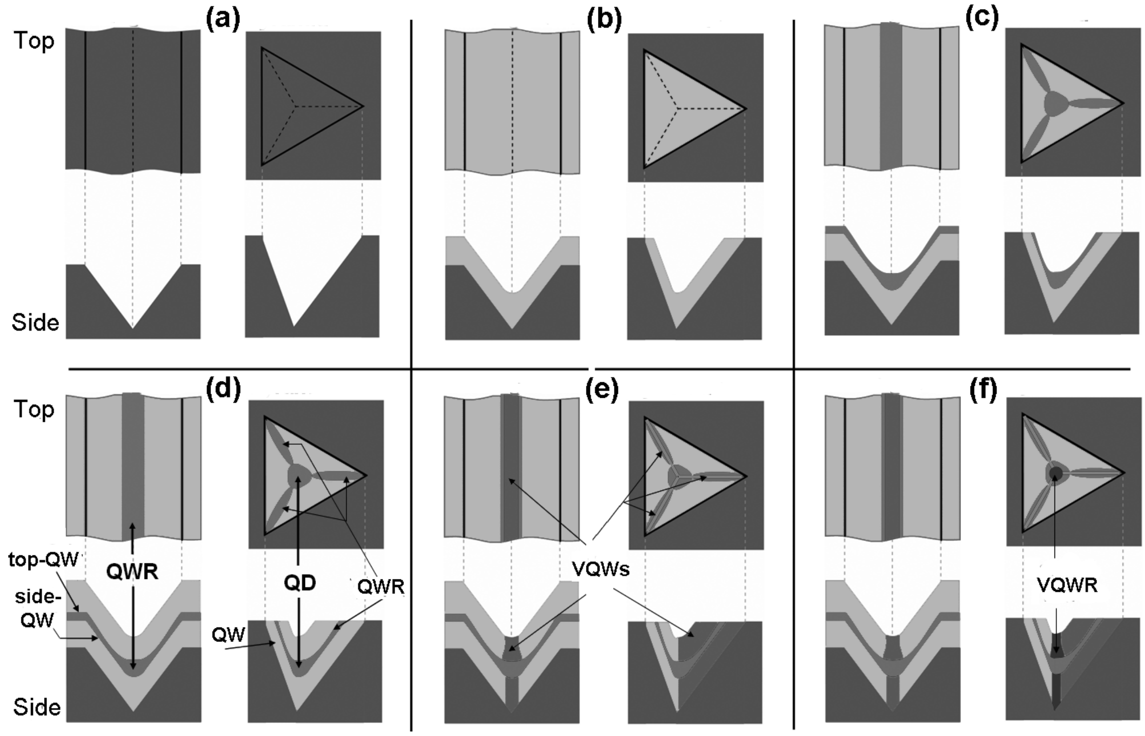

Figure 2.6: Formation of V-groove GaAs QWRs (left) and pyramidal GaAs QDs (right): (a)Patterned substrates; Growth of bottom AlGaAs cladding layer(b), core GaAs layer(c), top AlGaAs cladding layer(d); Formation of VQWs (e) and VQWRs (f) in the cladding layers.

(111)B surface is nearly a non-growing plane so that the growth only takes place inside the pyramids on patterned (111)A facets. A similar effect caused by one-dimensional diffusion of Al and Ga adatoms, takes place between every two side-connected sidewalls of the three sidewalls in the pyramid, resulting in formation of three VQWs (with lower Al concentration) at the wedges of the AlGaAs layer. More over, two-dimensional diffusion from the sidewalls to the center creates a VQWR with even lower Al concentration along the center axis of the pyramid. In Fig 2.6, we put side by side the V-groove (left) and the pyramid (right) to illustrate the steps of AlGaAs/GaAs/AlGaAs layer growth inside them and the low-dimensional structures formed spontaneously in each layer.

Focusing more on the growth of AlGaAs layers, we found that the growth of an otherwise homogeneous layer of $\mathrm{Al_xGa_{1-x}As}$ in a pyramid yields three distinct phases with different Al content. An $\mathrm{Al_zGa_{1-z}As}$ running through the center of the pyramid, connects three $\mathrm{Al_yGa_{1-y}As}$ VQWs at the three wedges. Besides, there is also bulk $\mathrm{Al_xGa_{1-x}As}$ materials filling the spaces in between the VQWR and the VQWs. Here, we have fixed relations: $x > y > z$, due to the alloy segregation. For the growth of a GaAs layer, segregation does not apply, so it results in formation of three lateral QWRs, meeting at the center to form a lens-shaped GaAs QD. If we sandwich the QD layer by two AlGaAs barrier layer, the QD will be confined from three dimensions. Another possibility is to replace the thin GaAs layer by a AlGaAs layer with lower nominal Al content than the barrier layers, which is the main approach in the present thesis. In this way, AlGaAs VQWR or AlGaAs QD (depending on the thickness of the layer) will be formed in the center of the middle layer due to the 3D confinement from the higher bandgap (in another words, higher Al concentration) structures surrounded. Fig 2.7 presents an example of the complex nanostructures formed inside a pyramid when a nominal $Al_{0.2}Ga_{0.8}As$ layer is sandwiched between two $Al_{0.35}Ga_{0.65}As$ barrier layers (cladding layers) was grown. The barrier layers are also used to confine carriers in order to achieve better optical quality. Fig 2.7 (a) is the schematics of the structures formed at the pyramid wedges and the center both from top view and side view. Fig 2.7 (b) shows all the structures involved in such a pyramid. The vertical bar gives the estimation of Al concentration in each structure and approximate bandgap energy accordingly. The dashed lines are pointed to the VQWRs formed in the core layer and the barrier layers. The way to estimate the Al content in each structure will be introduced in Chapter 3.

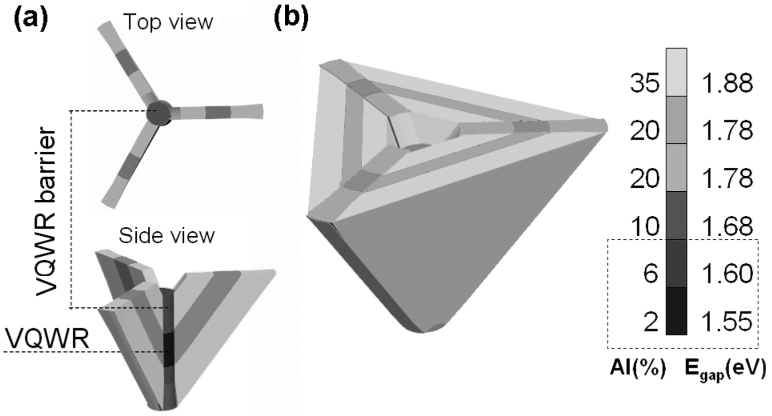

Figure 2.7: (a) Sketch of nanostructures formed at the wedges and center of the pyramid; (b) All the structures involved in a pyramid with indication of estimated Al content and bandgap value of each structure.

Apart from the three main AlGaAs layers (1 core, 2 cladding), a thin GaAs buffer layer and a thin GaAs cap layer are always grown as the first and the last layers of the epitaxial growth respectively. The buffer layer is used for facilitating the crystalline transition between the GaAs substrate and the grown layers and the cap layer is employed for reducing the oxidation of the AlGaAs layers (insulating the AlGaAs layers from the air). Besides, an $Al_{0.75}Ga_{0.25}As$ layer is often grown right after the GaAs buffer layer, serving as an etch-stop layer for the post-growth processing (more details in Subsection 2.1.3).

2.1.3 Post-growth processing

After MOVPE growth of the pyramidal structures, post-growth precessing is often performed to either remove irregular growth on the (111)B surface by surface-etching or to improve the PL collection efficiency by back-etching.

Surface-etching: The previous study reveals that at the interface between growing (111)A sidewalls and "non-growing" (111)B wafer surfaces, irregular takes place at the wavelength range between 760 nm and 800 nm and may screen the emission of the quantum structures of interest, forming inside the pyramids. In order to avoid spectral coincidence of these states with the important VQWR or QD emission, we used a surface-etching technique to remove these spurious areas.

The surface-etching process we used is a post-growth, self-aligned etching procedure. The detailed steps are illustrated in Fig 2.8. First, we spin a thick layer of photo resist on the as grown sample surface (Fig 2.8 (b)). Second, we perform O_2 plasma etching to diminish the thickness of the resist until only the inner part of the pyramid remains covered by the resist (Fig 2.8 (c)). Subsequently, wet chemical etching (in a (H_2SO_4 : H_2O_2 : H_2O solution) will be applied to remove the non-covered surface layer of the grown substrate (Fig 2.8 (d)). The final step is to remove the residual photo resist by rinsing the sample with aceton, isopropanol, and water (Fig 2.8 (e)). Note that surface-etching can be applied only if the pyramids are not completely planarized after growth. The parameters used for surface-etching the grown samples can be found in Appendix C.

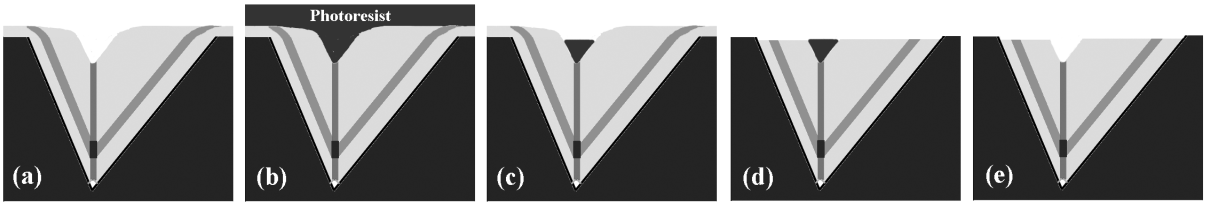

Figure 2.8: Schematics of surface-etching process: (a)As-grown sample;(b)photo resist covering the sample surface;(c)O_2 plasma etching to preferentially remove part of the resist;(d)chemical etching to remove the spuriouos facets;(e)removal of photo resist.

Back-etching: Photoluminescence spectra measured by collecting light from the grown side of the structure show very weak emission from the VQWRs/QDs. One reason for this is that most of the light emitted by the VQWRs/QDs is totally internally reflected by the interface between the steep pyramid sidewalls and the air and then partially absorbed by the GaAs bulk around (Fig 2.9 (a)). By using a back-etching technique, the extraction efficiency for photons emitted by the VQWRs/QDs can be increased by a factor of $\sim 10^3$ [83]. Fig 2.9 illustrates the process of back-etching.

First of all, we evaporate a Ti/Au bi-layer on the surface-etched sample. This bi-layer acts as a mechanical support in the final structure and also an highly reflective mirror to avoid light absorption in the growth direction (Fig 2.9 (b)). Next, the sample is glued with black wax upside down on a (111)B GaAs substrate (as a support) of similar shape, but slightly larger than the sample. Then, we use mechanical lapping to reduce the thickness of the original substrate down to 80 μm. After that, a NH_4OH : H_2O_2 solution is used to selectively etch the remaining GaAs using a liquid rotation equipment. The parameters used for back-etching the grown samples can be found in Appendix

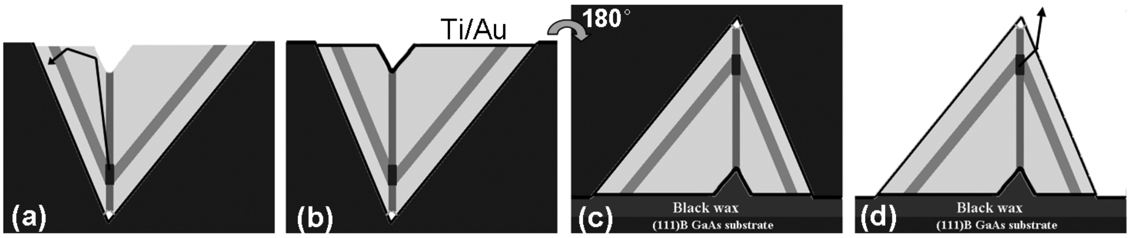

Figure 2.9: Schematics of the back-etching process: (a)Sample after surface-etching;(b)Metallization;(c)Support attachment; (d)Mechanical and chemical removal of the original substrate.

C. It was found previously that a $NH_4OH : H_2O_2$ solution is quite selective to stop on a 100 nm thick etch-stop layer of $Al_{0.75}Ga_{0.25}As$ (this layer is normally grown before the first barrier layer of the main structures). But still, experimentally we observed a non-uniform etching, resulting in a non-flat etched surface. The SEM image in Fig 2.10 shows the etched surface where on one side the GaAs is still partially covering the standing pyramids, but on the other side the etching has already penetrated into the pyramids. The partially embedded pyramids (e.g. the one marked by black circle) are better candidates for the optical measurement since the others (e.g. the one marked by white circle) might be already over-etched.

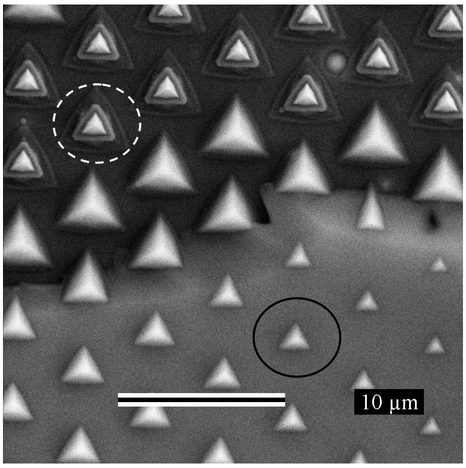

Figure 2.10: Top-view SEM images showing non-uniform back etching.

2.1.4 Structural Characterization using AFM, SEM, TEM

Electron microscopy and atomic force microscopy (AFM) are often used for structural characterization of nanostructures. In this subsection, we review the basic measurement techniques and functions of these microscopes.

Atomic force microscopy (AFM): AFM is a scanning probe microscopy technique introduced in 1986, with which the topographical information of the surface being scanned is provided by measuring forces on the atomic scale [116]. In general, an AFM can be operated in contact or non-contact modes, which means the tip is dragged across the surface or stands 10-100nm above the sample, respectively. Working in the non-contact mode usually provides smaller spatial resolution than in the contact mode, but gives possibility of imaging soft surfaces, which could be damaged in the contact mode.

In our experiments, the VQWR/VQW structures are characterized using cross-sectional AFM in ambient air. The pyramid arrays are arranged so that their rows deviated slightly (by ~ 0.05 degree) from the [011] cleavage directions. Cleaving the sample thus exposed a row of pyramids cut at different planes, showing sequentially the cross-section throughout the entire pyramid. Oxidation of the (Al)GaAs cleaved surface yields an oxide layer protruding at an extent that depends on the exposure time and Al content in a reproducible manner, making it possible to map the AlGaAs composition directly from the AFM topography image [117]. Fig 2.11(b) is an example of such a cross-sectional AFM image for a pyramidal structure with an $Al_{0.3}Ga_{0.7}As$ layer nominally 17.5 nm thick, sandwiched between two $Al_{0.55}Ga_{0.45}As$ cladding layers. The cleaved surface runs about 100 nm from the center of the pyramid, and thus the revealed structure corresponds to the VQWs of the core and cladding. The darker parts represent the Ga-rich VQWs formed by Ga-Al segregation. With such images, we determined that the actual growth rate of the core $Al_{0.3}Ga_{0.7}As$ VQWR structure is about 4.5 times the nominal growth rate.

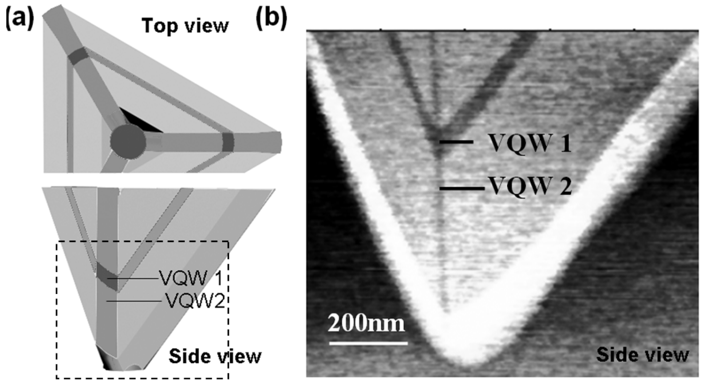

Figure 2.11: (a)Sketch of top view and side view of cleaved edge of pyramidal structure, the AFM scanning takes place at the marked (by dashed square) area; (b)Reprensentative flattened cross-section AFM image of a pyramidal heterostructure, VQW1 and VQW2 have different Al contents, and the lowest, bright layer represents the thin $Al_{0.75}Ga_{0.25}As$ etch-stop layer.

The actual Al concentration in different structures can be also estimated from the AFM images if an accurate calibration of layer oxidation rate as a function of Al content is performed [114]. In the present thesis, we will not go deeper into this topic.

Scanning electron microscopy (SEM): In SEM, electrons are thermionically emitted from a cathode and are accelerated towards an anode. The electron beam, which typically has an energy ranging from a few hundred eV to 100 keV, is focused by one or two condenser lenses into a beam with a very fine focal spot size of 0.4 nm to 5 nm. When the primary electron beam interacts with the sample, the electrons lose energy by repeated scattering and absorption within a teardrop-shaped volume of the specimen known as the interaction volume, which extends from less than 100 nm to around 5μm below the surface. The energy exchange between the electron beam and the sample results in the emission of electrons and electromagnetic radiation, which can be detected to produce an image. Contrast in SEM images originates from surface topography and chemical composition of the sample. Fig 2.12 (a) shows a top-view SEM image of an array of pyramids after surface-etching. A zoom in of the pyramid corner is shown in Fig 2.12 (b). The bright contrast at the pyramid wedge is an evidence of the formation of the thin VQW (width $\lessapprox$ 20nm).

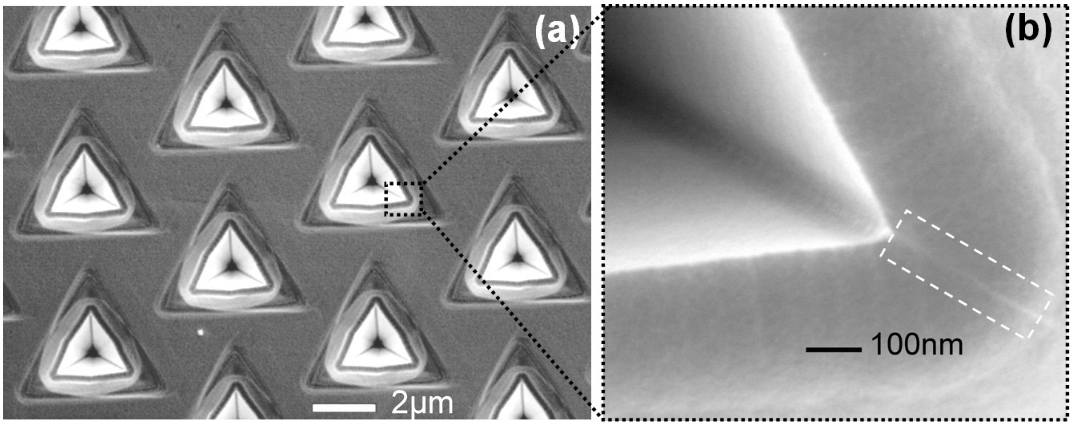

Figure 2.12: (a)Top-view SEM image of an array of pyramids after surface-etching;(b)Close up of one corner of a single pyramid, evidencing the formation of the VQW at pyramid wedge.

Transmission electron microscopy (TEM): TEM is an imaging technique whereby a beam of electrons is transmitted through a specimen, then an image is formed, magnified and directed to appear either on a fluorescent screen or a layer of photographic film, or can be detected by a sensor such as a CCD camera.

The origin of the contrast in a TEM image is different than that in an optical microscope image. A crystalline material interacts with the electron beam mostly by diffraction rather than absorption, although the intensity of the transmitted beam is still affected by the volume and density of the material through which it passes. The intensity of the diffraction depends on the orientation of the planes of atoms in a crystal relative to the electron beam; at certain angles the electron beam is diffracted strongly from the axis of the incoming beam, while at other angles the beam is largely transmitted.

A high-contrast image can therefore be formed by blocking electrons deflected away from the optical axis of the microscope by placing the aperture to allow only unscattered electrons through. This produces a variation in the electron intensity that reveals information on the crystal structure. This technique is known as Bright Field or Light Field. It is particularly sensitive to extended crystal lattice defects in an otherwise ordered crystal, such as dislocations.

It is also possible to produce an image from electrons deflected by a particular crystal plane. By either moving the aperture to the position of the deflected electrons, or tilting the electron beam so that the deflected electrons pass through the centered aperture, an image can be formed of only deflected electrons, known as a Dark Field image.

The resolution of TEM is about 1 nm, while with High Resolution Transmission Electron Microscopy (HRTEM), this value can be even smaller. Fig 2.13 is a top-view TEM image of the center of an $Al_{0.30}Ga_{0.70}As$ layer grown inside a pyramidal recess. The sample was prepared using plan-view techniques with final grazing Ar-ion bombardment. The image was acquired in a Hitachi HF2000 FEG transmission electron microscope operating at 200 keV with electron beam directed parallel to the VQWR axis. The electron beam propagated along (111)zone axis and the electron beam scattered at angles larger than 20 mrad were collected using an annular dark field detector. In this Z contrast image, brighter regions correspond to higher Ga content in the alloy.

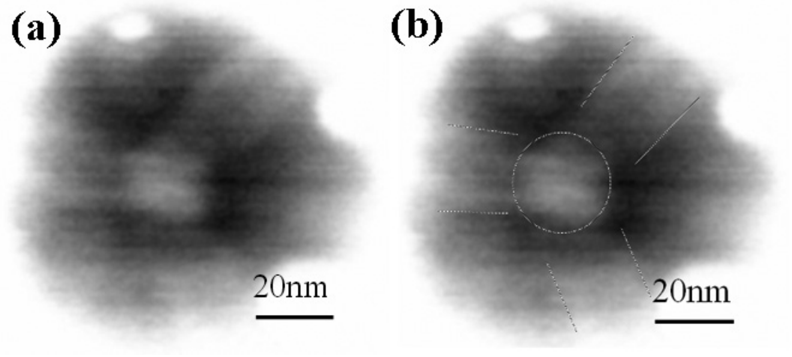

Figure 2.13: (a)Top-view TEM image of an $Al_{0.30}Ga_{0.70}As$ layer grown inside a pyramidal recess, showing 3 VQWs branches and 1 VQWR in the center. (b)Copy of (a), dashed lines are added to emphasize the structures.

2.2 Optical characterization techniques

Luminescence spectroscopy is widely used for studying the optical properties and electronic structures of semiconductors. Luminescence is the optical radiation emitted by a physical system (in excess of the thermal equilibrium black body radiation) resulting from relaxation from a non-equilibrium state. There are many different ways to excite the system: sound (sonoluminescence), heat (thermoluminescence), light (photoluminescence (PL)), electron beams (cathodoluminescence (CL)), voltage bias (electroluminescence). The resulting spectra contain information about the energy states of these carriers. In the present thesis, our VQWR/QD structures are optically characterized by luminescence spectroscopy. Here, we will introduce several luminescence-based techniques, namely PL spectroscopy (Subsection 2.2.1), Micro-PL spectroscopy (Subsection 2.2.2), Linear polarization-resolved PL spectroscopy (Subsection 2.2.3), Time-resolved PL spectroscopy (Subsection 2.2.4), PL excitation spectroscopy (Subsection 2.2.5), Photon correlation spectroscopy (Subsection 2.2.6), and CL (Subsection 2.2.7).

2.2.1 Photoluminescence spectroscopy

Photoluminescence spectroscopy is a very powerful, easy-to-use, and non-destructive tool, consisting of using excitation light at a fixed wavelength and measuring the spectral distribution of the luminescence. To create an electron-hole pair in semiconductor heterostructure, it requires a minimal excitation energy of the incident light. This energy must be larger than the energy bandgap of the bulk materials plus the lowest single particle electron and hole confinement energies (in a single particle picture). In our QD PL spectroscopy, electron-hole pairs can be created directly in the discrete QD energy levels, or in the barrier continuum of states (e.g. bulk, QW or QWR structures surrounded). After excitation, the system returns to its equilibrium state via non-radiative and radiative process. In the first step, photoexcited carriers relax to the center of the Brillouin zone by interaction with optical and acoustic phonons. After relaxation to the band edge, carriers recombine either radiatively (luminescence) or non-radiatively. PL spectra correspond to the intensity of the emitted light as a function of the wavelength (or emission energy).

2.2.2 Micro-Photoluminescence spectroscopy

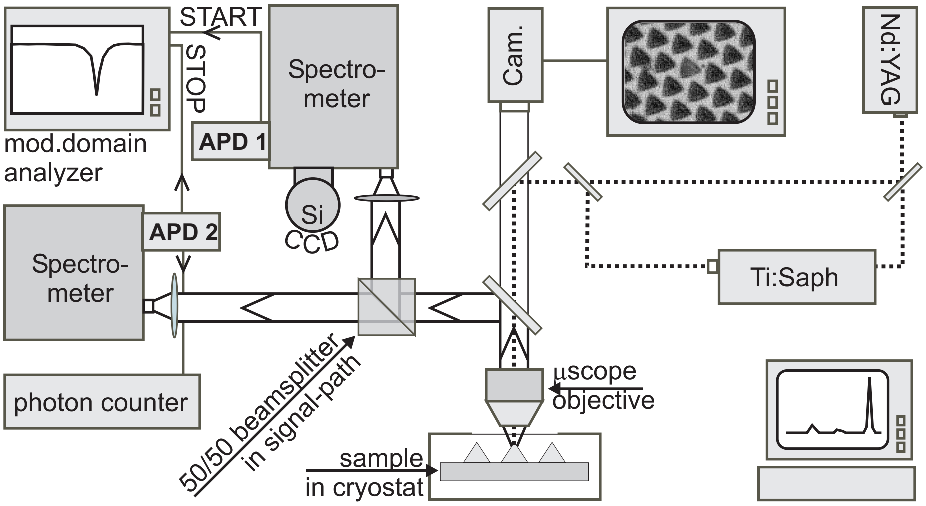

Figure 2.14: Full experimental setup for μPL, PLE and photon correlation measurement. [19]

In order to get rid of the inhomogeneous broadening of the energy levels due to the size variation of the nanostructures inside different pyramids, one can use one microscope objective with high numerical aperture for collecting the emitted photons in a conventional PL setup. In this way, it is possible to achieve a spatial resolution of 1 μm or even less, which enables the opportunity to study individual quantum structures, e.g. the structures inside one single pyramid in the case of 5μm pitch array (most frequently used array configuration). Micro-PL spectroscopy is a very powerful technique and is employed intensively through out this thesis work. The whole setup for μPL spectroscopy consists of three main components: the excitation part (laser sources), the sample part (the cryostat) and the detection part (with the spectrometer and the light detection part)(see Fig 2.14 for an overview). The samples are mounted in a He-flow cryostat (Janis Research, CO., Inc. ST-500, or Cryovac Konti) under high vaccum ($< 10^{-5}$ mbar) and kept at constant temperature down to 4 K (usually, at 10 K, controlled by a Lakeshore 330 Autotuning temperature controller). Single pyramids are excited by a frequency-doubled diode-pumped Nd:YVO$_4$ laser (Spectra Physics Millenia V-s) (or an Argon-ion laser (Coherent Innova 400) at a wavelength of 532 nm (514.5 nm) or by a wavelength tunable Ti:Saphire laser (Spectra Physics Tsunami (or Coherent Mira 900)) at a wavelength between 700-1000 nm. The laser spot is focused by a microscope objective (50×, f = 3.6 mm, NA = 0.5) into a spot size of ~ 1 μm in diameter. The luminescence is collected by the same lens, and then redirected by a beam splitter and a set of mirrors. The spectra are acquired using a grating spectrometer (55 cm Jobin Yvon Triax 550, 1200 l/mm) combined with computer-connected nitrogen-cooled Si-CCD array detector (Jobin Yvon Spex Spectrum One, 2048 × 512 pixels). The spectral resolution is about 120 μeV while using a 100 μm wide spectrometer entrance slit. A combination of spectrometer and Si-avalanche-photo-diode (APD) is also an option for the luminescence detection, but its detection efficiency is much lower than detecting with a CCD.

2.2.3 Linear polarization-resolved photoluminescence spectroscopy

It is well known that the different hole characters are related to different polarization selection rules for optical transitions between conduction band (CB) and valence band (VB) [118]. The strongest different in linear polarization is expected between pure heavy and light hole states, having the polarization vector oriented (mainly) parallel or perpendicular to the quantization axis, respectively. In search of such characteristics, we performed linear polarization-resolved PL spectroscopy on our pyramidal VQWRs and QDs (details can be found in Chapter 4 and 5). The PL spectra can be measured either in top-view geometry, where the exciting beam and collected light propagated along the VQWRs, or in cleaved-edge geometry, where the beams propagated perpendicular to the axis of the VQWRs (see Fig 2.15). Here, the same experimental setup as for micro-PL is used, except that a linear polarizer is mounted in front of the entrance of the spectrometer at a fixed polarization direction and the slow axis of a preceding

$\lambda/2$-plate is rotated to resolve the linear polarization content of the detected PL signal. Because of the symmetry of the VQWR or QD, in the top-view geometry, the PL of the VQWR or QD is normally perfectly unpolarized. It will be more interesting to measure in the cleaved-edge geometry, in which we can get access to the linear polarization vectors oriented along (light hole associated, direction of gray arrow in the figure), as well as perpendicular to the VQWR (heavy hole associated, direction of black arrow in the figure). Depending on the effective aspect ratio of VQWR or QD, we expect a different linear polarization degree, exhibiting different hole characters.

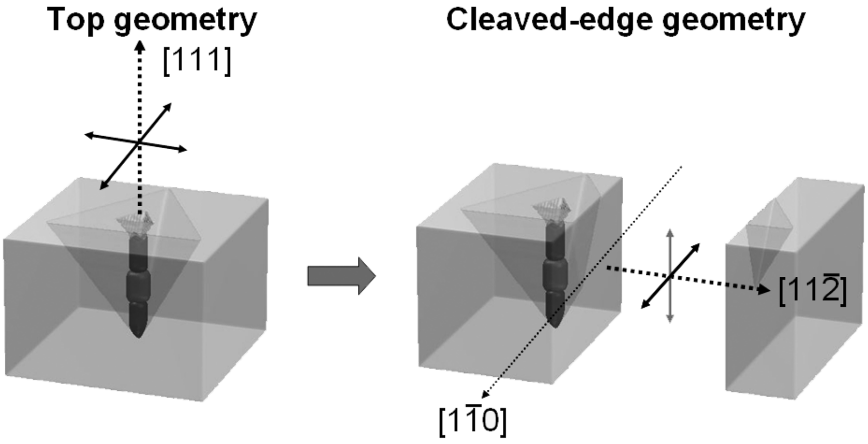

Figure 2.15: Detection geometry of Linear polarization-resolved PL measurement.

2.2.4 Time-resolved photoluminescence spectroscopy

Dynamical properties of semiconductors (carrier relaxation, diffusion, recombination lifetimes, etc.) can be investigated in time-resolved PL spectroscopy. The PL of a sample is monitored as a function of time after excitation by a flash of light produced by a pulsed laser. The time resolution can be obtained in a number of ways, depending on the required sensitivity and time resolution. In our experiments, the Ti:Sa laser is operated in the mode-locking regime for time-resolved experiments, generating ~ 3 ps pulses at 76 MHz. For the detection part, we use the same spectrometer but after dispersion, the luminescence is deflected towards a micro-channel plate (MCP). The MCP is coupled to a time-correlated photon counting unit. The temporal resolution of the detection system is ~ 60 ps. Part of the exciting laser beam is taken by a beam-splitter and sent towards the trigger diode which is also coupled to the time-correlated photon counting unit. Moreover, a bandpass filter is mounted in front of the spectrometer in order to attenuate the laser light reflected by the sample.

In the present thesis, time-resolved PL spectroscopy is applied to measure the recombination time of the excitons in our pyramidal VQWR and QDs (details can been seen in Chapter 4).

2.2.5 Photoluminescence excitation spectroscopy

Photoluminescence excitation (PLE) spectroscopy is used to study excited states by combining the absorption and the luminescence properties of the sample. To achieve PLE spectra, the spectrometer is normally set to detect emission at a particular photon energy. The intensity of this emission is recorded by an APD as a function of the excitation photon energy, highlighting in this way the absorption resonances of the heterostructure. We also developed a so-called multi-channel PLE spectroscopy technique using a home-made programme to move the excitation laser wavelength in fixed steps precisely (down to 0.1 nm steps), and detecting PL in a wide spectral range by CCD. Then, the PLE spectra can be reconstructed by software (e.g. using a Matlab program) from series of PL spectra obtained experimentally. In the PLE measurement, a filter is normally placed in front of the spectrometer to reject the laser light reflected by the sample.

2.2.6 Photon correlation spectroscopy

Photon correlation spectroscopy is a very powerful tool to probe exciton dynamics. In this thesis, we will not go deep into this topic, but just use this tool to demonstrate the observation of single-photon emission from our pyramidal QD (see in Chapter 4) and the presence of coupling in the QD-molecule (details will be discussed later on in Chapter 5).

From the experimental point of view, the photon correlation measurement is implemented using two single photon detectors in a *Hanbury Brown and Twiss* (HBT) configuration(see Fig 2.14 left half) [87]. The experiment is performed only under continuous wave excitation for this work. The signal beam coming from the sample is split by the 50/50 beam splitter. Then, one branch enters the 55-cm-spectrometer combined with APD1 for time-resolved single photon counting. The second branch enters an 32-cm spectrometer with APD2 (identical to APD1). The outputs of the two APDs will serve as start- and stop-signals for a modulation domain analyzer (Hewlett Packard 53310A), which produces histograms displaying the cumulative number of recorded time delays between start- and stop-signals. In the limit of low collection and detection efficiency ($\sim 10^{-4}$), these histograms are proportional to the second order temporal correlation functions $g^{(2)}(\tau)$ for photon pairs, which are spectrally selected by the two spectrometers. The expression of the second order correlation function can be found in Eq. 1.33 (auto-correlation) and Eq. 1.34 (cross-correlation).

To have an idea of the significance of correlated photon emission, we use as an example of correlation between exciton and biexciton (e.g. inset of Fig 1.22). After the emission of a 2X photon the QD is left populated with an X, which implies a photon cascade between 2X and X recombinations. The probability for X photon emission is increased for small positive delay times after 2X photon emission. This will result in a bunching peak at delay time $\tau < 0$ in the histograms if we take X as start- and 2X as stop-signal.

2.2.7 Cathodoluminescence

Cathodoluminescence (CL) spectroscopy and wavelength-dispersive imaging are powerful tools (see Ref. [119] for a review) for investigating the carrier transport and recombination mechanisms in complex semiconductor nanostructures. CL is mostly performed in either a SEM or a scanning TEM. In these cases, the highly focused beam of electrons impinges on a sample and induces it to emit light from a localized area. This light is collected and detected by optical systems. The high energy electrons can excite the wide-bandgap materials, e.g. Gallium-nitride based structures, which can not be easily excited optically. Another big advantage of the CL spectroscpopy is that the small beam can probe selected nanostructure with a spatial resolution down to several tens of nanometers depending on the generation voltage. This approach has been applied successfully for studying carrier capture phenomena in GaAs/AlGaAs quantum wires (QWRs) formed in the V-grooves, revealing efficient capture from adjacent quantum wells (QWs) into the QWRs [120]. Later on, similar methods were employed in GaAs/AlGaAs and InGaAs/AlGaAs quantum dots (QDs) grown in inverted tetrahedral pyramids, to identify different structures formed in the pyramids and also to get information on the alloy disorder/ nonuniformity layer growth [121].

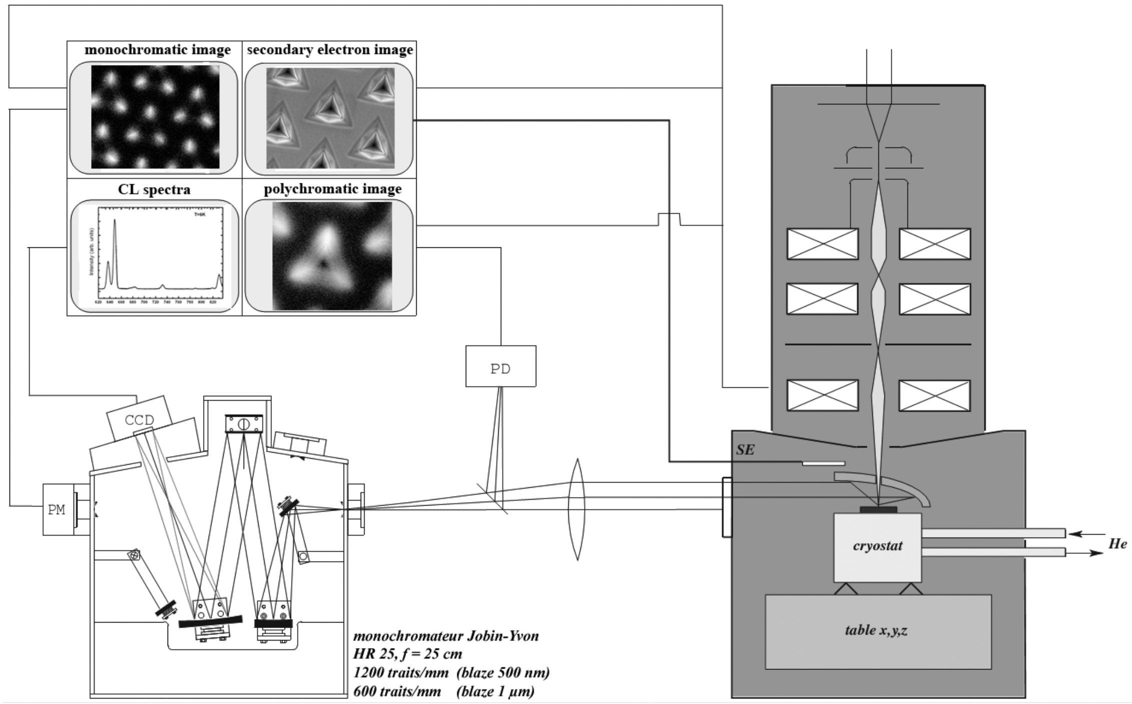

Figure 2.16: Cathodoluminescence setup.

The experimental setup used for cathodoluminescence spectroscopy is shown in Fig 2.16. The measurements are carried out in a Cambridge S-360 SEM that can be operated between 10 K and 340 K using acceleration voltages ranging from 0.5 to 40 kV and beam currents ranging from 1 pA to 1 μA. An Oxford CL stage comprising a parabolic mirror is used to send the CL signal to a Jobin-Yvon HR 25 monochromator (f = 25 cm, 1200 l/mm grating). The spectra are acquired by a nitrogen-cooled CCD detector (Spex Spectrum one 2000 × 800 pixels), while monochromatic or polychromatic CL imaging is performed using a Hamamatsu photomultiplier operating in photon-counting mode. The spectral resolution of the system is about 0.8 meV. The samples were mounted in a He-flow cryostat and kept at several constant temperatures between 8 K and room temperature. The CL spectra were measured either in top-view geometry, where the exciting beam and collected light propagated along the VQWRs, or in cleave-edge geometry, where the beams propagated perpendicular to the axis of the VQWRs.

2.3 Summary

In this chapter, we first summarized the method for fabricating pyramidal VQWR and QD including substrate patterning and epitaxial growth by MOVPE, and two post-growth processing steps: surface-etching and back-etching. Second, we overviewed the structural and optical characterization techniques that are used during this thesis work. The structure characterization is mainly done by using different microscopies like AFM, SEM, and TEM. We also described some details about the principles of how these microscopies work. Several optical characterization techniques (mainly spectroscopy) are involved in this study and their working principles and configurations were presented and explained.

Chapter 3

Pyramidal Vertical Quantum Wires: a New QWR System

Semiconductor quantum wires (QWRs) represent a particularly intriguing and challenging class of quantum nanostructures, useful for studies and applications of quasi one-dimensional (1D) systems [122]. However, whereas in ideal QWRs carrier motion is not restricted along the wire axis, realistic wires suffer from structural disorder that lends itself to potential fluctuations and carrier localization. Such disorder-induced effects have been observed in different high quality III-V compound QWR systems such as cleaved-edge overgrown T-shaped QWRs [57] and V-groove QWRs grown on nonplanar substrates [123] [56]. Considerable efforts have been devoted recently in developing more uniform QWRs suitable for studying the properties of near-ideal one-dimensional (1D) systems [124] [59]. These efforts involve understanding and controlling effects responsible for inducing wire disorder, particularly the heterostructure interfaces along its axis. For wires formed parallel to the substrate plane (e.g., T-shaped or V-groove wires), the interface features are closely related to the quality of the patterned substrate and cannot be controlled by the growth process alone. For nanowires formed along the growth direction, on the other hand, the structure and composition can be adjusted via the growth conditions and parameters, which offers the possibility of achieving QWR structures with significantly reduced disorder.

Related to this issue of obtaining near-ideal, uniform QWR heterostructures is the perspective of fabricating QWRs with controlled variations in the potential along the wire axis. Controlling the wire potential along its axis would be useful for constructing novel low-dimensional structures such as tapered QWRs for directional exciton transport and quantum dot (QD) molecules or superlattices coupled via QWRs. Such structures have been demonstrated using patterned growth in modulated V-grooves [125] and cleaved-edge overgrowth on multiple QW heterostructures [79]. However, such modulated QWRs might be best produced using crystal growth techniques in which the wire axis is formed along the growth direction. This would allow changing the QWR structure with monolayer precision following given designs. An example of such approach is the seeded self-ordering of nanowires (or nano whiskers) grown ”under” metal particles, with which several different types of modulated nanowires have been demonstrated and studied [126] [127].

In this chapter we describe the structure and the luminescence characteristics of a new class of AlGaAs QWRs, self-formed during MOVPE in inverted tetrahedral pyramids etched on (111)B GaAs substrates. These nanometer-size VQWRs are formed due to strong Ga-Al segregation effects driven by capillarity fluxes generated at the highly-curved bottom of the pyramid, as introduced in Subsection 2.1.2. First, our study will be focused on the evaluation and model explanation of the segregation effect involved in the formation of these VQWRs and the structures connect to the VQWR (Section 3.1). Then, in Section 3.2, quantum confinement of electrons and holes in VQWRs is evidenced by peculiar transition observed in PL spectra at high excitation levels, as confirmed by theoretical modeling of these structures. Moreover, the wires grow connected to a set of higher bandgap, self-ordered AlGaAs VQWs that promote efficient carrier capture into the wires; investigation of carrier capture phenomena within this complex system, by temperature dependent PL, will be reported as well in Section 3.3.

3.1 Formation of pyramidal VQWR

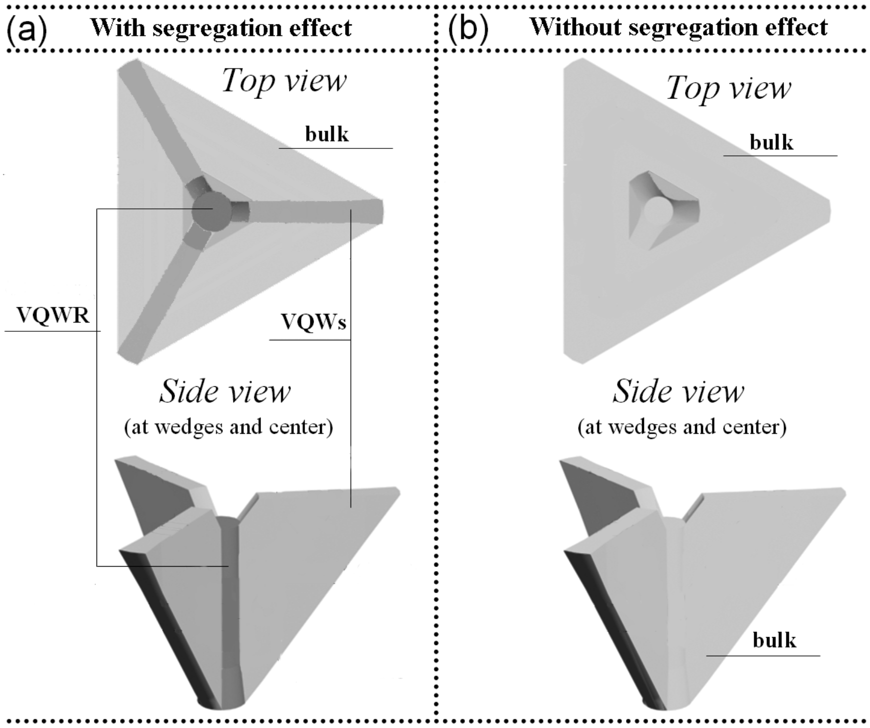

Figure 3.1: Schematics of the single layer growth inside a tetrahedral pyramid with (a) (actual case) and without(b)(imaginary case) segregation effect.

As described in Subsection 2.1.2, the epitaxial growth of an AlGaAs layer inside a pyramid by MOVPE will result in formation of pyramidal VQWR heterostructure containing several interconnected nanostructures of different dimensionality. Growth of an otherwise homogeneous layer (Fig 3.1 (b)) of $\mathrm{Al_xGa_{1-x}As}$ in such pyramids yields a 3D heterostructure formed due to growth rate anisotropy and capillarity at the three wedges and the bottom corner of the pyramid (Fig 3.1 (a)). In particular, Ga segregation effect yields three thin ($\sim$ 20 nm) $\mathrm{Al_yGa_{1-y}As}$ VQWs at the wedges, meeting at the center to form an $\mathrm{Al_zGa_{1-z}As}$ VQWR. Here, in single grown layer, the relation $\mathrm{x > y > z}$ always holds for any chosen x value. One outstanding question is how to achieve a qualitative formula to deduce the y and z values for a given x. To answer this question, we designed a set of samples for this particular study (Subsection 3.1.1). First, microscopy measurements and cathodoluminescence spectroscopy are performed to identify the different structures involved inside the pyramids (Subsection 3.1.2 and 3.1.3). Then, in Subsection 3.1.4, optical and microscopic measurements are employed to estimate the effective alloy composition and size of individual structures. Finally, a simple model is introduced to explain the segregation effect taking place in the pyramid system (Subsection 3.1.5).

3.1.1 Structures designed for studying the growth mechanism

Two sets of structures were grown by low-pressure (20mbar) MOVPE on (111)B GaAs substrates patterned with 5μm-pitch inverted pyramid arrays. They consist of two nominally $\sim$130nm thick layers of higher Al content $\mathrm{Al_{x'}Ga_{1-x'}As}$ cladding layers with $\mathrm{x'} = 0.55$ (or $\mathrm{x'} = 0.75$) sandwiching a $\sim$ 140 nm thick layer of $\mathrm{Al_xGa_{1-x}As}$, with $\mathrm{x} = 0.1, 0.2, 0.3, 0.4$ (or $\mathrm{x} = 0.5, 0.6, 0.7$, respectively), respectively. Details of the growth conditions, and epitaxy layer sequences can be found in Appendix B (growth ♯1612, ♯1665, ♯1666, ♯1670, ♯1710-1712, ♯1747). A total of seven samples were grown and characterized. Here, all nominal thicknesses correspond to growth on a control (100) GaAs substrate. An additional $\mathrm{Al_{0.75}Ga_{0.25}As}$ layer was grown right after the substrate, serving as an etch stop layer for the back-etching steps. The $\mathrm{Al_xGa_{1-x}As}$ served for forming the VQWRs investigated here, whereas the $\mathrm{Al_{x'}Ga_{1-x'}As}$ layer produced heterostructure barriers for vertical carrier confinement.

3.1.2 Microscopy of pyramidal heterostructures

TEM and AFM studies of the above mentioned or similar VQWR heterostructures were performed in order to characterize the size and the composition of the segregated structures. The sample preparation techniques have already been described in the Subsection 2.1.4. From the top-view TEM image (Fig 2.13 in Chapter 2) of the center of an $\mathrm{Al_{0.3}Ga_{0.7}As}$ layer grown inside a pyramid, we can clearly evidence Ga segregation. This is a Z contrast image, where brighter regions correspond to higher Ga content in the alloy. The brighter region in the center of the image is identified as the cross section through the VQWR, indicating a VQWR diameter of about 20 nm. The three star-like contrast segments extending away from the VQWR are the Ga-enriched VQW cross sections and are structurally connected to the VQWR. Because the VQW contrast is lower than that of the VQWR one, it is concluded that the Ga concentration in the VQW is lower than that in the VQWR. Because of the complex pyramid geometry and structure, quantitative determination of Ga content from these images is difficult and is deferred to the analysis of PL as described in Subsection 3.1.4. The cross-sectional AFM images for a pyramidal structure with an $Al_{0.3}Ga_{0.7}As$ layer nominally 17.5nm thick, sandwiched between two $Al_{0.55}Ga_{0.45}As$ cladding layers, give the information on the actual layer thickness inside the pyramid (see Fig. 2.11b in Chapter 2); for instance, the length of the VQWR in the center is about 4.5 times the nominal thickness of the corresponding AlGaAs layer.

The formation mechanism and the structure of segregated AlGaAs VQWs formed in V-grooved (100) GaAs substrates was studied in detail in Ref. [114] by systematic AFM measurements on series of samples grown using different growth parameters. The three VQWs observed in the pyramidal structure are expected to have a similar structure. Strong impact of the nominal Al content and growth temperature on the VQW width was revealed in the V-groove case. Qualitatively, the higher the nominal Al content is, the smaller the VQW width is, other conditions being fixed. The VQW width in V-grooves ranges between 29 nm for x = 0.13 to 5 nm for x = 0.75 at T = 700°C (x represents the nominal Al content). Similarly, while keeping x value fixed, in the temperature range between 650°C and 750°C, the value of the VQW width changes by a factor of 2.3 for x = 0.21 and a factor of 3.0 for x = 0.45 [114]. The width increases with growth temperature, as a result of the increased surface diffusion length of the adatoms involved.

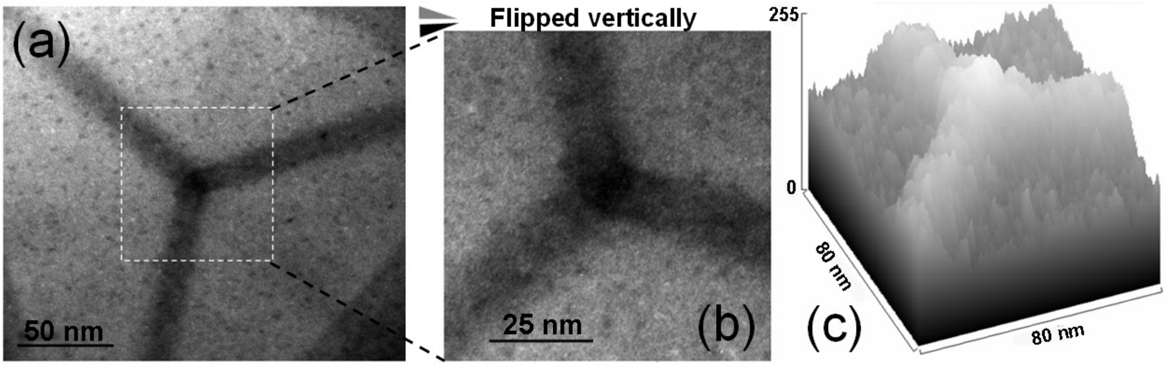

Figure 3.2: (a)Top-view TEM image of an $Al_{0.4}Ga_{0.6}As$ layer grown inside a pyramid, showing the cross sections of 3 VQW branches and 1 VQWR in the center; (b)Vertically flipped part of (a); (c)3D representation of the contrast in image (b).

Similar effect is expected in the pyramidal structure. The top-view TEM image (Fig 3.2) of the center of an $Al_{0.4}Ga_{0.6}As$ layer grown inside a pyramid shows the three VQW branches, each ∼15nm wide, meeting at the center of the pyramid, forming a VQWR of roughly triangular cross section with a side of ~15nm. The measured width of the VQW in the pyramidal structure of Fig 3.2 (15 nm) is close to the value of 12nm, expected for the width of a V-groove VQW with similar composition and growth conditions [101]. The darker contrast of the VQWR in Fig 3.2 suggests a stronger segregation and hence lower Al content. The composition of the VQWR is investigated using luminescence spectroscopy in the next sections. As in the case of V-groove VQWs, the segregation parameters (width, composition) are expected to depend on the growth conditions, such as temperature, V/III ratio and growth rate.

3.1.3 Cathodoluminescence spectrosopy for probing the barrier structures

In order to identify different structures involved in each pyramid, CL spectrosopy can be also applied [83]. One sample (x = 0.2, x′ = 0.55) from the sample series described above was characterized by CL spectroscopy at T = 10K, under an acceleration voltage of 10kV. Figure 3.3(a) is a representative CL spectra measured in spot mode at the pyramid center. The inset shows the corresponding secondary electron microscopy image of the sample, showing the back-etched pyramid array. Three main peaks emitting at ~ 1.55 eV, ~ 1.68 eV, and ~ 1.78 eV are observed. The monochromatic CL images measured at these three energies are presented in Fig 3.3(b).

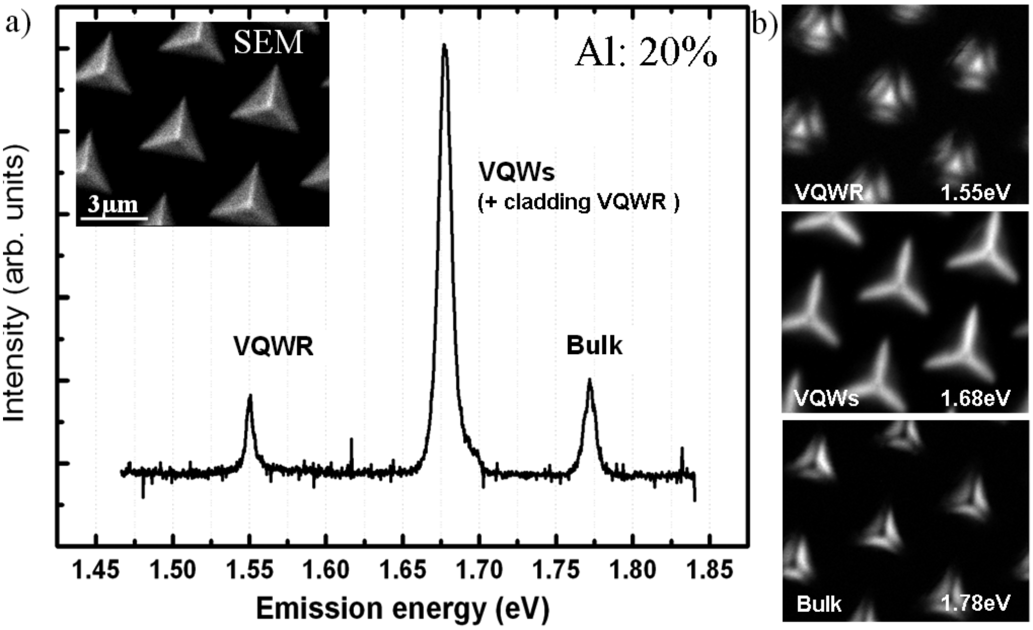

Figure 3.3: (a)Low temperature (10 K) CL spectra; (inset) Top-view secondary electron microscopy image. (b)Monochromatic CL images measured at different energies. Measured on sample (x = 0.2, x′ = 0.55) from the sample series.

The image measured at ~ 1.55 eV (Fig 3.3 (b) top) shows a bright triangle (diameter:

$\sim$ 500 nm) at the center of pyramids and three lens shaped stripes close to the three sides of the triangle. Comparing to the secondary electron image, we assign this peak to VQWR emission. This diameter of the triangle is much larger than the expected VQWR diameter ($\sim$ 20 nm) due to efficient carrier capture mainly from the surrounding structures into the VQWR. (This issue is further discussed in Section 3.3.) The images taken at $\sim$ 1.68 eV (see Fig 3.3 (b) middle) show a threefold symmetric contrast, bright at the three wedges of the pyramids. Therefore, the corresponding peak is assigned to emission from the three VQWs. The images taken at $\sim$ 1.78 eV (Fig 3.3 (b) bottom) again exhibit a three-fold symmetric contrast, but bright in between the three wedges of the pyramids. Tentatively, we assign it to the emission from bulk $\mathrm{Al_{0.2}Ga_{0.8}As}$ in the middle layer. Using the following relation for the dependence of bandgap of AlGaAs on Al content x at low temperature [128],

$$\mathrm{E_{gap}} = 1.5194 + 1.36\mathrm{x} + 0.22\mathrm{x}^2 \tag{3.1}$$

we assign an "effective" Al content to each spectral feature by replacing $\mathrm{E_{gap}}$ with the photon energy. We can roughly estimate the effective Al content in the bulk, VQWs and VQWR parts are 20%, 10% and 2% respectively.

3.1.4 Evaluation of Al-Ga segregation effect by optical measurement

Additional evidence and more quantitative information about the segregated VQWR and VQW nanostructures were obtained using micro-PL studies. Figure 3.4 (a-d) shows representative low-temperature micro-PL spectra of $\mathrm{Al_{0.1}Ga_{0.9}As/Al_{0.55}Ga_{0.45}As}$, $\mathrm{Al_{0.2}Ga_{0.8}As/Al_{0.55}Ga_{0.45}As}$, $\mathrm{Al_{0.3}Ga_{0.7}As/Al_{0.55}Ga_{0.45}As}$ and $\mathrm{Al_{0.4}Ga_{0.6}As/Al_{0.55}Ga_{0.45}As}$ pyramidal heterostructures acquired at two different photoexcitation levels, respectively. These are all measured on surface-etched samples. Several spectral lines are observed in each spectra and their identifications are indicated in the figure. Based on the CL spectroscopy study on $\mathrm{Al_{0.2}Ga_{0.8}As/Al_{0.55}Ga_{0.45}As}$ pyramidal heterostructures in the previous subsection, we assign the lowest energy line corresponds to the lowest Al content in the structure, and hence is attributed to the emission from the VQWR. Using Eq. 3.1, again we assign an "effective" Al content to each spectral feature by replacing $\mathrm{E_{gap}}$ with the photon energy. Consider the sample with $\mathrm{Al_{0.3}Ga_{0.7}As/Al_{0.55}Ga_{0.45}As}$ as an example. For the lowest energy feature, attributed to the VQWR, we obtain an effective content of $\mathrm{x} = 0.04$. The higher energy line matches in energy the emission from similar AlGaAs VQW structures grown in V-grooves on (100) GaAs substrates [129], and therefore is assigned to recombination in the three VQWs in this pyramidal structure. The effective Al content of the VQW is $\mathrm{x} = 0.17$, which agrees well with the content of the V-groove VQW structures.

Similarly, the emission lines related to transitions of the ground states of the VQWR and the VQW were identified in the micro-PL spectra of the entire series of pyramidal structures investigated. The resulting effective Al content of the VQWR and of

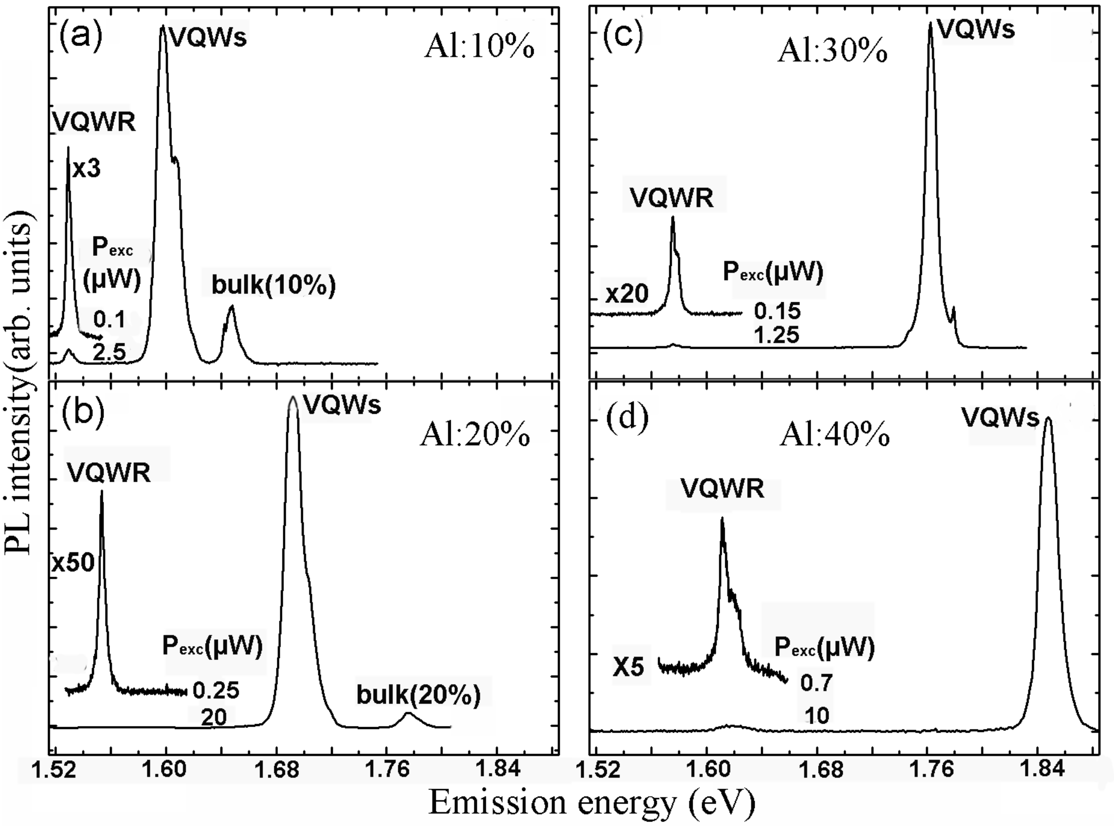

Figure 3.4: Representative low-temperature micro-PL spectra of (a) $Al_{0.1}Ga_{0.9}As/Al_{0.55}Ga_{0.45}As$, (b) $Al_{0.2}Ga_{0.8}As/Al_{0.55}Ga_{0.45}As$, (c) $Al_{0.3}Ga_{0.7}As/Al_{0.55}Ga_{0.45}As$ and (d) $Al_{0.4}Ga_{0.6}As/Al_{0.55}Ga_{0.45}As$ pyramidal heterostructure acquired at two different photoexcitation levels, P_{exc}.

the VQWs in the different samples is plotted as a function of the nominal Al concentration in Fig 3.5. (this procedure neglects quantization and excitonic effects, which partly compensate each other, without significantly affecting our composition estimation.) No lines that could be attributed to emissions from the VQWs were observed for the samples with nominal Al content of x = 0.6 and 0.7 at the core layer. This can be explained by the transition of an AlGaAs alloy from a direct bandgap to indirect bandgap semiconductor, which takes place in the gray regions shown in Fig 3.5. The measured photon energies show significant Ga-enrichment of the VQWR region, much stronger than for the VQWs. In particular, this segregation renders the VQWR direct bandgap for nominal x = 0.6 and 0.7, whereas the VQWs for these nominal Al contents are indirect due to much weaker Ga enrichment.

3.1.5 Simple model of segregation effect in pyramids

Significant segregation is evident with respect to the nominal alloy composition (dotted line in the graph) in both the VQWR and VQWs. Supposing that capillarity and other

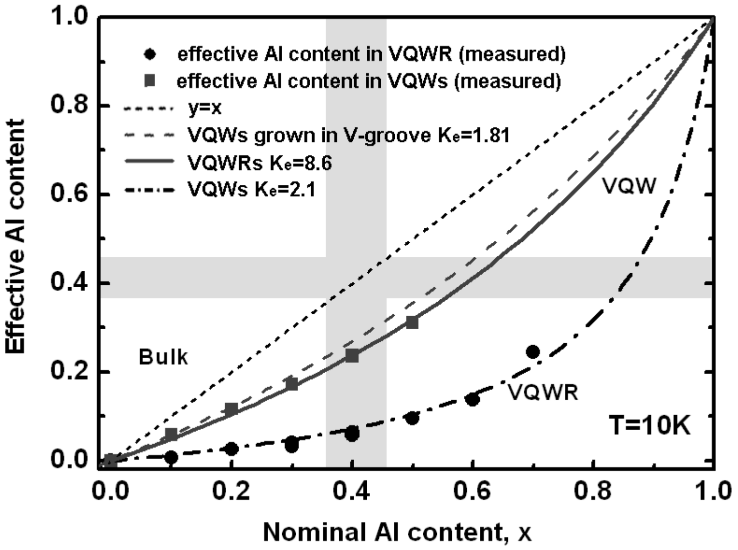

Figure 3.5: Effective Al content of AlGaAs VQWs and VQWR versus the nominal Al content (see text).

effects induce a net increase of Ga atoms flux by a factor of K_e with respect to the nominal one, one finds that the Al concentration in either the VQWR or the VQWs reads [114],

$$x_{segr}(x) = n_{Al}/(n_{Al} + K_e n_{Ga}) = x/[x + K_e(1 - x)] \tag{3.2}$$

where x is the nominal Al concentration of the grown alloy, and n_{Al} and n_{Ga} represent respectively the density of Al and Ga atoms in the alloy. Figure 3.5 presents fits of the effective Al contents determined as discussed above using the expression $x_{segr}(x)$, which show very good agreement with $K_e \cong 2.1$ for the VQWs and $K_e \cong 8.6$ for the VQWR. Also shown in Fig 3.5 is $x_{segr}(x)$ for the case of VQWs grown in V-grooves at a slightly different temperature, for which the value $K_e \cong 1.81$ was determined [114], demonstrating the expected similarity to the VQWs in the pyramidal samples.

Insight into the difference between the segregation in the VQW and the VQWR structures is obtained by considering the different geometry at the bottom of the V-groove (along the wedges of the pyramid) and at the bottom of the pyramid (see Fig 3.6). In the case of the VQWs, the increase in Ga content is related to a 1D diffusion process, due to capillarity-induced fluxes of adatoms directed normal to the axis of the groove. The number of Ga atoms deposited at the bottom facet of the groove, of length l_0, is thus:

$$a \cdot l_0 + k \cdot a \cdot l_1 = a \cdot l_0(1 + k \cdot l_1/l_0) \tag{3.3}$$

where a is the nominal (without capillarity) flux per unit length, l_1 is the effective length of the (111)A surface contributing to capillarity fluxes, and k is the fraction of adatoms on the side facet contributing to the growth at the (100) facet. The flux enhancement factor for such 1D diffusion is $K_e = (1 + k \cdot l_1/l_0)$.

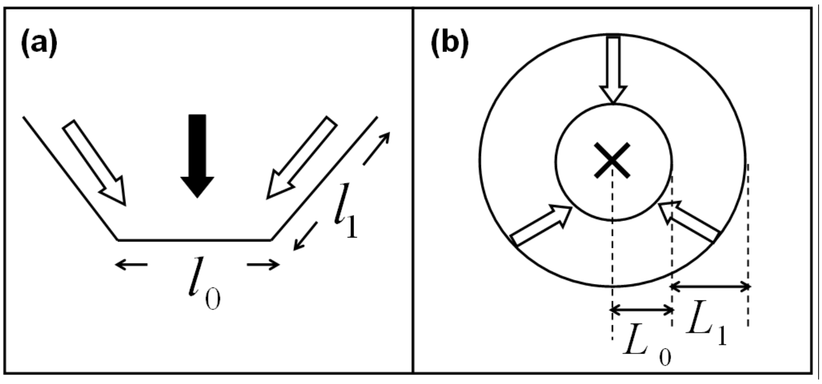

Figure 3.6: Schematic illustration of the diffusion models describing capillarity-induced fluxes in V-groove (a) and pyramidal (b) structures.

Similar analysis in the case of 2D diffusion fluxes into the VQWR region, assuming circular symmetry (Fig 3.6(b)), yields:

$$A\pi L_0^2 + KA[\pi(L_1 + L_0)^2 - \pi L_0^2] = A\pi L_0^2[K(L_1/L_0)^2 + 2K(L_1/L_0) + 1] \tag{3.4}$$

with A being the nominal flux per unit area, L_0 the radius of the cross section of the VQWR, L_1 the width of the ring on the sidewalls contributing to the diffusion, and K the fraction of adatoms on the sidewall contributing to the VQWR growth. Thus, we find that $K_e = K(L_1/L_0)^2 + 2K(L_1/L_0) + 1$. Assuming $k \approx K$, $l_1 \approx L_1$, which is reasonable as the same crystallographic planes are involved, putting $l_0 \approx L_0 \approx 20$ nm and using $K_e \approx 2.1$ for the VQWs and $K_e \approx 8.9$ for the VQWRs (from our fits), one obtains $l_1 \approx L_1 \approx 100$ nm. This value is consistent with diffusion lengths of Ga adatoms on the (111)A planes [130] [131]. We can thus conclude that the much greater segregation effect in the VQWRs is primarily due to the 2D nature of the capillarity-driven diffusion fluxes.

3.2 2D quantum confinement

The diameter of the AlGaAs VQWR inferred from the TEM images ($\sim$ 20 nm) suggests that significant quantum confinement in the plane perpendicular to the growth direction is present in these wires. Experimentally, in the PL spectra at higher excitation levels, additional peaks appear implying the formation of 1D carrier subbands in the VQWRs (see Fig 3.13).

In order to verify that these peaks appearing at high excitation indeed correspond to the intersubband (electron-hole) transitions in the VQWR, a theoretical model was built up in Subsection 3.2.1 to simulate the states in the VQWR. Then in Subsection 3.2.2, we compare the transitions observed experimentally to that predicted by the model.

3.2.1 Infinitely long QWR modeling

The pyramidal structure was modeled as an $Al_zGa_{1-z}As$ [111]-oriented, cylinder of D nm diameter, representing the VQWR, connected to three symmetrically arranged, d nm thick $Al_yGa_{1-y}As$ slabs, representing the VQWs, all embedded in bulk $Al_xGa_{1-x}As$(see Fig 3.7). The 2D problem was formulated in effective mass approximation and discretized by finite length. A single band describes the electrons in the conduction band, while the holes in the valence band are described by a 4 × 4 Luttinger Hamiltonian. The numerical codes were implemented by Dr. Fredrik Karlsson. Related theoretical background can refer to Section 1.1, 1.2 and some details on our formalism can be found in Appendix A.

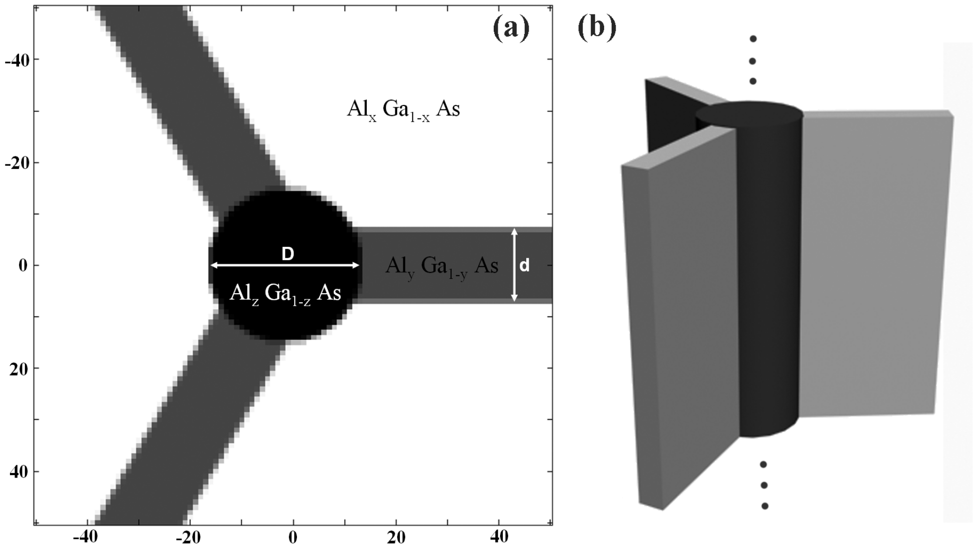

Figure 3.7: Cross section(a) and side view (b) of VQWR/VQW/bulk system used in the model.

The model includes two groups of fitting parameters: the value of Al concentration (x,y,z) and the size (D,d) of the structures (see Fig 3.7). Let us consider them one by one. The x value for the bulk is determined by the growth calibration, while the segregation model in Subsection 3.1.5 gives first clues for the y and z. Note that, in Subsection 3.1.5 we only discussed the effective Al content in the VQWR and VQWs as a function of a given nominal Al content. But for QWR states modeling, we need to input the actual Al content. The difference between the actual and effective Al content reflects the difference between the material bandgap and the first confined electron-hole states energy, i.e., the ground state confinement energy of the structure. This confinement energy is not constant, but is rather related to the potential well depth and geometry of the heterostructure. Hence to set the value of actual y and z for a given x in the QWR model, one needs to perform a series of pre-simulations to estimate the confinement energy. The effective values of y and x obtained from the segregation model can be regarded as the upper limit of the actual ones.

To simplify this complex procedure, we can first try to find the values of Al content y and width d of the VQWs using a square QW model (Fig 3.8 (a))as a separate computation step, independent to the VQWR model. We know that the VQW in the pyramid structure is very similar to the V-groove VQW, as discussed previously. It is therefore quite reliable to refer to some results achieved from V-groove VQW study. For example, we know from V-groove VQW studies that, for $x = 0.3$ (nominal Al content), the self-limiting growth in V-groove results in formation of ~ 15 nm wide VQW. We therefore input $d = 15$nm and $x = 0.3$ into the square QW model and plot the QW ground transition energy as a function of the actual Al content in the VQW, (see Fig 3.8 (b)). From PL spectra measured on the real sample, we can see that the VQW in nominal 30% Al pyramidal VQWR sample emits at around 1.74 eV (Fig 3.13). Thus, we conclude that the actual Al content in the VQW is 13% here (note that, the segregation model gives effective $y = 0.17$). More generally, we listed in Fig 3.8 (c), for 5 different nominal Al content x, the results of the measured Al content of the VQW in V-grooves and their widths, the ground state emission energy of VQW in the pyramids and the estimated effective Al content there, and finally, the estimated actual Al content in pyramidal VQWs obtained using the square QW model.

Now, we already have three of the five parameters needed for the infinitely-long QWR model mentioned at the beginning of this subsection: x, y, and d. The remaining question is how to get the values of D and z for the VQWR. Similar to the way used for the estimation of y in the last paragraph, the QWR model can produce pairs of z and D values, matching the ground emission energy of the VQWR observed in PL spectra. Taking as an example, the nominal 30% VQWR, we input $x = 0.3$, $y = 0.13$, $d = 15$ nm in the VQWR model and vary the values of D and z systematically. Figure 3.9 shows how the VQWR ground transition energy changes with the VQWR diameter D and the actual Al content in the VQWR. The transition energy is presented in gray scale. The x axis gives the value of D, and the y axis shows the actual Al content in VQWR. Experimentally, the VQWR emits at ~ 1.56 eV as shown in the PL spectra of Fig 3.13. Several contours (dash-dot lines) of energies at 1.56 eV, 1.57 eV, 1.575 eV and 1.58 eV are plotted in Fig 3.9. In principle, all the points falling into the contour of 1.56 eV have calculated ground transition energy of 1.56eV in our model. Note that, first, we did not account for the exciton binding energy in the model, which can red shift the transition energy by about $10 - 20$ meV (in V-groove QWR, this binding energy is ~ 17 meV [114]). Second, the PL spectra (Fig 3.13) were measured in a back-etched sample. From our experience, the emission energy of back-etched samples are systematically lower than that of the surface-etched ones, due to the presence of a surface-related electric field in the back-etched geometry. This systematic red shift is around 10 meV. Taking into account these two effects, we shall look for points that give the calculated ground transition energy ~ 20 meV above the observed values in the PL

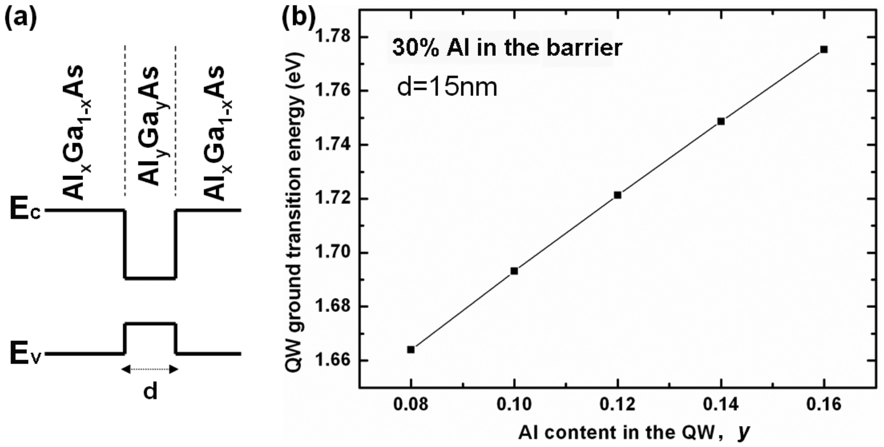

(c)

Sample No.	Nominal Al (%)	V-groove VQW studies		PL spectra studies on pyramidal VQWR samples		Estimated Al (%)in VQW by square QW modeling
		VQW width (nm)	Al (%) in VQW	Ground transition energy of VQW (eV)	Effective Al (%) in VQW	
#1	10	28	6	1.60	6	4
#2	20	23	12	1.68	12	9
#3	30	15	19	1.74	17	13
#4	40	12	27	1.85	24	20
#5	50	8.5	35	1.96	31	28

Figure 3.8: (a)Schematic illustration of the square QW model used for calculation;(b)QW ground transition energy as a function of Al content in the QW; (c)Results on estimation of Al content in VQWs using different approaches, for 5 different nominal Al content.

spectra with back-etched geometry, which corresponds to the contour of 1.58 eV in the present example.

If we only account for the VQWR ground transition, all the points falling in this contour can agree with the experiments. Actually, we can further limit the range of possible pairs of parameters (D, z) by other criteria, e.g. to determine the diameter of VQWR more precisely using microscopy or, to take into account the energies of the VQWR excited states. In Fig 3.10, the dash-dot lines and solid lines show the contours of the calculated VQWR ground (e1h1) and first excited transition (e2h2) energies as function of the VQWR diameter and Al content. The PL spectra show that the first excited state emits at around 1.579 eV. As discussed in the last paragraph, the calculated value should be 20 meV higher than the observed one to include the effects of the electric field induced by back-etched geometry and the exciton binding energy of 10 meV. The crossing point of contour 1.58 eV of the ground transition and contour 1.599 eV of the first excited transition determines the D and z values that can fit the experiments. Its coordinates are: D = 29 nm, z = 0.0275 (2.75% in the figure). Thus, we finally determined all the parameters needed in our QWR model for this example based on our measurement. This also demonstrates an indirect way to

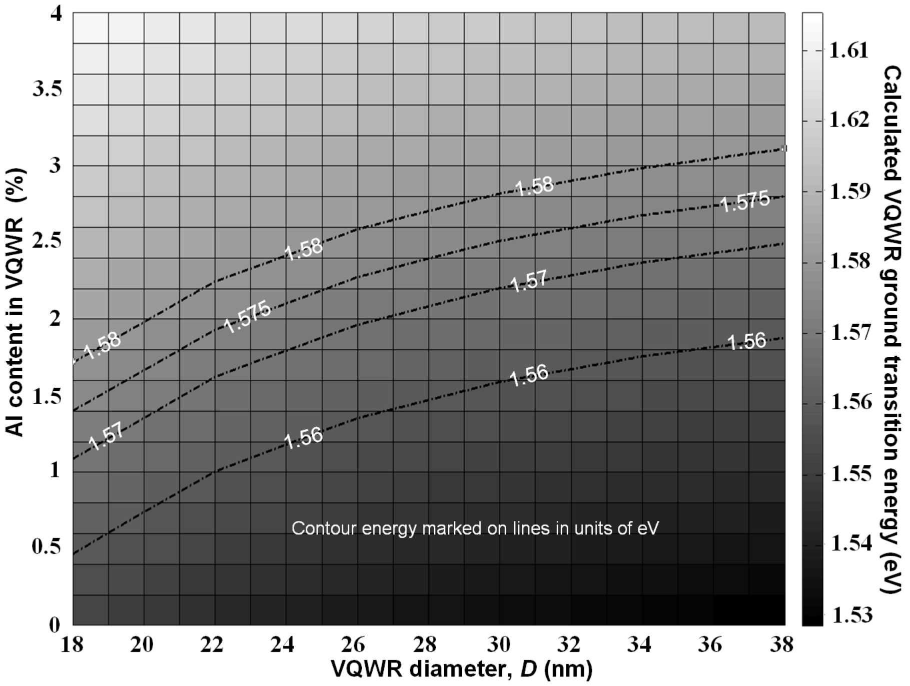

Figure 3.9: Calculated VQWR ground transition energy (gray scale) vs VQWR diameter *D* and its actual Al content(%). The vertical bar shows the corresponding energy of the gray scale.

estimate the diameter of the VQWR and the Al content in the VQWR without the aid of microscopy techniques.

Another useful conclusion we can draw from Fig 3.10 is that the VQWR diameter is mainly determined by the ground to first excited transition separation. The points correspond to $\Delta(\mathrm{s}-\mathrm{p}) = 19$ meV have very similar D values, as shown by gray circles in Fig 3.10. Roughly speaking, the s-p separation can be used as a criterion for determination of VQWR diameter in the modeling.

From Subsection 3.1.2, we know the VQW width (d) and VQWR diameter (D) can be varied by changing the growth parameters and conditions. Therefore, it is necessary to check the sensitivity of the VQWR transition energies to these parameters. Using our QWR model, we computed the ground and first excited transition energies of VQWR as a function of the VQWR diameter D for three different VQW widths: $\mathrm{d} = 12, 15, 18$ nm. Here, the x, y, z are set to be 0.3, 0.13, 0.02, respectively, in the model. From Fig 3.11, it can be seen that, for given d, the VQWR ground (e1h1) and first excited (e2h2) transition energy varies with D rapidly: for instance, changing D from 34 nm to 14 nm, the e1h1 and e2h2 transitions blue shift by more than 30 meV and 80 meV, respectively. On the contrary, the VQWR transition energies change slowly while changing d: for large D value ($24 \sim 34$ nm), almost no difference occurs in VQWR transition energy between $\mathrm{d} = 12$nm and $\mathrm{d} = 18$ nm, while for smaller D ($14 \sim 24$ nm), this difference is less than 5 meV. Thus, the precision of the estimation of D is more important than

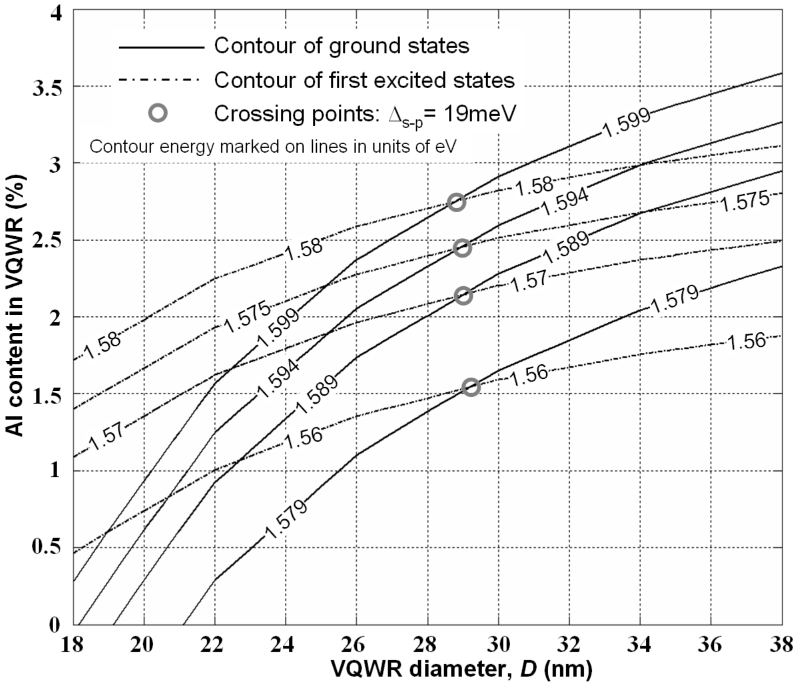

Figure 3.10: Contours of calculated VQWR ground (dash-dot lines) and first excited (black lines) transition energies as function of VQWR diameter D and its actual Al content(%). Gray circles mark the points where the ground to first excited states separation equals to 19 meV.

that of d.

Similarly, we also checked the sensitivity of the VQWR transition energies on the Al content in VQWR and VQWs using our infinitely long QWR model. Figure 3.12 shows the ground and first excited transition energies of VQWR as a function of the Al content in the VQWR for two different Al content in the VQWs: 10% and 16%. Clearly, the ground and first excited transition energies of the VQWR increase (almost linearly) with increasing Al content in the VQWR, whereas there is almost no change in VQWR transition energy, changing the Al content in the VQWs from 10% to 16%. Hence, we can conclude that the VQWR transition energy is very sensitive to the Al content in the VQWR, but much less sensitive to the Al content in the VQW barriers.

In summary, the steps for setting the parameters in QWR model are the following: First, assume that the width of the VQW in the pyramid and in the V-groove cases is the same and use these values to determine the VQW width d directly. Second, read the VQW emission energy from the PL spectra and use the square QW model to obtain the VQW composition for given d, so that the calculated results fit the measured ones. Third, input x, d, y to the infinitely long QWR model, taking the VQWR ground and first excited transition energies from the PL spectra to determine the value of D and z of the VQWR. The parameter sensitivity tests demonstrate that the precision of D and z is much more important than that of d and y for better simulation.

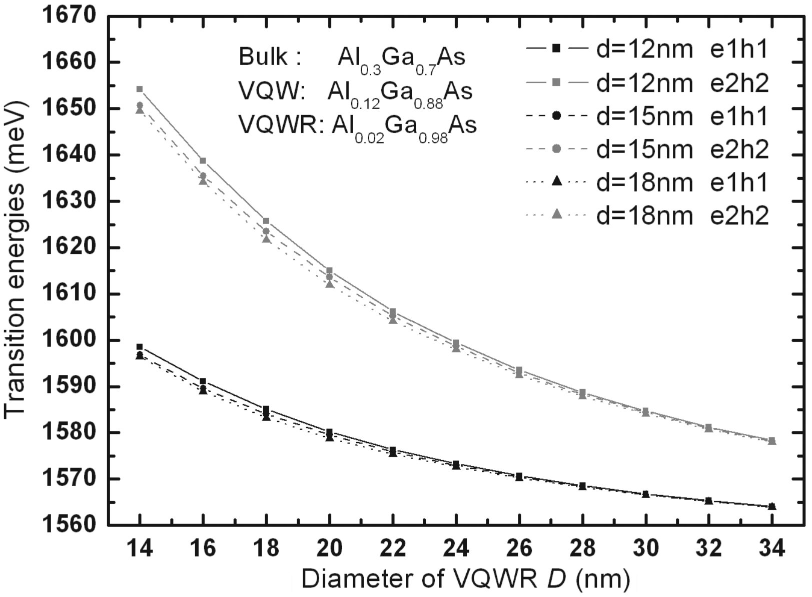

Figure 3.11: Ground and first excited transition energies of the VQWR as a function of VQWR diameter D for three different VQW width d = 12, 15, 18 nm.

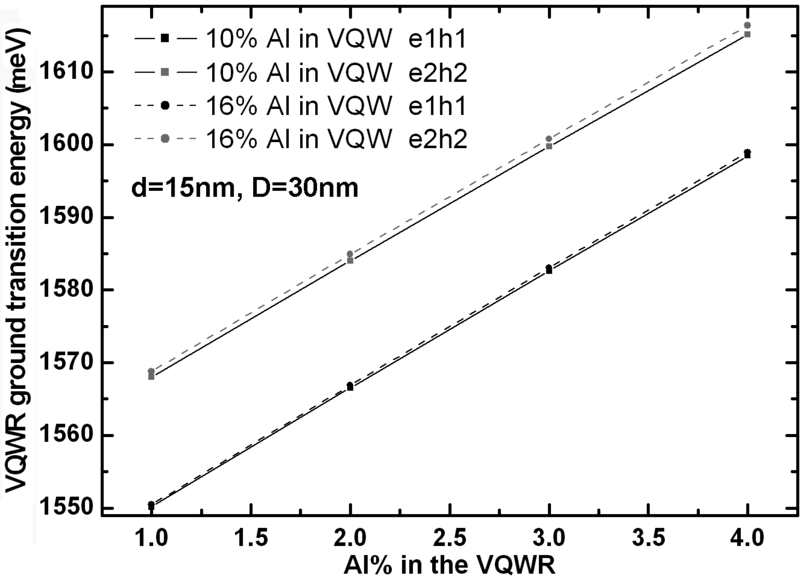

Figure 3.12: Ground and first excited transition energies of the VQWR as a function of Al cotent in VQWR, for two different Al content in VQWs: 16% and 10%.

3.2.2 Comparison of calculation and measurement

In the last subsection, a 2D infinitely long QWR model was built up based on the realistic VQWR structure. We were able to obtain the values of all the 5 parameters required in the model on one existing sample (0.3 nominal Al content in the core region

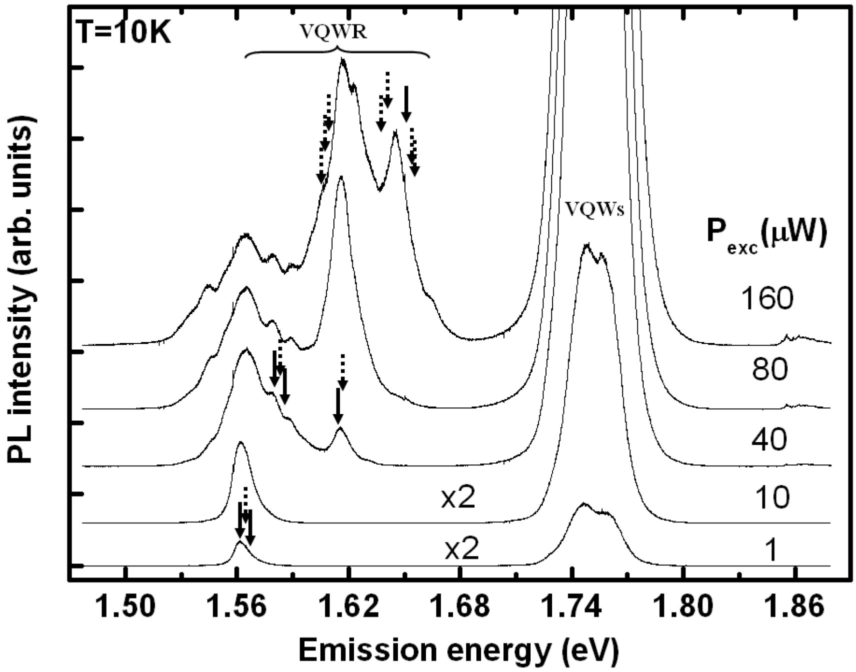

Figure 3.13: Representative low-temperature micro-PL spectra of an $Al_{0.3}Ga_{0.7}As/Al_{0.55}Ga_{0.45}As$ pyramidal heterostructure acquired at different photoexcitation levels, P_{exc}. Arrows represent the calculated transition energies (shifted by 19 meV).

and 0.55 nominal Al content in the cladding layers, back etched geometry), based on several criteria. In this subsection, we will present a more detailed comparison between calculations and measurements made on the same sample. The sample was photoexcited by Ar+ laser with different excitation power (Fig 3.13). The barely resolved doublet in the emission line of the VQW is probably related to the ground state heavy hole and light hole transitions, respectively [118]. At low excitation power, the VQWR ground transition is pronounced (1.56 eV), while at high excitation power, several more peaks corresponding to VQWR excited states emission appear at 1.565 eV, 1.579 eV, 1.589 eV, 1.616 eV and 1.646 eV. With the assistance of modeling, we are able to identify all these peaks.

In the previous subsection, we finally obtained D = 28.7 nm, d = 15 nm, x = 0.3, y = 0.13, z = 0.0275 for the model parameters. With these, we could calculate the energy and the matrix element of each transition in this VQWR structure.

The observed and the calculated transition energies are compared in Fig 3.14 (lower panel), which plots the energies of the observed transitions versus the calculated energies as filled squares. Several of the predicted transitions could be identified in the measured μPL spectra (Fig 3.13). The upper panel of Fig 3.14 presents the calculated matrix element (normalized) of each transitions for two linear polarizations: along and perpendicular to the VQWR. In general, the matrix element represents the transition rate from one state to another state due to the absorption of photon. However,it should

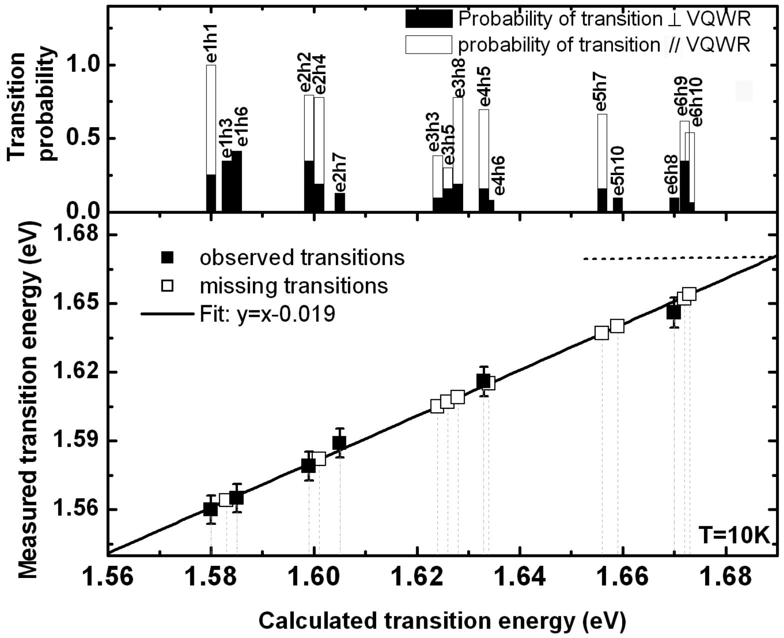

Figure 3.14: Comparison of the transitions in VQWRs found experimentally and theoretically. The upper pannel shows the calculated matrix elements of the different transitions for two linear photon polarizations. The lower pannel shows the energies of the measured and calculated transitions (filled squares) and the calculated transitions that were not observed (empty transitions), fitted with a linear curve.

be pointed out that a direct comparison between the calculated matrix elements and the observed peak intensities in the PL spectra is made difficult by several factors. First, the calculated matrix element spectra have to be weighted by a level population factor that depends on the actual carrier density in the VQWR, which is difficult to determine. Secondly, polarization effects are not resolved in this experiment; thus, a weighted average between the two polarizations is measured, with a preference to the perpendicular polarization since the spectra were measured in top-view geometry. Thirdly, the finite width of each peak limits the resolution of closely spaced transitions. Finally, population of the lowest lying subbands of the cladding VQWR, which are expected to be at $\sim$ 1.67 eV (indicated by the dash line in the Fig 3.14), may mask the higher energy transitions of the core VQWR.

The experimental results in Fig 3.14 are well fitted with a linear function $y = x - 0.019$. The shift of 19 meV has been explained in Subsection 3.2.1 to compensate the neglected exciton binding energy in the model and the energy shift in PL spectra induced by the back-etched geometry. Moreover, the fitted slope is unity showing very good agreement between the measured and calculated QWR subband separations. It confirms that the criteria we used to determine the 5 parameters in the model are reliable. The calculated transition energies (shifted by 19 meV) are marked by arrows in Fig 3.13 for a clear comparison between experiment and simulation. The solid arrows represent the measured transitions that are confirmed by the calculations, whereas the dashed arrows show the predicted transitions that could not be identified in the PL spectra.

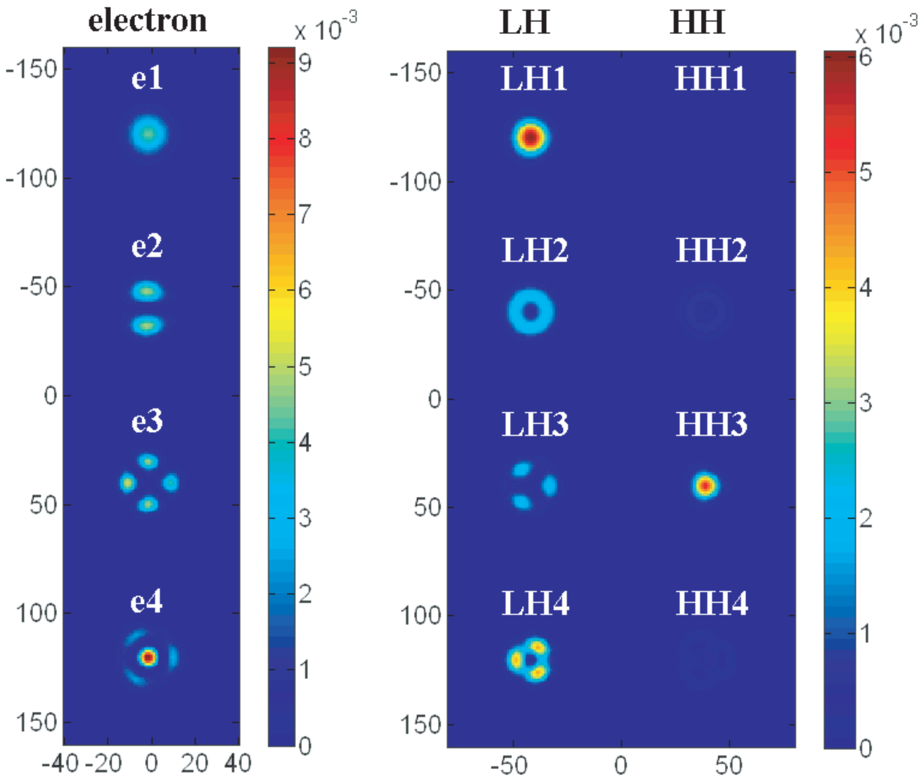

Figure 3.15: Computed probability distributions on the cross-section of the VQWR, for four lowest electron(left panel) and hole states (right panel, LH and HH components are separated) of the VQWR. The vertical bar indicates the corresponding probability density of the color scale.

Moreover, computed probability distributions for four lowest electron and hole states in this VQWR (D = 28.7 nm, d = 15 nm, x = 0.3, y = 0.13, z = 0.0275) are presented in Fig 3.15 (degenerate states are represented by one of it: e2 and e3 are both degenerate by a factor of 2). The light and heavy components of the holes are illustrated separately. Qualitatively, if a certain electron state has very similar probability distribution (in other words, larger overlap) to that of a given hole state, recombination of these carriers might take place with higher probability, resulting in a larger matrix element. For instance, Fig 3.15 shows that the first valence band is mainly LH-like and the probability distribution of LH1 component has a similar, circular shape like that of e1. Therefore, the e1h1 transition has high transition probability and its emission is mainly polarized along the VQWR axis. In addition, the polarization properties can also be deduced by this picture. This qualitative conclusion agrees with the calculated matrix element shown in the upper panel of Fig 3.14. Following the same method, we find that the e1h3 transition will be the next higher probability transition and its emission is mainly polarized perpendicular to the VQWR axis.

3.3 Carrier capture phenomena inside a pyramid

In GaAs/AlGaAs V-groove QWR structures, the Ga-rich AlGaAs VQWs were shown to provide an efficient channel for carrier transport to and capture into the lower bandgap GaAs QWRs [120]. A similar effect is expected in the pyramidal structures [121], where the three VQWs can act as efficient carrier collection and transport channels into the lower bandgap VQWR. Evidence for such carrier-capture effects can be provided by the temperature dependence of the PL spectra .

The temperature dependence of the PL spectra was measured on one sample (0.2 nominal Al content in the core region and 0.55 nominal Al content in the cladding layers, back-etched geometry) from the sample series described in Subsection 3.1, as shown in Fig 3.16. The sample was photo-excited at a photon energy higher than all heterostructure barriers (514 nm line of an Ar+ laser) at an excitation power of 0.5 μW between 10 K and room temperature.

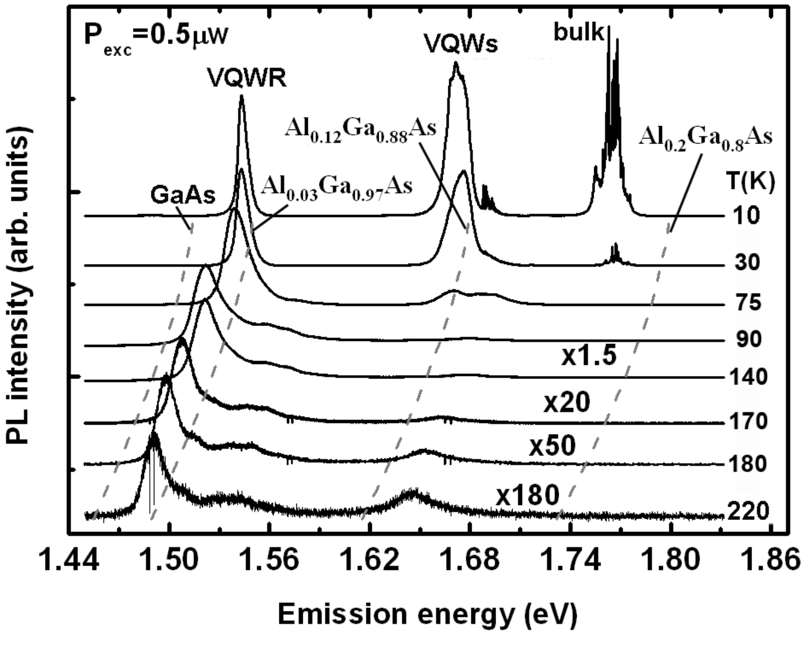

Figure 3.16: Photoluminescence spectra of a pyramidal AlGaAs heterostructure for different temperatures. The dashed lines shows the bandgap variation with temperature for the corresponding AlGaAs alloy [132].

At 10 K, three main peaks are observed, at 1.543, 1.672 and 1.767 eV. The lowest energy ones originate from recombination at the VQWR and the VQW of the core AlGaAs layer. The peak at 1.767 eV results from recombination at the $Al_{0.2}Ga_{0.8}As$ barrier grown on the near-(111)A facets; it exhibits multiple sharp lines, probably due to random Ga-Al segregation and carrier localization effects. At higher temperatures, the intensity of the higher energy peaks decreases, and above $\sim$ 90 K the spectra are dominated by the emission from the core VQWR. Simultaneously with the almost complete disappearance of the VQW and the barrier peaks, emission from the excited

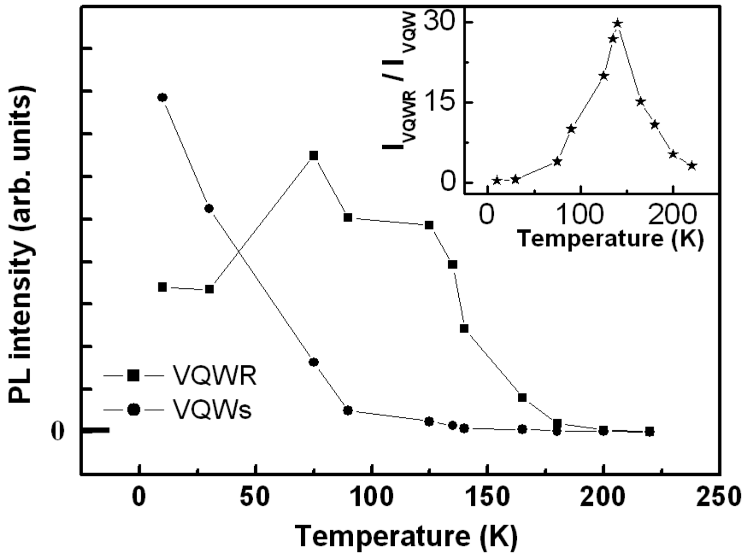

Figure 3.17: Temperature dependence of the integrated PL intensity of the VQWR and the VQW peaks. Inset shows the ratio between the integrated intensity of the VQWR and VQWs as a function of temperature.

states of the core VQWR becomes more prominent. This evolution is interpreted as resulting from the enhanced mobility of charge carriers, initially captured by the VQWs and barriers, towards the core VQWR, where they are captured and recombine. The enhanced mobility results from the thermal activation of carriers that are trapped at potential minima induced by alloy disorder in the VQWs and VQWRs.

Figure 3.17 shows the integrated intensities of the core VQWR and VQW peaks as well as their ratio (see inset). The integrated intensity of the VQW decreases monotonically with increasing temperature, due to the increase in non-radiative (phonon assisted) recombination effects as well as the increase in carrier transfer to the core VQWR. In spite of the expected decrease in radiative efficiency in the VQWR, its integrated intensity first increases, and then decreases close to room temperature. The ratio between the intensities of the core VQWR and the VQWs attains a maximum near 140 K. The enhancement of carrier transfer from the VQWs to the core VQWR peaks at intermediate temperatures since the carrier mobility is expected to be highest at that temperature range. This is because of the increased mobility due to thermal activation at lower temperatures, on one hand, and the reduced mobility due to the effect of phonons at higher temperatures [133].

3.4 Summary

In this chapter, we studied a new class of QWR realized in pyramid system. Firstly, a series of samples were designed and characterized, revealing the formation mechanism of these VQWRs. The results were explained by a segregation model. Then, quantum confinement of electrons and holes in the VQWR was evidenced by peculiar transitions observed in PL spectra at high excitation levels, as confirmed by theoretical modeling of these structures. An infinitely long QWR model formulated by effective mass approximation approach was developed to help the identification of the VQWR states. Moreover, the carrier capture process within bulk, VQW, VQWR was evidenced by temperature dependent PL spectroscopy in Section 3.3.

Chapter 4

Quantum Wires of Controlled Length: from QWR to QD

The electronic structures of QWRs and QDs has been extensively investigated in different semiconductor structures, revealing many features characteristic of 2D and 3D confined systems [122] [134] [135]. Many optical features of these low-dimensional structures, e.g., polarization anisotropy [136] [137], exciton lifetime [61] [62] [138], binding energies of excitons and exciton complexes [42] [139] [140] and other many-body effects [123] [141] [142] depend crucially on the dimensionality of the system. A useful way of examining the effect of dimensionality in these systems would be to consider a QWR of finite length and explore the modifications in its optical properties as its length is decreased. Our pyramid system is a very good candidate for realizing this because it offers control of the QWR heterostructure potential along its axis. In the previous chapter, we have studied 2D quantum confinement in VQWRs achieved in the pyramid system. In this chapter, we will consider systematically shortened VQWRs to realize transition from 2D to 3D quantum confinement. We will implement a continuous transition between the regimes of 2D and 3D quantum confinement supported by several evidences observed experimentally and confirmed theoretically in Section 4.1. Then, studies of optical properties of our pyramidal AlGaAs QDs will be presented in Section 4.2.

4.1 Transition from 2D to 3D quantum confinement

Concerning quantum confinement effects, one can distinguish between two QWR length scales. For finite-length QWRs that are long enough such that only the center-of-mass motion of excitons is quantized (”weak” 3D confinement), the impact of quantum confinement on the carrier envelope functions is negligible. For QWR lengths comparable to the exciton Bohr diameter (”strong” 3D confinement), more fundamental effects such as modified exciton life time and valence band mixing are expected to take place. Such nanostructures of "tailored dimensionality" would also be interesting for constructing mixed-dimensionality systems, e.g., QD molecules and superlattices coupled by QWR segments.

In real QWR structures, potential disorder may induce carrier localization into QD-like sections with slightly different confining potentials [123] [56] [143] [144] [57]. Certain features of exciton localization, e.g., luminescence spectra exhibiting QD-like, sharp features at low temperatures, have been observed in such disordered wires [123] [56] [143] [144] [57]. Transition between QD-like and QWR-like excitonic features have been assigned to such structures incorporating 50nm long QD-segments at 10K [59]. In general, however, disordered QWRs exhibit random localization potential profiles, which does not make them suitable for elucidating the transition from a 1D (QWR) to a 0D (QD) structure in a systematic way.

Such investigation requires a model system in which the dimensionality of the nanostructure can be controlled in sufficiently fine and reproducible manner. Several techniques in which both QWRs and QDs can be realized in the very same low-dimensional system have been explored and developed, including cleaved-edge overgrowth of T-shaped QWRs and QDs [79], core-shell nanowires and dots grown by catalyzed MOVPE [145] [146], and pyramidal QWRs/QDs grown by MOVPE on patterned substrates [147] [148]. The latter approach is particularly attractive since it offers both control of the QWR heterostructure potential along its axis and, simultaneously, results in site-controlled, embedded QWR/QD structures of high optical quality, amenable for luminescence studies.

In Subsection 4.1.1, we will introduce the series of samples designed for studying transition from 2D to 3D quantum confinement. Subsequently, several experimental evidences of this transition are demonstrated from Subsection 4.1.2 to Subsection 4.1.4, showing good agreement with theoretical predictions.

4.1.1 Structures designed for studying 2D to 3D quantum confinement

A series (Series I) of samples consisting of $Al_{0.3}Ga_{0.7}As$ VQWR layers sandwiched between $Al_{0.55}Ga_{0.45}As$ cladding layers were grown by MOVPE. The substrate preparation and the growth conditions are summarized in Appendix C and B (growth ♯1612, ♯1713, ♯1716, ♯2071, ♯2072, ♯2075, ♯2076, ♯2181, ♯2183). All investigated samples had nominally identical structure, except that the thickness of the $Al_{0.3}Ga_{0.7}As$ VQWR core layer was varied systematically from sample to sample (see below for further details). In all structures, a thin $Al_{0.75}Ga_{0.25}As$ etch-stop layer was grown between the GaAs substrate and the $Al_{0.3}Ga_{0.7}As/Al_{0.55}Ga_{0.45}As$ heterostructure to help in the subsequent back-etch procedure.

Schematic illustration of the grown structure at the pyramid wedges and center is shown in Fig 4.1(a), left panel, in which the gray scale represents the Al concentration in the corresponding region. In the particular structures studies, a lower Al-content wire, designated VQWR1, is formed in the $Al_{0.3}Ga_{0.7}As$ layer, and is bounded below and above by higher Al-content wires, VQWR2, formed in the $Al_{0.55}Ga_{0.45}As$ cladding layers. VQWR1 thus defines a lower potential QWR inserted between higher potential QWRs. The lowest bandgap (lowest Al content) regions of the pyramidal heterostructure consist thus of a VQWR segment of specific length L clad by two, higher bandgap VQWRs, as schematically shown in Fig 4.1(a), right panel. The length of the VQWR segment is directly determined by the growth time. Its composition and width can be tuned by adjusting the growth conditions (rate, temperature, V/III ratio, etc.) and growth parameters of the corresponding layer, as discussed in the previous chapter.

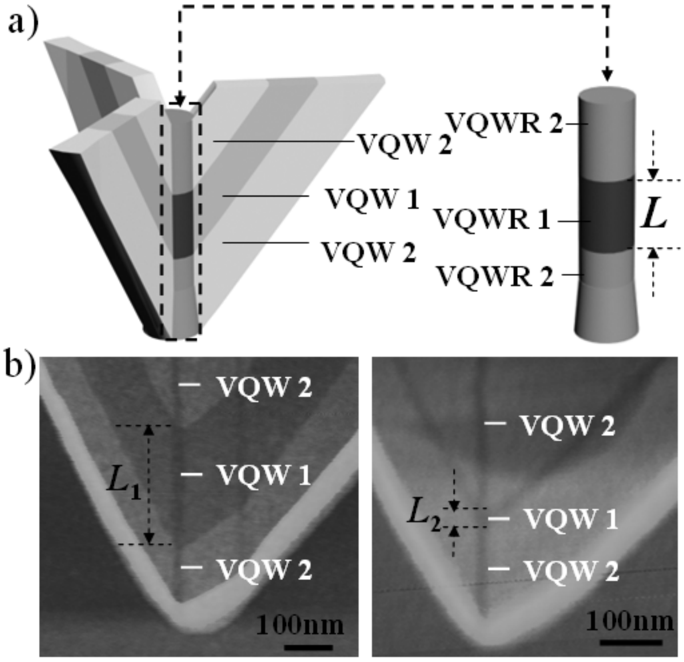

Figure 4.1: (a)Schematic illustration of the nanostructures formed inside the inverted pyramid, including AlGaAs VQWR1,2 and VQW1,2(left panel); simplified illustration of the VQWR heterostructure in the center of the pyramid (right panel); (b)Flattened cross-sectional AFM images of pyramidal heterostructures containing 300 nm (left panel) and 24 nm (right panel) thick VQW1; The lowest, bright layer represents the thin $Al_{0.75}Ga_{0.25}As$ etch-stop sacrificial layer.

The grown samples were structurally characterized using cross sectional atomic force microscopy (AFM) in air ambiance. Figure 4.1(b) shows representative AFM cross sections of two of the grown samples. From such images, we conclude that the actual VQWR length is about 4.5 times the nominal thickness of the grown AlGaAs layer. This factor varies somewhat from sample to sample because of slightly accelerated growth rate along the wire axis. Using these measurements, we deduced the actual lengths L of VQWR1 in the grown samples, which range between ~9 and 630 nm. TEM images indicate that the width of VQWR1 is ~20 nm (Fig 2.13).

We also grew another series (Series II) of samples, which is identical to Series I, except that the nominal Al contents in the core and cladding layer are 20% and 35%, respectively. The details of the growth condition and parameters can be found in in Appendix B (growth ♯2387, ♯2388, ♯2394, ♯2395, ♯2396, ♯2397). The study of transition from QWR to QD configuration is mainly based on Series I.

4.1.2 Effect on ground state energies and s-p separation

Based on the segregation model in Subsection 3.1.4, we estimate the effective Al contents in the VQWR1, VQWR2, VQW1 and VQW2 of Series I to be 4%, 12%, 17% and 37%, respectively. The resulting potential landscape of the corresponding pyramidal heterostructures is depicted schematically in Fig 4.2, upper panel, where the gray scale corresponds to larger bandgap and hence higher potential energy for carriers.

The samples were optically characterized by micro-PL spectroscopy at 10K, excited by Ar+ laser at a wavelength of 514nm. Figure 4.2(a) displays the micro-PL spectra of a single pyramid incorporating a VQWR1 structure of length L = 79nm, measured at different excitation levels. The origin of the observed transitions can be identified by referring to the potential landscape plotted at the upper panel of Fig 4.2. At the lowest excitation levels, the emission is due to recombination at the ground state of VQWR1, at ~ 1.575 eV. At higher excitation levels, transitions between excited states of VQWR1 are also observed due to state filling. The emission at ~ 1.775 eV is due to recombination at the VQW1 regions. No emission from the cladding heterostructure (VQWR2 and VQW2) was observed at this excitation range, probably due to fast carrier transfer from those heterostructures to VQWR1 and VQW1.

For comparison, Fig 4.2(b) shows the power dependence spectra of a QD-like (L = 18 nm) sample. It can be seen that the ground state transition is blue shifted (by ~ 22 meV) as compared to that of the longer wire of L = 79 nm. Moreover, the spectra of the QD-like structure show only few emission peaks between the ground state and the energy corresponding to the lowest energy transition in the barrier, VQWR2 (broader peak at ~ 1.67 eV). These features are consistent with the additional confinement expected for sufficiently short VQWRs. In particular, for wire lengths comparable to its width, a QD structure should form; the spectra in Fig 4.2(b) are indeed similar to typical QD spectra, particularly at low excitation levels. Representative power dependent PL spectra of three other samples (back-etched) with different VQWR1 length ($L = 36, 27, 9$ nm) are given in Fig 4.3 (a)-(c), respectively. The spectra of samples with L = 36 nm and L = 27 nm are very similar to each other. At lowest excitation levels, only the emissions corresponds to the ground state of VQWR1 are observed. The emission peaks are composed by several closely spaced (not very well resolved) lines that are related to the recombinations between the ground electron state, and ground and excited hole states. At higher excitation powers, transitions related to the excited states of VQWR1 are also observed due to state filling. The highest energy peaks in the measured spectra range are related to the emissions from the VQW1 region. For the sample with L = 36 nm,

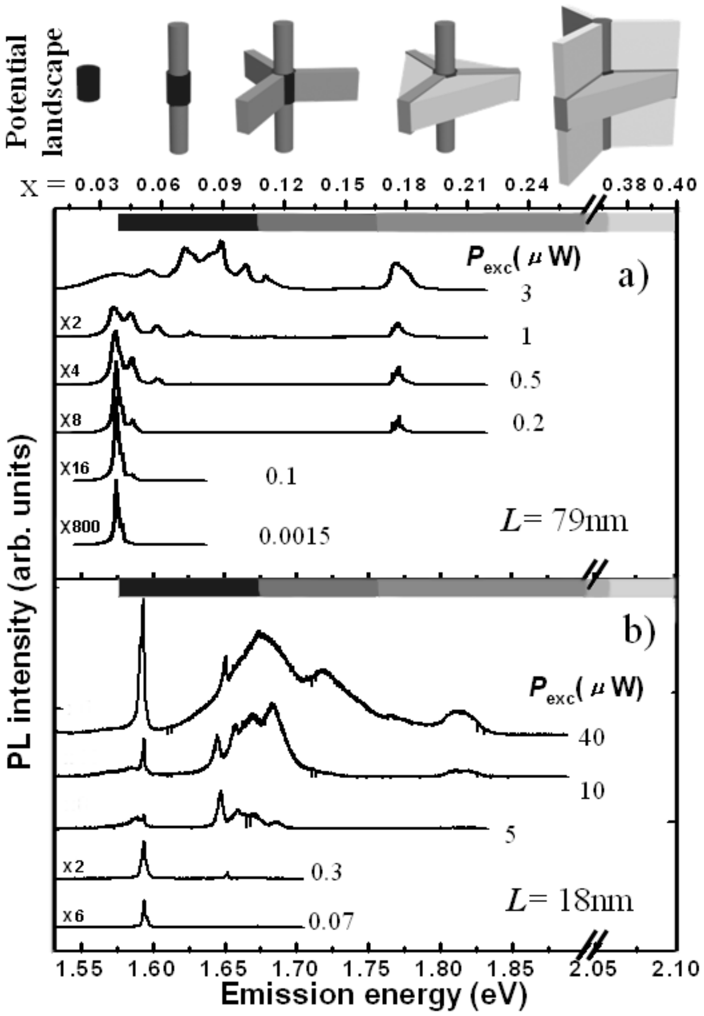

Figure 4.2: Top panel: Build-up of the potential landscape in an AlGaAs pyramidal structure with increasing energy/Al content, from left to right, showing the VQWR1, VQWR2, VQW1, $Al_{0.3}Ga_{0.7}As$ bulk, and VQW2 components. The indirect gap $Al_{0.55}Ga_{0.45}As$ bulk is omitted. Main part: Two representative power dependence series of PL spectra of 2 samples with L = 79 nm (a) and L = 18 nm (b). The abscissa shows the photon energy (bottom scale) and the Al concentration x of the corresponding $Al_xGa_{1-x}As$ alloy (top scale). The horizontal gray scale is correlated with the potential energy of the structures in the top panel, indicating the energy between the bandgap of the corresponding structure and that of the next lowest bandgap structure.

VQW1 emits at ~ 1.78 eV, whereas for the sample with L = 27 nm, it emits at ~ 1.75 eV. The small difference in VQW1 emission energies might be due to small fluctuation of Al content between the two sample growth process. The spectra of the sample with L = 9 nm (Fig 4.3 (c)) look different from the others (Fig 4.3 (a) and (b)). At low excitation level, very sharp emission peak (~ 1.62 eV) from ground state of VQWR1 is observed (FWHM < 800 μ eV). At higher excitation levels, two emission peaks around 1.67 and 1.69 are observed. The lower energy one can be the emission from the excited state of VQWR1. The higher energy one might be the emission from the cladding QWR (VQWR2) since its energy is very close to the expected emission energy of the VQWR2. The emission of the cladding QWR is more visible in this sample than that in other samples with longer VQWR1, probably because the VQWR1 layer is very thin so that a saturation of its states can be more easily reached here. Moreover, the emission from VQW1 of this sample is not observed in the measured spectra range. This can be explained by the extremely thin VQWR1 layer as well: the VQW1s are indeed QWRs. The strong quantum confinement related to the reduction of dimensionality from QW to QWR blue shifts the emission energy. Therefore, the VQW1 emission might be out of the measured photon energy range ($\sim$ 1.83 eV).

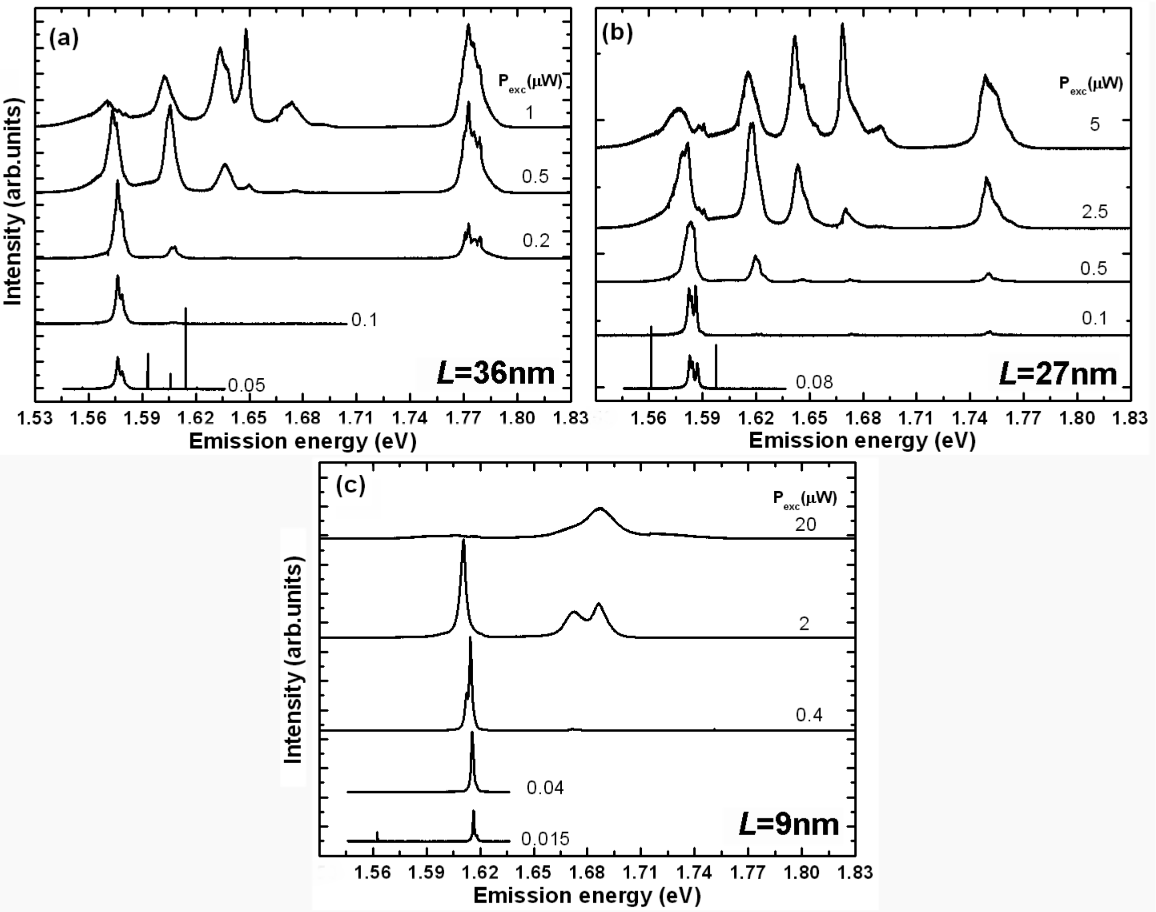

Figure 4.3: Representative low temperature power dependent PL spectra of three samples with (a) L = 36 nm (b)L = 27 nm and (c)L = 9 nm.

The complete trend of the variation in the measured transition energy of VQWR1 as a function of wire length is presented in Fig 4.4 (squares). These values were extracted from the PL spectra measured on the surface-etched samples. The vertical error bars indicate the full width at half maximum (FWHM) of the corresponding emission peak.

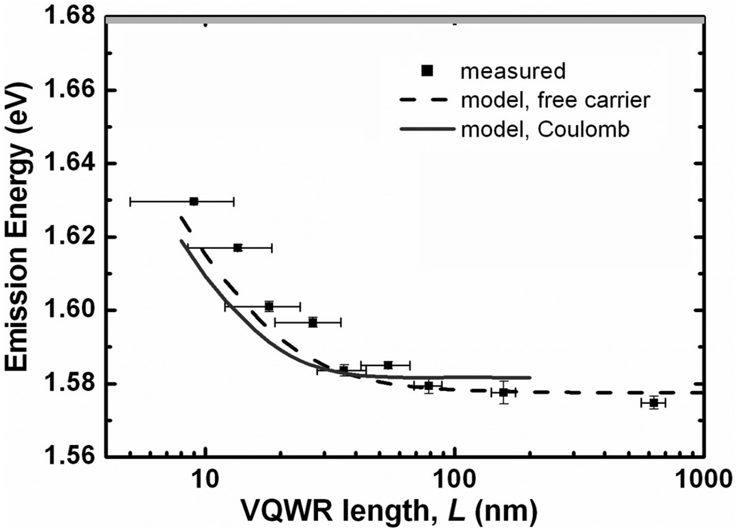

Figure 4.4: Measured ground state transition energy (of the surface-etched samples) versus VQWR1 length ***L*** (squares). Dashed line represents the transition energies calculated by a free carrier model, then corrected by adding a constant exciton binding energy 14.5 meV. Solid line shows the calculation accounting for the exciton binding energies.

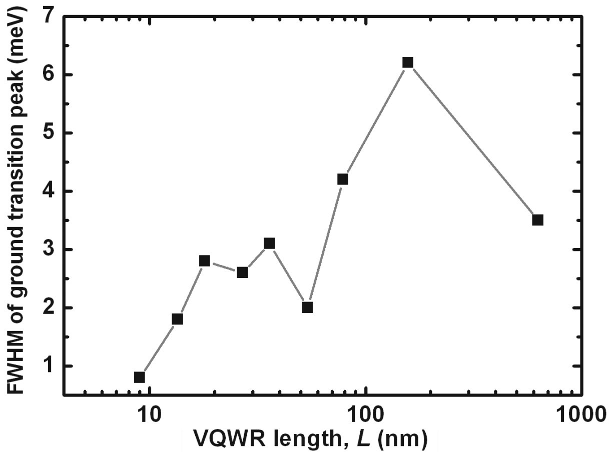

Figure 4.5: Linewidth of VQWR1 ground state emission peak as a function of VQWR1 length.

More clearly, the linewidth of the VQWR1 ground state transition as a function of VQWR1 length L is presented in Fig 4.5, showing narrower emission line for decreased VQWR1 length. This can be explained by the inhomogeneous broadening of emission peak of long QWR and reduced density of states from QWR to QD. The horizontal error bars account for the error in determining the actual wire length due to possible growth rate variations along the axis of the pyramid. Figure 4.6 shows the ground (black squares) and first excited (black circles) states transition energy measured for the back etched samples of the same series as a function of VQWR1 length. The ground state transition energies measured on the surface etched samples are also plotted

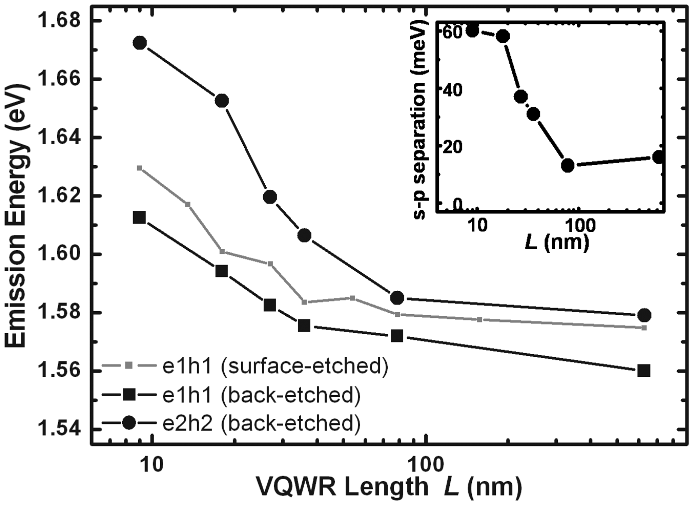

Figure 4.6: (Main) Measured ground (black squares) and first excited (black circles) states transition energy versus VQWR1 length ***L***. (Inset) Measured energy separation of the ground and the first excited state transitions as a function of VQWR1 length ***L***.

in the same figure by gray square as a reference. (As usual, a systematic red shirt in energy by ~10meV of the back-etched samples with respect to that of the surface-etched ones occurs due to the presence of the electric field in the back-etched geometries.) A monotonous increase in the ground state transition energy with decreasing wire length is observed, although the increase becomes more abrupt for L $\leq$ 30 nm. A similar trend of increase in the energy separating the ground and the first excited state transition is also noticeable, as shown in the inset of Fig 4.6. Moreover, we observed narrower linewidth of ground state transitions for L $\leq$ 30 nm, particularly at low excitation power; e.g., for L = 9 nm (Fig 4.3 (c)) we measured FWHM~ 800 μeV.

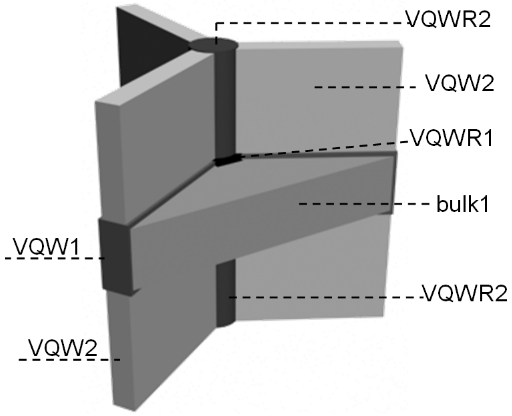

Figure 4.7: Side-view of flattened structures used in the model (see text).

To gain insight into the role of quantum confinement effects on the evolution of the optical spectra, we used a model implemented by Dr. Fredrik Karlsson, with simplified geometry to calculate the confined states and the transition energies in these QWR/QD structures. The details concerning the 3D model formalism can be found in Appendix A. The model system consists of three parallel layers of similar structures but different Al concentrations, corresponding to the core part and the two cladding regions, as shown in Fig 4.7. Each layer contains an $Al_zGa_{1-z}As$, [111]-oriented uniform cylinder of 16nm diameter, representing the VQWR/QD, connected to three symmetrically arranged, 16 nm thick uniform $Al_yGa_{1-y}As$ slabs, representing the VQWs, all embedded in bulk $Al_xGa_{1-x}As$. The core layer consists of VQWR1, VQW1 and bulk1, whereas the two cladding layers (above and below the core layer) are composed of VQWR2, VQW2 and bulk2 (not shown in Fig 4.7). Based on our earlier studies of AlGaAs VQWRs, we used $z = 0.02$, $y = 0.145$ and $x = 0.3$ for the core layer and $z = 0.09$, $y = 0.37$ and $x = 0.55$ for the cladding layers to model Series I. The thickness of the core layer was varied to simulate the different values of the VQWR/QD length/thickness. The interfaces between the grown layers are not abrupt on a nanometer scale; therefore, a 4 nm thick region of graded potential was introduced in the model at each interface [129]. In order to explore the impact of excitonic effects, the calculations were performed with and without the Coulomb interaction between the electrons and holes. In the former case, the exciton binding energies were computed using a self-consistent Hartree approach.

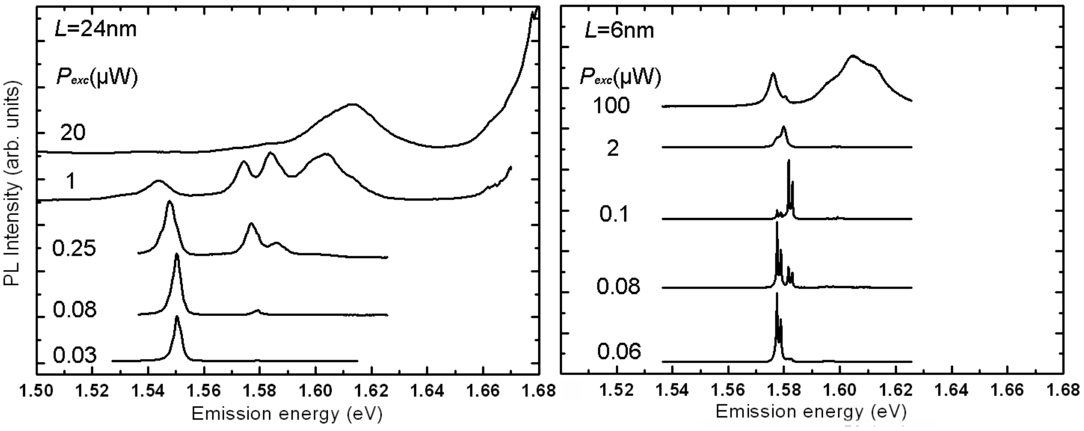

Figure 4.8: Two representative power dependence series of PL spectra of 2 samples from the Series II with L = 24 nm (left) and L = 6 nm (right).

The calculated variation of the ground state transition (e1h1) with VQWR length is shown in Fig 4.4. The dashed line shows the results obtained for free carriers (Coulomb interaction neglected), shifted down in energy by 14.5 meV for good fit with the experimental data. The value of 14.5 meV is interpreted as the average exciton binding energy, and it is in fact in good agreement with values reported for other QWRs of the same material system [149]. The solid line in Fig 4.4 represents the excitonic calculation, without any adjustable parameter. Remarkable agreement is obtained between theory and experiments, demonstrating that the blue shift is indeed caused by additional quantum confinement along the axis of the VQWR for decreasing lengths. Note that the energy shifts with and without Coulomb interaction are comparable, indicating the onset of a strong quantum confinement regime in the vertical direction for the short

VQWRs. In this QD regime, the model yields slightly lower transition energies than the measured ones as an effect of the simplified geometry used. In the real pyramidal geometry, the short VQWRs experience a higher potential due to the surrounding bulk AlGaAs. This effect is negligible for long VQWRs.

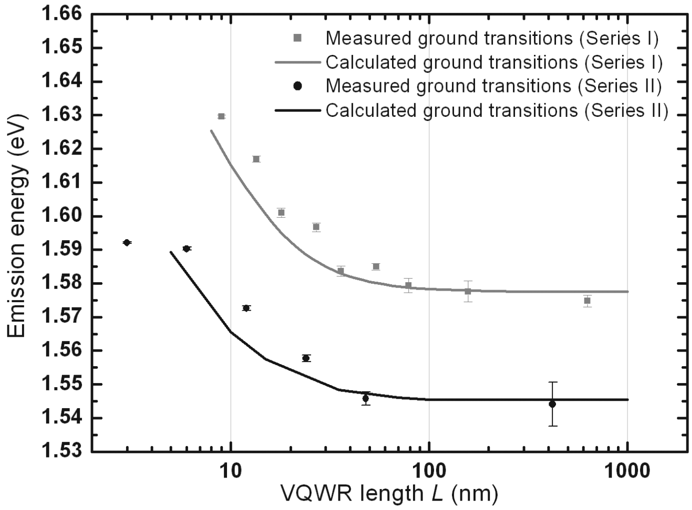

Figure 4.9: (Main) Measured ground state transition energy versus VQWR1 length $\boldsymbol{L}$ of Series II (black circles) and Series I (gray squares). The black solid line represents the transition energies of Series II calculated by a free carrier model, then corrected by subtracting a constant exciton binding energy 8 meV. The gray solid line represents the calculated ground transition energies of Series I by free carrier model, then corrected by subtracting a constant exciton binding energy 14.5 meV.

We also measured the PL spectra of Series II under the same photon excitation condition (Ar+ laser at a wavelength of 514 nm) and temperature (10 K). Two representative PL spectra at various excitation powers of two samples (back-etched) with L = 24 nm and L = 6 nm are shown in Fig 4.8. The sample with L = 6 nm exhibits well resolved sharp lines emitted from the VQWR1 region (here becoming a QD), with a FWHM around 300 μeV. Series II and I should be very similar (Fig 4.9), except: 1) the confinement potential for the VQWR/QD in Series II is shallower than that in Series I; 2) the VQWR/QD in Series II contains lower Al content than that in Series I. For easy comparison, Fig 4.9 shows the measured and calculated (free carrier model corrected with constant exciton binding energy) ground transition energy as a function of VQWR1 length of both Series II and Series I. Again, we achieved good agreement between experimental and calculated results for Series II. The emission energy of the VQWR1 is not sensitive to its length when the wire is long (> 60 nm), but increases dramatically when it becomes shorter and shorter into the QD regime. The saturation around L = 3 nm occurs probably because the energy of the state is very close to the VQWR2 bandgap, therefore the state is not very well confined in VQWR1. Studies of the optical properties of these QDs from Series II with narrow emission peaks will be given later in Section 4.2. The trends of the two series are very similar. For large L

(L > 80 nm), the ground transition energies of samples in Series II are 30 meV lower than those in Series I due to the lower Al concentration in VQWR1 of Series II. For small L, the energy difference between the two series is larger (e.g. for L $\sim$ 10 nm, $\triangle$E $\sim$ 50 nm) probably because the confinement potential along the wire axis of Series II is shallower than that of Series I. Therefore, the increase of the confinement energy of the VQWR/QD due to the decrease of the VQWR/QD thickness in Series II is less dramatic than that in Series I.

4.1.3 Size dependent polarization properties

To illustrate the impact of the confinement along growth axis, iso-surfaces of the computed electron and hole probability density functions for the three lowest states in VQWRs of two different lengths, 10 nm and 40 nm, respectively are shown in Fig 4.10 (Series I). It can be seen that the excited-states electron wavefunctions, shown in green, primarily extend transversely for the 10 nm VQWR (Fig 4.10(a)) and longitudinally for the 40 nm VQWR (see Fig 4.10(b)), always corresponding to directions of weakest confinement. The two p-like states e2 and e3 for the 10 nm VQWR are degenerate, conforming to the C_{3v} symmetry of the structure potential [150].

In contrast to the electron state, degeneracy does not apply to the hole states due to the presence of two hole types in this semiconductor. The heavy and light holes are distinguished by the angular momentum projection (J_z) on a quantization axis, chosen here as the z direction (i.e., the VQWR axis along [111]), for which $J_z = 3/2$ and $J_z = 1/2$, respectively. Note that the hole masses are anisotropic: a heavy (light) hole possesses a large (small) mass in the direction of quantization, but a small (large) mass in the perpendicular plane. For a system with 3D confinement, as studied here, the hole states are not expected to be purely "heavy" or "light" as for QWs; rather, a certain degree mixing occurs for each hole state. In Fig 4.10, the probability density distributions for the holes states are depicted as superposition of the heavy hole component (in red) and the light hole component (in blue). The hole ground states (h1) for the 10 nm and the 40 nm VQWRs are very different, exhibiting predominantly heavy (87 %) and light (94 %) hole characters, respectively. The first excited state (h2) has a switched character for the 10 nm VQWR and is strongly (85%) of light hole character, while the corresponding hole state for the 40 nm VQWR remains predominantly light (86%) as is the ground state. The second excited states (h3) have transversely modulated wavefunctions and are of strongly mixed hole character for both VQWRs. Still, this state is mainly light (63 %) for the 10 nm VQWR, but it switches character to become mainly heavy (64%) for the 40 nm VQWR.

The anisotropic hole masses yield interesting shapes of the probability density functions for the ground and excited state (h1 and h2) for the 10 nm VQWR. Due to the heavy hole character of the ground state, the large mass in the vertical direction results in strong confinement along z, while the small mass in the x-y plane leads to lateral spreading. The situation is reversed for the excited state, which exhibits light hole

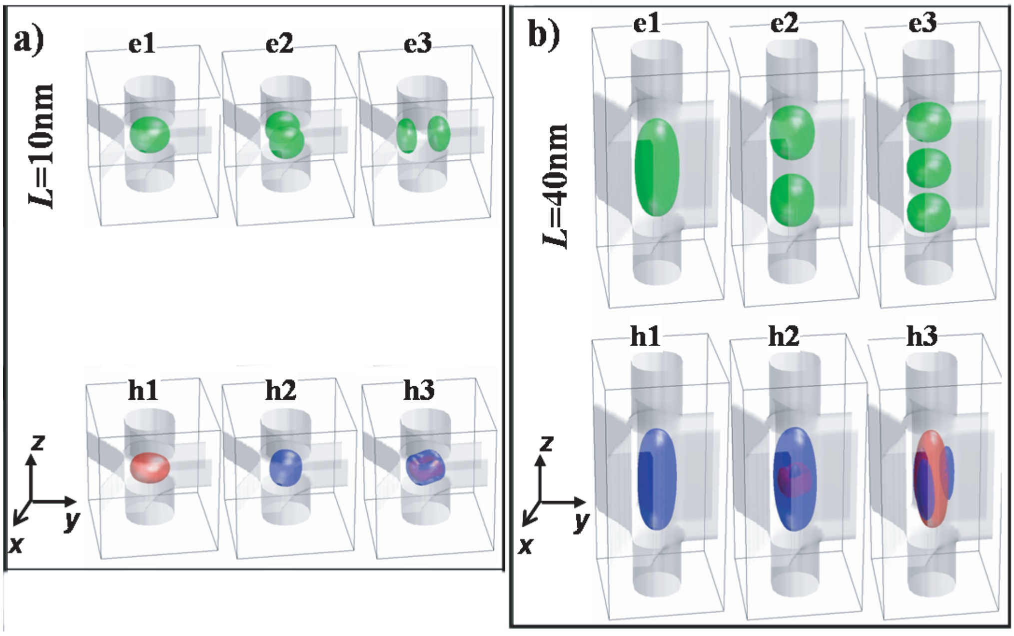

Figure 4.10: (color) Isosurfaces of computed probability distributions for the three lowest electron and hole states in VQWRs of length 10 nm (a) and 40 nm (b), corresponding to probability densities of 4×10^{-4} nm^{-3} and 1×10^{-4} nm^{-3}, respectively. The gray structures represent the shapes of the three lowest potential regions, corresponding to VQWR1, VQWR2, and VQW1 (see Fig 4.1). The electrons are represented by green, while the heavy and light components of the holes are represented by red and blue, respectively (see text for details).

character; it is elongated in the z direction, and the lateral spreading is reduced as compared to the ground state.

It is well known that the different hole characters are related to different polarization selection rules for optical transitions between the conduction band and the valence band [118]. Strongest difference in linear polarization is expected between pure heavy and light hole states, having the polarization vector oriented (mainly) parallel or perpendicular to the quantization axis, respectively. Different polarization dependence is therefore expected for VQWRs of different lengths exhibiting different hole characters (e.g., those of Fig 4.10). In search of such characteristics, which can serve as an indication of the carrier dimensionality, we performed polarization-resolved micro-PL spectroscopy on the series of VQWR samples discussed above. To allow access to linear polarization vectors oriented along, as well as perpendicular to, the VQWR, the luminescence was collected from the cleaved-edge of the sample (see Fig 2.15). The same experimental set-up as for conventional PL was used, except that a linear polarizer was mounted in front of the entrance of the spectrometer at fixed polarization direction and the slow axis of a preceding $\lambda/2$-plate was rotated in order to resolve the linear polarization content of the detected PL signal.

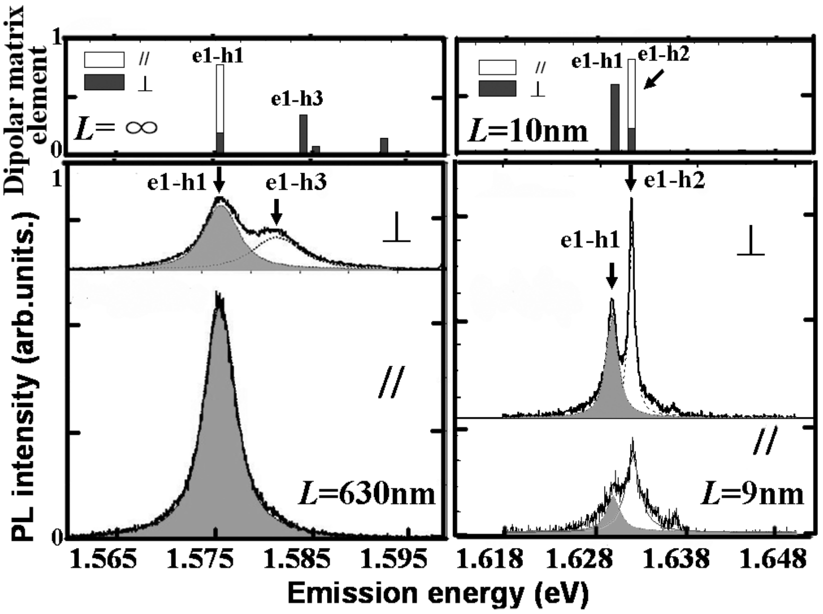

Figure 4.11: (Top)Computed dipolar matrix elements versus the transition energy, where a horizontal shift was introduced for exact match with the e1-h1 transition in the measured spectra shown below for convenient comparison. (Bottom)PL spectra acquired from VQWR samples of different lengths: L = 630 nm (left), and L = 9 nm (right), with emission polarized perpendicular (upper panel) and parallel (bottom panel) to the wire axis. The filled regions show the Voigt fittings for the ground transition.

Polarization resolved PL spectra showing the lowest energy transitions, obtained for two samples of different lengths of VQWR1 (L = 630 nm and L = 9 nm) are shown in Fig 4.11. Two closely spaced transitions are observed, with weights that depend on the orientation of the polarization plane. The lower energy peak corresponds to the e1-h1 transition, whereas the higher energy peak is identified with the aid of our model as related to excited hole states, corresponding to e1-h3 (1D subbands) for L = 630 nm and e1-h2 (0D states) for L = 9 nm. The top part in Fig 4.11 presents the computed dipolar matrix elements for parallel and perpendicular polarization vectors, above the corresponding spectra. For the QWR-like structure of L = 630 nm, the excited hole state (h3) has a predominantly heavy-hole character, and thus it is essentially completely extinct for the parallel polarization direction ($\|$). For the QD-like structure of L = 9 nm, as already discussed, the excited hole state (h2) is expected to be predominantly of light-hole character (see also Fig 4.10(a)), but the strong intensity detected for perpendicular polarization direction ($\perp$) suggests a mixed heavy- and light-hole character. For the other samples studied, with intermediate VQWR1 length, the two transitions shown in Fig 4.11 were not well resolved, but the lowest energy peak shows a similar dependence on polarization as the e1-h1 transitions for L = 630 nm and L = 9 nm.

Figure 4.12 shows representative PL spectra acquired from VQWR samples of three intermediate wire lengths: L = 157 nm (left), L = 27 nm (middle) and L = 18 nm

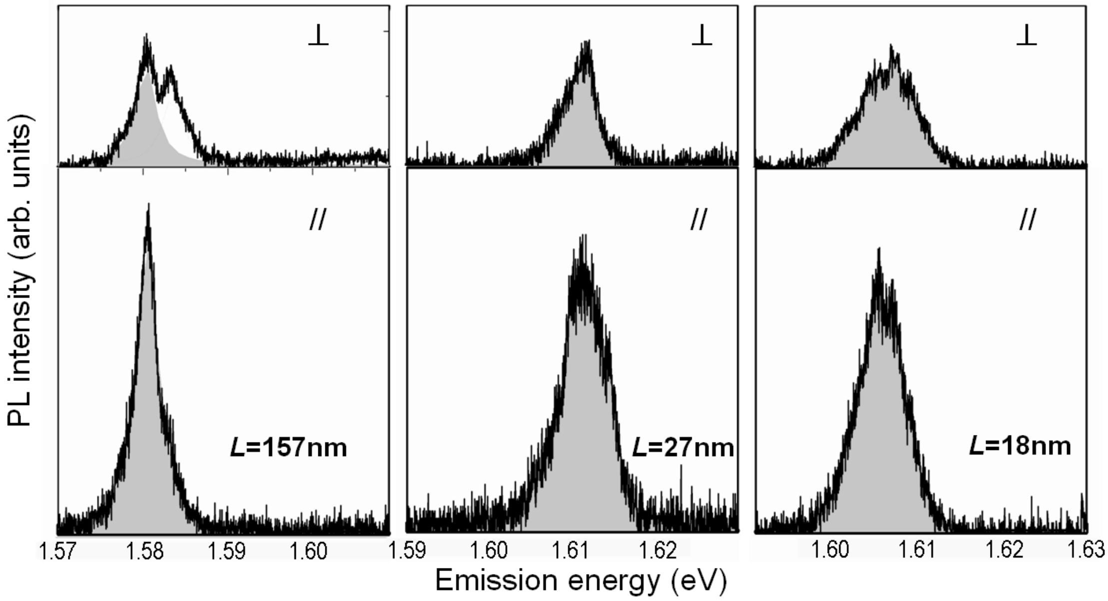

Figure 4.12: PL spectra acquired from VQWR samples of Series I of different lengths: L = 157 nm (left), L = 27 nm (middle) and L = 18 nm (right), with emission polarized perpendicular (upper panel) and parallel (bottom panel) to the wire axis.

(right), with emission polarized perpendicular (upper panel) and parallel (bottom panel) to the wire axis (growth direction). For sample with L = 157 nm, two closely spaced transition are observed, with weights that depend on the polarizations. The lower and higher energy peak corresponds to e1-h1, e1-h3 transitions, respectively. For samples with L = 27 nm and L = 18 nm, the transitions related to the ground and excited hole states are not well resolved: single broad peaks (FWHM $4 \sim 5$ eV) correspond to the ground electron states are observed for both polarizations. The full dependence of the polarization resolved PL spectra on the length of VQWR1 is summarized in Fig 4.13, which depicts the degree of linear polarization $P \equiv (I_{\perp} - I_{\parallel})/(I_{\perp} + I_{\parallel})$ versus L, where $I_{\perp}(I_{\parallel})$ is the integrated intensity for light polarized perpendicular (parallel) to the VQWR axis for the lowest energy transition. For the VQWR1 lengths where the two lowest energy transitions were resolved, Voigt functions were used to fit the two line shapes (see Fig 4.11 , Fig 4.12(left)). When only one transition was resolved, the intensity of the full spectral line was evaluated (Fig 4.12(middle)&(right)). In Fig 4.13, the open circles show the results for several pyramidal structures characterized for each VQWR1 length, whereas the filled squares show the average measured values. The three VQWR samples with $L \geq 30$ nm show emission strongly polarized along the wire axis, with $P \approx -0.6$, consistent with QWR-like polarization characteristics. For L = 18 nm the samples still exhibit negative values of P, although reduced in magnitude. Finally, for the L = 9 nm sample, positive values of the degree of polarization are observed, as large as $P = 0.375$ and with an average value of 0.061, indicating QD-like polarization characteristics.

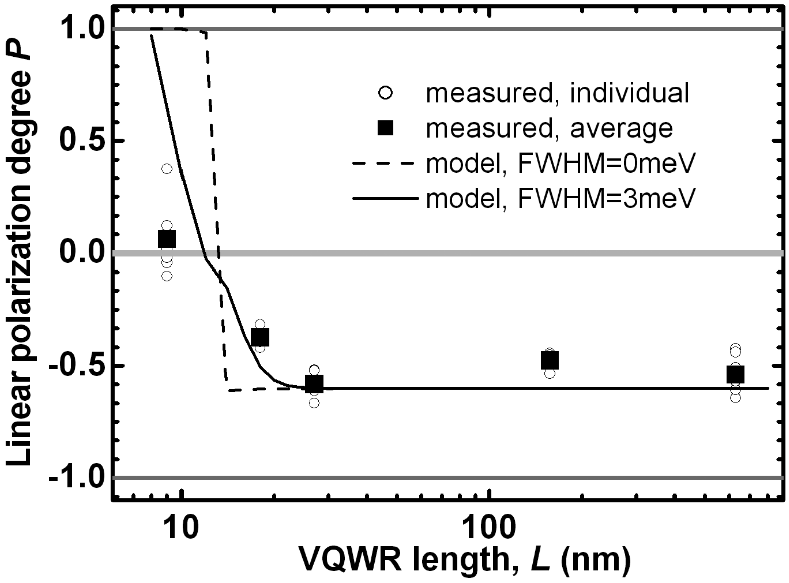

Figure 4.13: Degree of linear polarization P of the ground-state emission versus wire length (Series I). The open circles represent P measured from PL spectra whereas the filled squares represent the corresponding average values. The solid and dashed lines show the calculated P versus wire length with (FWHM = 3 meV) and without broadening of the transitions involved, respectively.

The theoretical values of the degree of linear polarization were extracted from the above-mentioned model by computing the dipolar matrix elements for the lowest energy transitions, for polarization vectors parallel and perpendicular to the QWR axis. The results are shown in Fig 4.13 neglecting (dashed line) and including (solid line) spectral line broadening. The model calculations predict a rather abrupt switching from negative (QWR-like) to positive (QD-like) polarization anisotropy for wire lengths in the range $15 - 30$ nm, i.e., lengths comparable to the width of the VQWR potential well. The transition between the two regimes is made softer for finite (FWHM = 3 meV in this case) spectral linewidths, since the splitting between the heavy-hole and light-hole transition decreases near the switching length and thus merges the opposite behaviors of the two corresponding spectral lines. The calculated results accounting for the finite linewidths are in very good agreement with the measured ones. The spread in measured P values for each QWR/QD length, especially in the QD regime, probably reflects small variations in the aspect ratio of the QWR/QD involved. It is also interesting to note that the QWR length for which P changes from wire-like to dot-like depends quite sensitively on the assumed width of the VQWR. This can serve as another means for determining the QWR width in these structures. The assumed value of 16 nm is consistent with TEM measurements of similar structures [147]; however, the degree of linear polarization in the switching range of Fig 4.13 is much more sensitive to the value of the wire diameter as compared with the TEM data. Note also that both the polarization properties as well as the abrupt change in the ground state energy (Fig

4.4) occur at wire lengths that are comparable to the exciton Bohr diameter. Hence, these effects correspond to the "strong" 3D confinement regime alluded to earlier.

The characteristics of optical polarization of semiconductor QWRs were studied by many groups both theoretically [20] [151] and experimentally [94] [152] using different model systems such as cylindrical, T-shaped or V-grooved QWRs. The degree of linear polarization P for GaAs/AlGaAs QWRs, originating purely from 2D quantum confinement and consequent valence band mixing, has been predicted [20] [151] and confirmed experimentally [94] [152] to be ~ 0.6. (Note that in previous studies the assignment of "heavy" and "light" hole masses refers to the direction of confinement [94] [152] and not to the direction of free motion as in our case, because of the different choice of the axis of quantization of the angular momentum.) Note that the strong polarization anisotropy ($P > 0.95$) related to electron-hole exchange exciton fine structure is not resolved in our experiments, due to very small splitting ($\sim 100\ \mu$ eV) of the exciton components in the present AlGaAs material. This is in contrast to in CdSe/ZnS nanorod systems, where the exciton fine structure splitting is significant (between $1.4 - 2.0$ meV) [153]. It should also be mentioned that the "giant" polarization anisotropy ($P \sim 0.96$) observed for nanowires [154], arising from pure electromagnetic effects, can be excluded in our experiments.

4.1.4 Effect on exciton radiative lifetime

Time-resolved PL spectroscopy was applied on the samples in Series I to study the impact of dimensionality on exciton radiative lifetime. The experiment setup was already introduced in Subsection 2.2.4. The back-etched samples are photon-excited by Ti : Sapphire laser at a wavelength of 740 nm (~ 1.676 eV in energy, excited in the cladding VQWR), at 10K. The excitation power is about 1.5 μW. Two representative power dependent PL spectra of two samples with L = 630 nm and L = 9 nm are shown in Fig 4.14 (left) and (right), respectively. The PL intensity here is very low because the samples are excited resonantly in the cladding VQWR, therefore fewer electron hole pairs are generated than the case when they are excited by the green laser. Emissions from VQWR1 are observed at energies of ~ 1.565 eV for the sample with L = 630 nm and ~ 1.62 eV for the sample with L = 9 nm.

Figure 4.15 (left) shows representative temporal profiles of the PL emission from VQWRs of two different lengths, L = 630 nm (detector at ~ 1.565 eV) and L = 36 nm (photon detector at ~ 1.576 eV). The measured profiles are characterized essentially by a monoexponential decay of PL. The decay time is obtained by fitting the temporal profile to an exponential function over one order of magnitude from the point corresponding to half the maximum intensity.

An increase of average exciton decay time (τ) with decreasing VQWR length was observed, as shown in Fig 4.15 (right). Especially, for the long QWRs, $\tau \sim 320$ ps, which is longer than the intrinsic exciton radiative lifetime in ideal QWR (~ 150 ps, [61]), but very close to the exciton radiative lifetime extracted from the best reported V-

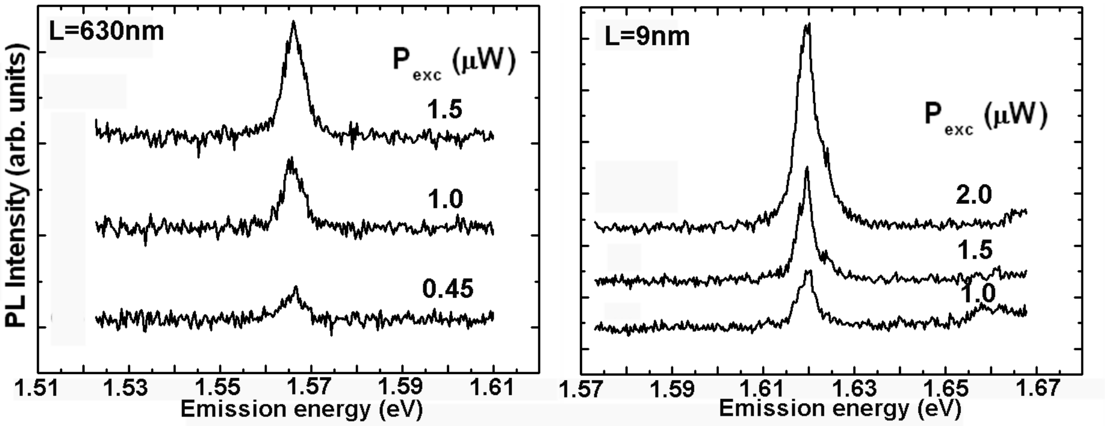

Figure 4.14: (Series I) Power dependent PL spectra of two samples with L = 630 nm and L = 9 nm. The back-etched samples are photon-excited by Ti : Saphire laser at a wavelength of 740 nm.

groove and T-shaped QWR samples [59] [64], indicating significantly low alloy disorder in our VQWRs. This is consistent with our expectation since here the VQWR is formed along the growth direction so that the VQWR/surrounding interface features are not so sensitive to the quality of the patterned substrate as compared to those wires formed parallel to the substrate plane (e.g. T-shaped or V-groove wires). Therefore, it is more promising to obtain QWRs with weaker disorder, higher optical quality with this approach. For shorter QWRs (or QDs), exciton decay times between 350ps ~ 450 ps were observed.

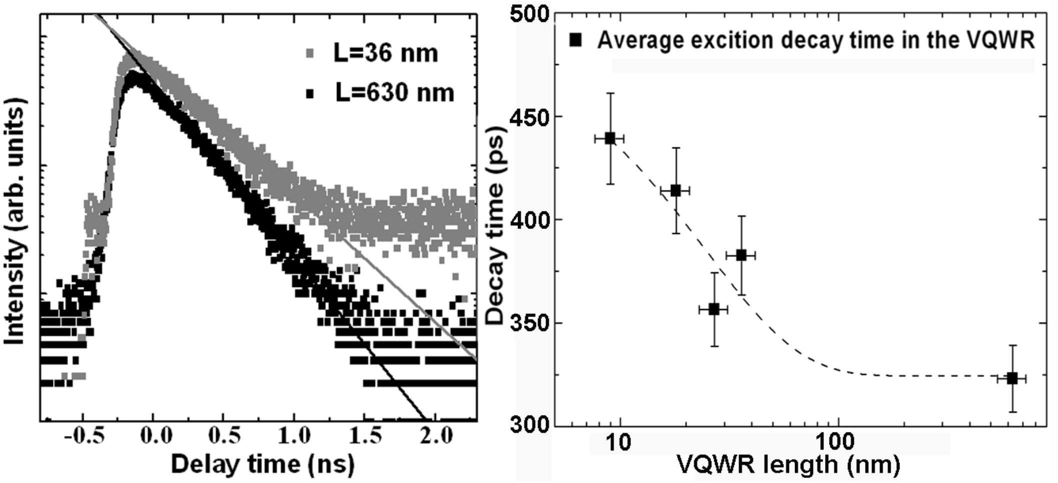

Figure 4.15: (Left) Temporal profiles of the PL emission from VQWRs of Series I of two different lengths, L = 630 nm and L = 36 nm, measured at T = 10 K, P_{exc} = 1.5 μW. (Right)Average exciton decay time as a function of VQWR length. The vertical error bars represent the spreading of measured decay time over tens of pyramids from same piece of sample. The dashed line is drawn to emphasize the tendency.

At low temperature (10 K), we can consider that the value of exciton decay time is very close to the radiative lifetime at the same temperature. Therefore, the increase of exciton radiative lifetime with decreasing VQWR length can be considered as a clear evidence of the impact of additional quantum confinement in the vertical direction (along the QWR axis) when the VQWR gets shorter and shorter into the QD regime. This is because the confinement spreads the exciton wave function in k-space to cover states that are not optically active and thereby prolong the radiative lifetime [61]. In realistic QWRs, a large fraction of excitons are bound to interface defects. The localizing potential mixes a non-radiative large-wave-vector component into the states and yields lifetimes longer than the intrinsic free-exciton lifetime.

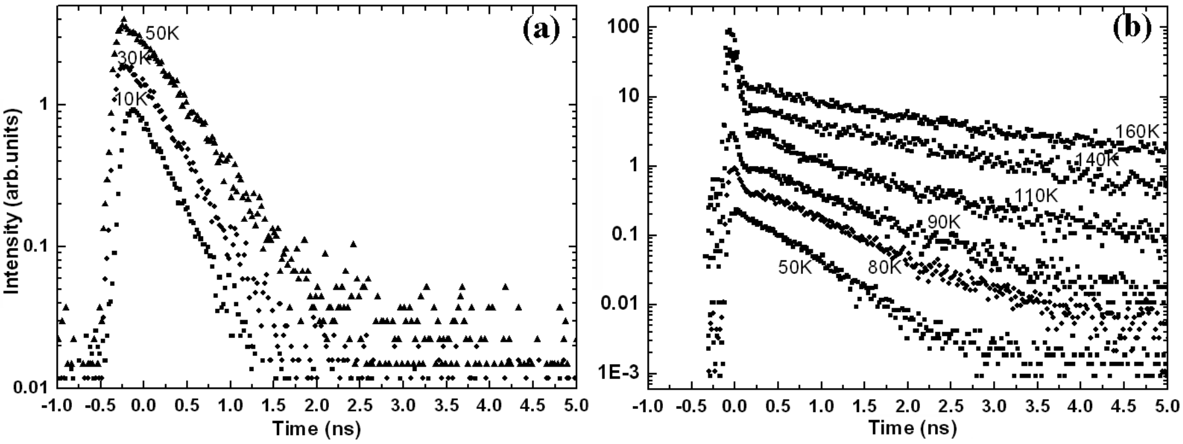

Figure 4.16: Temporal profiles of the PL emission from VQWRs measured at different temperatures: (a)10K, 30K, 50K, (b)50K , 80K, 90K, 110K, 140K and 160K. $P_{\text{exc}} = 3\ \mu$W.

In addition, a temperature dependence of exciton decay time in long VQWR is also observed, as shown in Fig 4.16. (Note: the measurements in (a) and (b) were done on two different pyramids and at different dates. Therefore, the size and the emission energy of the two measured VQWRs are slightly different due to the growth inhomogeneity.) The unusual peaks around zero delay time in (b) originate from the excitation laser that is not completely filtered. Clearly, the decay time increases with the increasing temperature, as summarized in Fig 4.17. (Again, the decay time is obtained by fitting the temporal profile in Fig 4.16 with a exponential function.) The radiative lifetime is linked to the integrated PL intensity through the radiative efficiency

$$\eta(\mathrm{T}) = \frac{\tau_{\text{decay}}}{\tau_{\text{radiative}}} = \frac{\mathrm{I(T)}}{\mathrm{I}_0} \tag{4.1}$$

in which I_0 is the PL intensity at low temperature. (For simplicity, we approximate I at T = 10K as I_0.) According to this expression, the exciton radiative lifetime was calculated and plotted as a function of temperature in Fig 4.17 (gray circles). The trend $\tau_{\text{decay}}(\mathrm{T})$ does not follow the $\sqrt{\mathrm{T}}$ dependence that is predicted for 1D QWR theoretically. In fact, there have been very few observations of such a dependence among varies types

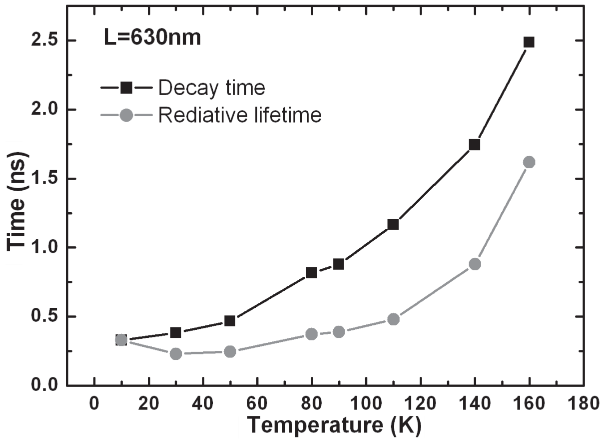

Figure 4.17: Exciton decay time and rediative time as a function of temperature.

of QWR systems [59] [64]. This is because the localized excitons play an important role in PL decay time over a large temperature range [63] [138] [155]. In particular, the interface-defect potential mixes both radiative and nonradiative free-exciton states, leading to long decay times compared with the free excitons [156]. (Several models have been proposed to describe the temperature dependence of the exciton radiative lifetime in disordered systems, e.g. Ref. [157].) In our case, the observed $\tau_{\text{radiative}}(\text{T})$ is similar to what has been reported previously for other QWR systems [59] [64].

4.1.5 Summary

In summary, we have investigated the impact of dimensionality on several features of the optical spectra of semiconductor nanostructures, as their dimensionality is reduced from 1D (QWRs) to 0D (QDs). This was accomplished using a novel system of pyramidal nanostructures, in which QWRs of specified length can be realized in a reproducible and reliable way. By systematically shrinking the length of the QWR, we observe the changes in the optical characteristics when the wires become sufficiently short, and in particular when their lengths are comparable or smaller than the exciton Bohr diameter. As expected, we observe increasing effective bandgaps and carrier state separations for decreasing wire length. Consistent with previous studies of "long" QWRs, we also observe the peculiar polarization anisotropy feature for luminescence from sufficiently long VQWRs. Interestingly, the switching from a QWR-like behavior to QD-like behavior observed in the features of the polarization anisotropy takes place for wires that are only 30nm long. This explains the QWR-like features of polarization anisotropy exhibited by many experimental QWR systems, although they all suffer from certain degrees of carrier localization, sometimes refers to as "QD behavior", due to wire imperfections. Time-resolved PL spectroscopy shows increasing exciton lifetime in VQWR with decreasing VQWR length, confirming the transition from 2D to 3D quantum confinement as well.

4.2 Optical properties of pyramidal AlGaAs QDs

The previous section demonstrated a transition from 2D to 3D quantum confinement realized in pyramidal VQWR/QD system. It also proves that we are able to fabricate AlGaAs QD with good optical quality by self-limiting layer growth inside pyramidal recesses. In the present section, we will focus on the optical properties of these QDs. First, Subsection 4.2.1 will give a brief overview on the novelty of our QD system. Second, in Subsection 4.2.2, cathodoluminescence spectroscopy will be employed to study the carrier capture phenomena within the pyramidal heterostructures. Then, Subsection 4.2.3 and 4.2.4 will show the power and temperature dependence of sharp emissions of excitonic states from the QDs. Next, Subsection 4.2.5 and 4.2.6 will demonstrate single and correlated photon emission from single QD under continuous wave excitation.

4.2.1 Pyramidal AlGaAs QD: a novel QD system

In general, our pyramidal QD system is a novel QD system for studying zero dimensional phenomena in several aspects.

Novel Material system. We studied AlGaAs QDs, which are different from previously studied InGaAs QDs formed in pyramids [19] or SK QDs made of heterostructures composed by different lattice mismatched materials. In those QD systems, the strain induced by lattice mismatch sets several constrains on the growth parameters, particularly in the case of SK dots, and introduces a more complex confinement potential distribution. In the new QD system, we are dealing with the nearly perfect lattice matched GaAs/AlGaAs system, which also opens a door for studying indirect bandgap 0D system.

Controllable QD geometry. The QD forms during the self-limiting growth inside the pyramid so that it has more regular geometry as compared to other QD systems, e.g. SK dots. As a results of strain relaxation, the SK QDs become increasingly wider as the thickness of the QD increases [76]. However, our pyramidal dots have quasi-hexagonal cross-section (as can be seen from TEM and HRSEM images), uniform along the growth direction. Moreover, the fully controllable QD thickness with monolayer accuracy enables flexible tuning of the QD aspect ratio (width/thickness). Therefore, we can control the emission polarization (which is related to the QD aspect ratio) of QDs during the growth procedure.

Tunable barrier structures. We have shown that growth of a given nominal Al content layer results in three different barrier types inside the pyramid: bulk, 3 VQWs at the wedges and 1 VQWR in the center. This type of barriers form both in core layer and in the cladding layers of the dot. By tuning the nominal Al content in these layers, one can tune the potential profiles of the barrier structures around the VQWR intentionally to modify the confinement potential and carrier capture process. Consider two examples: (a) nominal 10% Al in the core layer and 40% in the cladding; (b)nominal

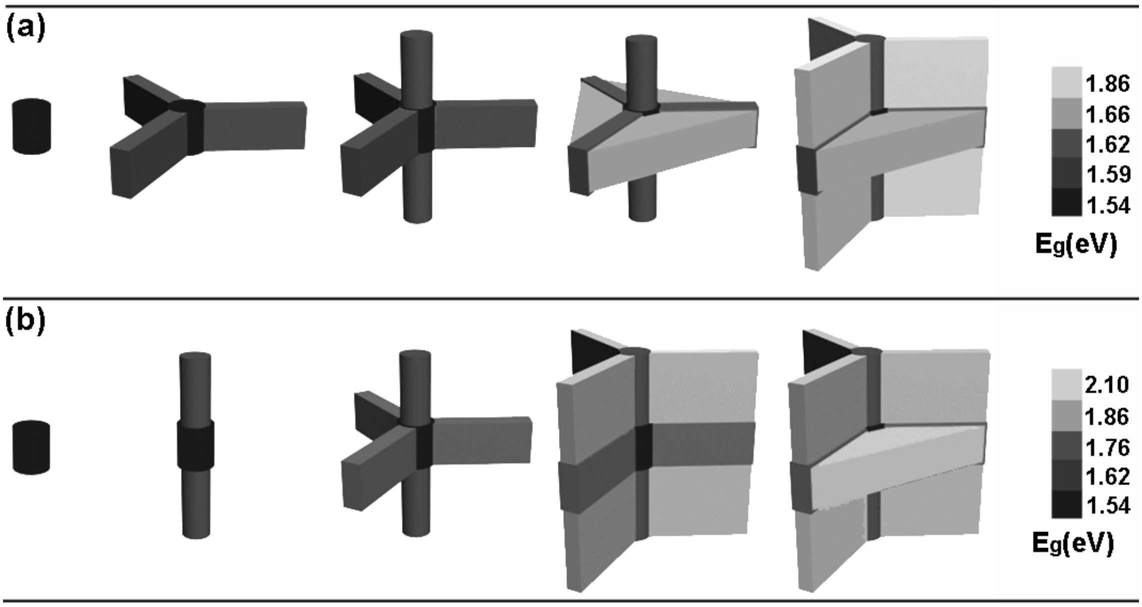

Figure 4.18: Build-up of potential landscape in an AlGaAs pyramidal structure with increasing energy / Al content, from left to right. (a)nominal 10% Al in the core layer and 40% in the cladding layer. (b) nominal 30% Al in the core layer and 40% in the cladding layer. The vertical bar (grey scale) indicates the effective bandgap energies of the corresponding structures.

30% Al in the core layer and 40% in the cladding. Based on the segregation model, the resulting potential landscapes of the pyramidal structures (flattened) of these two examples are depicted schematically in Fig 4.18 (a) and (b), respectively. The vertical bar (grey scale) indicates the effective bandgap energies of the corresponding structures. It might be quite interesting for studying carrier capture process or preferential carrier injection by this approach. Assuming that the carrier capture is more efficient from one barrier structure into another barrier structure where the potential well depth between the two barriers is deeper, one can image that the carriers (electron-hole pairs) generated in the barrier structures will be captured by the lowest potential QD structure more efficiently in case (a) than that in (b). The detailed study of the carrier capture process between the different connected individual nanostructures is outside the scope of this thesis, but in principle, this can be realized by performing time-resolved cathodoluminescence spectroscopy [158]. Moreover, the confinement potential tuned by the barrier structures will change the "effective" aspect ratio of the QD. Comparing examples (a) and (b), apparently, even the QD layers have identical thickness, the QD in (a) will result in a lower "effective" aspect ratio (thickness to width ratio) than the QD in (b) because its lateral confinement is much weaker than that in (b). Based on the studies of size dependent polarization properties of pyramidal QWR/QD structures in Subsection 4.1.3, we can expect the critical QD length (where a switching of the QD ground state emission from linearly polarized mainly parallel to the growth direction to mainly polarized perpendicular to the growth axis occurs) in (a) should be bigger than that in (b). Therefore, it can be regarded as an other approach for controlling the QD emission polarization.

4.2.2 Cathodoluminescence spectroscopy for studying carrier capture within the pyramidal heterostructure

As already introduced in Subsection 2.2.7, CL spectroscopy and wavelength-dispersive imaging are very powerful tools for investigating the carrier transport and recombination in complex semiconductor nanostructures. The small cross-section electron beam can probe a single selected nanostructure with a spatial resolution down to several tens of nanometers depending on the acceleration voltage. In subsection 3.1.3, we employed this approach to distinguish the emission peaks originated from different parts of the pyramidal VQWR structures. Here, a similar method is applied to pyramidal QD structures for studying carrier transport phenomena within the interconnected 0D-1D-2D-3D complex heterostructures.

A special sample was made for this experiment. The substrate was patterned by 7.5 μm pitch pyramid array, which is larger than the most commonly used 5 μm pitch. In this way, we can obtain more space (larger volume of the pyramid) for growth. The main structure contains an $Al_{0.2}Ga_{0.8}As$ QD layer, sandwiched by two $Al_{0.35}Ga_{0.65}As$ cladding layers (nominal Al contents are given). The QD is about 20 nm thick and $\sim$ 20 nm in diameter. The two cladding layers are of different thickness: the bottom cladding is $\sim$ 200 nm thick and the top one is more than 1 μm long. The measurement was performed in a top-view configuration.

Figure 4.19(a) is a representative CL spectrum measured in spot mode at pyramid center at 10 K (under an accelaration voltage of 10 kV, probe current of 300 pA). Several peaks corresponding to the emission energies at $\sim$ 1.57 eV, $\sim$ 1.60 eV, $\sim$ 1.69 eV, $\sim$ 1.82 eV, $\sim$ 1.91 eV and $\sim$ 1.95 eV are observed. Monochromatic CL images detecting at these photon energies are shown in Fig 4.19(b), respectively. Besides, a SEM image is also presented in the figure inset for easy comparison between the CL image and the structure distribution. Based on the segregation model in Subsection 3.1.4, we can estimate the effective Al content in QD, LQWRs, LQWs in the QD layer and VQWR, VQWs, and bulk in the cladding layers. The estimation of the effective Al content and the corresponding bandgap energy are listed in Fig 4.20 (b). A schematic illustration of the cross section of the pyramidal QD heterostructure (cleaving through one of pyramid wedge)is shown in Fig 4.20 (a) as a reference. Note that, for this sample, the growth conditions are a little different from the series studied in Subsection 3.1.4: the V/III ratio is higher (680) and the growth temperature is slightly lower. The pitch of the patterned pyramid array is also larger. Therefore, the relation between effective Al content in the structures and the nominal Al content might differ a little from the previously concluded ones (Fig 3.5). Moreover, the QD and the LQWR layers are rather thin so that the confinement will increase the emission energy as well. Based on these compositions, we assign the peaks in the CL spectra as follows: QD($\sim$ 1.57 eV), VQWR($\sim$ 1.60 eV), LQWR($\sim$ 1.69 eV), bulk($\sim$ 1.91 eV and $\sim$ 1.95 eV), as labeled in

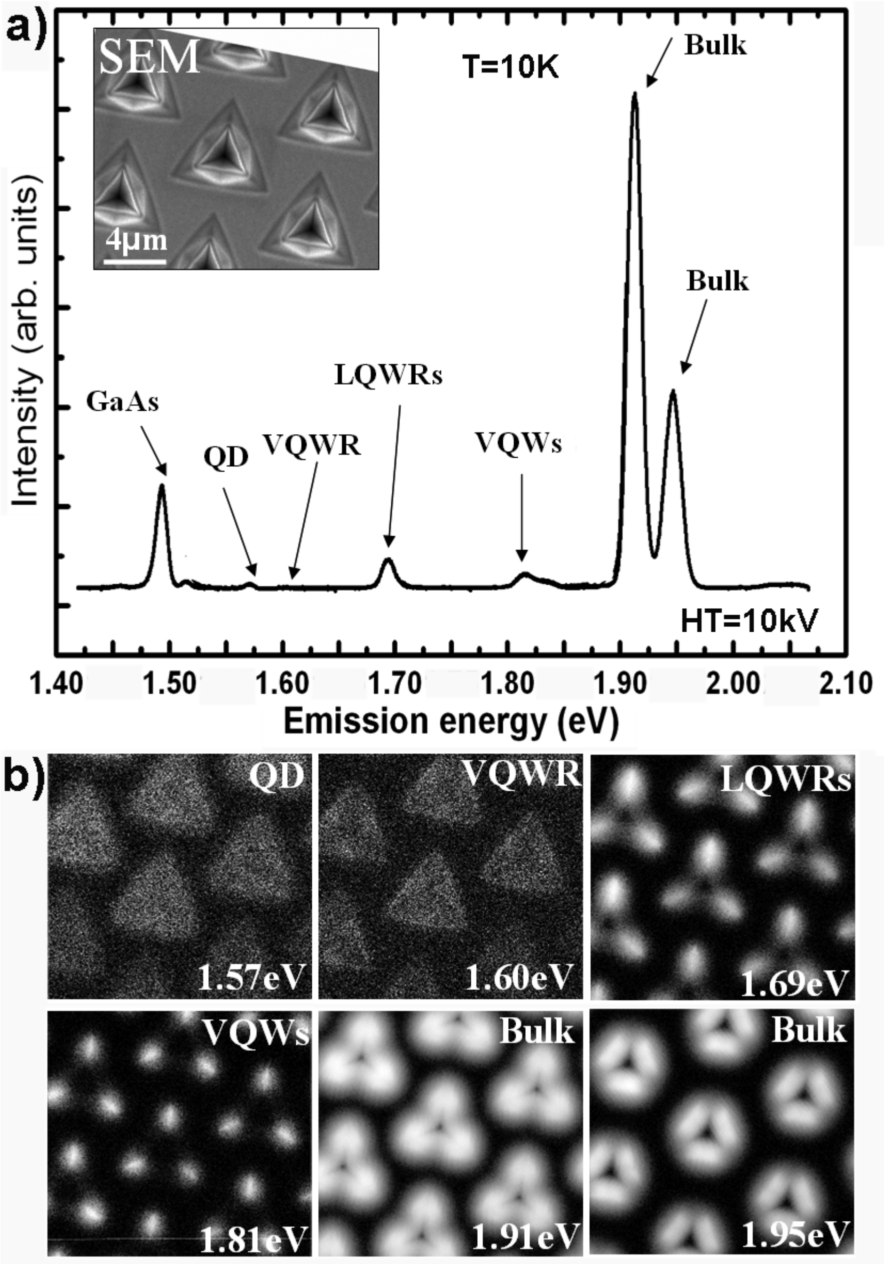

Figure 4.19: Top view CL spectroscopie of an AlGaAs QD pyramidal structure (see text). (a)Low temperature (10 K) CL spectrum measured at 10 K, under acceleration voltage 10kV and probe current 300 pA; (inset) top-view secondary electron microscopy image. (b)Monochromatic CL images measured at different photon energies.

the figure. The peak at ∼ 1.82 eV can be either from VQWs or LQWs or the overlap of both, but referring to the shape of monochromatic CL image, we tend to assign it as emission of VQWs since the CL image show three lens shaped stripes positioned at the three wedges.

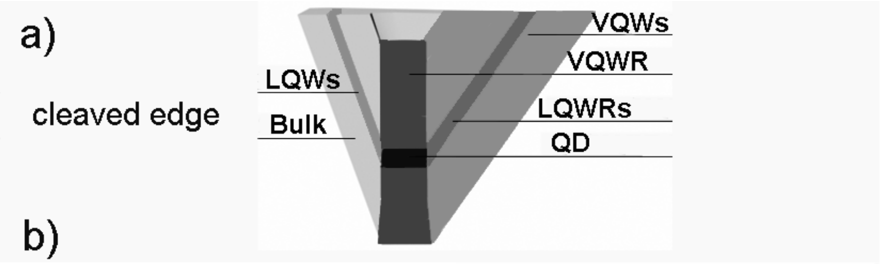

b)

	QD	LQWRs	LQWs	VQWR	VQWs	Bulk
Effective Al content	[1]2.8%	[3]10.6%	[4]20%	[2]5.9%	[4]20.4%	[5]35%
Effective bandgap	1.56 eV	1.67 eV	1.80 eV	1.60 eV	1.81 eV	2.02 eV

Figure 4.20: (a)Schematic illustration of the cross section of the pyramidal QD heterostructures. (b) Estimation of effective Al content and effective bandgap energy in all the structures of QD, LQWRs, LQWs, VQWR, VQWs and bulk insde a pyramid based on the segregation model in Subsection 3.1.4.

The monochromatic CL image measured at the QD and VQWR energies both show bright triangles covering the entire area of the pyramid, indicating efficient carrier capture from the surrounding structures into the QD and the VQWR. The weak intensity can be attributed to the small QD volume and the low photon extraction efficiency due to the measurement geometry. The CL images measured at LQWRs and VQWs show three lens shaped stripes situated at the three wedges of the pyramid, which indicates the location of the related structures taking into account the carrier capture length. We know that the width of LQWRs or VQWs is of the order of 20 nm, but the bright stripe in the corresponding CL image has a width in the order of 1 μm, which is 50 times larger than the structure width. It clearly evidences the carrier capture from the vicinal-(111)A QW structures.

The images taken at 1.91 eV and 1.95 eV (around the bulk emission energy) show a threefold-symmetry contrast. One (at 1.91 eV) is bright at the three wedges and center of the pyramids, the other (at 1.95 eV) is bright at three sides while dark at wedges and center. This is due to the alloy disorder and nonuniformity layer growth. The bulk layer is also affected from the segregation, therefore the part close to the wedges is more segregated than the part close to the pyramid side, resulting in lower emission energy and different CL pattern.

4.2.3 The power dependence of X, X^- and 2X peaks

As described in Subsection 1.2.4, the X^-, X^+ and 2X excitons all have PL emission energies that differ from the X emission energy by a few meV due to Coulomb interaction between the confined carries. Thus, the emission peaks correspond to these states are spectrally separated if the linewidth of these peaks is smaller than the separation. In principle, the emission line broadening originates from several effects. One effect is intrinsic due to finite radiative lifetime of the exciton resulting in a Lorentzian-distribution of emission peak. Since the typical radiative lifetime in QD is about 1 ns, we can estimate that the natural linewidth should be within a few μeV by Heisenberg's uncertainty principle. Other effects can be due to the charges in impurities and surfaces that yielding a small and random electric field (when "distant" impurities charge and discharge the field varies). The field induces a quantum confined Stark shift and it varies in time. Moreover, in AlGaAs system, the hole states are densely spaced by a few hundreds of μeV separation. All these effects make the observation of sharp emission from excitonic states more difficult and the inhomogeneous broadening is not observed when only single QD is measured. Apart from these effects brought by the QD itself, the spectral resolution of our micro-PL setup is about 100 μeV, which also limits the observed linewidth. Only QDs with good optical quality can be used as single photon emitters and for studying excitonic states.

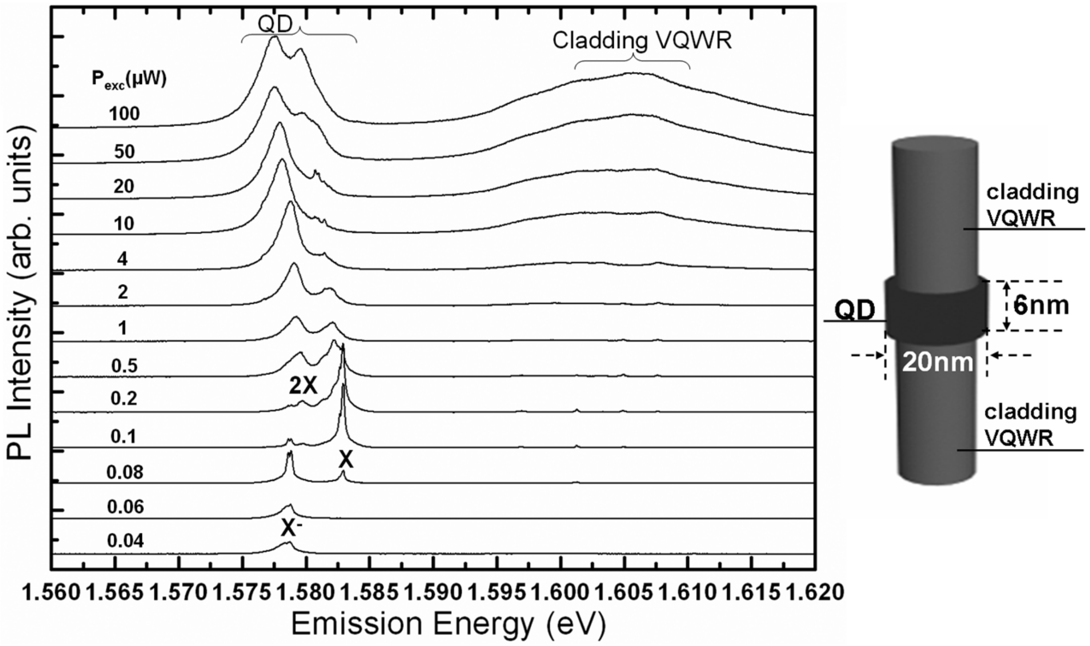

Figure 4.21: Power dependent PL spectra of single pyramidal AlGaAs QD at T = 10 K, showing QD and cladding VQWR emissions. (Right) Sketch of the core nanostructures involved.)

Figure 4.21 shows excitation power dependent μPL spectra measured on the single pyramidal AlGaAs QD. The spectra were obtained from a sample made of one nominally $Al_{0.2}Ga_{0.8}As$ QD layer sandwiched between two $Al_{0.35}Ga_{0.65}As$ cladding layers. The thickness of the QD is around 6 nm. The back-etched sample was excited by an Ar+ laser at 10 K. The excitation power varies between 0.04 μW and 100 μW. The X, X^- and 2X recombinations of very similar QD systems have been investigated both experimentally and in model calculations [139] [83] [19]. Based on these studies, we assign the X, X^- and 2X emission peaks of our QD accordingly, as marked in the Fig 4.21. We will further establish these pre-assignment by photon correlation experiments later in Subsection 4.2.6. From the power dependent spectra, we find that the X^- emission peak dominates at low excitation power. Subsequently, X appears and becomes dominate at higher power and the 2X emission appears at still higher excitation. All the emission lines get broader at high excitation power. The broad peaks red shift with increasing power due to many body effect. The broad X^- emission at low excitation can be explained by QD-impurity interaction [83]. The X^- and 2X lines are seperated by ~ 4 meV and ~ 2.5 meV with respect to X, respectively. The cladding VQWR emits at around 1.605 eV. Several sharp peaks related to the cladding VQWR are observed at medium excitation power. These peaks can be attributed to localized states in the long cladding VQWR.

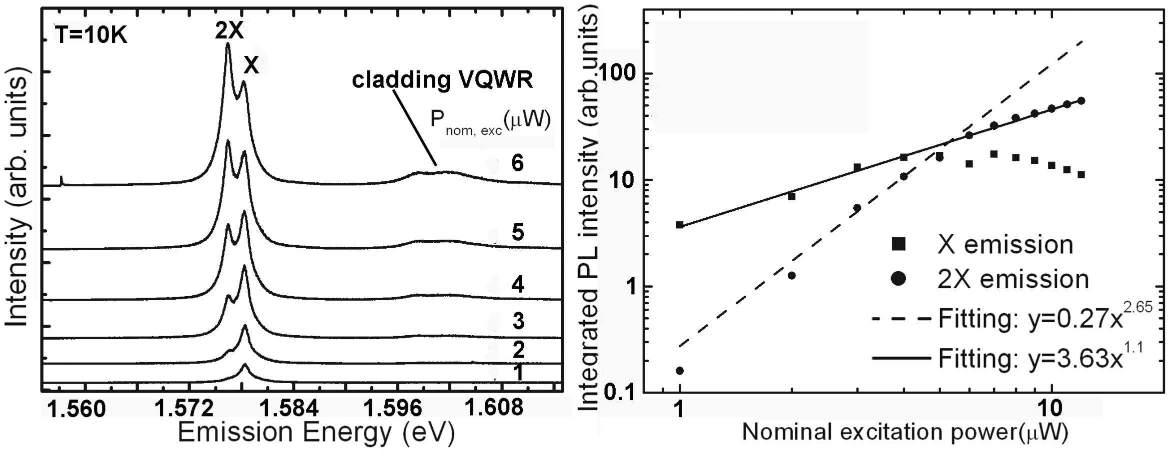

Figure 4.22: (Left)Power dependent PL spectra of single pyramidal AlGaAs QD at T = 10K, showing QD and cladding VQWR emissions. (Right)Integrated PL intensities of X and 2X emissions as a function of nominal excitation power.

Note that X and X^- peaks marked in the figure are both composed of two closely spaced sharp peaks with ~ 0.5 meV and ~ 0.5 meV separation, respectively. The close up of this feature will be found in the next subsection (Fig 4.23 and 4.24). Tentatively, we assign the lower energy one belongs to the transition of e1h1 and the higher energy one e1h2 transition related, because numerical simulation of these QDs reveals level separation of h1 and h2 of about 0.5 meV. The small difference (0.1 meV) between the splitting of the X and that of the X^- emission can be due to the slightly coulomb energies in these two exciton configurations.

In spectra acquired from some other QDs from the same sample, X and 2X peaks with similar relative energetic positions can be observed, but the linewidths of the peaks are slightly larger, as shown in Fig 4.22 (left). The X^- emission peak is not observed under low excitation power , indicating that this particular QD is not charged under thermal equilibrium [19]. The integrated PL intensity as a function of nominal excitation power is summarized in Fig 4.22 (right), showing nearly linear and quadratic dependence of the X and 2X peaks, respectively. The integrated PL intensity was extracted from the PL spectra using a Lorentzian fitting of the corresponding peaks.

The quadratic dependence of the 2X peak confirms our assignment since two excitons are required to form a biexciton, so that its intensity depends quadratically on the average number of excitons (the single exciton intensity has naturally a linear dependence on average number of excitons) [159].

4.2.4 Temperature dependence of X, X^- peaks

The present subsection discusses the influence of the sample temperature on the X and X^- peaks. Figure 4.23 shows two series of power dependent PL spectra of single AlGaAs QD measured at T = 10 K (left) and T = 30 K (right). The excitation power varies between $0.017 \sim 2$ nW. The relative intensity between the X and X^- peaks changes with increasing excitation power, as discussed in the previous subsection. At the same excitation power level but higher sample temperature, the X^- peaks are more pronounced as compared to the X peaks. The temperature dependence of the PL spectra at $P_{exc} = 0.5$ nW is presented in Fig 4.24 to illustrate the evolution of the relative intensity between X and X^- as a function of the temperature. The X, X^- spectral evolution with increasing temperature is very similar to the evolution with decreasing power: X^- emission is more pronounced at higher temperature (or lower power). This can be explained by the decreasing effective power (more power contributed to non-radiative process) with increasing temperature. In addition, increasing the temperature will enhance the back-hoping rates of donor-bound electrons to the QD, increasing the stationary number of QD electrons at low excitation power, consequently the QD is more charged at higher temperature [83] [139] . This mechanism has been investigated both experimentally and theoretically on similar QD samples in Ref. [139] [83].

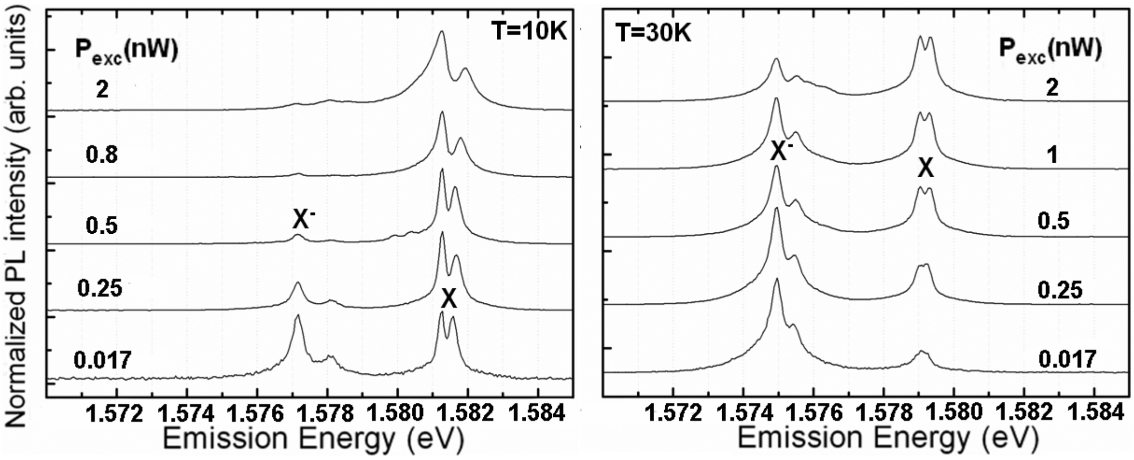

Figure 4.23: Power dependent PL emission of single AlGaAs QD at T = 10 K (left) and T = 30 K (right).

Another spectral evolution observed with increasing temperature is the following: there is a 3 meV energy shift of the QD emission to the lower energy side from 10 K to 40 K, which can be attributed to band-gap renormalization. Apart from this, one

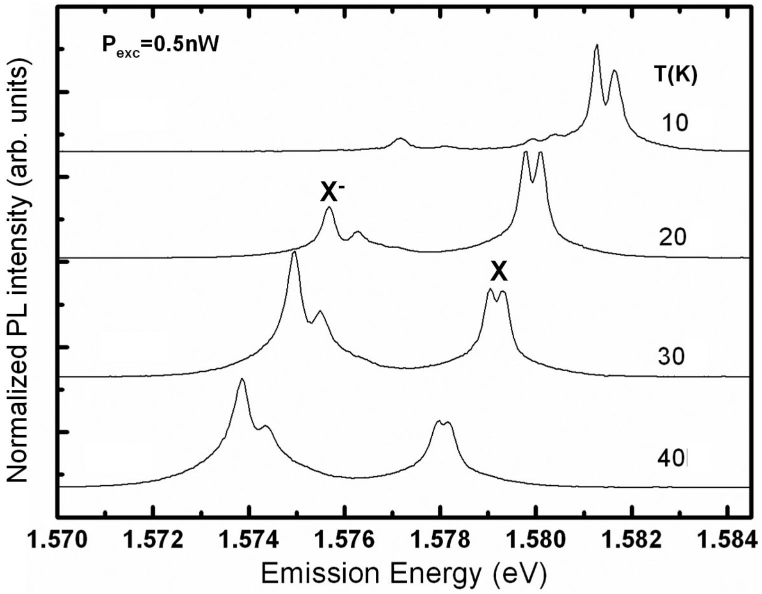

Figure 4.24: Temperature dependent PL spectra of single AlGaAs QD at $P_{exc} = 0.5$ nW. Temperature varies between 10 K and 40 K.

can also observe a spectral broadening for T = 40 K and above 40 K (not shown here). There can be two reasons for this behavior: the interaction of QD exciton with acoustic phonons [160] [161] and temperature induced population of excited hole states.

4.2.5 Single photon emission from single AlGaAs QD

Single photon emission is regarded as an important signature of discrete QD states. In this subsection, single photon emission from our pyramidal AlGaAs QDs will be demonstrated by photon correlation measurement.

As discussed in Subsection 4.2.3, both X and X^- are doublets, corresponding to e1h1 and e1h2 transitions. Therefore, we mark the higher energy peaks of the X, X^- groups as X', X'^-, respectively. Figure 4.25 (a) shows PL spectra measured on a single QD (the same sample as described in Subsection 4.2.3) for two different excitation powers: 0.15 μW and 0.1 μW, under non-resonant excitation at a wavelength of 532 nm. Sample temperature is 10 K. X^- and X'^-, 2X, X and X' emission peaks are marked accordingly in the spectra.

We have measured auto-correlations function of the X and X' photons emitted by this QD under continuous wave excitation, as shown in Fig 4.25 (b) and (c), respectively. They both exhibit typical symmetric anti-bunching dips around zero delay time. The antibunching dip indicates the vanishing probability of emitting two photons with zero delay time, in other words, of having two X (or X') photons emitted at the same time. This is a direct proof of single photon emission from our single QD. The reason for the curve not dropping to zero for $\tau = 0$ is because the contribution of uncorrelated

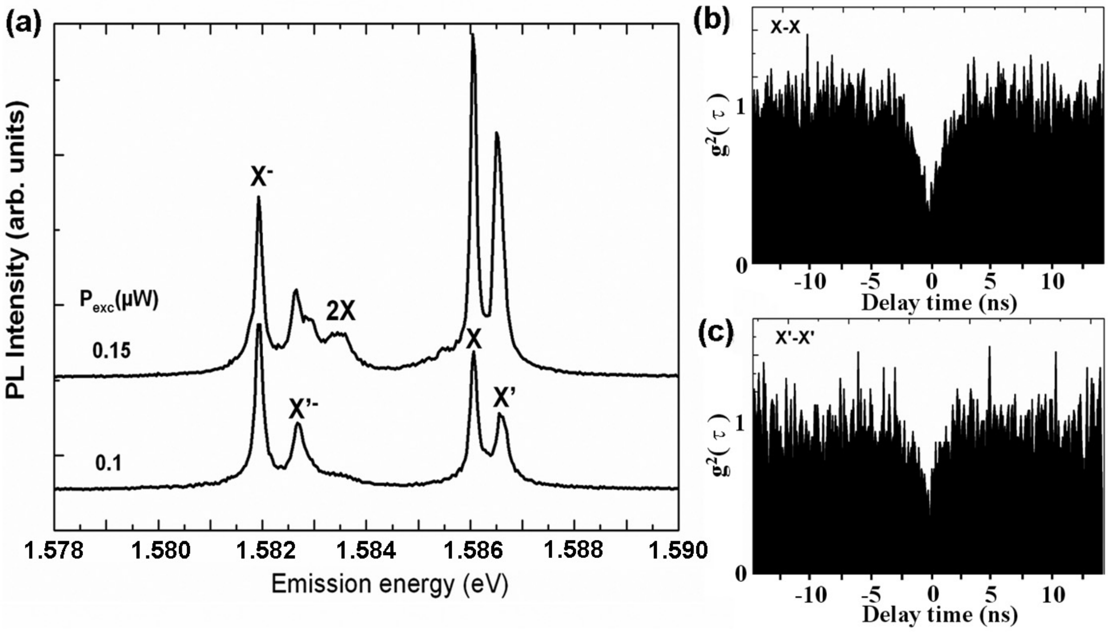

Figure 4.25: (a)μPL spectra of an AlGaAs QD, showing X^-, X'^-, 2X, X, X' emissions. (b) and (c) Auto-correlation functions of X and X' photons, showing photon antibunching, measured at $P_{exc} = 0.15$ μW.

background photons and the limit of temporal resolution of the setup. The fact that the dips ($g^2(0)$)of auto-correlation function of the X photons is less closed (smaller) than that of the X' photons can be explained as follows: at $P_{exc} = 0.15\mu$W (the excitation power used for autocorrelation measurements), X emission is stronger, hence the signal to noise ratio is higher than that of the X' emission. Moreover, we also observed another peak between X'^- and 2X coming up at higher excitation power, which might be attributed to the multiexciton complex. Experimentally, it is hard to employ systematic cross correlation measurements between this emission and any of other emission lines due to its relatively broad emission line and tiny energy separation with respect to the X'^-.

4.2.6 Correlated photon emission from single QD

Second order cross correlation functions between 2X and X, X^- and X, X and X', X^- and X'^- were measured at $P_{exc} = 0.15$ μW, as shown in Fig 4.26 (a)-(d), respectively. The schemes of X, 2X, X^-, X' and X'^- in QD is drawn in Fig 4.27 to assist the understanding of the correlation between different excitons.

The 2X and X cross-correlation curve (Fig 4.26 (a)) exhibit pronounced bunching behavior for small positive delay time, which reflects the increased probability of X photon emission right after the 2X emission. The reason is obvious: the QD is left behind with an X after 2X decay. In contrast, an empty QD has to repopulate with 2

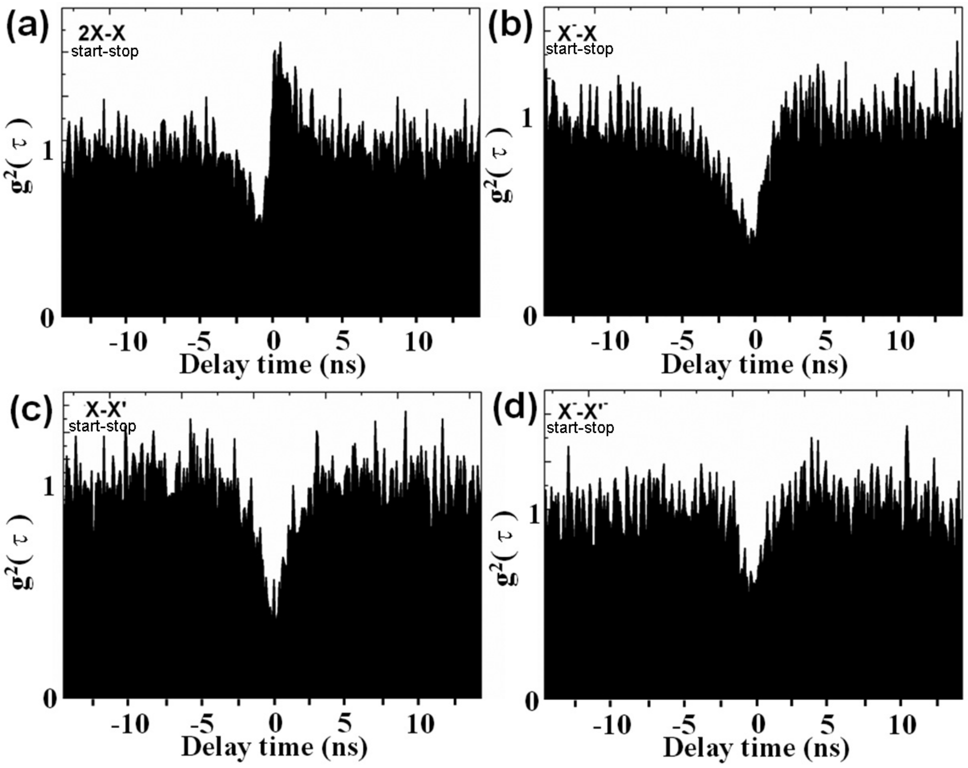

Figure 4.26: Second order correlation functions for (a) 2X (start) and X (stop) (b) X^- (start) and X (stop) (c)X (start) and X' (stop) (d) X' (start) and X'^- (stop) photons from an AlGaAs QD, showing either bunching peak (in (a)) or anti-bunching dips (in (b)-(d)), measured at $P_{exc} = 0.15\ \mu W$.

electrons and 2 holes before getting a 2X photon. Therefore, the probability of detecting an X directly before a 2X photon is suppressed, resulting in a dip in the correlation curve for small negative delay time. The bunching behavior between 2X and X in other types of QDs has been reported by many groups previously, e.g. in Ref. [19].

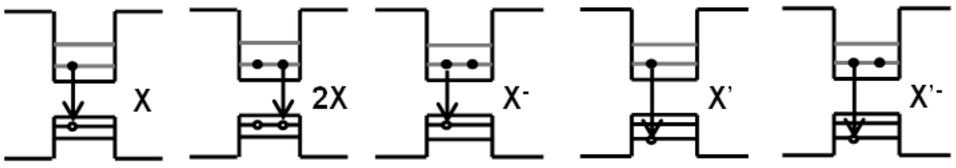

Figure 4.27: Schemes of different types of excitons in a QD: X, 2X, X^-, X' and X'^-.

Figure 4.26 (b) presents the cross-correlation curve between X^- and X photons. It shows an asymmetric anti-bunching dip, with lower $g^2(\tau)$ at small negative delay time τ. This can be explained by the fact that the X photon emission after the X^- emission can happen relatively quickly by capture of a single hole, while to let X photon emission before X^- emission take place, one acquires longer time to capture two electrons and one hole. This kind of asymmetric anti-bunching behavior between neutral and charged excitons in other types of QDs have been studied by several groups [97] [98] and is well understood [98] [19].

The cross-correlation curve between the photons emitted by single exciton X and excited single exciton X$'$ was also measured, as shown in Fig 4.26 (c). It exhibits pronounced, nearly symmetrically shaped anti-bunching dip at zero delay time under the employed excitation power (0.15 μW). This means that for an empty QD, the time acquired to populate one electron at the ground conduction band and one hole at the ground valence band is very similar to that needed for populating one electron at the ground conduction band and one hole at the second valence band. Due to analogous reasons, the X$^-$ and X$'^-$ cross-correlation curves also exhibit anti-bunching signatures (Fig 4.26 (d)). Moreover, we observed that the dips (g^2(0))of the cross-correlation function between the X and X$'$ photons is less closed (smaller) than that between the X$^-$ and X$'^-$ photons. This can be explained by two reasons: first, at P$_{\mathrm{exc}}$ = 0.15 μW (the excitation power used for autocorrelation measurements), X and X$'$ emissions are more pronounced, hence the signal to noise ratio is higher than those of the X$'$ and X$^-$ emissions, and second, another peak (on the higher energy shoulder of the X$^-$ peak) is coming up which can be mixed with the detected X$^-$ photons due to the limited spectral resolution of the setup.

4.3 Summary

In this chapter, we realized a continuous transition from 2D to 3D quantum confinement by systematically decrease the length of the pyramidal VQWR all the way into a QD. Several experimental observations of size-dependent ground transition energy and polarization supported this conclusion, consistent with the model calculation. Time-resolved PL measurements reveal longer exciton decay time with reduced VQWR length. The second part of this chapter was focused on the optical properties study of these novel AlGaAs QDs formed inside the pyramids. Cathodoluminescence spectroscopy was employed to study the carrier capture within the pyramidal QD heterostructure. Single and correlated photon emissions from these AlGaAs QDs were observed and studied.

Chapter 5

QD Molecules and QD Superlattices

The present chapter focuses on QD molecules and superlattices realized in the pyramid system. First, in Section 5.1, hybridization of electrons and holes in QD molecules are studied by model simulation in two different coupled-QD configurations. Next, Section 5.2 demonstrates the evolution of the photoluminescence spectra from a single QD to multi-QD molecules, proving the presence of coupling in QD molecules. Section 5.3 then details how to tune the coupling strength in double-QD molecules, and Section 5.4 demonstrates an approach for engineering the wavefunctions of QD molecules.

5.1 Hybridized electron and hole states in QD molecules

The controlled coupling of excitonic states in semiconductor QD molecules and superlattices (SLs) is an important ingredient in the utilization of QD systems for quantum computing and quantum communications applications [99] [162] [102] [163] [104]. In particular, hybridization of excitonic states in QD molecules and SLs would allow achieving entanglement and wavefunction switching of excitons, forming the basis for quantum manipulation of spatial and spin degrees of freedom in the solid state [164] [165]. Moreover, such hybridization will permit the construction of a new class of "QD solids" based on collective excitonic states [166] [167]. The realization of such quantum nanostructures is highly challenging, requiring reproducible fabrication of ordered QD systems with predetermined sites and electronic spectra. Recent attempts to produce molecules consisting of closely positioned, self assembled QD pairs have demonstrated hybridization of electron states [168] [105] [108]) and tuning of either electron or hole levels into resonance by applying electrical fields [106] [169]. A brief review of these works are presented in Subsection 1.3.5. Outstanding challenges in this area include the achievement of the deterministic, simultaneous coupling of electronic and hole states and the extension of such hybridization to larger QD SLs.

5.1.1 Structure of vertically stacked pyramidal QDs

Our pyramidal QWR/QD system is very attractive for constructing novel QD molecules structures. In the previous chapters, we already showed that growth of AlGaAs inside pyramids results in formation of a VQWR, running through the center of the pyramid. The QDs can be produced by systematically varying the Al mole fraction along the growth direction and adjusting the layer thickness. As a result, the wire breaks into a series of lower-Al content (hence lower potential), short VQWR segments, functioning as QDs, connected by short, higher-Al content VQWRs, acting as QWR barriers. Similarly, the VQWs break into a series of lateral QWRs (LQWRs) connected by short, higher-Al content VQWs. Figure 5.1 (a) is a schematic illustration of such nanostructures formed inside the pyramid, showing two coupled QDs as well the low dimensional QWR/QW barriers surrounding them. Since the lateral confinement in this system is provided mainly by the segregation effect and the vertical potential variations are determined by the growth process, it is possible with this approach to obtain coupled QD systems with precise (~ 1 nm) positioning and proximity of the dots with respect to each other.

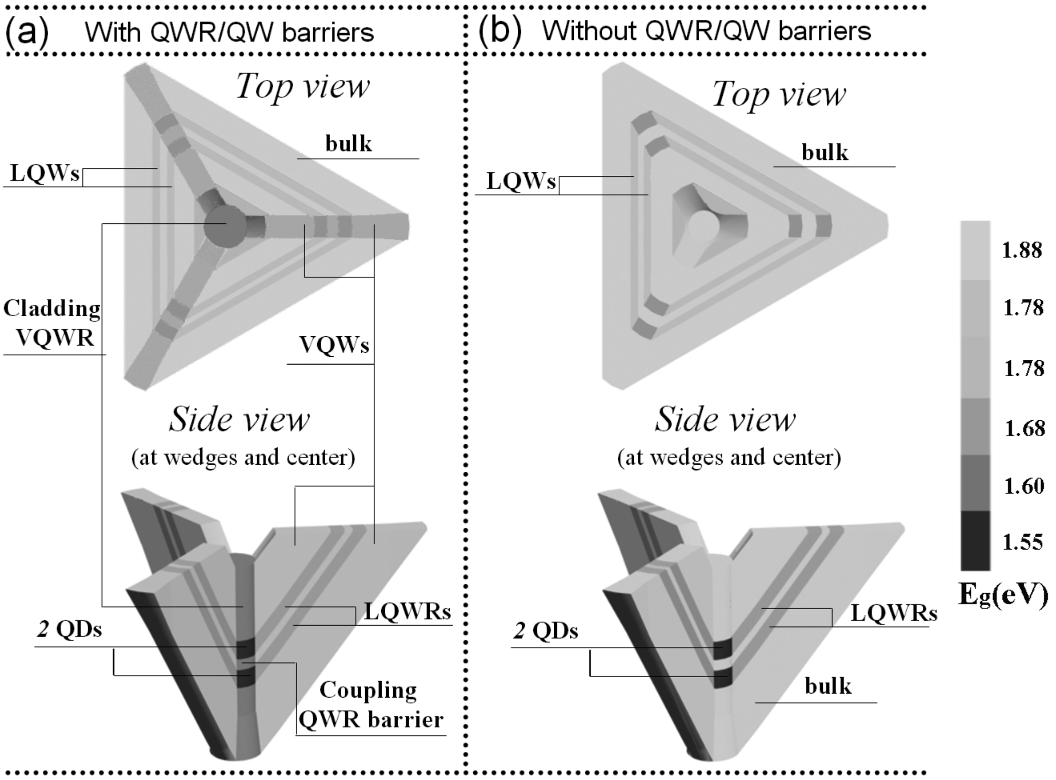

Figure 5.1: (a)Schematic illustrations of the nanostructures of pyramidal QD molecule system, showing 2 coupled QDs as well as the low dimensional QWR/QW barriers surrounding them; (b)Sketch of similar nanostructures but with homogenous barrier surrounding the 2 stacked QDs. The vertical bar (gray scale) indicates the effective bandgap energies of the corresponding structures.

In our system, the QDs are naturally connected by the VQWR formed in the barrier layers during the growth process. The QWR connecting the QDs provides efficient tunnel coupling of the electrons and holes confined in the QDs via a "wavefunction focusing effect" taking place in the 1D QWR barrier. This is different than in QDs coupled via 2D barriers, in which the coupling is weaker and hence small QD dissimilarities and low symmetry may prevent carrier hybridization, especially for holes, which are heavier than the electrons [112]. Figure 5.1 (b) is a schematic illustration of such stacked QDs system, coupled via homogeneous 2D barrier.

The difference between the structures shown in Fig 5.1 (a) and (b) is only in the barriers. The former presents the actual situation of growth inside our pyramid system. The latter is an imaginary case, where we assume that the segregation effect does not take place in the barrier and cladding layers, but it does happen in QD layer. Therefore, the QD layer in (a) and (b) are the same (in other words, keeping the lateral confinement for the QD the same as in the real structures) in order to have meaningful comparison for two situations. The later configuration does not exist in real AlGaAs pyramidal QD structures, but it has some similarities with coupled SK QDs. The SK QDs are normally formed due to strain induced by lattice mismatch. Those QDs can be stacked to form coupled QDs if the spacing between the QDs is sufficiently small. The QDs composing coupled QDs are connected by 2D QW barriers there, although residual strain effects may induce some lateral variations in the barriers as well.

5.1.2 Enhanced QD coupling using QWR barriers

To demonstrate the impact of the QWR barriers on the carrier coupling, we have computed the lowest-energy conduction and valence band states in AlGaAs pyramidal double-QD molecule systems, with (DQD A) and without (DQD B) the VQWR/VQW barrier structures. The model of DQD A reflects the realistic three-dimensional (3D) structure of the pyramidal system, as shown in Fig 5.1 (a); 0.35 Al content is assumed in the AlGaAs bulk material. Based on the segregation model in Subsection 3.1.5, the Al contents assumed were 1%, 5%, 10% and 15% in the QDs, VQWR, LQWRs, and VQWs regions, respectively. The QDs and VQWR segments were modeled as solid cylinders with 16 nm diameter and of uniform composition. For DQD B, the AlGaAs barriers above, in between and below the QDs were assumed to be uniform (0.35 Al content), simulating a situation in which tunneling takes place in a laterally homogeneous barrier. The 3D problem was formulated in effective mass approximation accounting for possible valence band mixing. More details of the formulation is described in Appendix A, the two components of the valence band states, heavy-hole (HH) and light-hole (LH), refer to hole masses along the (111) growth direction.

To illustrate the impact of QWR-mediated coupling in a realistic case, the two dots were assumed to be slightly different in size due to fabrication imperfections, with the bottom (top) dot height set at 7 nm (7.5 nm). The chosen heights correspond to effective QD width-to-height aspect ratios larger than unity. The thickness of the

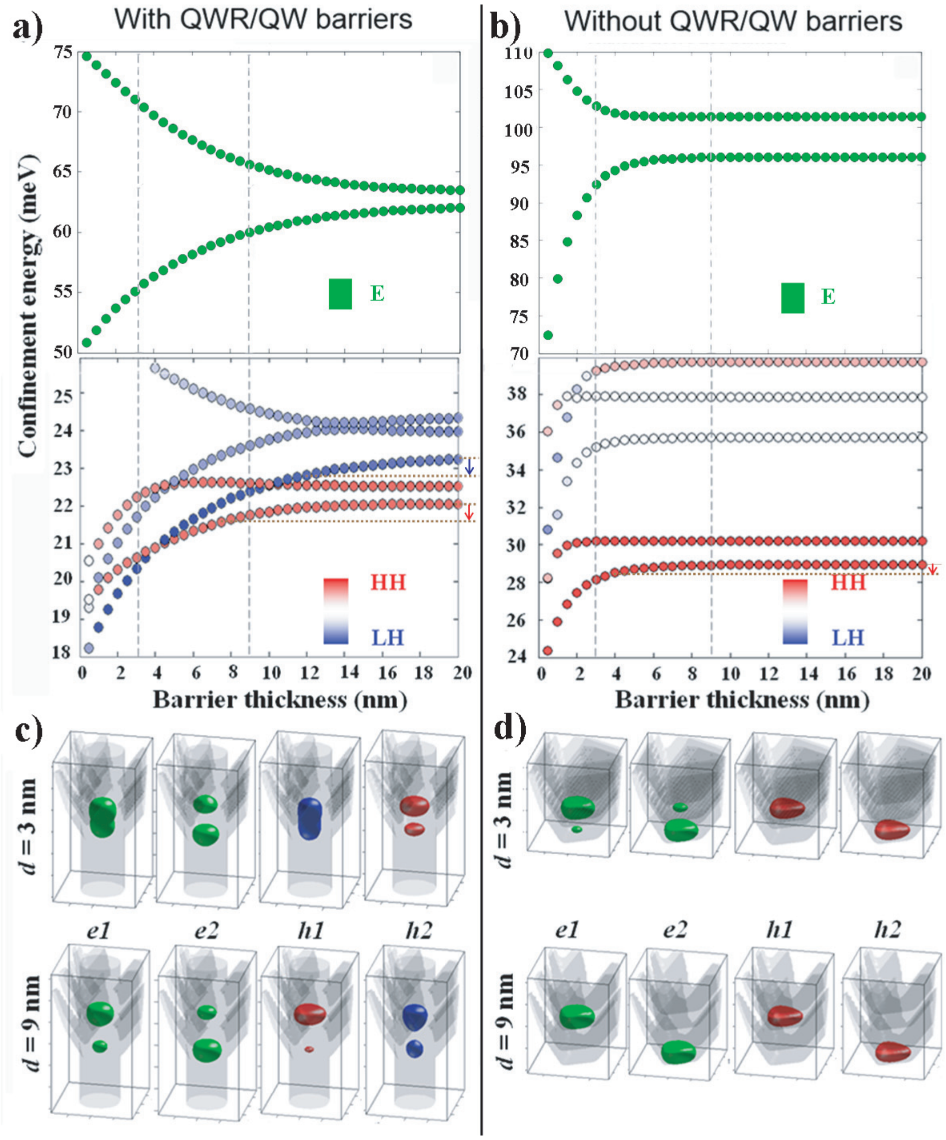

Figure 5.2: (Top) Calculated confinement energies of the lowest-energy electrons and holes confined in QD molecules consisting of two AlGaAs pyramidal dots as a function of separating barrier thickness, (Bottom) Isosurfaces of computed probability distributions (corresponding to probability density of 2.5×10^{-4} nm^{-3}) for the two lowest-energy conduction (green) and valence band (HH and LH components indicated in red and blue, respectively) states for pyramidal AlGaAs QD molecule structures corresponding to barrier thicknesses of d = 3 nm and d = 9 nm. The shape of the QD molecule structure is represented by the grey surfaces.

inter-dot QWR barrier was systematically varied between 0.5 to 20 nm. Figure 5.2 (a) and (b) show the calculated confinement energies (with respect to the GaAs band edge) of the two lowest conduction band states and five lowest valence band states as a function of the barrier thickness, with and without QWR barriers, respectively.

In general, as the coupling between the two QDs increases, the energy levels shift from the zero-coupling values and the states approach hybridization into bonding- and antibonding-like wavefunctions. Here, the coupling is tuned by the QD separation (d); it increases for smaller barrier thicknesses, i.e., when the QDs get closer. The magnitudes of the separation-dependent energy shifts are related to the coupling strength. For the case with QWR barriers (Fig 5.2 (a)), an energy shift of 0.5 meV for the LH-like components occurs already at d = 12 nm, whereas this shift is achieved at d = 7.5 nm for the HH-like components. (The LH-like states penetrate the barrier deeper along the growth-direction than the HH-like states, therefore they couple more effectively.) In the other case, without QWR barriers (Fig 5.2(b)), this value of energy shift is observed for d = 4 nm. Similar situation takes place also for the electron states. Clearly, the coupling strength is enhanced by the QWR barrier.

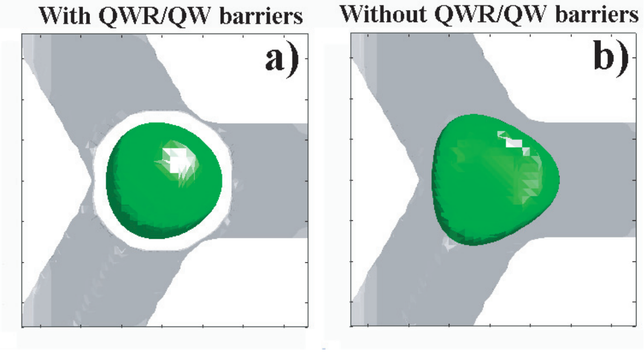

Figure 5.3: (Top-view) Iso-surfaces of computed probability distributions (corresponding to probability density of 2.5×10^{-4} nm^{-3}) for the ground electron states for pyramidal AlGaAs QD molecule structures corresponding to barrier thicknesses of d = 3 nm.

Thus, to ensure carrier hybridization for non-identical QDs, it is useful to insert QWR barriers between the QD potential wells. This effect is further illustrated in the bottom panel of Fig 5.2, which depicts the computed probability distributions of the two lowest energy states of electrons (green) and holes (HH component in red, LH component in blue) for the two types of double-QD molecules, with (Fig 5.2 (c)) and without (Fig 5.2 (d)) QWR barriers of two different thicknesses: d = 3 nm (top) and d = 9 nm (bottom). In the absence of a QWR barrier, the difference in QD size is sufficient to essentially decouple all carrier states at the assumed spacing (d = 9 nm), as manifested by the localized probability distributions (Fig 5.2 (d)). On the other hand, the insertion of the QWR barrier yields delocalized electron and LH probability distributions (Fig 5.2 (c)). This enhanced coupling is a result of the lower barrier between the dots, introduced by the lower Al content of the connecting QWR. Such "wavefunction focusing effect" made by the barrier QWR is illustrated in Fig 5.3, where a top-view of the iso-surfaces of computed probability distributions for the ground electron states (the same as that in Fig 5.2 (c) and (d), but observed from the top) is demonstrated. It shows that in the situation with QWR/QW barriers, the electron wavefunction is more concentrated in the QDs (Fig 5.3 (a)), whereas for the situation

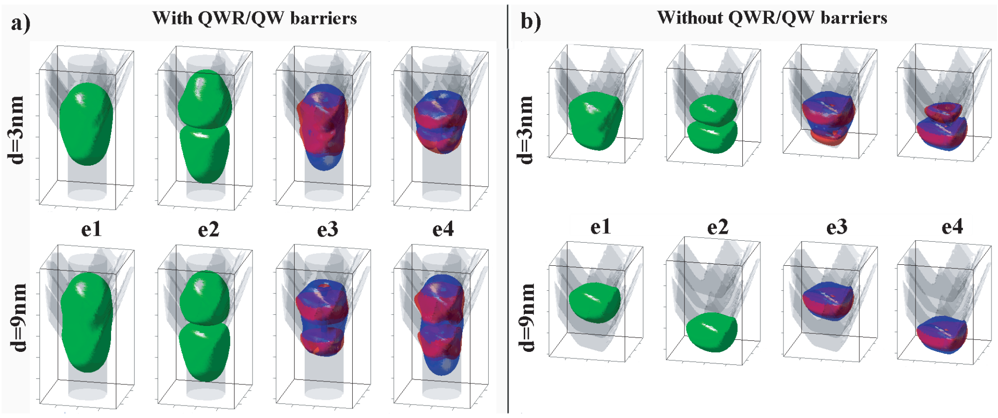

Figure 5.4: Iso-surfaces of computed probability distributions (corresponding to probability density of 2.5×10^{-6} nm^{-3}) for the two lowest-energy conduction (green) and valence band (HH and LH components indicated in red and blue, respectively) states for pyramidal AlGaAs QD molecule structures corresponding to barrier thicknesses of d = 3 nm and d = 9 nm. The shape of the QD molecule structure is represented by the grey surfaces.

without QWR/QW barriers, the wavefunction is more extended into the three lateral QWRs , resulting in a triangular-like isosurface(Fig 5.3 (b)). Moreover, by using a probability density of 2.5×10^{-6} nm^{-3} (100 times lower than that used in Fig 5.2 (c)(d)), the iso-surfaces of computed probability distributions for the electron and hole states can be re-plotted, as shown in Fig 5.4. It clearly shows the confined carrier wavefunction in the barrier QWR (Fig 5.4 (a)). Note, however, that this enhanced coupling made by lower potential barrier is achieved without losing the strong lateral confinement (in the plane perpendicular to the VQWR axis), due to the high Al content of the AlGaAs alloy laterally surrounding the dots.

A feature of the QWR-coupled QD molecules (DQD A) that is essential for the work reported here is the switching of hole character of the valence band ground state from HH-like (red circles in Fig 5.2)) to LH-like (blue circles) below a certain barrier thickness (4 nm for the structure of Fig 5.2). (The hole character of each state is encoded according to the color bars in the figure; HH and LH components are indicated in red and blue, respectively.) This switching is caused by the different coupling strength of LH and HH: when the QDs are brought together the stronger coupling of LH induces a larger downshift of the bonding-like LH-state than for the corresponding HH-state. At the switching point (d = sp) their energies cross. Furthermore, the switching indicates that the width/height aspect ratio of the QD molecule system has changed from larger than unity, as is the case for isolated or well-separated (d > sp) QDs, to smaller than unity in the case of strongly coupled QD (d < sp) [170]. Hence, the change in aspect ratio is indicative of coupling-induced, hole wavefunction delocalization, (i.e., hole hybridization).

The latter feature provides an important clue for probing the hybridization of the valence band states in QD molecules, since the switching of hole character of the valence ground state is accompanied by a corresponding change in the degree of linear polarization of photons emitted or absorbed by the corresponding QD systems [171]. This prediction will be further investigated in the next section.

5.2 From single QD to multi-QD molecules

5.2.1 Structures designed for studying electron and hole hybridazation

To investigate the consequence of carrier hybridization, we studied the confined states and the optical spectra of a series of pyramidal-QD systems consisting of a single- and multiple-QD structures (Appendix B, growth ♯2587, ♯2616, ♯2618), as shown in Fig 5.5. The structures were fabricated using MOVPE of $Al_{0.2}Ga_{0.8}As/Al_{0.35}Ga_{0.65}As$ multi-layer heterostructures on 0.2°-off-(111)B GaAs substrates patterned with 5 μm pitch pyramid array. The QDs formed in the $Al_{0.2}Ga_{0.8}As$ layers were nominally identical, with a thickness of ~ 9 nm and ~ 16 nm in diameter, and had an Al content of 1% in their core. The single- or multi-QD parts were sandwiched between $Al_{0.35}Ga_{0.65}As$ claddings of similar structure as the $Al_{0.35}Ga_{0.65}As$ barriers; the Al content in the VQWR barriers is estimated to be $\sim 5\%$ [148]. The composition and dimensions of the pyramidal nanostructures were extracted from microscopy and optical measurements of these and other similar QD samples.

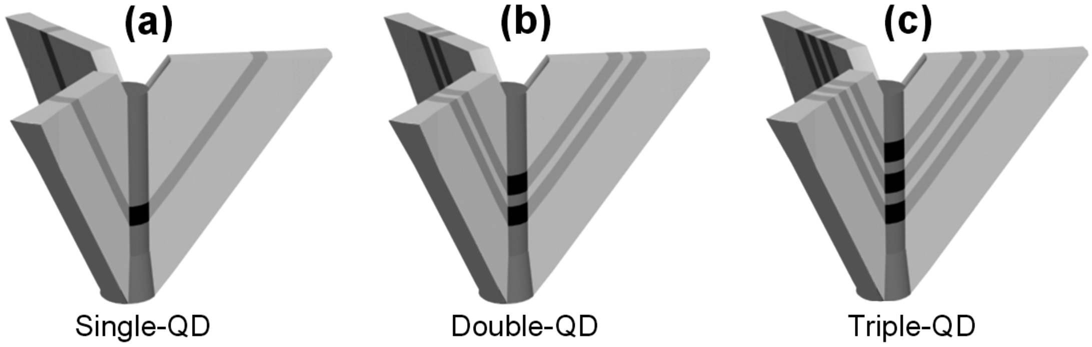

Figure 5.5: Schematic illustrations of the nanostructures at the wedges and center of the pyramids for (a)single-, (b)double-, and (c) triple QD molecules.

Apart from these samples designed for optical studies, a special sample consisting of five coupled $Al_{0.1}Ga_{0.9}As$ QD layers in an $Al_{0.55}Ga_{0.45}As$ barrier material was grown for transmission electron microscopy (TEM) studies (Appendix B, growth ♯2694). Figure 5.6 (a) is the schematic illustration of such sample in top-view and side-view geometry. The TEM samples were prepared using side-view thinning techniques with final grazing Ar-ion bombardment, and they were observed in a CM30 transmission electron microscope operating at 300 keV with the electron beam directed perpendicular to the

VQWR axis. Figure 5.6 (b) shows a side-view TEM image of the center of such pyramidal structure. In these images, darker regions correspond to lower Al content in the alloy. Because of the special symmetry of the pyramids, one can only clearly distinguish the multi-layer structures on one side, for which the electron beam is parallel to one side of the triangular bottom of the pyramid (see Fig 5.6 (b) (main)). The inset of Fig 5.6 (b) is the TEM image of the same sample, but observed with a slightly different detection angle to make the multi-layer structure visible on both sides of the structure. These images confirm the formation of five, vertically stacked dots at the bottom of the pyramid, in addition to the lateral QWs and QWRs placed around them.

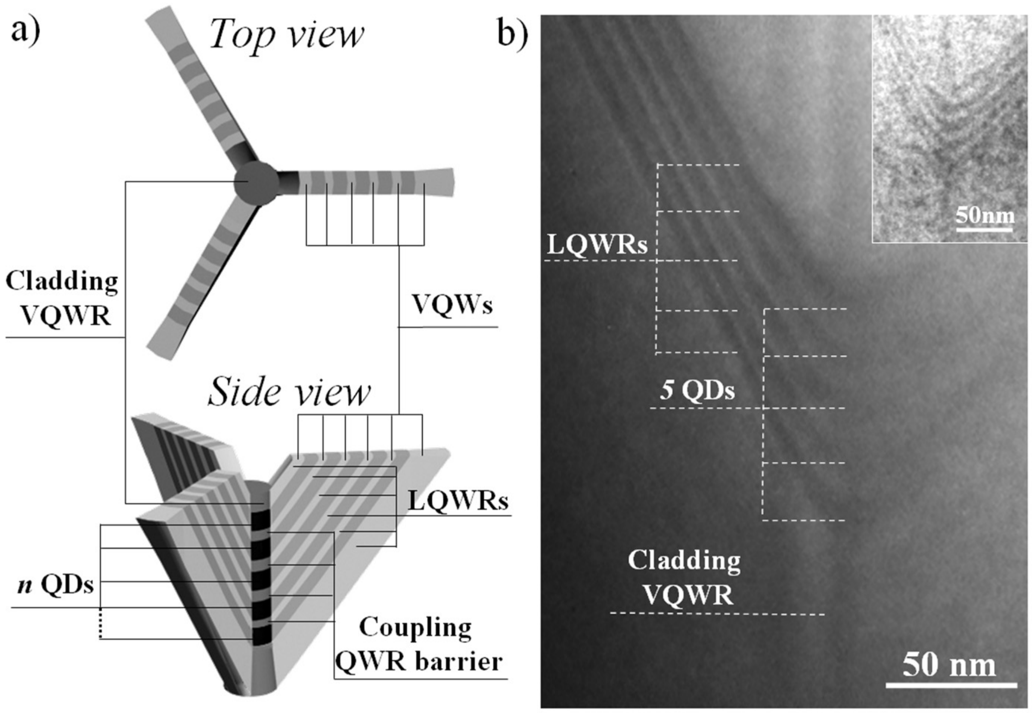

Figure 5.6: (a) Schematic illustration of the nanostructures at the wedges and center of the pyramidal quantum dot molecule system, showing the n coupled dots as well as the low-dimensional heterostructure barriers surrounding them. (b) Dark-field transmission electron micrograph of a five-dot AlGaAs molecule structure observed with electron beam parallel to (main) or slightly tilted from (inset) one side of the triangular base of the pyramid.

5.2.2 Calculated wavefunctions of single-, double- and triple-QD molecules

The calculated probability density functions for the investigated series of QD samples are shown in Fig 5.7. For the single-QD structure, the valence band ground state has a HH character (red), whereas the higher energy states have a mixed but predominantly LH character. This is a typical situation in an isolated QD of a width-to-height aspect ratio larger than unity [170] [171]. In the dot molecules, the computed ground electron state splits into two or three hybridized states. Note that even though the coupled dots in the model have identical geometries, some degree of localization of the electron wavefunctions is noticeable. This is due to the absence of reflection symmetry about the x-y plane, which yields a slightly higher effective potential at the lower dot. Note also that the slight localization of the coupled states in either dot is more noticeable for the HHs, because of their larger mass along the growth direction. For the chosen designs of QD-molecules, the coupling induces hole hybridization as well as switching to LH character, as in the case discussed previously.

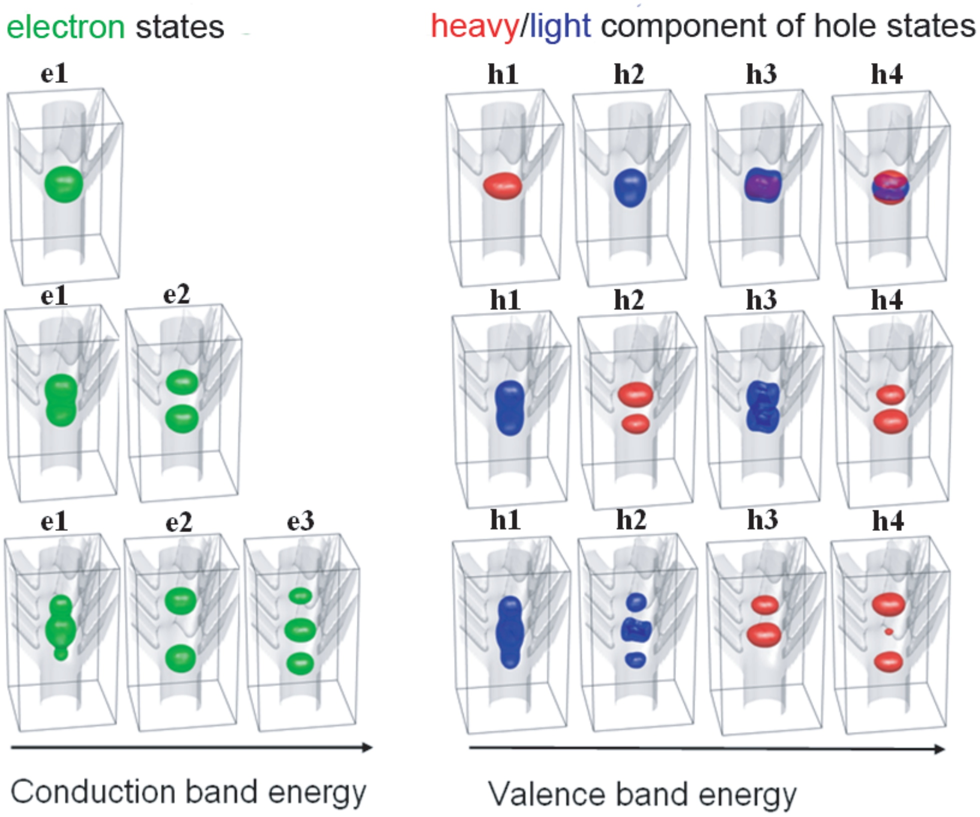

Figure 5.7: Isosurfaces of computed probability distributions (corresponding to probability density of $2.5 \times 10^{-4}\mathrm{nm}^{-3}$) for the lowest-energy conduction (green) and valence band (HH and LH components indicated in red and blue, respectively) states for single-, double- and triple-QD pyramidal AlGaAs structures. The shape of the QD molecule structure is represented by the grey surfaces.

5.2.3 Comparison of calculated absorption spectra and measured photoluminescence spectra

Figure 5.8 shows a representative low temperature (10K) power dependent micro-PL spectra of a back-etched double-dot molecule structure. The sample was excited by Ar+ laser at a wavelength of 514nm. The excitation power varies between 8 and 218 nW for 9 different values. Two groups of transitions can be found from the spectra, corresponding to ground (∼ 1.572 eV) and (∼1.59 eV) excited states of the molecule. Narrow emission peaks with less than 200 μeV linewidth are observed. The spectra look very similar to the spectra we obtained from single QD structure in Subsection 4.2.3, confirming that these QD molecules behave as QD structures of high optical quality. Here, we will not go into details of the assignment of each peak to an excitonic state. Discussions related to this issue will be presented later in the next subsection by correlation measurement.

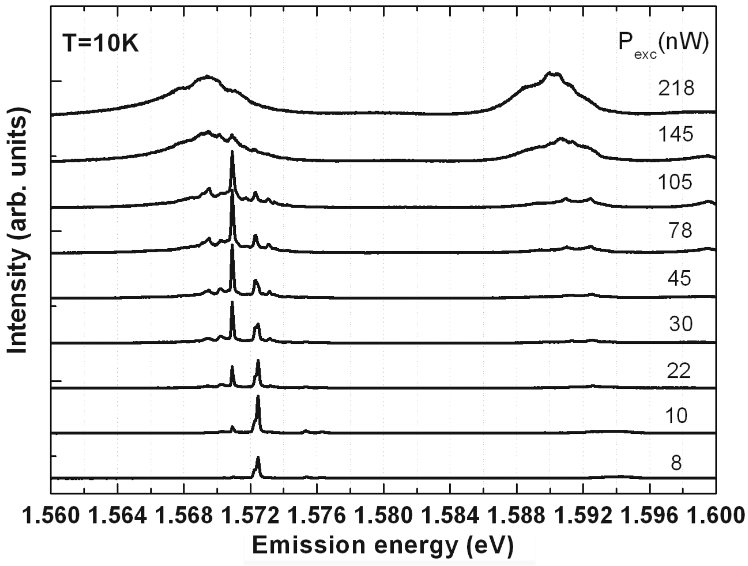

Figure 5.8: Measured low temperature power dependence PL spectra of double-dot molecule structure.

The computed optical absorption spectra (see Fig 5.9(a)) reveal the impact of the change in hole character on the polarization-resolved spectra (for simplicity, only transitions involving the four lowest energy hole states are shown). Each transition acquires a characteristic degree of linear-polarization related to the character of the hole component involved. Both for the double- and the triple-QD structures, the coupling leads to ground state transitions that are polarized mainly in the growth direction, whereas the excited states are strongly polarized perpendicular to the growth direction.

Taking advantage of the perfect site-control for pyramidal QD structures, the polarization of the emission from the QDs and QD molecules was measured in a side view geometry at 10 K. Single pyramids were excited at a wavelength of 532 nm. The measured polarization-resolved micro-PL spectra generally show the expected polarization

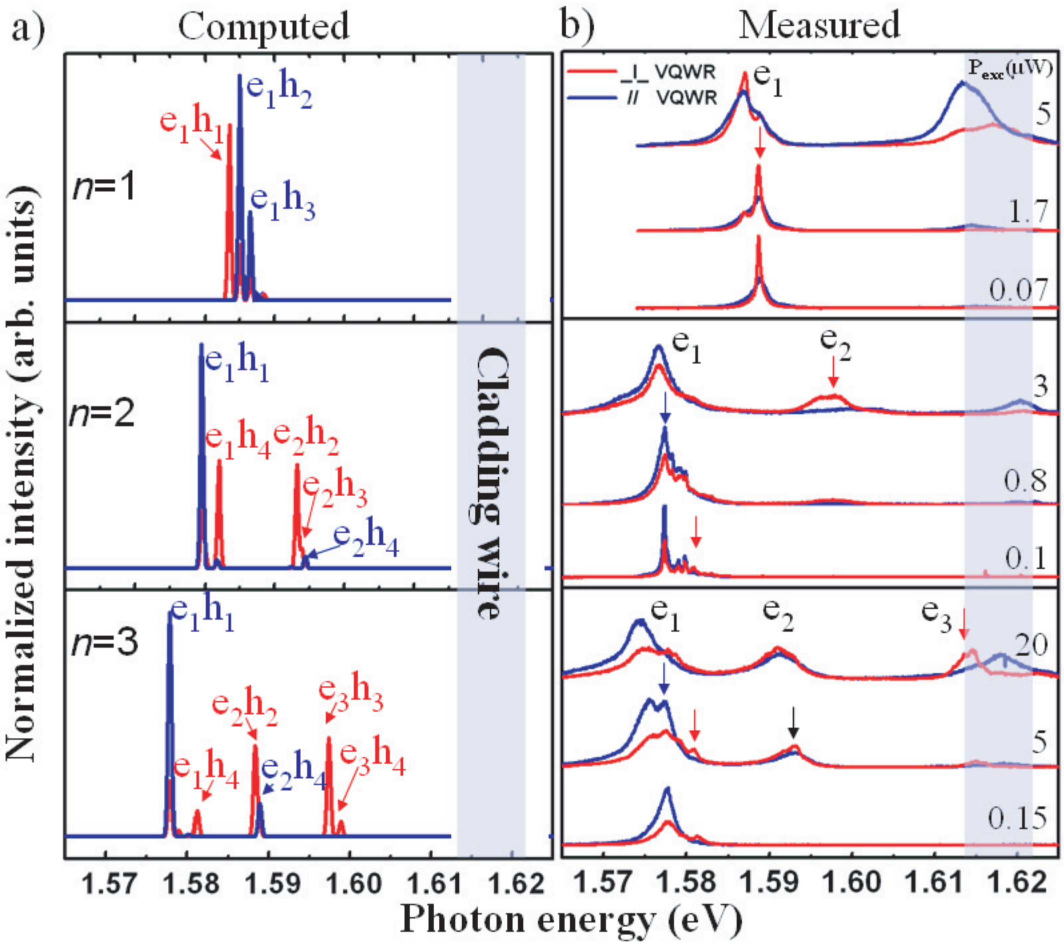

Figure 5.9: (a) Computed absorption spectra of the single-QD and QD molecules of Fig 5.5 for linear polarization vector oriented along (blue) and perpendicular to (red) the growth direction. (b) Low temperature (10K) photoluminescence spectra for the three structures, measured in a side-view geometry, for detected linear polarization oriented along (blue) and perpendicular to (red) the growth direction.

features associated with hole-state hybridization, as predicted by the model (see Fig 5.9(b)). In particular, whereas the emission related to the ground state of the single-QD structure shows HH-like polarization behavior, it is rather LH-like for the double-QD and triple-QD molecules. The higher order transitions show HH-like or mixed transitions, in agreement with the model calculations. The hybridization of the hole states evidenced by this change in hole character is achieved here without the aid of external fields, as opposed to electric-field assisted coupling in double-QD molecules reported earlier [168] [105] [106] [169]. Note that small mismatches between computed absorption spectra and the measured PL spectra can happen due to several reasons. First, the parameters of the structure input in the model were estimated based on the PL and microscopy images of the calibration samples. They can deviate slightly from the actual values. Second, the state filling is not present in the absorption spectra, while it does exist in the PL spectra, especially at higher excitation power. The population of the excited hole states can broaden the peak since in our AlGaAs QD/QD molecule system, different valence band levels are closely spaced (< 0.5 meV). Indication for the importance of fluctuating electric fields in these systems is provided by the fact that the LH like transitions systematically show larger spectral linewidths (see Fig 5.9). This can be due to the larger extension of the light hole wavefunction along the cladding and barrier QWR segments, where charged impurities reside. Examining Fig 5.9 again, we found the experimental observation is consistent with our expectation, e.g. the ground state of the single-dot has broader emission line for polarization oriented along the growth direction than emission polarized perpendicular to the growth direction.

5.2.4 Correlated photon emission from QD molecules

The impact of carrier hybridization on the photon emission statistics was investigated using second order cross-correlation measurements between the different excitonic lines of our double-QD molecule. Figure 5.10 shows the PL spectra of such double-QD molecule sample (back etched) excited using a continuous wave mode Ti-sapphire laser emitting at 700 nm wavelength at four different excitation power levels. Two main groups of transitions, separated by ~ 22 meV, are observed; based on our QD states model, they are assigned to transitions involving bonding and antibonding electron states, respectively. Only at higher excitation power can the antibonding emission group be observed, indicating efficient relaxation from the antibonding- to the bonding-states. From the power dependence characteristics of the lower energy lines situated between 1.570 eV and 1.575 eV, they are identified as the biexciton (2X), charged exciton (X^*) and neutral exciton (X), as indicated in Fig 5.10 [98] [172]. According to the power dependence of X^* transition intensity, X^* is probably a X^- (see Ref. [83], and Subsection 4.2.3). However, the energy difference between X^* and X is about 1 meV, which is much smaller than the typical energy difference between X^- and X in our pyramidal QD (see Ref. [19],and Subsection 4.2.3). Therefore, we cannot conclude if the X^* here is a X^- or X^+. To further identify it, precise calculation of the binding energy of the exciton complex in the corresponding structure is needed.

The second order correlation functions, measured using the Hanbury Brown and Twiss interferometer and micro-PL set up described in Subsection 2.2.6, further confirm these spectral line assignments. The cross-correlation between X (start) and X^* (stop) shows an asymmetric antibunching dip at $\tau = 0$ (Fig 5.10 b (II)), and the correlation between X (start) and 2X (stop) shows a bunching peak ($\tau > 0$) (Fig 5.10 b (I)), as expected. More importantly, we observed a clear bunching between the X in the bonding state, and the peak denoted $2X'$ at ~ 1.595 eV within the electron anti-bonding emission group, which implies a radiative cascade between these two transitions. Moreover, clear bunching between X^* and $2X'$ is also observed. This $2X'$ transition can be thus interpreted as due to the recombination of a biexciton composed of an antibonding electron state and an antibonding hole state (e2 and h2, see Fig 5.7) in the presence of a pair of bonding electron (e1) and bonding hole (h1) states, as shown in the insets of

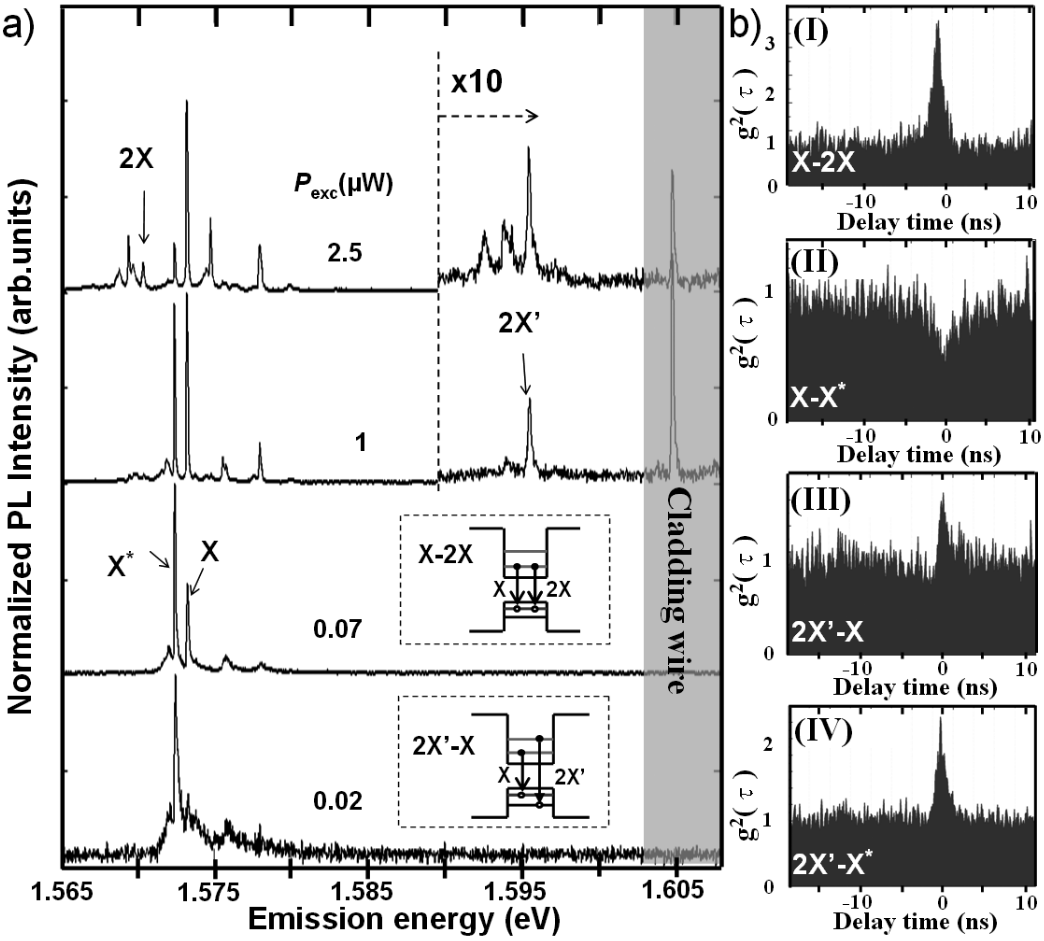

Figure 5.10: (a) Low temperature (10 K) power dependent PL spectra acquired from a double-QD molecule, showing several identified excitonic lines; (insets) scheme of X-2X and 2X′-X transitions (b) Measured second order cross correlation function between X and 2X′, X and 2X showing photon bunching, and the corresponding measurement between X and X* showing photon anti-bunching.

Fig 5.10.

The correlation measurements between bonding and antibonding states of the QD molecules demonstrated the presence of the coupling between the two QDs. This is because if the two photons were emitted from two independent QDs, the emission of one of the two photons should neither prevent nor stimulate the emission of the other photon. In another words, these two photons should also be independent of each other: no correlation will take place. Experimentally, we observed photon-bunching between bonding and antibonding electron states of the QD molecules, supporting the fact that the QDs are coupled.

5.3 Tuning the coupling between two QDs in double-QD molecule

Until now, we have demonstrated strongly coupled QD molecule system realized by connecting QDs with a lower potential 1D QWR channel. In this section, we will show how tuning of the coupling between the two QDs in double-QD molecule can be achieved either by changing the barrier in between the QDs (Subsection 5.3.1) or by modifying the QDs dissimilarity (Subsection 5.3.2).

5.3.1 Systematically changing the barrier in between the QDs

In the ideal case of identical, spherical dots coupled via electron and hole tunneling, hybridization of molecular states is always achieved, no matter how far apart the dots are. However, in realistic structures, it is practically impossible to produce identical QDs because of limitations in size and composition control. Moreover, in QDs of low symmetry, effective differences between the dots persist even when their parameters are identical, preventing wavefunction hybridization above certain spacing [112]. In some approaches, for example, vertical stacking of self-assembled SK QDs, the effective barrier potential increases with reducing distance between dots due to strain relaxation, so that the hole states cannot be coupled at zero external electric field [112].

Subsection 5.1.2 has already illustrated the evolution of carrier wavefunction and transition energy when the thickness of the barrier in between the two QDs changes (Fig 5.2 left). Clearly, the coupling strength between QDs is reduced when the dots are more distant from each other, resulting in more localized electron hole wavefunctions and larger energy level differences.

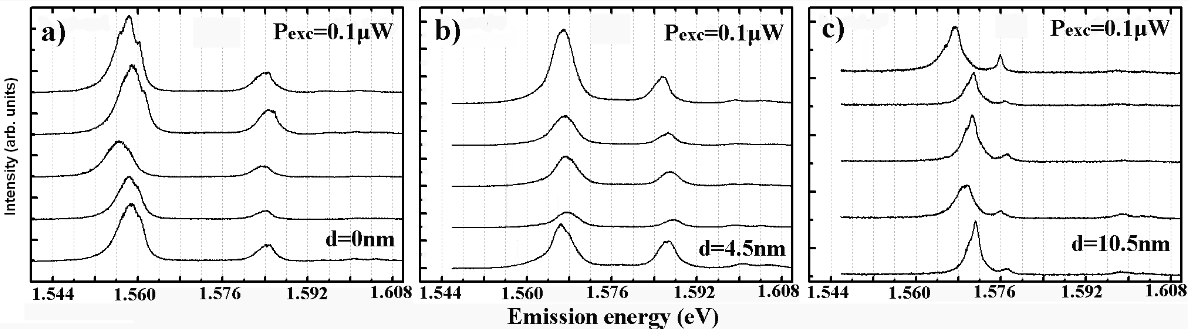

Figure 5.11: Low temperature PL spectra measured on different pyramids (5 in each sample)containing double QD molecules of three samples with interdot thickness (a) 0 nm; (b) 4.5 nm; (c) 10.5 nm. $P_{exc} = 0.1\ \mu W$.

To study the dependence on barrier thickness, a series of double-QD samples was prepared. Keeping both QDs thickness as ∼10 nm, the interdot barrier thickness was systematically changed between 0∼10 nm (Appendix B, growth ♯2434, ♯2512, ♯2514,

♯2515, ♯2586). The nominal Al contents in QD layer and barrier layer were 20 % and 35%, respectively. The whole structures were sandwiched between two thick cladding layers (nominal 35% Al content) as usual. Figure 5.11 shows low temperature (10 K) PL spectra measured on three different samples with interdot thickness of (a) 0 nm, (b) 4.5 and (d) 10.5 nm, respectively. The spectra were acquired at 5 different pyramids for each sample at an excitation power 0.1 μW.

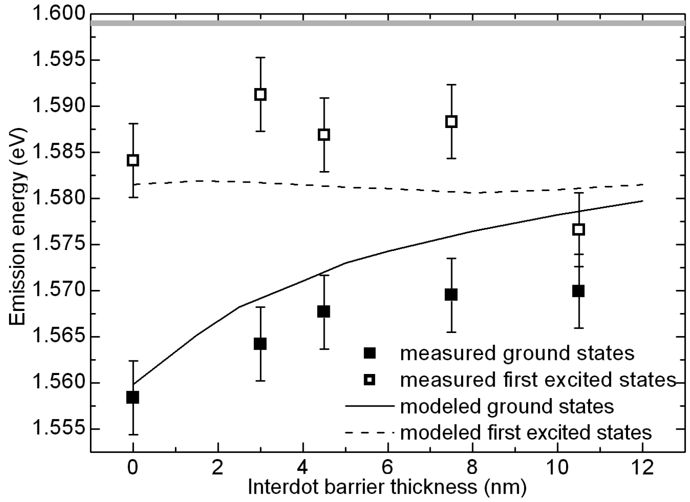

Figure 5.12: Measured and computed ground (e1h1) and first excited (e2h2) transition energies of double-QD molecule as a function of interdot barrier thickness. The horizontal gray line represents the ground transition energy of QWR barrier.

The measured and computed ground (e1h1) and first excited (e2h2) transition energies are plotted in Fig 5.12. The observed ground and excited transition energies follow the predicted trend, but slightly deviate from the energies obtained by modeling. This can be explained by the uncertainty in structure parameters introduced by the fabrication procedure. Every time the Al content of a layer is changed during growth, the self-limiting profile at the bottom of the pyramid does not form immediately, but needs to be reestablished after several nanometers growth of the barrier layer [114]. This means that the diameter and actual Al content of QD(or VQWR) formed in a thin layer can be slightly different from that in a thick grown layer of the same nominal Al content. The growth rate acceleration along the growth axis due to the pyramid filling makes the nominally identical QD layers differ in different actual thickness. Accounting to all these factors, the values of QD (and barrier) size and the Al content input in the model might deviate from the actual values, depending on the individual grown structure.

5.3.2 Systematically modifying the QDs dissimilarity

The dependence of coupling between the two QDs on their distance was presented in the previous subsection. An alternative way to tune the coupling is by modifying the dissimilarity of the two QDs. In the realistic structures, the QDs are never identical. Large QD dissimilarity can break the coupling even if the QDs are quite close to each other.

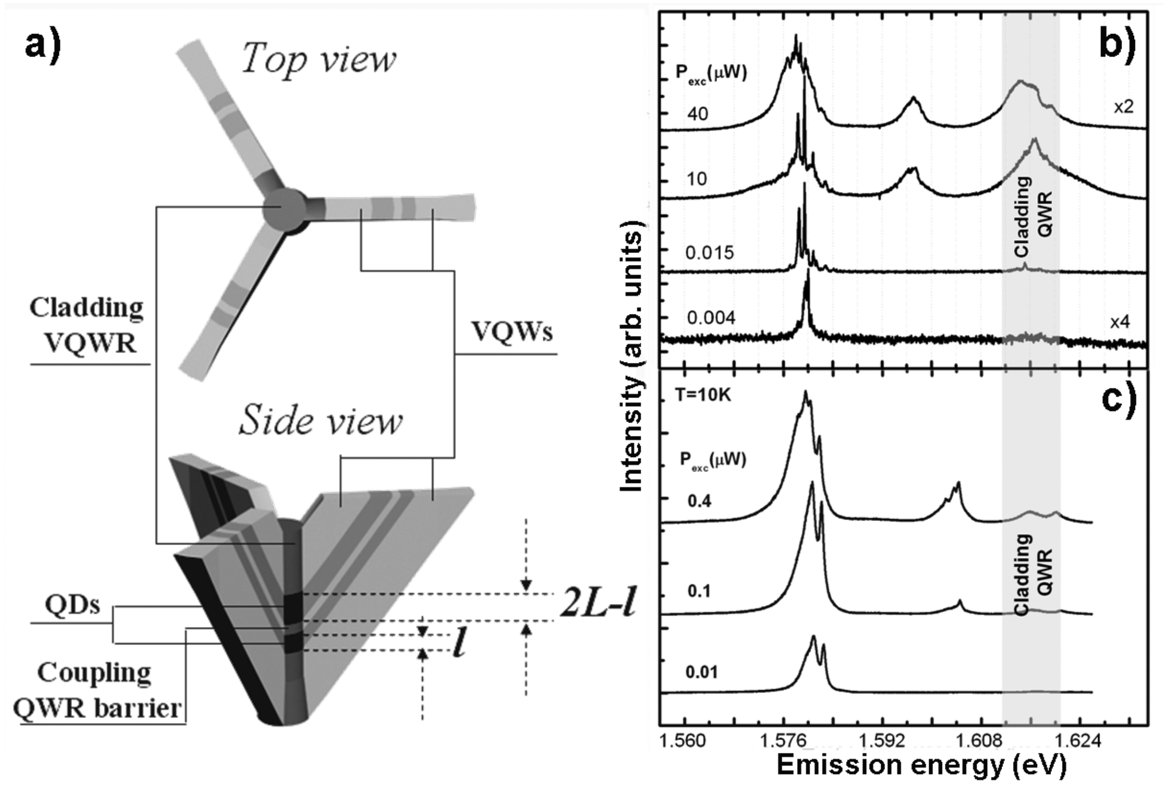

Figure 5.13: (a) Schematic illustration of vertically stacked pyramidal QDs forming asymmetric double-QD molecules; Low temperature (10K) power dependent PL spectra of symmetric double-QD structure with bottom (and top) QD thickness of (a) 10.5 (10.5) nm, (b) 13.5 (7.5) nm.

Several approaches are used in this work to modify the QDs dissimilarity in double-QD molecule structures. First, we realized a series of QD-QWR heterostructures as shown schematically in Fig 5.13 (a). By modulating the Al content in the AlGaAs vertical QWR, structures containing asymmetric double-QD heterostructure embedded in a higher bandgap AlGaAs cladding VQWR were fabricated. For the structures discussed here, the nominal Al content in QD and barrier layer is again 20% and 35%. The QDs are about 16nm in diameter, and have only 1% Al content ($z \sim 0.01$) in their core. The coupling QWR barrier in between the QDs is about 4.5 nm thick, with 5% Al content ($z \sim 0.05$) in its core. The two QDs thicknesses were varied systematically between 3 and 18 nm, keeping their total thickness fixed at $2L = 21$nm (Appendix B, growth ♯2587, ♯2592-2593, ♯2597-2600, ♯2608-2613, ♯2617). The thicknesses were estimated based on atomic force microscopy and transmission electron microscopy of similar pyramidal QD heterostructures.

Figure 5.13 (b) shows measured PL spectra ($T = 10$ K) of the symmetric double-

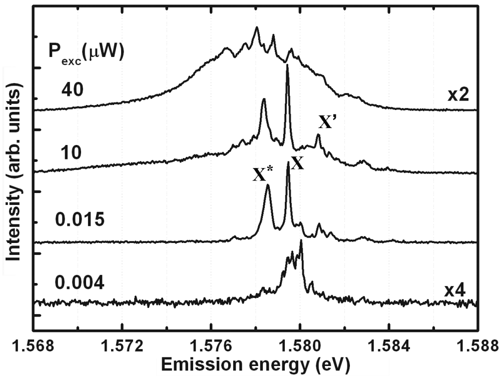

Figure 5.14: Close up of the bonding state in Fig 5.13 (b).

QD structure with bottom (and top) QD thickness of 10.5 nm. Two groups of emission lines, corresponding to transitions between the bonding ($\sim$ 1.580 eV) and antibonding ($\sim$ 1.598 eV) carrier states of the QD molecule can be observed. The narrow lines in the first group can be identified as the charged exciton X*($\sim$ 1.5785 eV), single exciton X($\sim$ 1.5795 eV) and excited hole exciton X$'$ ($\sim$ 1.581 eV) corresponding to the bonding states, respectively. These identifications are indicated in Fig 5.14, where a close up of the bonding state is shown. There are not enough evidences here to conclude whether the X* is a negatively or positively charged exciton.

Measured PL spectra (T = 10 K) of one of the asymmetric double-QD structure with bottom (and top) QD thickness of 13.5 (7.5) nm is shown in Fig 5.13 (c). Again, two groups of emission lines, corresponding to transitions between the bonding ($\sim$ 1.580 eV) and antibonding ($\sim$ 1.604 eV) carrier states of the QD molecule can be observed.

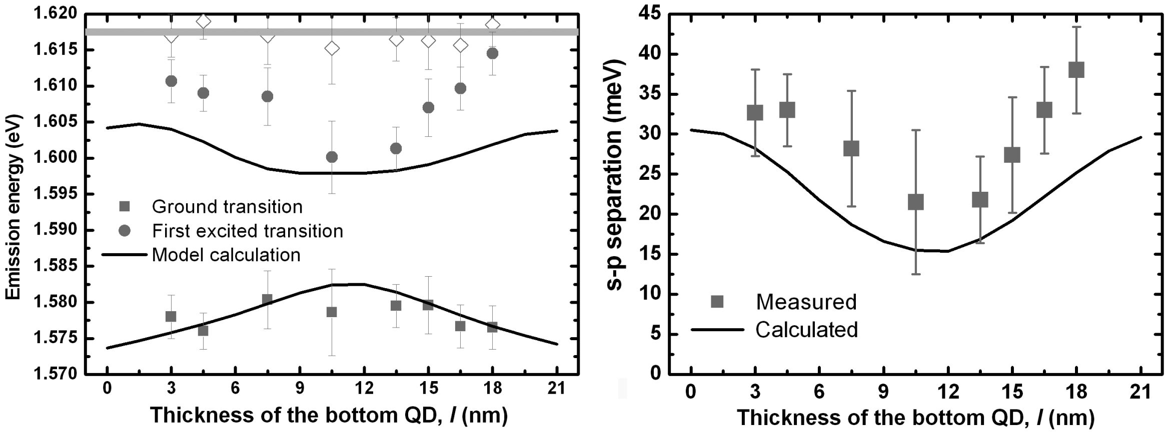

Figure 5.15: (Left)PL emission energies of ground (gray squares) and first excited (gray circles) transition of QDMs as function of bottom dot thickness. Hollow diamonds: ground states of the cladding QWR. (Right)Energy separation between ground and first excited transitions as a function of the thickness of the bottom QD.

Figure 5.15 (left) shows the measured emission energies of the ground (gray squares)

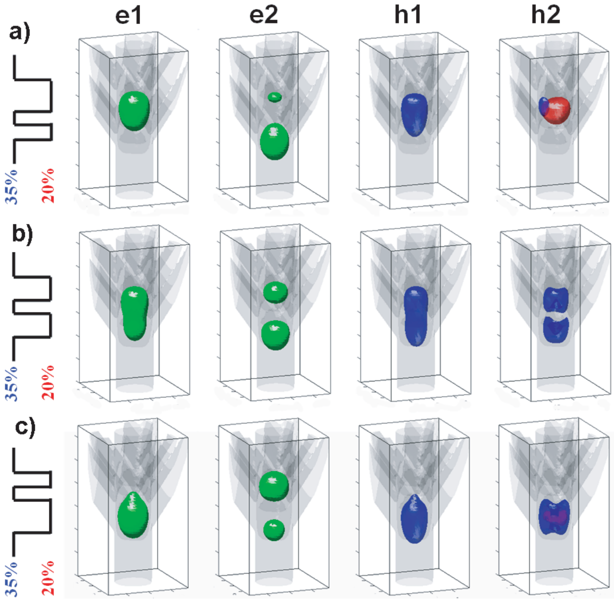

Figure 5.16: Isosurfaces of computed probability distributions (corresponding to probability density of 2.0×10^{-4} nm^{-3}) for for two lowest conduction (green) and valence band (HH and LH components indicated in red and blue, respectively) states of double-dot structures with bottom dot thickness of (a)6.5 nm, (b)10.5 nm and (c)14.5 nm.

and first excited (gray circles) transitions of the QD molecules as a function of the bottom dot thickness l. The hollow diamonds and the thick horizontal light gray line indicate the energies above which the transitions in the QWR barriers appear. The vertical error bars correspond to the spread in the values of the emission energy measured on different pyramids (between 10 to 20 different positions) in the same sample. The energy separation between the ground and first excited transitions (s-p separation) is depicted in Fig 5.15 (right), as a function of the bottom dot thickness. It can be seen that, the more symmetric the QDM is (that is, QD thicknesses closer to $l = 10.5$nm), the smaller is the s-p separation.

The model calculation is again formulated accounting for valence band mixing. Figure 5.16 shows the computed isosurfaces of computed probability distributions (corresponding to probability density of 2.0×10^{-4} nm^{-3}) for for two lowest conduction (green) and valence band (HH and LH components indicated in red and blue, respectively) states of double-dot structures with bottom (top) dot thickness of 6.5 (14.5) nm, 10.5 (10.5) nm and 14.5 (6.5) nm, respectively. Due to the pyramidal geometry, the bottom dot is surrounded by slightly higher (effective) barrier potential than the top dot. By examining Fig 5.16, we clearly seen that for two dots with identical thickness (b) the wavefunction is not perfectly delocalized in the two dots, and for the structure corresponding to (a) and (c), the two probability distributions are not exactly a mirror to each other with respect to the inter-dot barrier.

The calculated energies are indicated by solid black lines in Fig 5.15, accounting for a 4 nm grading region at the QD/barrier interfaces. These values are in fair agreement with the observed transition energies in μPL spectra. The expected level splitting due to carrier hybridization from the model is also consistent with spectral line splitting observed in the experiment. Notice that the calculated lowest s-p separation (strongest coupling) is obtained for a slightly larger bottom dot thickness ($\mathrm{l} \sim 12$ nm) (Fig 5.15 (left)), which is not the symmetric QDM case as might be expected. This is a consequence of the nonplanar layer profile, which removes the inversion symmetry with respect to the VQWR axis as mentioned previously in Subsection 5.2.2. More discussions on how to eliminate such a effect will be shown at the end of this subsection.

Second, we also computed another series of double-QD molecule structures by keeping the bottom QD (9 nm) and barrier (4 nm) thickness, and continuously changing the top QD thickness from 18 nm to 1 nm. The Al contents in the QD and barrier layers are again 1% and 5%, respectively.

In Fig 5.17, isosurfaces of computed probability distributions for the ground conduction and valence band (HH and LH components indicated in red and blue, respectively) states are presented for this series of double-QD structures. It can been seen that the ground electron state is mainly localized in the top QD (QD2) when it is much thicker than the bottom one (QD1), for $\mathrm{D_{QD2}} = 18$ nm and $\mathrm{D_{QD2}} = 12$ nm. Once the two QDs become equivalent ($\mathrm{D_{QD2}} = 10 \sim 6.5$ nm in the figure), the ground electron wavefunction are more delocalized. Keeping on reducing the top QD thickness, ground electron states becomes localized again, but to the bottom QD. Similar behavior takes place for the ground valence band states. The valence band mixing makes the hole states more complicated than the electron states. Apart from the states localization induced by the QDs dissimilarity, the ground hole state changes from mainly LH to HH hole character when the top QD gets very thin (see the cases of $\mathrm{D_{QD2}} = 2$ nm and $\mathrm{D_{QD2}} = 1$ nm in Fig 5.17).

A more careful examination of Fig 5.17 reveals an interesting point. As mentioned previously, because of the pyramidal shape of the structure, the bottom QD is surrounded by slightly higher (effective) barrier potential than the top QD. As a result, even for two dots of identical thickness, the wavefunctions are slightly localized. Referring to Fig 5.7 (middle) and Fig 5.17 (the case: $\mathrm{D_{QD1}} = \mathrm{D_{QD2}} = 9$ nm), the ground electron and hole states are more localized in the top QD. This asymmetric barrier potential for the two dots can be compensated by reducing a little the top QD size (or enlarging the bottom QD thickness) during growth. For example, for $\mathrm{D_{QD1}} = 9$ nm and $\mathrm{D_{QD2}} = 7.5$ nm (in Fig 5.17), the probability distribution of ground electron state becomes completely delocalized, resulting in a symmetric distribution with respect to the barrier in between the two QDs.

To illustrate the carrier delocalization in a quantitative way, we define the carrier delocalization degree (Deloc) in the following way. First sum up the probability density of state electrons (or holes) in QD1 and QD2 separately. Then, take the smaller value

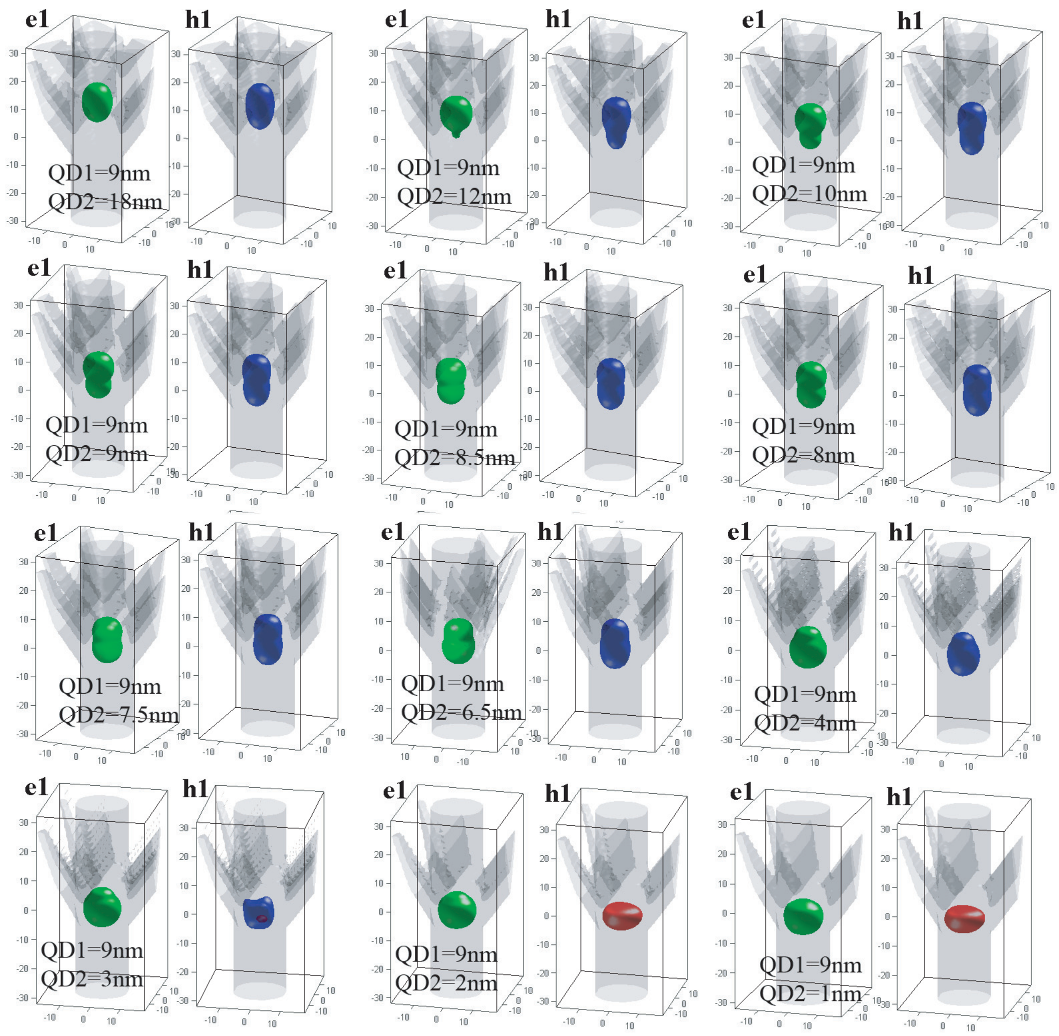

Figure 5.17: Isosurfaces of computed probability distributions (corresponding to probability density of 2.0×10^{-4} nm^{-3}) for the ground conduction (green) and valence band (HH and LH components indicated in red and blue, respectively) states for a series of double-QD structures. The bottom QD and the barrier in between the two QD are fixed to 9 nm and 4 nm thick. The top QD thickness changed from 18 nm to 1 nm from left to right, top to bottom. The shape of the double-QD molecule structure is represented by the grey surfaces.

of the two and divide by the larger value of the two:

$$\mathrm{Deloc} = \frac{\min(\mathrm{sum}(\mathrm{QD1}), \mathrm{sum}(\mathrm{QD2})}{\max(\mathrm{sum}(\mathrm{QD1}), \mathrm{sum}(\mathrm{QD2}))} \tag{5.1}$$

Using this formula, the ground state electron and hole (LH, HH components separately and together) delocalization degrees in the QD molecules as a function of top QD thickness are calculated and presented in Fig 5.18. The straight dark gray horizontal line (Deloc = 1) indicates a situation of completely (100%) delocalized carrier states, whereas the light gray line (Deloc = 0) means carrier state 100% localized in one of the two QDs. The black squares represent the ground state electron delocalization degree(Deloc$_{\mathrm{e1}}$), whereas the open (or filled) circles represent the delocalization degree of the LH (or HH) component of the ground hole state. The half-filled circles is the delocalization degree of the ground hole state (Deloc$_{\mathrm{h1}}$), achieved by adding up both LH and HH components. The dashed and dotted lines represent the percentage of LH and HH component of the ground hole state respectively. They clearly show the predominated LH component for top QD thickness (D$_{\mathrm{QD2}}$) larger than 4 nm. Then, the LH component drops down quickly and finally the HH component becomes dominant for D$_{\mathrm{QD2}}$ $<$ 2nm. Such switched hole character indicates the hole wavefunction localization($>$ 95%) in the bottom QD because the effective width/height aspect ratio of the QD molecule system has changed from smaller than unity, as is the case for strongly coupled QD molecule, to larger than unity. The aspect ratio of the isolated bottom QD determines the character of the ground hole state.

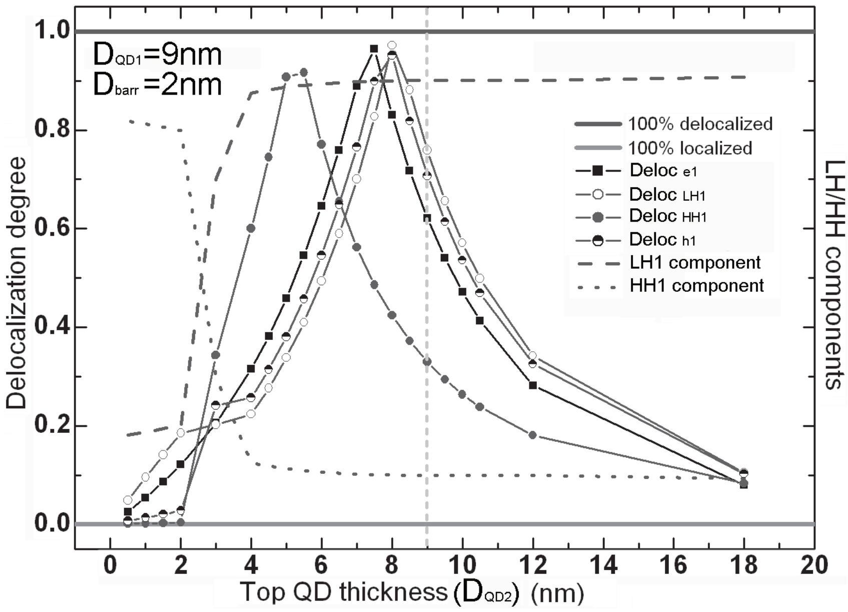

Figure 5.18: Ground electron and hole states delocalization degrees in the QD molecule as a function of top QD thickness.

Examining Fig 5.18 again, we find that the maximum Deloc takes place in the range between D$_{\mathrm{QD2}}$ = 4 nm and D$_{\mathrm{QD2}}$ = 9 nm (the situation D$_{\mathrm{QD1}}$ = D$_{\mathrm{QD2}}$, indicated by vertical dashed line in the figure), but at different D$_{\mathrm{QD2}}$ for electrons and for holes. Since the LH component is dominant in ground hole state within this range, the Deloc$_{\mathrm{LH1}}$ is very close to the Deloc$_{\mathrm{h1}}$ and the Deloc$_{\mathrm{HH1}}$ is negligible. Therefore, it is sufficient to consider only the Deloc$_{\mathrm{e1}}$ and Deloc$_{\mathrm{LH1}}$ here for comparison. From the figure, we obtain D$_{\mathrm{QD2}}$ = 7.5 nm and D$_{\mathrm{QD2}}$ = 8 nm for maximum Deloc$_{\mathrm{e1}}$ (98%) and Deloc$_{\mathrm{LH1}}$ (99%)

respectively. In our double-QD molecule configuration, due to the pyramidal geometry, carriers in the bottom QD1 "feel" higher effective potential as compared to the top QD2. This difference (or asymmetric potential) is more severe for electrons than for holes. This is because for $\mathrm{Al_yGa_{1-y}As}$ /$\mathrm{Al_xGa_{1-x}As}$ /$\mathrm{Al_yGa_{1-y}As}$ heterostructure (refer to Fig 1.4), the potential well of the VB is shallower than that of the CB ($\triangle E_v < \triangle E_c$) so that the electron and hole experience different effective potentials. Therefore, in order to reach the most symmetric situation (effective) for QD1 and QD2, one needs to introduce larger difference in the two QD sizes for electrons than for holes.

Figures 5.17-5.18 show the results of the calculations with a fixed interdot barrier thickness $D_{barr} = 2$ nm. We could image that if the two QDs are farther apart (larger barrier thickness), the asymmetric barrier potential caused by the pyramidal shape will be reduced. It might be then possible to have highest delocalization degree for electrons and holes at one given QD2 thickness within certain precision (e.g. 0.5nm steps), while sacrificing the strength of the coupling due to the enlarged dot-to-dot distance. Upon series of calculations by changing D_{barr} and the D_{QD2} one after another systematically, we found that the maximum $\mathrm{Deloc_{e1}}$ (95%), $\mathrm{Deloc_{LH1}}$(97%) and $\mathrm{Deloc_{h1}}$ (98%) are achieved for $D_{QD1} = 9$ nm, $D_{QD2} = 8.5$ nm, $D_{barr} = 6$ nm. In this case, the LH component is predominant(95%) in the ground hole state.

All these simulation results give us clues how to make better coupled QDs structures in pyramids. By growing intentionally a thicker bottom QD in the pyramidal QD molecule structure, one can achieve stronger coupling between the QDs. In reality, the growth rate acceleration makes the top QD thicker than the bottom one while the two QDs have the same nominal thickness. Therefore, one needs to grow even thicker (nominally) the bottom QD layer to eliminate the QDs dissimilarity caused by these two factors.

5.4 Perturbing the wavefunction in QD molecules

Besides QD molecules, the self-limiting growth in the pyramids can also produce more complex nanostructures that can be employed to study the features of the confined states. In the experiments described here, the high degree of structural control allowed the insertion of very thin potential barrier as local "wavefunction probes" in the studied QD or QWR structures.

In order to understand the idea of this wavefunction mapping, first, let us take a look at general results of the perturbation theory. The general idea is to split the Hamiltonian H′ of the system two parts, $H' = H + V$. H is the unperturbed system, which is "large" and can be solved exactly. V is the perturbation, which must be "small". The solutions to the Schrödinger equation of the unperturbed system is

$$H\chi_i = E_i\chi_i \tag{5.2}$$

where χ is the envelope function and i is the band index. We wish to find the solutions to

$$\mathrm{H}'\chi_\mathrm{i}' = (\mathrm{H}+\mathrm{V})\chi_\mathrm{i}' = \mathrm{E}_\mathrm{i}'\chi_\mathrm{i}' \tag{5.3}$$

The idea of the perturbation theory is to expand the energy and wave function in powers of the small potential V. One can find from many textbooks (e.g. Ref [10]), the results for the expansion of the energy to the first order:

$$\mathrm{E}_\mathrm{i}' = \mathrm{E}_\mathrm{i} + \int \chi_\mathrm{i}^* \mathrm{V} \chi_\mathrm{i} \tag{5.4}$$

Then, one can take the simplest case involving QWs to explain the idea of "wavefunction probing". Marzin et al measured the spatial variation of the probability densities in the first few electron states of a GaAs/$\mathrm{Al_xGa_{1-x}As}$ QW [173]. The results was obtained from the optical determination of the energies of the bound states as a function of the position of a highly localized perturbation, consisting of one isoelectronic substituted cation plane containing either In (attractive potential) or Al (repulsive potential) [173]. A series of samples was prepared, each with the probe plane in a different position, scanning the whole width of the QWs [173]. Assuming the perturbation in one sample is $\mathrm{W}\delta(\mathrm{z}-\mathrm{z_0})$ (the probe plane is at $\mathrm{z}=\mathrm{z_0}$), according to Eq. 5.4, the eigenenergies of the perturbed Hamiltonian H' can be given by

$$\mathrm{E}_\mathrm{i}' = \mathrm{E}_\mathrm{i} + \int \chi_\mathrm{i}^* \mathrm{W}\delta(\mathrm{z}-\mathrm{z_0})\chi_\mathrm{i} = \mathrm{E}_\mathrm{i} + \mathrm{W}|\chi_\mathrm{i}(\mathrm{z_0})|^2 \tag{5.5}$$

Here, $|\chi_\mathrm{i}(\mathrm{z_0})|^2$ corresponds to the carrier probability densities. Clearly, the eigenenergies E_i' will keep the unperturbed value E_i' if $\mathrm{W}|\chi_\mathrm{i}(\mathrm{z_0})|^2 = 0$ (i.e. if the probe plane is located at a node of the probability density distribution). However, if the perturbation is positioned at a place where $\mathrm{W}|\chi_\mathrm{i}(\mathrm{z_0})|^2$ is large, the effect of the perturbation on the eigenenergies will be large. To probe $|\chi_\mathrm{i}(\mathrm{z_0})|^2$ by measuring optical transitions (e.g. PL emissions), one has to consider the perturbations for the electrons and for the holes separately since the transition energies are affected by the state energies of both electrons and holes. By certain reasonable approximations, it is possible to determine the values of $|\chi_\mathrm{i}(\mathrm{z_0})|^2$ for electrons and for holes from the extracted transition energies [173].

In principle, this idea can be extended to QWR or QD states, especially in our AlGaAs pyramidal QWR, QD systems due to their high degree of controllabilities. Moreover, the formation of the QWR-QD is along the growth direction, which allows the insertion of the very localized probe planes. In the present thesis, we used a similar approach, not to fully map the wavefunctions, but to confirm certain aspects of the wavefunctions related to the comparison of single and coupled QDs, for example, the fact that the states are delocalized, the fact that some have low or high probability in the barriers or the center dot (in triple-dots), etc. As a first attempt for such kind of experiments, two pyramidal QD/QWR structures were modeled. One is a short QWR (nominal Al 20%) of 22 nm in length. The other is a double-QD structure: each QD is 9 nm thick and the barrier in between is 4 nm thick (the total length is 22 nm).

The nominal Al content in QD and barrier layer is 20% and 35%. The diameter of the QWR and QD parts are both 16 nm. Both samples have thick cladding layers (nominal Al 35%) below and above the main structures as usual. The double-QD structure is an analogue of a short QWR perturbed by 4 nm thin barrier (repulsive potential) in the middle. The isosurfaces of computed probability distributions for the ground (e1) and first excited (e2) electron states for these two samples are presented in Fig 5.19. Similar to the QW examples discussed in the last paragraph, because the barrier is situated in the middle of the short wire, e1 are more influenced than e2 by the barrier. A dip is clearly seen in center of the probability distribution of e1 due to the perturbation introduced by the barrier there (see Fig 5.19 (b) left). This effect also influences the state energies. The calculated confinement energies (with respect to the GaAs conduction band edge) of the corresponding electron states are shown on top of the probability distributions. The perturbation brought by the higher potential barrier blue shifts e1 by ~ 9 meV, but shifts e2 less than 2 meV.

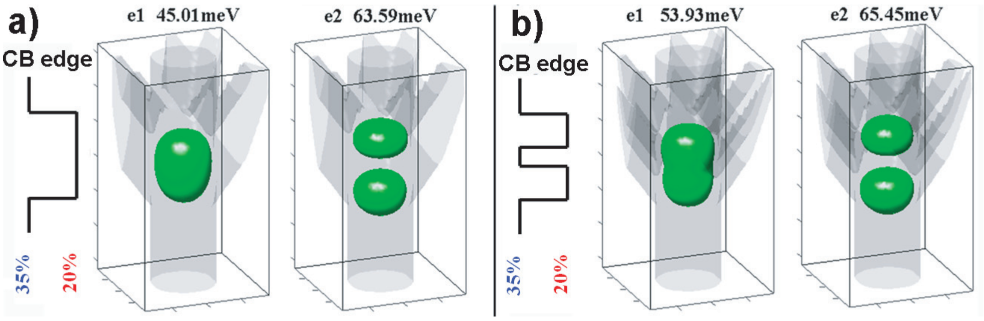

Figure 5.19: Isosurfaces of computed probability distributions (corresponding to probability density of 1.2×10^{-4} nm^{-3}) for the ground and first excited electron states of (a) short QWR and (b)double-QD structures. The calculated confinement energies (with respect to the GaAs conduction band edge) of the corresponding electron states are shown in the top.

It would be more interesting to know the influence of perturbation on the optical transition energies as they represent a directly measurable value. In order to estimate such influence, the valence band has to be taken into consideration as well, together with the conduction band, since the optical transition is related to the recombination of electron and hole pairs. Actually, the impact of the perturbation on the VB is very similar to that on the CB, except that the potential well depth is much shallower(about half of the conduction band potential depth) and the effective masses of carriers are larger. The valence band mixing also brings some complexity to the estimation. Anyway, we can approximately correlate the change in the transition energy and the influence of the perturbation on the CB electrons qualitatively. For example, a previous series of samples (first sample series in Subsection 5.3.2) can serve for this purpose with certain accuracy. There, the samples are constructed by inserting a thin AlGaAs barrier(4.5 nm) into different positions in a short VQWR ($21 + 4.5 = 25.5$ nm) to form asymmetric double-QDMs. From Fig 5.15 (left), we can already have an idea of the shape of the wavefunctions of the ground and first excited states. The ground and excited state energies were extracted from measured PL spectra as a function of inserted barrier positions in Fig 5.15 (left). It clearly shows that by applying the perturbation(the barrier) in the middle of the VQWR, the ground state energies are most strongly affected (largest blue shift of the emission energy), but the excited states are least influenced. This is because the perturbation takes place at the maximum amplitude of the ground state wavefunction, but it is exactly where the node of the excited state wavefunction is. However, the inserted barrier (4.5 nm) is quite thick as compared to the entire QWR length (25.5 nm), , and thus this structure is not ideal for sampling the local probability density quantitatively.

Moreover, the electron/hole probability distribution with more complicated symmetry can be also studied by applying perturbations in smart ways (special positions or regions) in short QWR and triple-QD molecule samples. To illustrate this, we designed and fabricated a set of pyramidal QWR/QD samples (Appendix B, growth ♯2618, ♯2655-2658, ♯2725, ♯2731). The details of their structures are summarized in Fig 5.20.

Sample NO.	Bottom QD layer		Middle QD layer		Top QD layer		Inter-dot barrier layers		Cladding layers
	D_{QD1}(nm)	Al%	D_{QD2}(nm)	Al%	D_{QD3}(nm)	Al%	D_{barr}(nm)	Al%	Al%
#1	8.75	20	8.75	20	8.75	20	3.75	20	35
#2	8.75	20	8.75	20	8.75	20	3.75	35	35
#3	8.75	20	8.75	20	8.75	20	3.75	40	40
#4	13.75	20	6.25	20	6.25	20	3.75	35	35
#5	6.25	20	13.75	20	6.25	20	3.75	35	35
#6	8.75	20	8.75	15	8.75	20	3.75	35	35
#7	8.75	15	8.75	20	8.75	15	3.75	35	35

Figure 5.20: Table of the important parameters of 7 different structures. The Al% shown in the table corresponds to the nominal Al content of the layers.

Figure 5.21 sketches the conduction band edges of the main part of these 7 structures. The nominal Al content and the thickness of the corresponding layer is also marked accordingly.

The isosurfaces of computed probability distributions for three lowest electron states of Sample ♯1 to ♯3 are presented in Fig 5.19 (a)-(c). The calculated confinement energies (with respect to the GaAs conduction band edge) of the corresponding electron states are shown on top of the probability distributions. Similarly to the previous discussions, by comparing (a) and (b), we can conclude that the perturbation made by two barriers results in $\sim$ 10.5 meV blue shift for e1, $\sim$ 7.3 meV for e2 and only $\sim$ 2.5 meV for e3, as expected. The small energy change in e3 is due to the fact that the perturbations (barriers) take place in the region close to the wavefunction nodes of e3. Fig 5.19 (b) and (c) shows that the effect of the perturbation increases with the increasing barrier

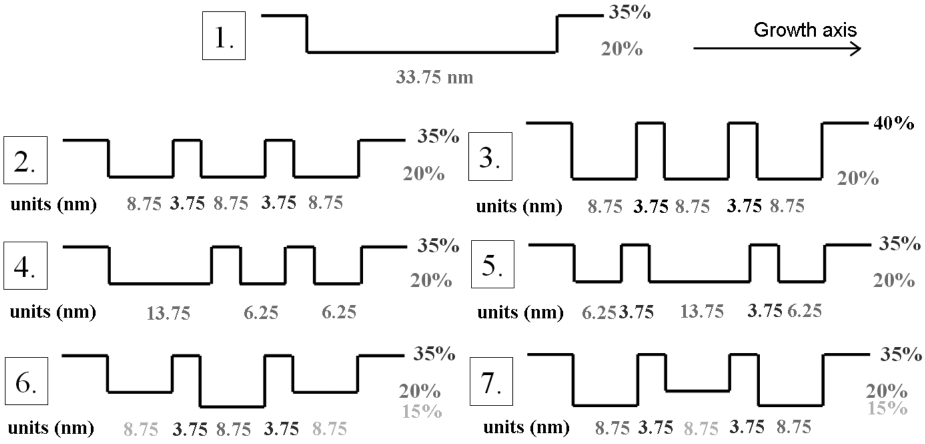

Figure 5.21: Simplified illustrations of the conduction band edges of seven designed structures serving for wavefunction perturbation studies. The corresponding growth details are described in the main text and in Appendix B.

potential height.

The computed polarization-resolved optical absorption spectra for these three structures are plotted in Fig 5.23(Left)(for simplicity, only transitions involving the four lowest energy hole states are shown). Transition energies of different states involved in these spectra show a combined effect of the perturbation on the conduction and valence band states. Here, we also included the binding energy of excitons in the calculations in order to obtain more precise absorption energy in the spectra. In principle, the binding energy of a given state varies little amongst these 7 structures because the most important factor is the spatial extent of the corresponding electron and hole wavefunction. We can therefore omit the influence of the exciton binding energy while inspecting the energy shift induced by the perturbation. The measured low temperature (10 K) linear polarization-resolved PL spectra from the cleaved edge of samples ♯1-♯3 are presented in Fig 5.23(Right). Blue and red lines correspond to transitions with linear polarization vector oriented along and perpendicular to the growth direction respectively. The exact calculated transition energies and the involved electron hole states of the corresponding transitions obtained from the computed absorption spectra and the measured transition energies from the PL spectra for sample ♯3, ♯2 and ♯1 are listed in the table in Fig 5.24. The measured transition energies are in good agreement with the calculated ones; in particular that the observed peak groups of ground transitions (transitions related to e1) and excited transition (transitions related to e2) show predicted blue shift in samples ♯2 and ♯3 as compared to that in Sample ♯1. The transitions related to the higher electron levels are more difficult to identify since their energies are very close or even higher than the ground states of the cladding VQWR (> 1.60 eV).

Moreover, the small differences between PL spectra of Sample♯2 and those of ♯3 are easy to understand since their structures are very similar except that the barrier potential is slightly higher in the case of Sample♯3. Based on the CB states probability

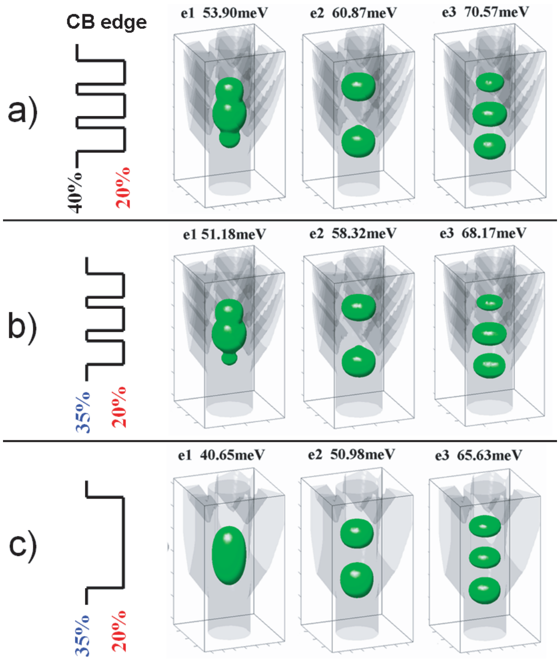

Figure 5.22: Isosurfaces of computed probability distributions (corresponding to probability density of 1.2×10^{-4} nm^{-3}) for three lowest electron states of (a) Sample ♯3, (b) Sample ♯2 and (c) Sample ♯1 structures. The calculated confinement energies (with respect to the GaAs conduction band edge) of the corresponding electron states are marked in the top.

distribution of Sample♯2 in Fig 5.22 (b), we can conclude that in Sample ♯3, small perturbations (from nominal 30% to 40% Al in all the barrier layers) are applied to regions around the local probability density minima, therefore, the state energies are only modified slightly. From another point of view, the molecular nature of the coupled triple-QD structure, which is different from that of a short QWR or an elongated single-QD, can be revealed by such comparison. Experimentally, we observed almost unchanged ground and excited transition energies as we increased simultaneously the separating barrier and cladding potential(by increasing locally the nominal Al content in the barrier from 35% to 40%). This is a clear evidence of a low carrier probability density inside the barrier. This approach can be extended for probing electron probability density distribution inside nanostructures with complicated or unknown symmetry and band configurations. [174]

To further clarify the profile of the electron wavefunctions, the dependence of computed probability densities (integrated in the x-y plane) for three lowest electron states of Sample ♯2 in z axis (the growth direction) is plotted in Fig 5.25. The dashed lines indicate the potential profiles also integrated in the x-y plane. Examining the wavefunction distributions, one can predict the expected effects for specific perturbations implemented on this structure. For instance, consider an increase in the middle QD thickness and a reduction in the thickness of the top and bottom QDs simultaneously by keeping a fixed total thickness of the three QDs (Sample ♯5). According to Fig 5.25,

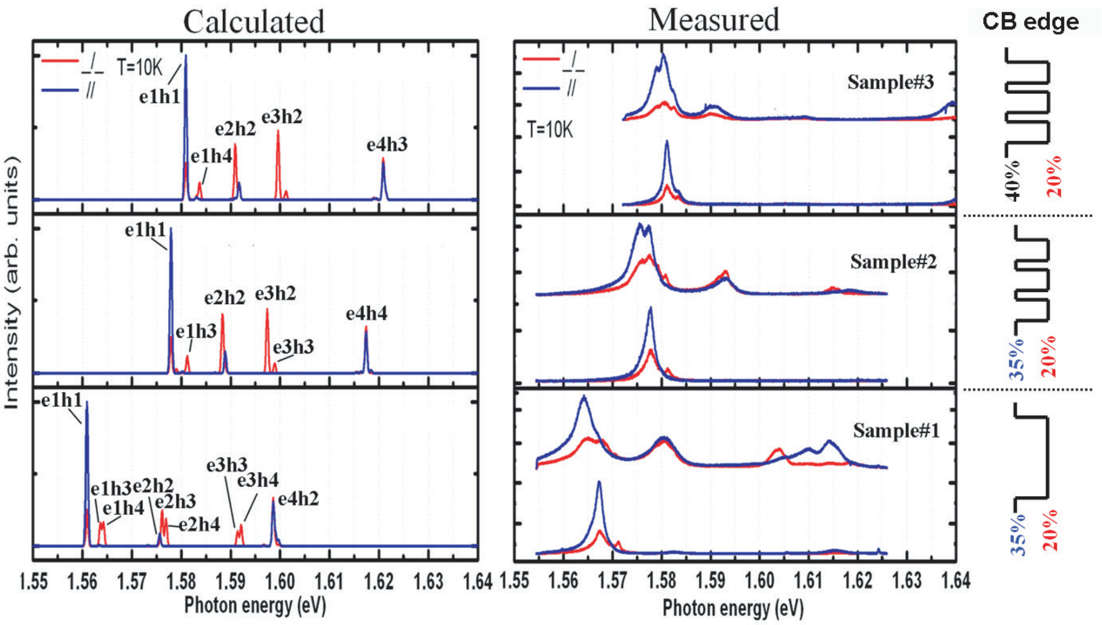

Figure 5.23: Computed absorption spectra (Left) and measured side-view polarization-resolved PL spectra (Right) of samples ♯1-♯3 for linear polarization vector oriented along (blue) and perpendicular to (red) the growth direction. T = 10 K.

	Calculated transition energies (eV)						Measured transition energies (eV)		
#3	e1h1	1.581	e2h2	1.591	e3h2	1.5996	1.581	1.5906	1.604
	e1h4	1.584	e2h3	1.592	e3h3	1.601	1.5835		
#2	e1h1	1.578	e2h2	1.588	e3h2	1.597	1.578	1.593	1.615 ?
	e1h3	1.581	e2h3	1.589	e3h3	1.599	1.581		
#1	e1h1	1.56	e2h2	1.5755	e3h3	1.5914	1.567	1.580	1.6035
	e1h3	1.5635	e2h3	1.576	e3h4	1.592			
	e1h4	1.564	e2h4	1.577			1.571		

Figure 5.24: Table of calculated (left) and measured (right) energies of transitions with high probabilities (PL intensities) for sample ♯3-♯1.

we can expect that the energy of e1 will decrease but that of e2 will increase. On the other hand, with perturbation implemented with Sample ♯4, we enlarged the bottom QD thickness and reduced the thickness of the other two QDs. Therefore, the situation is different from the previous one, e.g. we expect the ground state wavefunction will be more concentrated into the middle QD. Figure 5.26 plots the computed probability densities for the three lowest electron states of Sample ♯4 (a), ♯5 (b) along z axis. It clearly shows how the structures and their potential profiles can affect the electron wavefunctions.

Moreover, we computed absorption spectra of Sample ♯4, ♯5, ♯2 for linear polar-

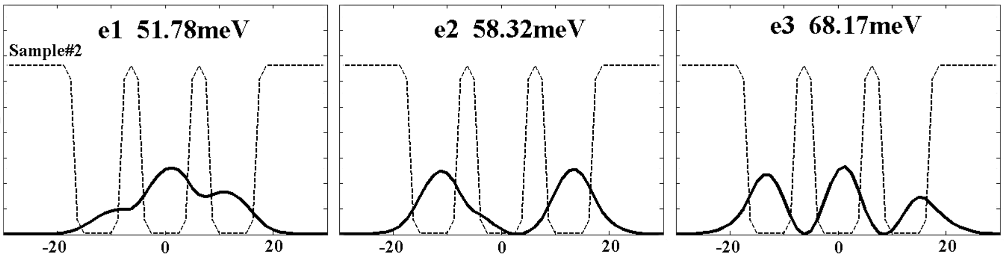

Figure 5.25: The computed probability densities (integrated in the x-y plane) for the three lowest electron states of sample ♯2 along z axis (the growth direction). The dashed lines indicate the x-y integrated potential profiles.

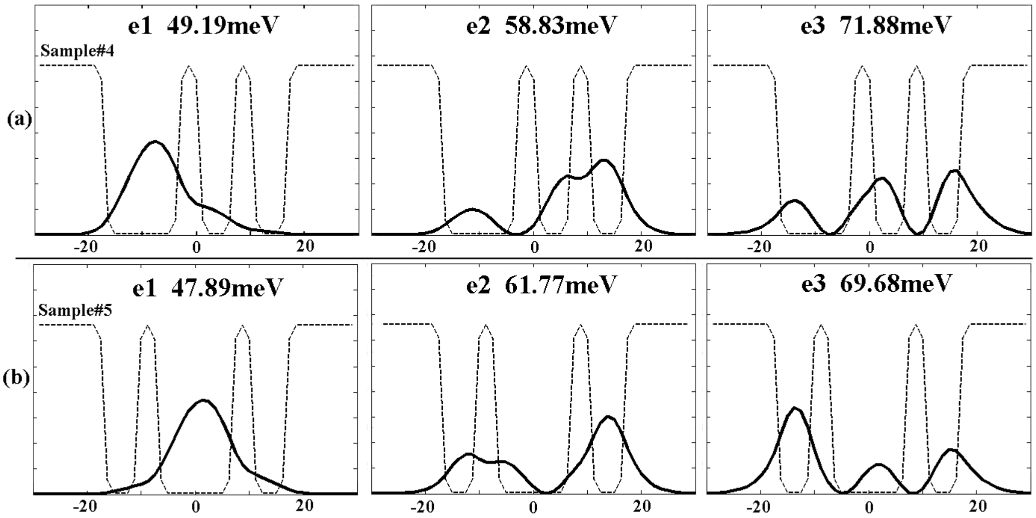

Figure 5.26: The computed probability densities for the three lowest electron states of Sample ♯4 (a), ♯5 (b) along z axis (the growth direction). The dashed lines indicate the x-y integrated potential profiles.

ization vector oriented along and perpendicular to the growth direction (see Fig 5.27 (left)). The measured low temperature (10 K) polarization-resolved PL spectra from the cleaved-edges of these three samples are presented in Fig 5.27 (right). Blue and red lines represent emission polarized along and perpendicular to the growth direction. Again, the exact calculated transition energies and the involved electron hole states of the corresponding transitions obtained from the computed absorption spectra and the measured transition energies from the PL spectra for sample ♯4, ♯5 and ♯2 are listed in the table in Fig 5.28. The experimental observations agree very well with the calculated ones (especially the ground transitions), further confirming the usefulness of our perturbation approach.

Another possible way to modify the potential profile of the structure is to change the Al content in one (or several) of the three QD layers. Following this idea, we fabricated Sample ♯6 and ♯7. The nominal Al content in the middle QD layer is reduced to

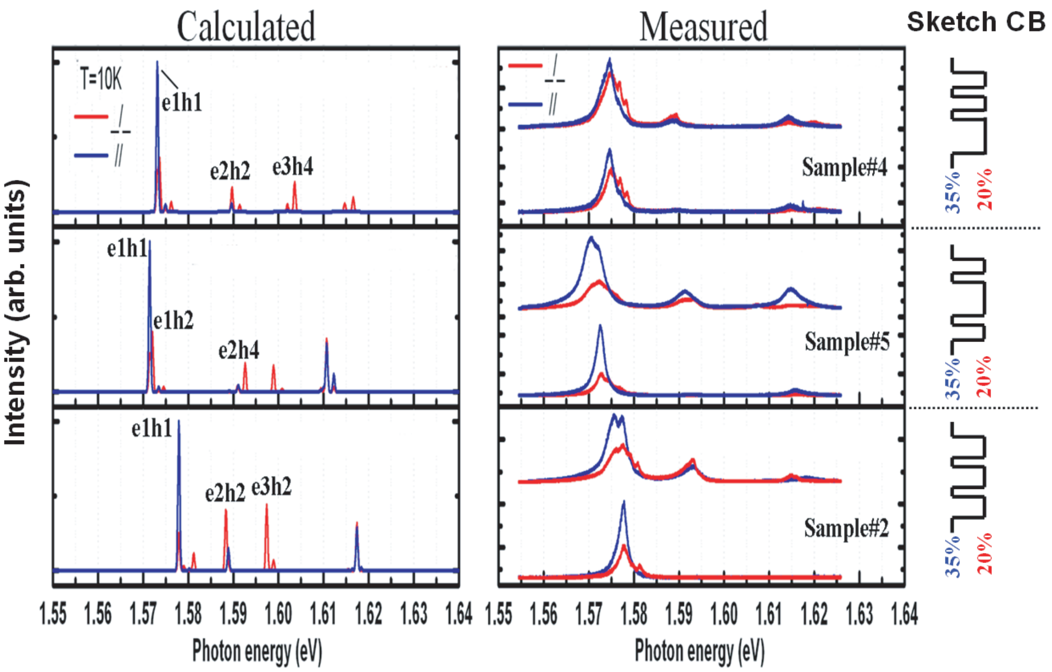

Figure 5.27: Computed absorption spectra (Left) and measured side-view polarization-resolved PL spectra (Right) of Sample ♯4, ♯5, ♯2 for linear polarization vector oriented along (blue) and perpendicular to (red) the growth direction. T = 10 K.

	Calculated transition energies (eV)						Measured transition energies (eV)		
#4	e1h1	1.573	e2h2	1.590	e3h3	1.602	1.575	1.5886	
	e1h3	1.575	e2h4	1.591	e3h4	1.6036	1.577		
	e1h4	1.576					1.5785		
#5	e1h1	1.5715	e2h2	1.591	e3h1	1.599	1.5725	1.591	
	e1h3	1.5734	e2h4	1.5925			1.5745	1.593	
	e1h4	1.5745							
#2	e1h1	1.578	e2h2	1.588	e3h2	1.597	1.578	1.593	1.615 ?
	e1h3	1.581	e2h3	1.589	e3h3	1.599	1.581		

Figure 5.28: Table of calculated (left) and measured (right) energies of transitions with high probabilities (PL intensities) for sample ♯4, ♯2 and ♯1.

15% in Sample ♯6, while for Sample ♯7, the nominal Al content is changed to 15% in bottom and top QD layers simultaneously. Other parameters stay the same as in Sample ♯2. Referring to Fig 5.25, we expect that the e1 and e3 states of Sample ♯6 will decrease significantly in energy, but e2 state will remain almost the same due to the low probability density in the middle dot, as compared to Sample ♯2. For Sample ♯7, all these three states will red shift. The computed absorption spectra of these three samples indicate the expected trend. Good consistence between the calculated and measured spectra of these samples is observed, as shown in Fig 5.29.

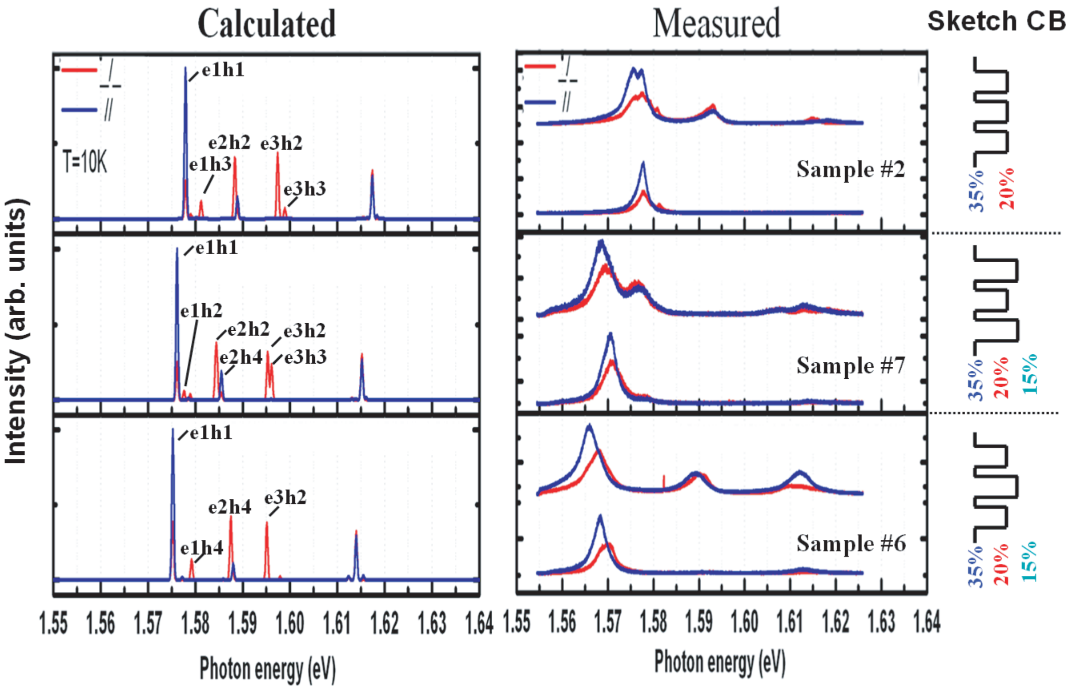

Figure 5.29: Computed absorption spectra (Left) and measured side-view polarization-resolved PL spectra (Right) of Sample ♯2, ♯7, ♯6 for linear polarization vector oriented along (blue) and perpendicular to (red) the growth direction. T = 10K.

In summary, our first attempt to perturb (or probe) the electron hole wavefunctions using triple-QD configurations shows striking feasibility. It indeed supports the picture of the molecular states by verifying lower carrier probability densities in the barriers of the QD-molecule structures. In principle, it can be further expanded to do full wavefunction mapping [173], if we could make thin enough barrier as probes and insert it to many different positions in a given structure. This could be extremely interesting for fundamental physics studies but this topic is outside the scope of this thesis. Moreover, this technique can be also useful in exploring new structures constructed by different materials, where there may be a doubt in the spatial probability distribution for a given electronic states.

5.5 Summary

In this chapter, electron and hole states hybridization in QD molecules with two different coupled QD configurations are studied, showing enhanced tunnel coupling realized by 1D QWR barrier connecting the QDs in pyramidal system. Moreover, we verified the presence of coupling in our QD molecules by investigation of optical properties of a set of single-, double- and triple-QD molecule structures. Furthermore, we discussed the possibilities of tuning the coupling between two QDs either by changing barrier thickness in between the QDs or by modifying the two QDs dissimilarity. Finally, an approach of perturbing/probing the electron wavefunctions using QD molecule structures was discussed.

Chapter 6

Conclusions and Future Direction

The objective of my thesis work was to investigate the optical and electronic properties of the complex AlGaAs quantum structures self-formed in inverted tetrahedral pyramids etched in (111)B GaAs substrates. Taking advantage of the high degree of controllability of the self-limiting growth inside such pyramids, we were able to explore deeply and systematically a novel QWR system formed by capillarity-induced alloy segregation effect. Moreover, a continuous transition from 2D to 3D quantum confinement was also achieved within the same system. The impact of the dimensionality on the nanostructures' properties were studied by side-view polarization-resolved micro-PL and time-resolved spectroscopy. Furthermore, the AlGaAs QD was also investigated by several optical means. Single photon emission from these QDs was observed, revealing the nature of discrete QD states.

Another important outcome of the present thesis work was the demonstration of hybridized electron and hole states in QD molecules formed in the pyramids by polarization-resolved PL spectroscopy and photon-correlation measurement. This is the first experimental evidences of coupling of both electron and hole states, hence the formation of direct excitons, in QD molecules, to our knowledge.

During the study of these topics, a theoretical model that well represents the pyramidal QWR, QD and the heterostructures connecting them and allows the evaluation of their electronic states was established. The numerical simulations played a very important role in predicting and verifying the experimental observations and also contributed in sample design.

These investigated structures hold promise for nano-photonic device applications and also are of high interest for application concepts in quantum information processing. For example, our pyramidal AlGaAs single QDs and QD molecules with controllable emission polarization can be used as single photon sources in quantum cryptography. Moreover, these QDs can be used as a medium for quantum computing due to their long carrier coherence time [99] [100]. The single QD is normally used for two qubit operations [101], whereas the QD molecule is even promising for application as building blocks in scalable quantum computing [102] [103] [104]. The modulated growth provides considerable freedom in designing complex nanostructures that are difficult to achieve with purely self-assembly approaches. The tailored dimensionality is also interesting for constructing mixed-dimensionality systems. This might open the way for generation of new class of QWRs, e.g. tapered wires, in which the electron and hole might be accelerated to the same direction.

The QD molecules described in Chapter 5 can be extended to larger, 1D QD SLs simply by stacking more dots along the VQWR axis. The hybridization of the carrier states in such SLs is expected to be more difficult to achieve because of structural disorder effects as well as the impact of uncontrolled electric fields produced by charged impurities in the vicinity of the dots. Inadvertent differences between the dots in size and composition can be minimized by better control of the growth rates along the VQWR, e.g., by compensating for systematic increase growth rate due to pyramid filling. The built-in difference between the bottom QD and the upper ones, resulting from the peculiar symmetry of the pyramidal structure, can be corrected by intentionally increasing the thickness of the lower dot.

Formation of three dimensional coupled, pyramidal QD array is limited by the achievable lateral proximity of such dots, which depends on the pyramidal pattern resolution and eventually the control of the growth on a ∼10nm lateral scale. Nevertheless, lateral coupling might be achieved using cavity photons in high-Q coupled optical resonators [175] [176], or other long range (dipole-dipole) dot interaction, possibly leading to the realization of QD-confined exciton "solids" (Fig 6.1).

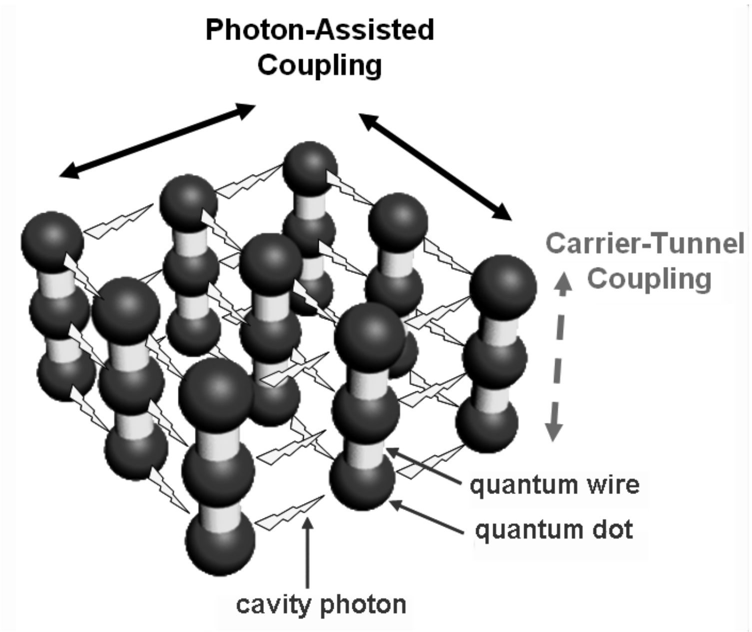

Figure 6.1: Schematics of QD "solid": A generic ordered QD system.

Appendix A

QWR and QD formalism

The numerical codes used for calculating electronic states of infinitely long QWR and pyramidal single and multiple QD structures were implemented by Dr. Fredrik Karlsson. The model was formulated in the envelope function approximation and discretized by finite differences. A single band describes the electrons in the conduction band, while the holes in the valence band are described by a 4 × 4 Luttinger Hamiltonian, accounting for the possible mixing between heavy and light holes. The conduction- and valence-band Hamiltonians as well as some theoretical backgrounds can be found in Chapter 1. The values of the various parameters needed for model were taken from Ref. [13]. Figure A.1 lists the most important band structure parameters of GaAs and AlAs that are used in the model. Here, $\mathrm{E_g^\Gamma}$ and $\mathrm{E_{VBO}}$ represent the bandgap at the Γ valley and valence band offset, respectively. $\mathrm{m_e^*}$ is the electron mass at the Γ valley andγ_1, γ_2, γ_3 are the three Luttinger parameters. The corresponding values for AlGaAs alloys are interpolated between GaAs and AlAs. The dependence of the bandgap of $\mathrm{Al_xGa_{1-x}As}$ on alloy composition is assumed to fit a simple quadratic form:

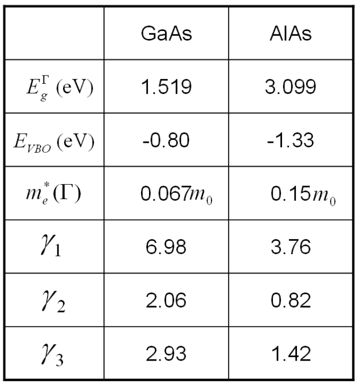

	GaAs	AlAs
E_g^Γ (eV)	1.519	3.099
E_{VBO} (eV)	-0.80	-1.33
$m_e^*(\Gamma)$	$0.067m_0$	$0.15m_0$
γ_1	6.98	3.76
γ_2	2.06	0.82
γ_3	2.93	1.42

Figure A.1: Band structure parameters for GaAs and AlAs. Adopted from [13]

$$\mathrm{E_g(Al_xGa_{1-x}As) = (1-x)E_g(GaAs) + xE_g(AlAs) - x(1-x)C} \tag{A.1}$$

where C is the so-called bowing parameter, which accounts for the deviation from a linear interpolation. In this case, $\mathrm{C} = -0.127 + 1.310\mathrm{x}$. The inverse of the Luttinger parameters are interpolated linearly. The other parameters are interpolated linearly.

In the confined directions, no definite k-values exist since the wavefunction will be continuously distributed in k-space. Therefore the k-components in the confined directions are replaced by the momentum operator

$$\mathrm{k_j} = -\mathrm{i}\frac{\partial}{\partial \mathrm{x_j}} = -\mathrm{i}\partial_{\mathrm{x_j}} \tag{A.2}$$

To obtain a matrix representations of the Hamiltonians, $\partial_{\mathrm{x_j}}$ is discretized by conventional first order central finite differences. For an infinitely long QWR, the computational domain is a rectangular grid with square unit cells and $\widetilde{\mathrm{N}} = \mathrm{N_x N_y}$ nodes, while for QD model, it is on a cuboid grid with rectangular unit cells and $\widetilde{\mathrm{N}} = \mathrm{N_x N_y N_z}$ nodes. The typical size of a QD domain used in the this is $\widetilde{\mathrm{N}} = 40 \times 40 \times 130$. Hence, the conduction band Hamiltonian (Eq. 1.8) becomes an $\widetilde{\mathrm{N}} \times \widetilde{\mathrm{N}}$ sparse matrice and the final dimension of Luttinger Hamiltonian Eq. 1.4 is $\mathrm{N} = 4\widetilde{\mathrm{N}} \times 4\widetilde{\mathrm{N}}$. The parameter matrices are diagonal, but matrices for the derivatives are non-diagonal and must be symmetrized carefully to reproduce the properties and the commutation relations of the k components ensuring numerical stability of the difference scheme. For an arbitrary function F, the discretized products $\mathrm{F}\partial_{\mathrm{x_i}}$, $\mathrm{F}\partial^2_{\mathrm{x_i}}$, $\mathrm{F}\partial_{\mathrm{x_i}}\partial_{\mathrm{x_j}}$ are symmetrized as follows:

$$\begin{aligned}
&\mathrm{F}\partial_{\mathrm{x_i}} = (\mathrm{F}\partial_{\mathrm{x_i}} + \partial_{\mathrm{x_i}}\mathrm{F})/2 \\
&\mathrm{F}\partial^2_{\mathrm{x_i}} = \partial_{\mathrm{x_i}}\mathrm{F}\partial_{\mathrm{x_i}} \\
&\mathrm{F}\partial_{\mathrm{x_i}}\partial_{\mathrm{x_j}} = (\partial_{\mathrm{x_i}}\mathrm{F}\partial_{\mathrm{x_j}} + \partial_{\mathrm{x_j}}\mathrm{F}\partial_{\mathrm{x_i}})/2
\end{aligned} \tag{A.3}$$

The eigenvalues and eigenvectors were obtained by using the Matlab function *eigs*. Dirichlet boundary conditions were used to handle the boundary nodes, where the amplitude of the wavefunction is forced to vanish at the boundary.

Appendix B

Epitaxial layer sequences

List of growth runs referred to in the main chapters: all layer thicknesses, growth rates are nominal and refer to growth on planar (100) substrates. (JT = jump to)

Samples used in Chapter 3

growth **#1612**						
layer	**material**	**%**	**thick (nm)**	**rate (nm/s)**	**T (°C)**	**V/III**
buffer	GaAs		10		770	
etch-stop	AlGaAs	75% Al	45	0.14	770	500
waitT 20s						
barrier 2	AlGaAs	55% Al	130	0.14	730	
barrier 1	AlGaAs	30% Al	70	0.14	“	
					“	
barrier 1	AlGaAs	30% Al	70	0.14	“	
barrier 2	AlGaAs	55% Al	130	0.14	JT770	
cap	GaAs		2		JT730	
stop						

growth **#1665**						
layer	**material**	**%**	**thick (nm)**	**rate (nm/s)**	**T (°C)**	**V/III**
buffer	GaAs		10		770	
etch-stop	AlGaAs	75% Al	45	0.14	770	500
waitT 20s						
barrier 2	AlGaAs	55% Al	130	0.14	730	
barrier 1	AlGaAs	20% Al	70	0.14	“	
					“	
barrier 1	AlGaAs	20% Al	70	0.14	“	
barrier 2	AlGaAs	55% Al	130	0.14	JT770	
cap	GaAs		2		JT730	
stop						

growth **#1666**						
layer	**material**	**%**	**thick (nm)**	**rate (nm/s)**	**T (°C)**	**V/III**
buffer	GaAs		10		770	
etch-stop	AlGaAs	75% Al	45	0.14	770	500
waitT 20s						
barrier 2	AlGaAs	55% Al	130	0.14	730	
barrier 1	AlGaAs	40% Al	70	0.14	“	
					“	
barrier 1	AlGaAs	40% Al	70	0.14	“	
barrier 2	AlGaAs	55% Al	130	0.14	JT770	
cap	GaAs		2		JT730	
stop						

growth **#1670**						
layer	**material**	**%**	**thick (nm)**	**rate (nm/s)**	**T (°C)**	**V/III**
buffer	GaAs		10		770	
etch-stop	AlGaAs	75% Al	45	0.14	770	500
waitT 20s						
barrier 2	AlGaAs	55% Al	130	0.14	730	
barrier 1	AlGaAs	10% Al	70	0.14	“	
					“	
barrier 1	AlGaAs	10% Al	70	0.14	“	
barrier 2	AlGaAs	55% Al	130	0.14	JT770	
cap	GaAs		2		JT730	
stop						

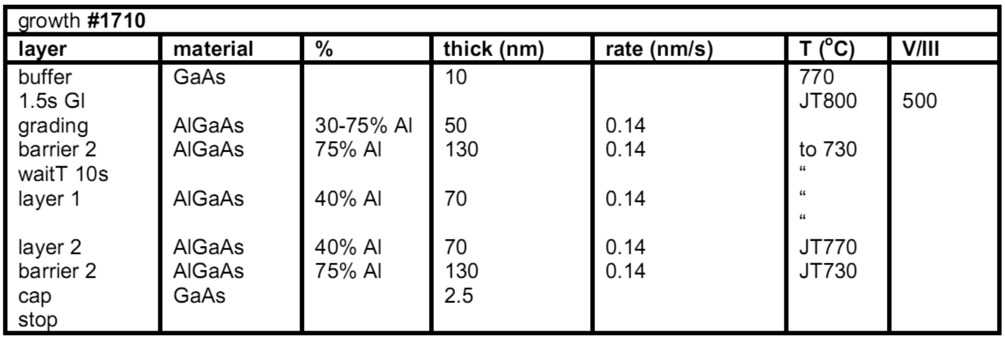

growth **#1710**

layer	**material**	**%**	**thick (nm)**	**rate (nm/s)**	**T (°C)**	**V/III**
buffer	GaAs		10		770	
1.5s GI					JT800	500
grading	AlGaAs	30-75% Al	50	0.14		
barrier 2	AlGaAs	75% Al	130	0.14	to 730	
waitT 10s					“	
layer 1	AlGaAs	40% Al	70	0.14	“	
					“	
layer 2	AlGaAs	40% Al	70	0.14	JT770	
barrier 2	AlGaAs	75% Al	130	0.14	JT730	
cap	GaAs		2.5			
stop						

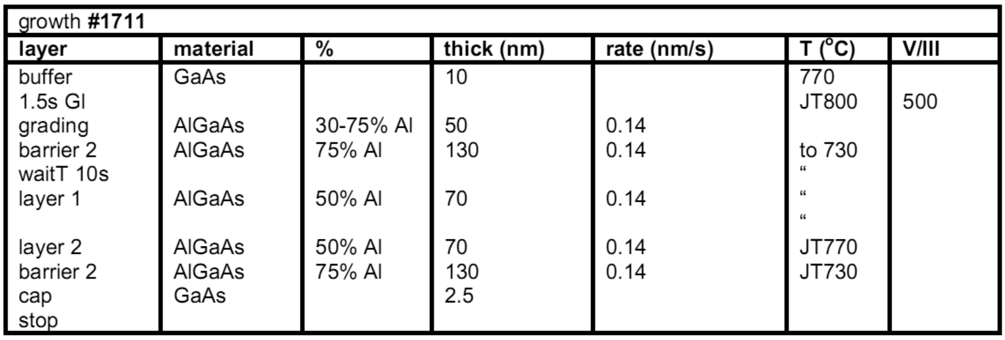

growth **#1711**

layer	**material**	**%**	**thick (nm)**	**rate (nm/s)**	**T (°C)**	**V/III**
buffer	GaAs		10		770	
1.5s GI					JT800	500
grading	AlGaAs	30-75% Al	50	0.14		
barrier 2	AlGaAs	75% Al	130	0.14	to 730	
waitT 10s					“	
layer 1	AlGaAs	50% Al	70	0.14	“	
					“	
layer 2	AlGaAs	50% Al	70	0.14	JT770	
barrier 2	AlGaAs	75% Al	130	0.14	JT730	
cap	GaAs		2.5			
stop						

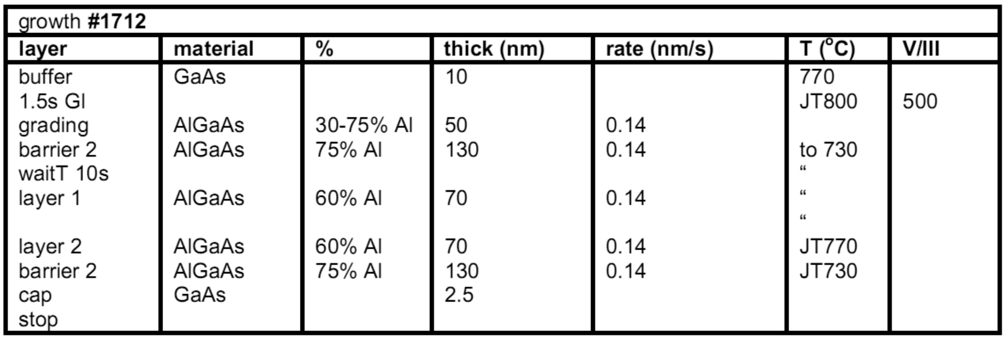

growth **#1712**

layer	**material**	**%**	**thick (nm)**	**rate (nm/s)**	**T (°C)**	**V/III**
buffer	GaAs		10		770	
1.5s GI					JT800	500
grading	AlGaAs	30-75% Al	50	0.14		
barrier 2	AlGaAs	75% Al	130	0.14	to 730	
waitT 10s					“	
layer 1	AlGaAs	60% Al	70	0.14	“	
					“	
layer 2	AlGaAs	60% Al	70	0.14	JT770	
barrier 2	AlGaAs	75% Al	130	0.14	JT730	
cap	GaAs		2.5			
stop						

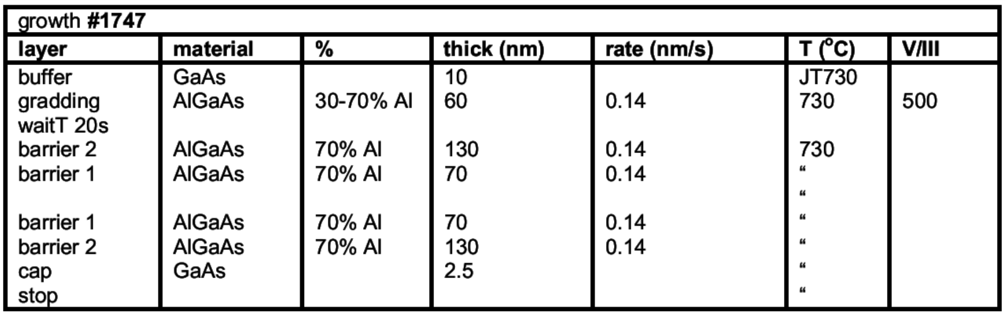

growth **#1747**

layer	**material**	**%**	**thick (nm)**	**rate (nm/s)**	**T (°C)**	**V/III**
buffer	GaAs		10		JT730	
gradding	AlGaAs	30-70% Al	60	0.14	730	500
waitT 20s						
barrier 2	AlGaAs	70% Al	130	0.14	730	
barrier 1	AlGaAs	70% Al	70	0.14	“	
					“	
barrier 1	AlGaAs	70% Al	70	0.14	“	
barrier 2	AlGaAs	70% Al	130	0.14	“	
cap	GaAs		2.5		“	
stop					“	

Series I in Chapter 4

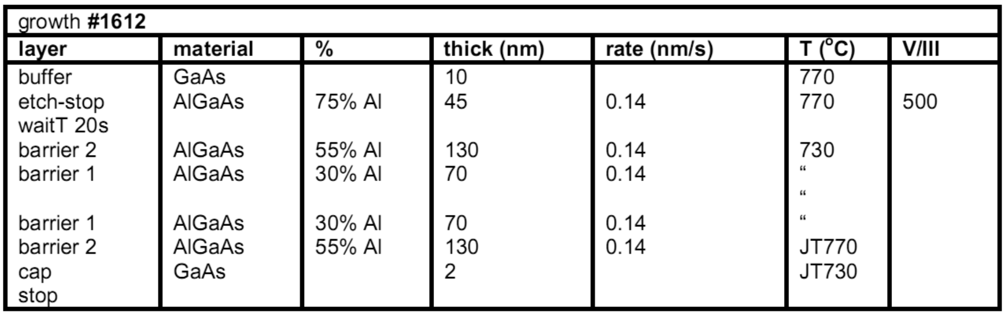

growth **#1612**

layer	**material**	**%**	**thick (nm)**	**rate (nm/s)**	**T (°C)**	**V/III**
buffer	GaAs		10		770	
etch-stop	AlGaAs	75% Al	45	0.14	770	500
waitT 20s						
barrier 2	AlGaAs	55% Al	130	0.14	730	
barrier 1	AlGaAs	30% Al	70	0.14	“	
					“	
barrier 1	AlGaAs	30% Al	70	0.14	“	
barrier 2	AlGaAs	55% Al	130	0.14	JT770	
cap	GaAs		2		JT730	
stop						

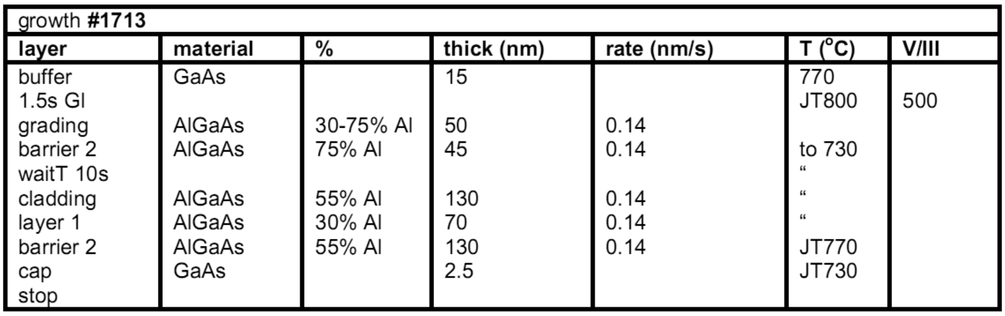

growth **#1713**

layer	**material**	**%**	**thick (nm)**	**rate (nm/s)**	**T (°C)**	**V/III**
buffer	GaAs		15		770	
1.5s GI					JT800	500
grading	AlGaAs	30-75% Al	50	0.14		
barrier 2	AlGaAs	75% Al	45	0.14	to 730	
waitT 10s					“	
cladding	AlGaAs	55% Al	130	0.14	“	
layer 1	AlGaAs	30% Al	70	0.14	“	
barrier 2	AlGaAs	55% Al	130	0.14	JT770	
cap	GaAs		2.5		JT730	
stop						

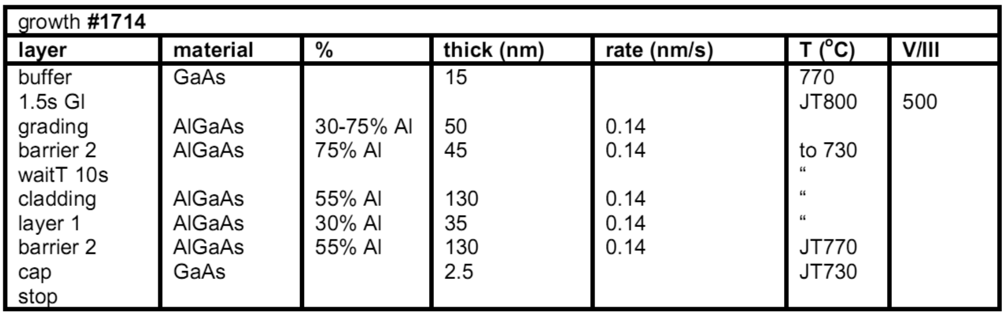

growth **#1714**

layer	**material**	**%**	**thick (nm)**	**rate (nm/s)**	**T (°C)**	**V/III**
buffer	GaAs		15		770	
1.5s GI					JT800	500
grading	AlGaAs	30-75% Al	50	0.14		
barrier 2	AlGaAs	75% Al	45	0.14	to 730	
waitT 10s					“	
cladding	AlGaAs	55% Al	130	0.14	“	
layer 1	AlGaAs	30% Al	35	0.14	“	
barrier 2	AlGaAs	55% Al	130	0.14	JT770	
cap	GaAs		2.5		JT730	
stop						

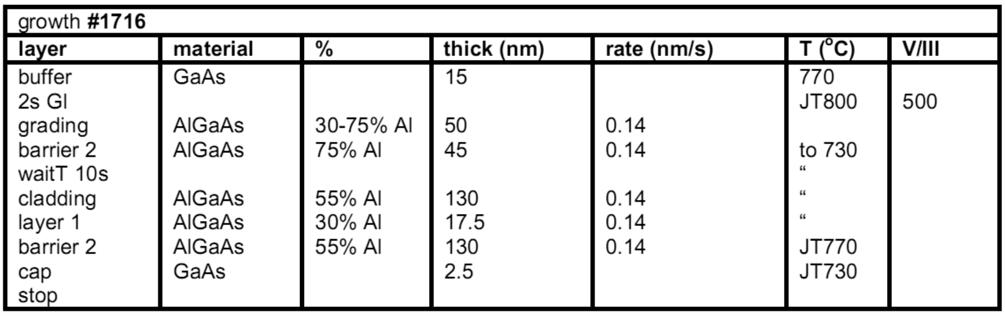

growth **#1716**

layer	**material**	**%**	**thick (nm)**	**rate (nm/s)**	**T (°C)**	**V/III**
buffer	GaAs		15		770	
2s GI					JT800	500
grading	AlGaAs	30-75% Al	50	0.14		
barrier 2	AlGaAs	75% Al	45	0.14	to 730	
waitT 10s					“	
cladding	AlGaAs	55% Al	130	0.14	“	
layer 1	AlGaAs	30% Al	17.5	0.14	“	
barrier 2	AlGaAs	55% Al	130	0.14	JT770	
cap	GaAs		2.5		JT730	
stop						

growth **#2071**

layer	**material**	**%**	**thick (nm)**	**rate (nm/s)**	**T (°C)**	**V/III**
buffer	GaAs		50		770	
2s GI						
grading	AlGaAs	30-75% Al	25	0.13	to 800	
barrier 2	AlGaAs	75% Al	45		to 770	
waitT 5s					JT730	
cladding	AlGaAs	55% Al	150		“	550
layer 1	AlGaAs*	30% Al	17.5		“	520
barrier 2	AlGaAs	55% Al	150		JT770	550
cap	GaAs		2.5		JT730	
stop						

growth **#2072**

layer	**material**	**%**	**thick (nm)**	**rate (nm/s)**	**T (°C)**	**V/III**
buffer	GaAs		50		770	
2s GI						
grading	AlGaAs	30-75% Al	25	0.13	to 800	
barrier 2	AlGaAs	75% Al	45		to 770	
waitT 5s					JT730	
cladding	AlGaAs	55% Al	150		“	550
layer 1	AlGaAs*	30% Al	8		“	520
barrier 2	AlGaAs	55% Al	150		JT770	550
cap	GaAs		2.5		JT730	
stop						

growth **#2075**

layer	**material**	**%**	**thick (nm)**	**rate (nm/s)**	**T (°C)**	**V/III**
buffer	GaAs		50		770	
2s GI						
grading	AlGaAs	30-75% Al	25	0.13	to 800	
barrier 2	AlGaAs	75% Al	45		to 770	
waitT 5s					JT730	
cladding	AlGaAs	55% Al	150		“	550
layer 1	AlGaAs*	30% Al	4		“	520
barrier 2	AlGaAs	55% Al	150		JT770	550
cap	GaAs		2.5		JT730	
stop						

growth **#2076**

layer	**material**	**%**	**thick (nm)**	**rate (nm/s)**	**T (°C)**	**V/III**
buffer	GaAs		50		770	
2s GI						
grading	AlGaAs	30-75% Al	25	0.13	to 800	
barrier 2	AlGaAs	75% Al	45		to 770	
waitT 5s					JT730	
cladding	AlGaAs	55% Al	150		“	550
layer 1	AlGaAs*	30% Al	2		“	520
barrier 2	AlGaAs	55% Al	150		JT770	550
cap	GaAs		2.5		JT730	
stop						

growth **#2181**

layer	**material**	**%**	**thick (nm)**	**rate (nm/s)**	**T (°C)**	**V/III**
buffer	GaAs		50		770	
2s GI						
grading	AlGaAs	30-75% Al	25	0.13	to 800	
barrier 2	AlGaAs	75% Al	45		to 770	
waitT 5s					JT730	
cladding	AlGaAs	55% Al	150		“	550
layer 1	AlGaAs*	30% Al	3		“	520
barrier 2	AlGaAs	55% Al	150		JT770	550
cap	GaAs		2.5		JT730	
stop						

growth **#2183**

layer	**material**	**%**	**thick (nm)**	**rate (nm/s)**	**T (°C)**	**V/III**
buffer	GaAs		50		770	
2s GI						
grading	AlGaAs	30-75% Al	25	0.13	to 800	
barrier 2	AlGaAs	75% Al	45		to 770	
waitT 5s					JT730	
cladding	AlGaAs	55% Al	150		“	550
layer 1	AlGaAs*	30% Al	12		“	520
barrier 2	AlGaAs	55% Al	150		JT770	550
cap	GaAs		2.5		JT730	
stop						

growth **#2184**

layer	**material**	**%**	**thick (nm)**	**rate (nm/s)**	**T (°C)**	**V/III**
buffer	GaAs		50		770	
2s GI						
grading	AlGaAs	30-75% Al	25	0.13	to 800	
barrier 2	AlGaAs	75% Al	45		to 770	
waitT 5s					JT730	
cladding	AlGaAs	55% Al	150		“	550
layer 1	AlGaAs*	30% Al	6		“	520
barrier 2	AlGaAs	55% Al	150		JT770	550
cap	GaAs		2.5		JT730	
stop						

Series II in Chapter 4

growth **#2387**

layer	**material**	**%**	**thick (nm)**	**rate (nm/s)**	**T (°C)**	**V/III**
buffer	GaAs		40		735	620
2s GI						
grading	AlGaAs	30-75% Al	25	0.13	to 770	to 775
barrier 2	AlGaAs	75% Al	45		770	775
waitT 2s						
cladding	AlGaAs	35% Al	90		JT705	
layer 1	AlGaAs*	20% Al	140		“	
barrier 2	AlGaAs	35% Al	90			
cap	GaAs		2.5			720
stop						

growth **#2388**						
layer	**material**	**%**	**thick (nm)**	**rate (nm/s)**	**T (°C)**	**V/III**
buffer	GaAs		40		735	620
2s GI						
grading	AlGaAs	30-75% Al	25	0.13	to 770	to 775
barrier 2	AlGaAs	75% Al	45		770	775
waitT 2s						
cladding	AlGaAs	35% Al	130		JT705	
layer 1	AlGaAs*	20% Al	16		“	
barrier 2	AlGaAs	35% Al	160			
cap	GaAs		2.5			720
stop						

growth **#2394**						
layer	**material**	**%**	**thick (nm)**	**rate (nm/s)**	**T (°C)**	**V/III**
buffer	GaAs		40		735	620
2s GI						
grading	AlGaAs	30-75% Al	25	0.13	to 770	to 775
barrier 2	AlGaAs	75% Al	45		770	775
waitT 2s						
cladding	AlGaAs	35% Al	130		JT705	
layer 1	AlGaAs*	20% Al	8		“	
barrier 2	AlGaAs	35% Al	160			
cap	GaAs		2.5			720
stop						

growth **#2395**						
layer	**material**	**%**	**thick (nm)**	**rate (nm/s)**	**T (°C)**	**V/III**
buffer	GaAs		40		735	620
2s GI						
grading	AlGaAs	30-75% Al	25	0.13	to 770	to 775
barrier 2	AlGaAs	75% Al	45		770	775
waitT 2s						
cladding	AlGaAs	35% Al	130		JT705	
layer 1	AlGaAs*	20% Al	4		“	
barrier 2	AlGaAs	35% Al	160			
cap	GaAs		2.5			720
stop						

growth **#2396**						
layer	**material**	**%**	**thick (nm)**	**rate (nm/s)**	**T (°C)**	**V/III**
buffer	GaAs		40		735	620
2s GI						
grading	AlGaAs	30-75% Al	25	0.13	to 770	to 775
barrier 2	AlGaAs	75% Al	45		770	775
waitT 2s						
cladding	AlGaAs	35% Al	130		JT705	
layer 1	AlGaAs*	20% Al	2		“	
barrier 2	AlGaAs	35% Al	160			
cap	GaAs		2.5			720
stop						

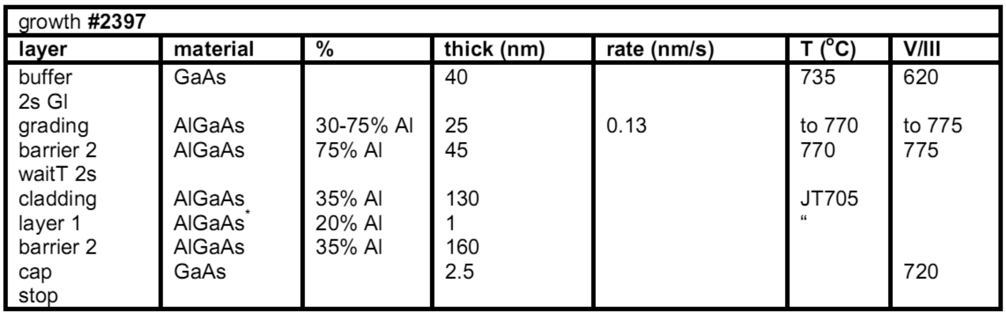

growth **#2397**

layer	**material**	**%**	**thick (nm)**	**rate (nm/s)**	**T (°C)**	**V/III**
buffer	GaAs		40		735	620
2s GI						
grading	AlGaAs	30-75% Al	25	0.13	to 770	to 775
barrier 2	AlGaAs	75% Al	45		770	775
waitT 2s						
cladding	AlGaAs	35% Al	130		JT705	
layer 1	AlGaAs*	20% Al	1		“	
barrier 2	AlGaAs	35% Al	160			
cap	GaAs		2.5			720
stop						

Samples used in Chapter 5

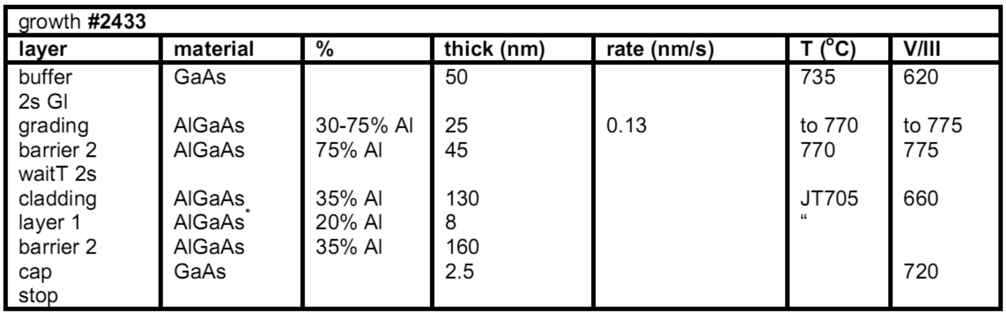

growth **#2433**

layer	**material**	**%**	**thick (nm)**	**rate (nm/s)**	**T (°C)**	**V/III**
buffer	GaAs		50		735	620
2s GI						
grading	AlGaAs	30-75% Al	25	0.13	to 770	to 775
barrier 2	AlGaAs	75% Al	45		770	775
waitT 2s						
cladding	AlGaAs	35% Al	130		JT705	660
layer 1	AlGaAs*	20% Al	8		“	
barrier 2	AlGaAs	35% Al	160			
cap	GaAs		2.5			720
stop						

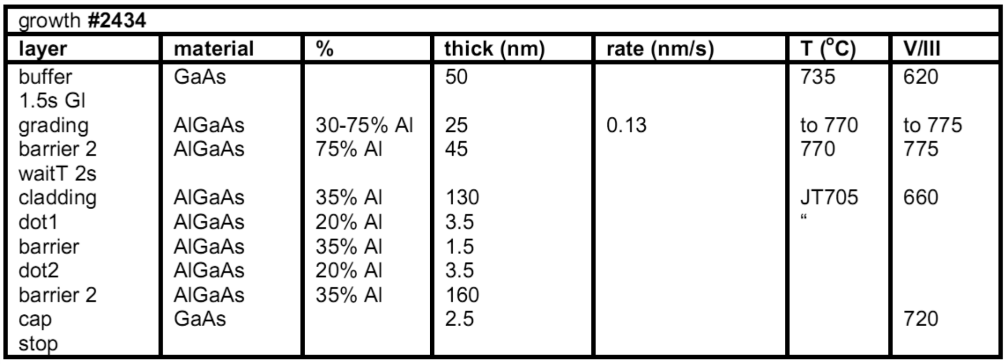

growth **#2434**

layer	**material**	**%**	**thick (nm)**	**rate (nm/s)**	**T (°C)**	**V/III**
buffer	GaAs		50		735	620
1.5s GI						
grading	AlGaAs	30-75% Al	25	0.13	to 770	to 775
barrier 2	AlGaAs	75% Al	45		770	775
waitT 2s						
cladding	AlGaAs	35% Al	130		JT705	660
dot1	AlGaAs	20% Al	3.5		“	
barrier	AlGaAs	35% Al	1.5			
dot2	AlGaAs	20% Al	3.5			
barrier 2	AlGaAs	35% Al	160			
cap	GaAs		2.5			720
stop						

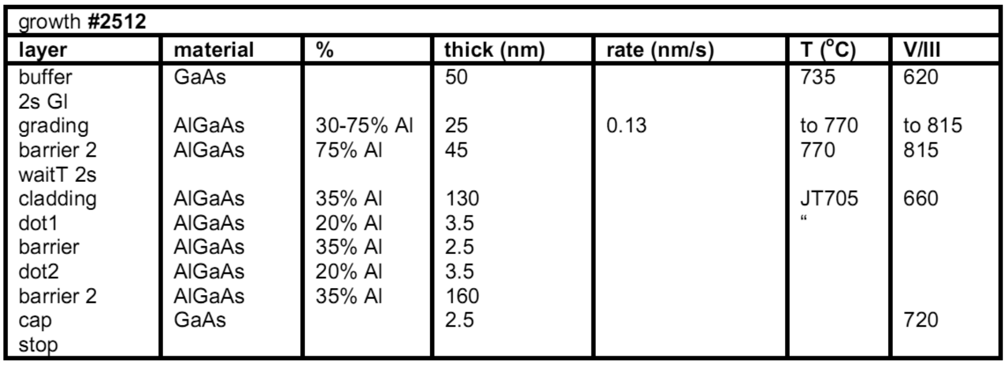

growth **#2512**

layer	**material**	**%**	**thick (nm)**	**rate (nm/s)**	**T (°C)**	**V/III**
buffer	GaAs		50		735	620
2s GI						
grading	AlGaAs	30-75% Al	25	0.13	to 770	to 815
barrier 2	AlGaAs	75% Al	45		770	815
waitT 2s						
cladding	AlGaAs	35% Al	130		JT705	660
dot1	AlGaAs	20% Al	3.5		“	
barrier	AlGaAs	35% Al	2.5			
dot2	AlGaAs	20% Al	3.5			
barrier 2	AlGaAs	35% Al	160			
cap	GaAs		2.5			720
stop						

growth **#2514**

layer	**material**	**%**	**thick (nm)**	**rate (nm/s)**	**T (°C)**	**V/III**
buffer	GaAs		50		735	620
2s GI						
grading	AlGaAs	30-75% Al	25	0.13	to 770	to 815
barrier 2	AlGaAs	75% Al	45		770	815
waitT 2s						
cladding	AlGaAs	35% Al	130		JT705	660
dot1	AlGaAs	20% Al	3.5		“	
barrier	AlGaAs	35% Al	3.5			
dot2	AlGaAs	20% Al	3.5			
barrier 2	AlGaAs	35% Al	160			
cap	GaAs		2.5			720
stop						

growth **#2515**

layer	**material**	**%**	**thick (nm)**	**rate (nm/s)**	**T (°C)**	**V/III**
buffer	GaAs		50		735	620
2s GI						
grading	AlGaAs	30-75% Al	25	0.13	to 770	to 815
barrier 2	AlGaAs	75% Al	45		770	815
waitT 2s						
cladding	AlGaAs	35% Al	130		JT705	660
dot1	AlGaAs	20% Al	3.5		“	
barrier	AlGaAs	35% Al	1			
dot2	AlGaAs	20% Al	3.5			
barrier 2	AlGaAs	35% Al	160			
cap	GaAs		2.5			720
stop						

growth **#2586**

layer	**material**	**%**	**thick (nm)**	**rate (nm/s)**	**T (°C)**	**V/III**
buffer	GaAs		50		735	620
2s GI						
grading	AlGaAs	30-75% Al	30	0.13	to 770	to 800
barrier 2	AlGaAs	75% Al	45		770	800
waitT 2s						
cladding	AlGaAs	35% Al	130		JT705	680
layer 1	AlGaAs*	20% Al	7		“	
barrier 2	AlGaAs	35% Al	160			
cap	GaAs		2.5			720
stop						

growth **#2587**

layer	**material**	**%**	**thick (nm)**	**rate (nm/s)**	**T (°C)**	**V/III**
buffer	GaAs		50		735	620
2s GI						
grading	AlGaAs	30-75% Al	30	0.13	to 770	to 800
barrier 2	AlGaAs	75% Al	45		770	800
waitT 2s						
cladding	AlGaAs	35% Al	130		JT705	680
dot1	AlGaAs	20% Al	3.5		“	
barrier	AlGaAs	35% Al	1.5			
dot2	AlGaAs	20% Al	3.5			
barrier 2	AlGaAs	35% Al	150			
cap	GaAs		2.5			720
stop						

growth **#2592**

layer	**material**	**%**	**thick (nm)**	**rate (nm/s)**	**T (°C)**	**V/III**
buffer	GaAs		50		735	620
2s GI						
grading	AlGaAs	30-75% Al	30	0.13	to 770	to 806
barrier 2	AlGaAs	75% Al	45		770	806
waitT 2s						
cladding	AlGaAs	35% Al	130		JT705	683
dot1	AlGaAs	20% Al	2.5		“	670
barrier	AlGaAs	35% Al	1.5			668
dot2	AlGaAs	20% Al	4.5			668
barrier 2	AlGaAs	35% Al	150			683
cap	GaAs		2.5			722
stop						

growth **#2593**

layer	**material**	**%**	**thick (nm)**	**rate (nm/s)**	**T (°C)**	**V/III**
buffer	GaAs		50		735	620
2s GI						
grading	AlGaAs	30-75% Al	30	0.13	to 770	to 806
barrier 2	AlGaAs	75% Al	45		770	806
waitT 2s						
cladding	AlGaAs	35% Al	130		JT705	683
dot1	AlGaAs	20% Al	4.5		“	670
barrier	AlGaAs	35% Al	1.5			668
dot2	AlGaAs	20% Al	2.5			668
barrier 2	AlGaAs	35% Al	150			683
cap	GaAs		2.5			722
stop						

growth **#2597**

layer	**material**	**%**	**thick (nm)**	**rate (nm/s)**	**T (°C)**	**V/III**
buffer	GaAs		50		735	620
2s GI						
grading	AlGaAs	30-75% Al	30	0.13	to 770	to 806
barrier 2	AlGaAs	75% Al	45		770	806
waitT 2s						
cladding	AlGaAs	35% Al	130		JT705	683
dot1	AlGaAs	20% Al	2.5		“	670
barrier	AlGaAs	35% Al	1.5			668
dot2	AlGaAs	20% Al	4.5			668
barrier 2	AlGaAs	35% Al	150			683
cap	GaAs		2.5			722
stop						

growth **#2594**

layer	**material**	**%**	**thick (nm)**	**rate (nm/s)**	**T (°C)**	**V/III**
buffer	GaAs		50		735	620
2s GI						
grading	AlGaAs	30-75% Al	30	0.13	to 770	to 800
barrier 2	AlGaAs	75% Al	45		770	800
waitT 2s						
cladding	AlGaAs	35% Al	130		JT705	680
layer 1	AlGaAs*	20% Al	7		“	
barrier 2	AlGaAs	35% Al	150			
cap	GaAs		2.5			720
stop						

growth **#2598**

layer	**material**	**%**	**thick (nm)**	**rate (nm/s)**	**T (°C)**	**V/III**
buffer	GaAs		50		735	620
2s GI						
grading	AlGaAs	30-75% Al	30	0.13	to 770	to 806
barrier 2	AlGaAs	75% Al	45		770	806
waitT 2s						
cladding	AlGaAs	35% Al	130		JT705	683
dot1	AlGaAs	20% Al	4		“	670
barrier	AlGaAs	35% Al	1.5			668
dot2	AlGaAs	20% Al	3			668
barrier 2	AlGaAs	35% Al	150			683
cap	GaAs		2.5			722
stop						

growth **#2599**

layer	**material**	**%**	**thick (nm)**	**rate (nm/s)**	**T (°C)**	**V/III**
buffer	GaAs		50		735	620
2s GI						
grading	AlGaAs	30-75% Al	30	0.13	to 770	to 806
barrier 2	AlGaAs	75% Al	45		770	806
waitT 2s						
cladding	AlGaAs	35% Al	130		JT705	683
dot1	AlGaAs	20% Al	5		“	670
barrier	AlGaAs	35% Al	1.5			668
dot2	AlGaAs	20% Al	2			668
barrier 2	AlGaAs	35% Al	150			683
cap	GaAs		2.5			722
stop						

growth **#2600**

layer	**material**	**%**	**thick (nm)**	**rate (nm/s)**	**T (°C)**	**V/III**
buffer	GaAs		50		735	620
2s GI						
grading	AlGaAs	30-75% Al	30	0.13	to 770	to 806
barrier 2	AlGaAs	75% Al	45		770	806
waitT 2s						
cladding	AlGaAs	35% Al	130		JT705	683
dot1	AlGaAs	20% Al	5.5		“	670
barrier	AlGaAs	35% Al	1.5			668
dot2	AlGaAs	20% Al	1.5			668
barrier 2	AlGaAs	35% Al	150			683
cap	GaAs		2.5			722
stop						

growth **#2608**

layer	**material**	**%**	**thick (nm)**	**rate (nm/s)**	**T (°C)**	**V/III**
buffer	GaAs		50		735	620
2s GI						
grading	AlGaAs	30-75% Al	30	0.13	to 770	to 806
barrier 2	AlGaAs	75% Al	45		770	806
waitT 2s						
cladding	AlGaAs	35% Al	130		JT705	683
dot1	AlGaAs	20% Al	5.5		“	670
barrier	AlGaAs	35% Al	1.5			668
dot2	AlGaAs	20% Al	1.5			668
barrier 2	AlGaAs	35% Al	150			683
cap	GaAs		2.5			722
stop						

growth **#2609**

layer	**material**	**%**	**thick (nm)**	**rate (nm/s)**	**T (°C)**	**V/III**
buffer	GaAs		50		735	620
2s GI						
grading	AlGaAs	30-75% Al	30	0.13	to 770	to 806
barrier 2	AlGaAs	75% Al	45		770	806
waitT 2s						
cladding	AlGaAs	35% Al	130		JT705	683
dot1	AlGaAs	20% Al	5		“	670
barrier	AlGaAs	35% Al	1.5			668
dot2	AlGaAs	20% Al	2			668
barrier 2	AlGaAs	35% Al	150			683
cap	GaAs		2.5			722
stop						

growth **#2610**

layer	**material**	**%**	**thick (nm)**	**rate (nm/s)**	**T (°C)**	**V/III**
buffer	GaAs		50		735	620
2s GI						
grading	AlGaAs	30-75% Al	30	0.13	to 770	to 806
barrier 2	AlGaAs	75% Al	45		770	806
waitT 2s						
cladding	AlGaAs	35% Al	130		JT705	683
dot1	AlGaAs	20% Al	4		“	670
barrier	AlGaAs	35% Al	1.5			668
dot2	AlGaAs	20% Al	3			668
barrier 2	AlGaAs	35% Al	150			683
cap	GaAs		2.5			722
stop						

growth **#2611**

layer	**material**	**%**	**thick (nm)**	**rate (nm/s)**	**T (°C)**	**V/III**
buffer	GaAs		50		735	620
2s GI						
grading	AlGaAs	30-75% Al	30	0.13	to 770	to 806
barrier 2	AlGaAs	75% Al	45		770	806
waitT 2s						
cladding	AlGaAs	35% Al	130		JT705	683
dot1	AlGaAs	20% Al	2.5		“	670
barrier	AlGaAs	35% Al	1.5			668
dot2	AlGaAs	20% Al	4.5			668
barrier 2	AlGaAs	35% Al	150			683
cap	GaAs		2.5			722
stop						

growth **#2612**

layer	**material**	**%**	**thick (nm)**	**rate (nm/s)**	**T (°C)**	**V/III**
buffer	GaAs		50		735	620
2s GI						
grading	AlGaAs	30-75% Al	30	0.13	to 770	to 806
barrier 2	AlGaAs	75% Al	45		770	806
waitT 2s						
cladding	AlGaAs	35% Al	130		JT705	683
dot1	AlGaAs	20% Al	6		“	670
barrier	AlGaAs	35% Al	1.5			668
dot2	AlGaAs	20% Al	1			668
barrier 2	AlGaAs	35% Al	150			683
cap	GaAs		2.5			722
stop						

growth **#2613**

layer	**material**	**%**	**thick (nm)**	**rate (nm/s)**	**T (°C)**	**V/III**
buffer	GaAs		50		735	620
2s GI						
grading	AlGaAs	30-75% Al	30	0.13	to 770	to 806
barrier 2	AlGaAs	75% Al	45		770	806
waitT 2s						
cladding	AlGaAs	35% Al	130		JT705	683
dot1	AlGaAs	20% Al	1.5		“	670
barrier	AlGaAs	35% Al	1.5			668
dot2	AlGaAs	20% Al	5.5			668
barrier 2	AlGaAs	35% Al	150			683
cap	GaAs		2.5			722
stop						

growth **#2614**

layer	**material**	**%**	**thick (nm)**	**rate (nm/s)**	**T (°C)**	**V/III**
buffer	GaAs		50		735	620
2s GI						
grading	AlGaAs	30-75% Al	30	0.13	to 770	to 800
barrier 2	AlGaAs	75% Al	45		770	800
waitT 2s						
cladding	AlGaAs	35% Al	130		JT705	680
layer 1	AlGaAs*	20% Al	8.5		“	
barrier 2	AlGaAs	35% Al	160			
cap	GaAs		2.5			720
stop						

growth **#2616**

layer	**material**	**%**	**thick (nm)**	**rate (nm/s)**	**T (°C)**	**V/III**
buffer	GaAs		50		735	620
2s GI						
grading	AlGaAs	30-75% Al	30	0.13	to 770	to 800
barrier 2	AlGaAs	75% Al	45		770	800
waitT 2s						
cladding	AlGaAs	35% Al	130		JT705	680
layer 1	AlGaAs*	20% Al	3.5		“	
barrier 2	AlGaAs	35% Al	160			
cap	GaAs		2.5			720
stop						

growth **#2617**

layer	**material**	**%**	**thick (nm)**	**rate (nm/s)**	**T (°C)**	**V/III**
buffer	GaAs		50		735	620
2s GI						
grading	AlGaAs	30-75% Al	30	0.13	to 770	to 806
barrier 2	AlGaAs	75% Al	45		770	806
waitT 2s						
cladding	AlGaAs	35% Al	130		JT705	683
dot1	AlGaAs	20% Al	1		“	670
barrier	AlGaAs	35% Al	1.5			668
dot2	AlGaAs	20% Al	6			668
barrier 2	AlGaAs	35% Al	150			683
cap	GaAs		2.5			722
stop						

growth **#2618**

layer	**material**	**%**	**thick (nm)**	**rate (nm/s)**	**T (°C)**	**V/III**
buffer	GaAs		50		735	620
2s GI						
grading	AlGaAs	30-75% Al	30	0.13	to 770	to 806
barrier 2	AlGaAs	75% Al	45		770	806
waitT 2s						
cladding	AlGaAs	35% Al	130		JT705	683
dot1	AlGaAs	20% Al	3.5		“	670
barrier	AlGaAs	35% Al	1.5			668
dot2	AlGaAs	20% Al	3.5			668
barrier	AlGaAs	35% Al	1.5			
dot3	AlGaAs	20% Al	3.5			683
barrier 2	AlGaAs	35% Al	150			722
cap	GaAs		2.5			
stop						

growth **#2655**

layer	**material**	**%**	**thick (nm)**	**rate (nm/s)**	**T (°C)**	**V/III**
buffer	GaAs		50		735	620
2s GI						
grading	AlGaAs	30-75% Al	30	0.13	to 770	to 800
barrier 2	AlGaAs	75% Al	45		770	800
waitT 2s						
cladding	AlGaAs	35% Al	130		JT705	680
layer 1	AlGaAs*	20% Al	13.5		“	
barrier 2	AlGaAs	35% Al	160			
cap	GaAs		2.5			720
stop						

growth **#2656**

layer	**material**	**%**	**thick (nm)**	**rate (nm/s)**	**T (°C)**	**V/III**
buffer	GaAs		50		735	620
2s GI						
grading	AlGaAs	30-75% Al	30	0.13	to 770	to 806
barrier 2	AlGaAs	75% Al	45		770	806
waitT 2s						
cladding	AlGaAs	40% Al	130		JT705	683
dot1	AlGaAs	20% Al	3.5		“	670
barrier	AlGaAs	40% Al	1.5			668
dot2	AlGaAs	20% Al	3.5			668
barrier	AlGaAs	40% Al	1.5			
dot3	AlGaAs	20% Al	3.5			683
barrier 2	AlGaAs	40% Al	150			722
cap	GaAs		2.5			
stop						

growth **#2657**

layer	**material**	**%**	**thick (nm)**	**rate (nm/s)**	**T (°C)**	**V/III**
buffer	GaAs		50		735	620
2s GI						
grading	AlGaAs	30-75% Al	30	0.13	to 770	to 806
barrier 2	AlGaAs	75% Al	45		770	806
waitT 2s						
cladding	AlGaAs	35% Al	130		JT705	683
dot1	AlGaAs	20% Al	5.5		“	670
barrier	AlGaAs	35% Al	1.5			668
dot2	AlGaAs	20% Al	2.5			668
barrier	AlGaAs	35% Al	1.5			
dot3	AlGaAs	20% Al	2.5			683
barrier 2	AlGaAs	35% Al	150			722
cap	GaAs		2.5			
stop						

growth **#2658**

layer	**material**	**%**	**thick (nm)**	**rate (nm/s)**	**T (°C)**	**V/III**
buffer	GaAs		50		735	620
2s GI						
grading	AlGaAs	30-75% Al	30	0.13	to 770	to 806
barrier 2	AlGaAs	75% Al	45		770	806
waitT 2s						
cladding	AlGaAs	35% Al	130		JT705	683
dot1	AlGaAs	20% Al	2.5		“	670
barrier	AlGaAs	35% Al	1.5			668
dot2	AlGaAs	20% Al	5.5			668
barrier	AlGaAs	35% Al	1.5			
dot3	AlGaAs	20% Al	2.5			683
barrier 2	AlGaAs	35% Al	150			722
cap	GaAs		2.5			
stop						

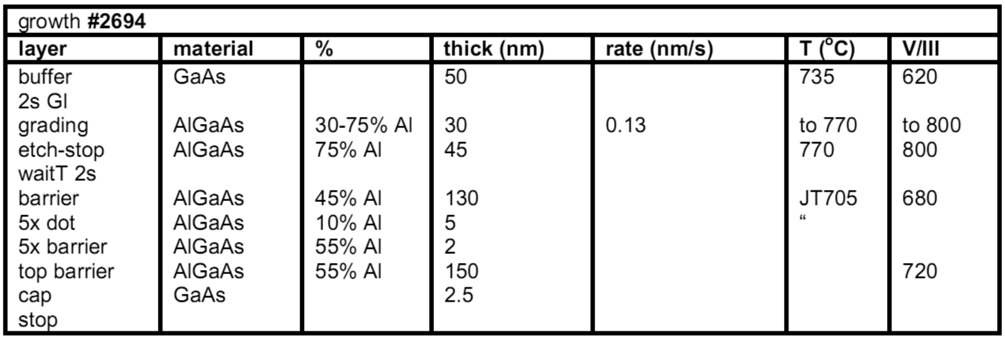

growth **#2694**

layer	**material**	**%**	**thick (nm)**	**rate (nm/s)**	**T (°C)**	**V/III**
buffer	GaAs		50		735	620
2s GI						
grading	AlGaAs	30-75% Al	30	0.13	to 770	to 800
etch-stop	AlGaAs	75% Al	45		770	800
waitT 2s						
barrier	AlGaAs	45% Al	130		JT705	680
5x dot	AlGaAs	10% Al	5		“	
5x barrier	AlGaAs	55% Al	2			
top barrier	AlGaAs	55% Al	150			720
cap	GaAs		2.5			
stop						

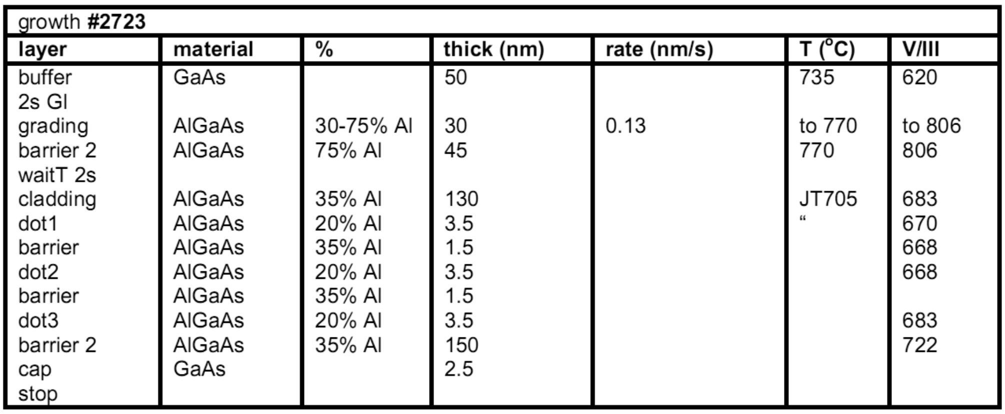

growth **#2723**

layer	**material**	**%**	**thick (nm)**	**rate (nm/s)**	**T (°C)**	**V/III**
buffer	GaAs		50		735	620
2s GI						
grading	AlGaAs	30-75% Al	30	0.13	to 770	to 806
barrier 2	AlGaAs	75% Al	45		770	806
waitT 2s						
cladding	AlGaAs	35% Al	130		JT705	683
dot1	AlGaAs	20% Al	3.5		“	670
barrier	AlGaAs	35% Al	1.5			668
dot2	AlGaAs	20% Al	3.5			668
barrier	AlGaAs	35% Al	1.5			
dot3	AlGaAs	20% Al	3.5			683
barrier 2	AlGaAs	35% Al	150			722
cap	GaAs		2.5			
stop						

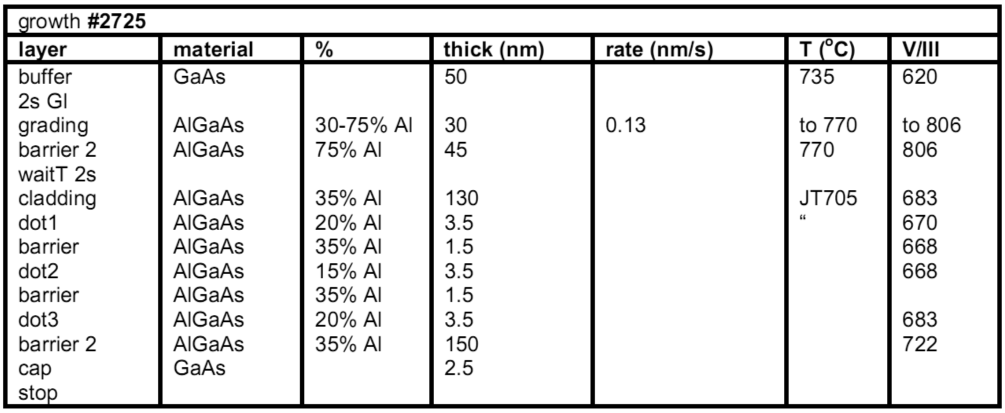

growth **#2725**

layer	**material**	**%**	**thick (nm)**	**rate (nm/s)**	**T (°C)**	**V/III**
buffer	GaAs		50		735	620
2s GI						
grading	AlGaAs	30-75% Al	30	0.13	to 770	to 806
barrier 2	AlGaAs	75% Al	45		770	806
waitT 2s						
cladding	AlGaAs	35% Al	130		JT705	683
dot1	AlGaAs	20% Al	3.5		“	670
barrier	AlGaAs	35% Al	1.5			668
dot2	AlGaAs	15% Al	3.5			668
barrier	AlGaAs	35% Al	1.5			
dot3	AlGaAs	20% Al	3.5			683
barrier 2	AlGaAs	35% Al	150			722
cap	GaAs		2.5			
stop						

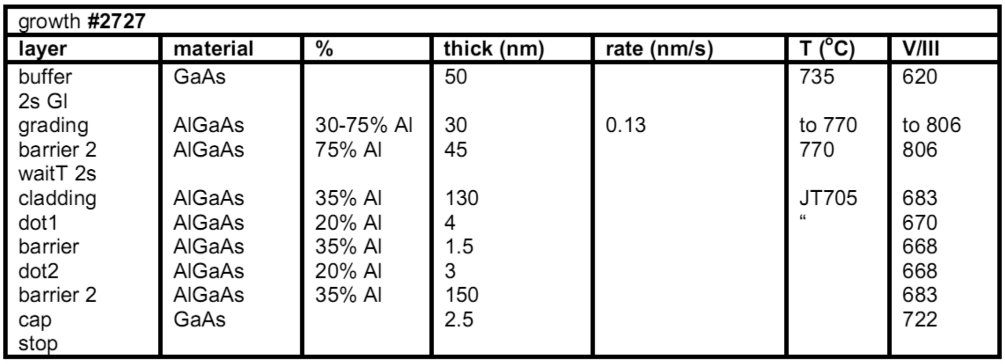

growth **#2727**

layer	**material**	**%**	**thick (nm)**	**rate (nm/s)**	**T (°C)**	**V/III**
buffer	GaAs		50		735	620
2s GI						
grading	AlGaAs	30-75% Al	30	0.13	to 770	to 806
barrier 2	AlGaAs	75% Al	45		770	806
waitT 2s						
cladding	AlGaAs	35% Al	130		JT705	683
dot1	AlGaAs	20% Al	4		“	670
barrier	AlGaAs	35% Al	1.5			668
dot2	AlGaAs	20% Al	3			668
barrier 2	AlGaAs	35% Al	150			683
cap	GaAs		2.5			722
stop						

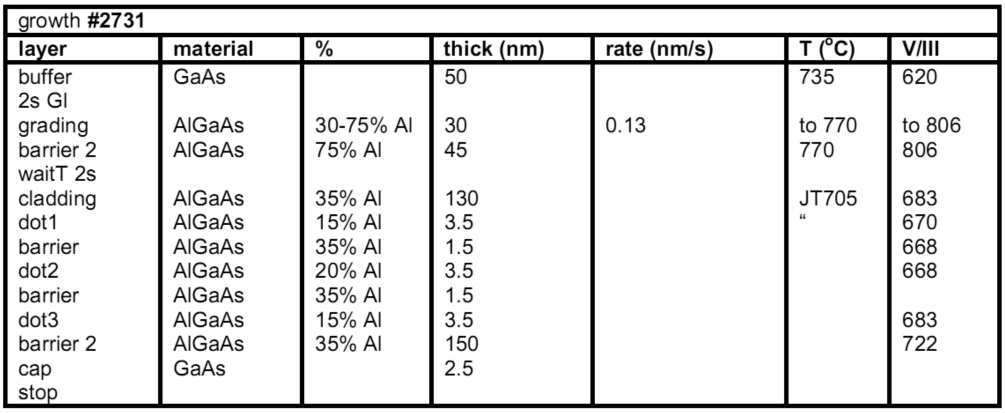

growth **#2731**

layer	**material**	**%**	**thick (nm)**	**rate (nm/s)**	**T (°C)**	**V/III**
buffer	GaAs		50		735	620
2s GI						
grading	AlGaAs	30-75% Al	30	0.13	to 770	to 806
barrier 2	AlGaAs	75% Al	45		770	806
waitT 2s						
cladding	AlGaAs	35% Al	130		JT705	683
dot1	AlGaAs	15% Al	3.5		“	670
barrier	AlGaAs	35% Al	1.5			668
dot2	AlGaAs	20% Al	3.5			668
barrier	AlGaAs	35% Al	1.5			
dot3	AlGaAs	15% Al	3.5			683
barrier 2	AlGaAs	35% Al	150			722
cap	GaAs		2.5			
stop						

Appendix C

Processing run sheets

Pyramid substrate preparation

1. SiO_2 **layer 500-600** $\AA$ **in** SiO_2 **(PECVD), 47 s deposition**

2. Wafer Preparation

a. Bake 160 °C, 5 min

b. HMDS primer spin 3500 rpm/3 s/30 s

c. 1805 Photoresist 3500 rpm/3 s/30 s

d. Clean spinner with Aceton

e. Bake 90 °C, 5min

3. Cleaving. Keep a test piece for step 5.

4. Mask Transfer

a. Exposure 2.2s, MF-319 development 40 s

b. Bake at 115°C, 15 min.

c. O_2-plasma etch, 2.5 min, 50 W, 300 mTorr

5. Oxide Patterning

a. BHF (Buffer HF, 15%) SiO_2 etch on test-piece (remove PR from test-piece before) Endpoint criterion: BHF stops wetting the surface, about 22 s, repeat with sample

b. H_20 Rinse

6. Resist Stripping

a. Aceton Ultrasonic 3 min/40% (with special holder for 6 pieces); Aceton, Propanol, H_2O

b. N_2 dry, back to box

7. Br Etch

a. Br2: Methanol 1 ml : 100 ml, 40∼50s

b. Methanol 10 s

c. Methanol Ultrasonic 1 min/80%

8. Oxide Removal

a. H_2O N2 dry BHF 3 times longer than determined in step 4.

b. H_2O rinse

c. N_2 dry, back to box.

9. Cleaning before growth

a. 0_2-Plasma: 0.4 Torr, 50 W, 3 min

b. HCl until hydrophobic

Surface-etching

1. Photoresist structuring

a. Photoresist 1805 3 s/30 s/5000 rpm

b. Bake 90 °C, 5 min

c. Bake 115 °C, 15 min

d. O_2-plasma etch, 25 – 35 min, 75 W, 0.8 Torr

2. Chemical etching

a. ($H_2SO_4 : H_2O_2 : H_2O \;=\; 1 : 8 : 160$) 50 s

b. H_2O rinse

3. Photoresist removal

a. Aceton rinse, ultrasound 3 min 80%

b. Aceton rinse

c. Propanol rinse

d. H_2O rinse, N_2 dry

Back-etching

1. preparation of the sample support

a. Preparing a (111)B support, with slightly larger size compared to sample.

2. Deposition of Ti(20 nm)/Au(200 nm) on top of the sample surface

3. Attach sample and support

a. Turn on a heater to heat the sample to ∼ 90°C

b. Glue the sample (shining side) and the support by the black wax

c. Turn off the heater and wait until is becomes cold (room temperature).

d. Turn on a heater to heat the sample (together with the support) to ∼ 45°C.

c. Glue the sample (together with the support) to a piece of glass by white wax.

4. Mechanical thinning

a. Mechanical etching by the polishing cream with 5 micron particle size

b. Thin down the sample (from the back side of the sample) to 200 micron (for original 350 micron thick substrate).

5. Chemical etching

a. Make a solution: ($NH_4OH : H_2O_2 = 8$ ml : 240 ml) (1 : 30)

b. Etching using the liquid rotation equipment.

Bibliography

[1] G. E. Moore. *Electronics*, 38:114–117, 1965.

[2] L. Esaki and Tsu R. *IBM Research Note*, pages RC–2418, 1969.

[3] Y. Arakawa and H. Sakaki. Multidimensional quantum well laser and temperature-dependence of its threshold current. *Applied Physics Letters*, 40(11):939–941, 1982.

[4] M. Asada, Y. Miyamoto, and Y. Suematsu. Gain and the threshold of 3-dimensional quantum-box lasers. *Ieee Journal of Quantum Electronics*, 22(9):1915–1921, 1986.

[5] Y. Liu, N. Yamamoto, Y. Nishimoto, N. Kamikubo, S. Shimomura, K. Gamo, K. Murase, N. Sano, A. Adachi, K. Fujita, T. Watanabe, and S. Hiyamizu. Inxga1-xas/gaas quantum-wire structures grown on gaas (100) patterned substrates with [001] ridges. *Journal of Crystal Growth*, 150(1-4):299–305, 1995. Part 1.

[6] R. Notzel, M. Ramsteiner, Z. C. Niu, H. P. Schonherr, L. Daweritz, and K. H. Ploog. Enhancement of optical nonlinearity in strained (inga)as sidewall quantum wires on patterned gaas (311)a substrates. *Applied Physics Letters*, 70(12):1578–1580, 1997.

[7] M. Grundmann, V. Tuerck, J. Christen, E. Kapon, D. M. Hwang, C. Caneau, R. Bhat, and D. Bimberg. Radiative recombination in pseudomorphic ingaas/gaas quantum wires grown on nonplanar substrates. *Solid-State Electronics*, 37(4-6):1097–1100, 1994.

[8] A. Hartmann, L. Loubies, F. Reinhardt, and E. Kapon. Self-limiting growth of quantum dot heterostructures on nonplanar 111b substrates. *Applied Physics Letters*, 71(10):1314–1316, 1997.

[9] K. F. Karlsson. *Spectroscopic studies of InGaAs/GaAs/AlGaAs quantum dots and wires.* PhD thesis, Linköping University, 2004.

[10] J. H Davies. *The physics of low-dimensional semiconductors.* The Cambridge University Press, US, 1998.

[11] E. O. Kane. Band structure of indium antimonide. *Journal of Physics and Chemistry of Solids*, 1(4):249–261, 1957.

[12] Thomas B. Bahder. Eight-band k · p model of strained zinc-blende crystals. *Physical Review B*, 41(17):11992, 1990.

[13] I. Vurgaftman, J. R. Meyer, and L. R. Ram-Mohan. Band parameters for iii-v compound semiconductors and their alloys. *Journal of Applied Physics*, 89(11):5815–5875, 2001. Part 1.

[14] G. Fishman. Hole subbands in strained-quantum-well semiconductors in [hhk] directions. *Physical Review B*, 52(15):11132–11143, 1995.

[15] T. Suntola and J. Hyvarinen. Atomic layer epitaxy. *Annual Review of Materials Science*, 15:177–195, 1985.

[16] A. Usui. Atomic layer epitaxy of iii-v compounds - chemistry and applications. *Proceedings of the Ieee*, 80(10):1641–1653, 1992.

[17] J. Gowar. *Optical communication system*. Prentice Hall, 1993.

[18] R. Dingle, W. Wiegmann, and C. H. Henry. Quantum States of Confined Carriers in Very Thin $\mathrm{Al_xGa_{1-x}As - GaAs - Al_xGa_{1-x}As}$ Heterostructures. *Physical Review Letters*, 33(14):827, 1974.

[19] M. Baier. *Correlated photon emission from pyramidal quantum dot heterostructures*. PhD thesis, Ecole Polytechnique Fédéale de Lausanne (EPFL), 2005.

[20] U. Bockelmann and G. Bastard. Interband absorption in quantum wires .1. zero-magnetic-field case. *Physical Review B*, 45(4):1688–1699, 1992.

[21] R. M. Eisberg. *Fundamentals of Modern Physics*. Wiley, New York, 1961.

[22] R. L. Weidner, R. T.; Sells. *Elementary Modern Physics*. Allyn and Bacon, Boston, 3rd edition edition, 1980.

[23] S. Adachi. *GaAs and Related Materials*. World Scientific, Singapore, 1994.

[24] F. H. Stillinger. Axiomatic basis for spaces with non-integer dimension. *Journal of Mathematical Physics*, 18(6):1224–1234, 1977.

[25] X. F. He. Anisotropy and isotropy - a model of fraction-dimensional space. *Solid State Communications*, 75(2):111–114, 1990.

[26] Xing-Fei He. Excitons in anisotropic solids: The model of fractional-dimensional space. *Physical Review B*, 43(3):2063, 1991.

[27] D. Birkedal, K. Leosson, and J. M. Hvam. Long lived coherence in self-assembled quantum dots. *Physical Review Letters*, 8722(22):art. no.–227401, 2001.

[28] R. J. Warburton, B. T. Miller, C. S. Durr, C. Bodefeld, K. Karrai, J. P. Kotthaus, G. Medeiros-Ribeiro, P. M. Petroff, and S. Huant. Coulomb interactions in small charge-tunable quantum dots: A simple model. *Physical Review B*, 58(24):16221–16231, 1998.

[29] Craig Pryor. Geometry and material parameter dependence of inas/gaas quantum dot electronic structure. *Physical Review B*, 60(4):2869, 1999.

[30] O. Stier, M. Grundmann, and D. Bimberg. Electronic and optical properties of strained quantum dots modeled by 8-band k center dot p theory. *Physical Review B*, 59(8):5688–5701, 1999.

[31] E. Kapon, M. C. Tamargo, and D. M. Hwang. Molecular-beam epitaxy of gaas/algaas superlattice heterostructures on nonplanar substrates. *Applied Physics Letters*, 50(6):347–349, 1987.

[32] E. Kapon, D. M. Hwang, and R. Bhat. Stimulated emission in semiconductor quantum wire heterostructures. *Physical Review Letters*, 63(4):430, 1989.

[33] X. L. Wang, M. Ogura, and H. Matsuhata. Flow-rate modulation epitaxy of algaas/gaas quantum wires on nonplanar substrate. *Applied Physics Letters*, 66(12):1506–1508, 1995.

[34] S. Koshiba, H. Noge, H. Akiyama, T. Inoshita, Y. Nakamura, A. Shimizu, Y. Nagamune, M. Tsuchiya, H. Kano, H. Sakaki, and K. Wada. Formation of gaas ridge quantum-wire structures by molecular-beam epitaxy on patterned substrates. *Applied Physics Letters*, 64(3):363–365, 1994.

[35] T. Muranaka, S. Kasai, C. Jiang, and H. Hasegawa. Control of morphology and wire width in ingaas ridge quantum wires grown by atomic hydrogen-assisted selective molecular beam epitaxy. *Physica E-Low-Dimensional Systems & Nanostructures*, 13(2-4):1185–1189, 2002.

[36] R. Notzel, M. Ramsteiner, J. Menniger, A. Trampert, H. P. Schonherr, L. Daweritz, and K. H. Ploog. Micro-photoluminescence study at room temperature of sidewall quantum wires formed on patterned gaas (311)a substrates by molecular beam epitaxy. *Japanese Journal of Applied Physics Part 2-Letters*, 35(3A):L297–L300, 1996.

[37] X. L. Wang and V. Voliotis. Epitaxial growth on optical properties of semiconductor quantum wires. *Journal of Applied Physics*, 99:121301, 2006.

[38] E. Colas, S. Simhony, E. Kapon, R. Bhat, D. M. Hwang, and P. S. D. Lin. Growth of gaas quantum wire arrays by organometallic chemical vapor-deposition on submicron gratings. *Applied Physics Letters*, 57(9):914–916, 1990.

[39] E. Colas, E. M. Clausen, E. Kapon, D. M. Hwang, and S. Simhony. Application of organometallic chemical vapor-deposition mechanisms to lateral band-gap patterning on stepped surfaces. *Applied Physics Letters*, 57(23):2472–2474, 1990.

[40] Y. C. Chang, L. L. Chang, and L. Esaki. A new one-dimensional quantum well structure. *Applied Physics Letters*, 47(12):1324–1326, 1985.

[41] L. Pfeiffer, K. W. West, H. L. Stormer, J. P. Eisenstein, K. W. Baldwin, D. Gershoni, and J. Spector. Formation of a high-quality 2-dimensional electron-gas on cleaved gaas. *Applied Physics Letters*, 56(17):1697–1699, 1990.

[42] H. Akiyama. One-dimensional excitons in gaas quantum wires. *Journal of Physics-Condensed Matter*, 10(14):3095–3139, 1998.

[43] J. M. Gaines, P. M. Petroff, H. Kroemer, R. J. Simes, R. S. Geels, and J. H. English. Molecular-beam epitaxy growth of tilted gaas alas superlattices by deposition of fractional monolayers on vicinal (001) substrates. *Journal of Vacuum Science & Technology B*, 6(4):1378–1381, 1988.

[44] T. Fukui and H. Saito. (alas)1/2(gaas)1/2 fractional-layer superlattices grown on (001) vicinal gaas substrates by metal organic-chemical vapor-deposition. *Journal of Vacuum Science & Technology B*, 6(4):1373–1377, 1988.

[45] J. Y. Ishizaki, S. Goto, M. Kishida, T. Fukui, and H. Hasegawa. Mechanism of multiatomic step formation during metalorganic chemical-vapor-deposition growth of gaas on (001) vicinal surface studied by atomic-force microscopy. *Japanese Journal of Applied Physics Part 1-Regular Papers Short Notes & Review Papers*, 33(1B):721–726, 1994.

[46] S. Hara, J. Motohisa, and T. Fukui. Optical characterization and laser operation of ingaas quantum wires on gaas multiatomic steps. *Solid-State Electronics*, 42(7-8):1233–1238, 1998.

[47] E. Colas, E. Kapon, S. Simhony, H. M. Cox, R. Bhat, K. Kash, and P. S. D. Lin. Generation of macroscopic steps on patterned (100) vicinal gaas-surfaces. *Applied Physics Letters*, 55(9):867–869, 1989.

[48] Y. Oda and T. Fukui. Natural formation of multiatomic steps on patterned vicinal substrates by movpe and application to gaas qwr structures. *Journal of Crystal Growth*, 195(1-4):6–12, 1998.

[49] D. Litvinov, A. Rosenauer, D. Gerthsen, N. N. Ledentsov, D. Bimberg, G. A. Ljubas, V. V. Bolotov, V. A. Volodin, M. D. Efremov, V. V. Preobrazhenskii, B. R. Semyagin, and I. P. Soshnikov. Ordered arrays of vertically correlated gaas and alas quantum wires grown on a gaas(311)a surface. *Applied Physics Letters*, 81(6):1080–1082, 2002.

[50] H. P. Schonherr, J. Fricke, Z. C. Niu, K. J. Friedland, R. Notzel, and K. H. Ploog. Uniform multiatomic step arrays formed by atomic hydrogen assisted molecular beam epitaxy on gaas (331) substrates. *Applied Physics Letters*, 72(5):566–568, 1998.

[51] M. Higashiwaki, M. Yamamoto, S. Shimomura, and S. Hiyamizu. Highly uniform and high-density gaas/(gaas)(4)(alas)(2) quantum wires grown on (775)b-oriented gaas substrates by molecular beam epitaxy. *Applied Physics Letters*, 71(14):2005–2007, 1997.

[52] K. Y. Cheng, K. C. Hsieh, and J. N. Baillargeon. Formation of lateral quantum-wells in vertical short-period superlattices by strain-induced lateral-layer ordering process. *Applied Physics Letters*, 60(23):2892–2894, 1992.

[53] P. J. Pearah, A. C. Chen, K. C. Hsieh, and K. Y. Cheng. Algainp multiple-quantum wire heterostructure lasers prepared by the strain-induced lateral-layer ordering process. *Ieee Journal of Quantum Electronics*, 30(2):608–618, 1994.

[54] H. J. Fan, P. Werner, and M. Zacharias. Semiconductor nanowires: From self-organization to patterned growth. *Small*, 2(6):700–717, 2006.

[55] R. S. Wagner and W. C. Ellis. Vapor-liquid-solid mechanism of crystal growth and its application to silicon. *Transactions of the Metallurgical Society of Aime*, 233(6):1053–, 1965.

[56] J. Bellessa, V. Voliotis, R. Grousson, X. L. Wang, M. Ogura, and H. Matsuhata. High spatial resolution spectroscopy of a single v-shaped quantum wire. *Applied Physics Letters*, 71(17):2481–2483, 1997.

[57] H. F. Hess, E. Betzig, T. D. Harris, L. N. Pfeiffer, and K. W. West. Near-field spectroscopy of the quantum constituents of a luminescent system. *Science*, 264(5166):1740–1745, 1994.

[58] X. Q. Liu, X. L. Wang, and M. Ogura. Reduction of nonradiative recombination centers in v-grooved algaas/gaas quantum wires grown using tertiarybutylarsine. *Applied Physics Letters*, 79(11):1622–1624, 2001.

[59] T. Guillet, R. Grousson, V. Voliotis, X. L. Wang, and M. Ogura. Local disorder and optical properties in v-shaped quantum wires: Toward one-dimensional exciton systems. *Physical Review B*, 68(4), 2003.

[60] H. Akiyama, M. Yoshita, L. N. Pfeiffer, K. W. West, and A. Pinczuk. One-dimensional continuum and exciton states in quantum wires. *Applied Physics Letters*, 82(3):379–381, 2003.

[61] D. S. Citrin. Long intrinsic radiative lifetimes of excitons in quantum wires. *Physical Review Letters*, 69(23):3393–3396, 1992.

[62] R. Heitz, M. Veit, N. N. Ledentsov, A. Hoffmann, D. Bimberg, V. M. Ustinov, P. S. Kopev, and Z. I. Alferov. Energy relaxation by multiphonon processes in inas/gaas quantum dots. *Physical Review B*, 56(16):10435–10445, 1997.

[63] J. Bellessa, V. Voliotis, R. Grousson, X. L. Wang, M. Ogura, and H. Matsuhata. Quantum-size effects on radiative lifetimes and relaxation of excitons in semiconductor nanostructures. *Physical Review B*, 58(15):9933–9940, 1998.

[64] H. Akiyama, S. Koshiba, T. Someya, K. Wada, H. Noge, Y. Nakamura, T. Inoshita, A. Shimizu, and H. Sakaki. Thermalization effect on radiative decay of excitons in quantum wires. *Physical Review Letters*, 72(6):924–927, 1994.

[65] J. N. Randall, M. A. Reed, R. J. Matyi, and T. M. Moore. Nanostructure fabrication of zero-dimensional quantum dot diodes. *Journal of Vacuum Science & Technology B*, 6(6):1861–1864, 1988.

[66] R. C. Ashoori, H. L. Stormer, J. S. Weiner, L. N. Pfeiffer, K. W. Baldwin, and K. W. West. N-electron ground-state energies of a quantum-dot in magnetic-field. *Physical Review Letters*, 71(4):613–616, 1993.

[67] A. Lorke, J. P. Kotthaus, and K. Ploog. Coupling of quantum dots on gaas. *Physical Review Letters*, 64(21):2559–2562, 1990.

[68] R. Rinaldi, S. Antonaci, M. DeVittorio, R. Cingolani, U. Hohenester, E. Molinari, H. Lipsanen, and J. Tulkki. Effects of few-particle interaction on the atomiclike levels of a single strain-induced quantum dot. *Physical Review B*, 62(3):1592–1595, 2000.

[69] K. Kash, R. Bhat, D. D. Mahoney, P. S. D. Lin, A. Scherer, J. M. Worlock, B. P. Vandergaag, M. Koza, and P. Grabbe. Strain-induced confinement of carriers to quantum wires and dots within an ingaas-inp quantum well. *Applied Physics Letters*, 55(7):681–683, 1989.

[70] C. Obermuller, A. Deisenrieder, G. Abstreiter, K. Karrai, S. Grosse, S. Manus, J. Feldmann, H. Lipsanen, M. Sopanen, and J. Ahopelto. Mechanical nanomanipulation of single strain-induced semiconductor quantum dots. *Applied Physics Letters*, 75(3):358–360, 1999.

[71] K. Brunner, U. Bockelmann, G. Abstreiter, M. Walther, G. Bohm, G. Trankle, and G. Weimann. Photoluminescence from a single gaas/algaas quantum dot. *Physical Review Letters*, 69(22):3216–3219, 1992.

[72] J. Y. Marzin, J. M. Gerard, A. Izrael, D. Barrier, and G. Bastard. Photoluminescence of single inas quantum dots obtained by self-organized growth on gaas. *Physical Review Letters*, 73(5):716–719, 1994.

[73] M. Grundmann, J. Christen, N. N. Ledentsov, J. Bohrer, D. Bimberg, S. S. Ruvimov, P. Werner, U. Richter, U. Gosele, J. Heydenreich, V. M. Ustinov, A. Y. Egorov, A. E. Zhukov, P. S. Kopev, and Z. I. Alferov. Ultranarrow luminescence lines from single quantum dots. *Physical Review Letters*, 74(20):4043–4046, 1995.

[74] D. Leonard, M. Krishnamurthy, C. M. Reaves, S. P. Denbaars, and P. M. Petroff. Direct formation of quantum-sized dots from uniform coherent islands of ingaas on gaas-surfaces. *Applied Physics Letters*, 63(23):3203–3205, 1993.

[75] H. Ishikawa, H. Shoji, Y. Nakata, K. Mukai, M. Sugawara, M. Egawa, N. Otsuka, Y. Sugiyama, T. Futatsugi, and N. Yokoyama. Self-organized quantum dots and quantum dot lasers (invited). *Journal of Vacuum Science & Technology A*, 16(2):794–800, 1998.

[76] Z. R. Wasilewski, S. Fafard, and J. P. McCaffrey. Size and shape engineering of vertically stacked self-assembled quantum dots. *Journal of Crystal Growth*, 202:1131–1135, 1999.

[77] M. Grundmann and D. Bimberg. Formation of quantum dots in twofold cleaved edge overgrowth. *Physical Review B*, 55(7):4054, 1997.

[78] W. Wegscheider, G. Schedelbeck, G. Abstreiter, M. Rother, and M. Bichler. Atomically Precise GaAs/AlGaAs Quantum Dots Fabricated by Twofold Cleaved Edge Overgrowth. *Physical Review Letters*, 79(10):1917, 1997.

[79] G. Schedelbeck, W. Wegscheider, M. Bichler, and G. Abstreiter. Coupled quantum dots fabricated by cleaved edge overgrowth: From artificial atoms to molecules. *Science*, 278(5344):1792–1795, 1997.

[80] T. Fukui, S. Ando, Y. Tokura, and T. Toriyama. GaAs Tetrahedral Quantum Dot Structures Fabricated Using Selective Area Metalorganic Chemical Vapor-Deposition. *Applied Physics Letters*, 58(18):2018–2020, 1991.

[81] K. Kumakura, K. Nakakoshi, J. Motohisa, T. Fukui, and H. Hasegawa. Novel formation method of quantum-dot structures by self-limited selective-area metalorganic vapor-phase epitaxy. *Japanese Journal of Applied Physics*, 34(8B):4387–4389, 1995.

[82] J. Tatebayashi, M. Nishioka, T. Someya, and Y. Arakawa. Area-controlled growth of inas quantum dots and improvement of density and size distribution. *Applied Physics Letters*, 77(21):3382–3384, 2000.

[83] Y. Ducommun. *Semiconductor quantum dots grown in inverted pyramids.* PhD thesis, Ecole Polytechnique Fédéale de Lausanne (EPFL), 2001.

[84] H. Lee, J. A. Johnson, J. S. Speck, and P. M. Petroff. Controlled ordering and positioning of inas self-assembled quantum dots. *Journal of Vacuum Science & Technology B*, 18(4):2193–2196, 2000.

[85] O. G. Schmidt, C. Deneke, R. Kiravittaya, S.and Songmuang, H. Heidemeyer, Y. Nakamura, R. Zapf Gottwick, C. Muller, and N. Y. Jin-Phillipp. Self-assembled nanoholes, lateral quantum-dot molecules, and rolled-up nanotubes. *Ieee Journal of Selected Topics in Quantum Electronics*, 8(5):1025–1034, 2002.

[86] R. Songmuang, S. Kiravittaya, and O. G. Schmidt. Formation of lateral quantum dot molecules around self-assembled nanoholes. *Applied Physics Letters*, 82(17):2892–2894, 2003.

[87] R. H. Brown and R. Q. Twiss. Correlation between photons in 2 coherent beams of light. *Nature*, 177(4497):27–29, 1956.

[88] M. C.; Salah. B. E. A.; Khoo I. C.; Agrawal G. P.; Kratsov Y. A. and Teich. *Progress in Optics*, volume 26. North Holland, 1988.

[89] P. Michler, A. Kiraz, C. Becher, W. V. Schoenfeld, P. M. Petroff, L. D. Zhang, E. Hu, and A. Imamoglu. A quantum dot single-photon turnstile device. *Science*, 290(5500):2282–+, 2000.

[90] V. Zwiller, H. Blom, P. Jonsson, N. Panev, S. Jeppesen, T. Tsegaye, E. Goobar, M. E. Pistol, L. Samuelson, and G. Bjork. Single quantum dots emit single photons at a time: Antibunching experiments. *Applied Physics Letters*, 78(17):2476–2478, 2001.

[91] R. M. Thompson, R. M. Stevenson, A. J. Shields, I. Farrer, C. J. Lobo, D. A. Ritchie, M. L. Leadbeater, and M. Pepper. Single-photon emission from exciton complexes in individual quantum dots. *Physical Review B*, 6420(20), 2001.

[92] C. Becher, A. Kiraz, P. Michler, A. Imamoglu, W. V. Schoenfeld, P. M. Petroff, L. D. Zhang, and E. Hu. Nonclassical radiation from a single self-assembled inas quantum dot. *Physical Review B*, 63(12):art. no.–121312, 2001.

[93] E. M. Purcell. Spontaneous emission probabilities at radio frequencies. *Physical Review*, 69(11-1):681–681, 1946.

[94] F. Vouilloz, D. Y. Oberli, M. A. Dupertuis, A. Gustafsson, F. Reinhardt, and E. Kapon. Effect of lateral confinement on valence-band mixing and polarization anisotropy in quantum wires. *Physical Review B*, 57(19):12378–12387, 1998.

[95] E. Moreau, I. Robert, J. M. Gerard, I. Abram, L. Manin, and V. Thierry-Mieg. Single-mode solid-state single photon source based on isolated quantum dots in pillar microcavities. *Applied Physics Letters*, 79(18):2865–2867, 2001.

[96] M. Pelton, C. Santori, J. Vuckovic, B. Y. Zhang, G. S. Solomon, J. Plant, and Y. Yamamoto. Efficient source of single photons: A single quantum dot in a micropost microcavity. *Physical Review Letters*, 89(23), 2002.

[97] A. Kiraz, S. Falth, C. Becher, B. Gayral, W. V. Schoenfeld, P. M. Petroff, Lidong Zhang, E. Hu, and A. Imamoglu. Photon correlation spectroscopy of a single quantum dot. *Physical Review B*, 65(16):161303, 2002.

[98] M. H. Baier, A. Malko, E. Pelucchi, D. Y. Oberli, and E. Kapon. Quantum-dot exciton dynamics probed by photon-correlation spectroscopy. *Physical Review B*, 73(20), 2006.

[99] A. Barenco, D. Deutsch, A. Ekert, and R. Jozsa. Conditional quantum dynamics and logic gates. *Physical Review Letters*, 74(20):4083–4086, 1995.

[100] P. Borri, W. Langbein, S. Schneider, U. Woggon, R. L. Sellin, D. Ouyang, and D. Bimberg. Ultralong dephasing time in ingaas quantum dots. *Physical Review Letters*, 8715(15), 2001.

[101] X. Q. Li, Y. W. Wu, D. Steel, D. Gammon, T. H. Stievater, D. S. Katzer, D. Park, C. Piermarocchi, and L. J. Sham. An all-optical quantum gate in a semiconductor quantum dot. *Science*, 301(5634):809–811, 2003.

[102] E. Biolatti, R. C. Iotti, P. Zanardi, and F. Rossi. Quantum information processing with semiconductor macroatoms. *Physical Review Letters*, 85(26):5647–5650, 2000. Part 1.

[103] X. Q. Li and Y. Arakawa. Single qubit from two coupled quantum dots: An approach to semiconductor quantum computations. *Physical Review A*, 6301(1), 2001.

[104] Brendon W. Lovett, John H. Reina, Ahsan Nazir, and G. Andrew D. Briggs. Optical schemes for quantum computation in quantum dot molecules. *Physical Review B*, 68(20):205319, 2003. Copyright (C) 2008 The American Physical Society Please report any problems to prola@aps.org PRB.

[105] H. J. Krenner, M. Sabathil, E. C. Clark, A. Kress, D. Schuh, M. Bichler, G. Abstreiter, and J. J. Finley. Direct observation of controlled coupling in an individual quantum dot molecule. *Physical Review Letters*, 94(5), 2005.

[106] E. A. Stinaff, M. Scheibner, A. S. Bracker, I. V. Ponomarev, V. L. Korenev, M. E. Ware, M. F. Doty, T. L. Reinecke, and D. Gammon. Optical signatures of coupled quantum dots. *Science*, 311(5761):636–639, 2006.

[107] M. Scheibner, M. F. Doty, I. V. Ponomarev, A. S. Bracker, E. A. Stinaff, V. L. Korenev, T. L. Reinecke, and D. Gammon. Spin fine structure of optically excited quantum dot molecules. *Physical Review B*, 75(24), 2007.

[108] G. J. Beirne, C. Hermannstadter, L. Wang, A. Rastelli, O. G. Schmidt, and P. Michler. Quantum light emission of two lateral tunnel-coupled (in,ga)as/gaas quantum dots controlled by a tunable static electric field. *Physical Review Letters*, 96(13), 2006.

[109] D. Loss and D. P. DiVincenzo. Quantum computation with quantum dots. *Physical Review A*, 57(1):120–126, 1998.

[110] C. H. Bennett and D. P. DiVincenzo. Quantum information and computation. *Nature*, 404(6775):247–255, 2000.

[111] M. A. Nielsen and I. L. Chuang. *Quantum computation and quantum information.* Cambridge University Press, Cambridge, England, 2000.

[112] G. Bester, A. Zunger, and J. Shumway. Broken symmetry and quantum entanglement of an exciton in inxga1-xas/gaas quantum dot molecules. *Physical Review B*, 71(7), 2005.

[113] E. Pelucchi, S. Watanabe, K. Leifer, Q. Zhu, B. Dwir, P. De Los Rios, and E. Kapon. Mechanisms of quantum dot energy engineering by metalorganic vapor phase epitaxy on patterned nonplanar substrates. *Nano Letters*, 7(5):1282–1285, 2007.

[114] G. Biasiol. *Formation mechanisms of low-dimensional semiconductor nanostructures grown by MOCVD on nonplanar substrates.* PhD thesis, Ecole Polytechnique Fédéale de Lausanne (EPFL), 1998.

[115] F. Lelarge, G. Biasiol, A. Rudra, A. Condo, and E. Kapon. Self-ordered nanostructures grown by organometallic chemical vapor deposition on v-grooved substrates: experiments and monte-carlo simulations. *Microelectronics Journal*, 30(4-5):461–466, 1999.

[116] G. Binnig, C. F. Quate, and Ch Gerber. Atomic force microscope. *Physical Review Letters*, 56(9):930–933, 1986.

[117] F. Reinhardt, B. Dwir, and E. Kapon. Oxidation of gaas/algaas heterostructures studied by atomic force microscopy in air. *Applied Physics Letters*, 68(22):3168–3170, 1996.

[118] G. Bastard. *Wave mechanics applied to semiconductor heterostructures.* Springer.

[119] A. Gustafsson, M. E. Pistol, L. Montelius, and L. Samuelson. Local probe techniques for luminescence studies of low-dimensional semiconductor structures. *Journal of Applied Physics*, 84(4):1715–1775, 1998.

[120] M. Walther, E. Kapon, J. Christen, D. M. Hwang, and R. Bhat. Carrier capture and quantum confinement in gaas/algaas quantum wire lasers grown on v-grooved substrates. *Applied Physics Letters*, 60(5):521–523, 1992.

[121] K. Leifer, A. Hartmann, Y. Ducommun, and E. Kapon. Carrier transport and luminescence in inverted-pyramid quantum structures. *Applied Physics Letters*, 77(24):3923–3925, 2000.

[122] W. Jaskolski. Confined many-electron systems. *Physics Reports-Review Section of Physics Letters*, 271(1):1–66, 1996.

[123] F. Vouilloz, D. Y. Oberli, F. Lelarge, B. Dwir, and E. Kapon. Observation of many-body effects in the excitonic spectra of semiconductor quantum wires. *Solid State Communications*, 108(12):945–948, 1998.

[124] H. Akiyama, M. Yoshita, L. N. Pfeiffer, and K. W. West. One-dimensional excitonic states and lasing in highly uniform quantum wires formed by cleaved-edge overgrowth with growth-interrupt annealing. *Journal of Physics-Condensed Matter*, 16(35):S3549–S3566, 2004.

[125] B. Dwir, K. Leifer, and E. Kapon. Mixed dimensionality quantum heterostructures grown in axially modulated v grooves. *Physical Review B*, 67(7), 2003.

[126] T. Martensson, M. Borgstrom, W. Seifert, B. J. Ohlsson, and L. Samuelson. Fabrication of individually seeded nanowire arrays by vapour-liquid-solid growth. *Nanotechnology*, 14(12):1255–1258, 2003.

[127] Y. Cui, L. J. Lauhon, M. S. Gudiksen, J. F. Wang, and C. M. Lieber. Diameter-controlled synthesis of single-crystal silicon nanowires. *Applied Physics Letters*, 78(15):2214–2216, 2001.

[128] C. Bosio, J. L. Staehli, M. Guzzi, G. Burri, and R. A. Logan. Direct-energy-gap dependence on al concentration in alxga1-xas. *Physical Review B*, 38(5):3263–3268, 1988.

[129] G. Biasiol, E. Martinet, F. Reinhardt, A. Gustafsson, and E. Kapon. Low-pressure omcvd growth of algaas vertical quantum wells on non-planar substrates. *Journal of Crystal Growth*, 170(1-4):600–604, 1997.

[130] G. Biasiol and E. Kapon. Mechanisms of self-ordering of quantum nanostructures grown on nonplanar surfaces. *Physical Review Letters*, 81(14):2962–2965, 1998.

[131] G. Biasiol, A. Gustafsson, K. Leifer, and E. Kapon. Mechanisms of self-ordering in nonplanar epitaxy of semiconductor nanostructures. *Physical Review B*, 65(20), 2002.

[132] H. Shen, S. H. Pan, Z. Hang, J. Leng, F. H. Pollak, J. M. Woodall, and R. N. Sacks. Photoreflectance of gaas and ga0.82al0.18as at elevated-temperatures up to 600-degree-c. *Applied Physics Letters*, 53(12):1080–1082, 1988.

[133] H. Hillmer, A. Forchel, S. Hansmann, M. Morohashi, E. Lopez, H. P. Meier, and K. Ploog. Optical investigations on the mobility of two-dimensional excitons in gaas/ga1-xalxas quantum wells. *Physical Review B*, 39(15):10901–10912, 1989.

[134] M.; Ledentsov N. N. Dimberg, D.; Grundmann. *Quantum dot heterostructures.* John Wiley & Sons, New York, 1999.

[135] P. Michler. *Single quantum dots: fundamentals, applications and new concepts.* Topics in applied physics. Springer, New York, 2004.

[136] F. Vouilloz, D. Y. Oberli, M. A. Dupertuis, A. Gustafsson, F. Reinhardt, and E. Kapon. Polarization anisotropy and valence band mixing in semiconductor quantum wires. *Physical Review Letters*, 78(8):1580–1583, 1997.

[137] G. Goldoni, F. Rossi, E. Molinari, and A. Fasolino. Band structure and optical anisotropy in v-shaped and t-shaped semiconductor quantum wires. *Physical Review B*, 55(11):7110–7123, 1997.

[138] D. Y. Oberli, M. A. Dupertuis, F. Reinhardt, and E. Kapon. Effect of disorder on the temperature dependence of radiative lifetimes in v-groove quantum wires. *Physical Review B-Condensed Matter*, 59(4):2910–2914, 1999.

[139] A. Hartmann, Y. Ducommun, E. Kapon, U. Hohenester, and E. Molinari. Few-particle effects in semiconductor quantum dots: Observation of multicharged excitons. *Physical Review Letters*, 84(24):5648–5651, 2000.

[140] A. Crottini, J. L. Staehli, B. Deveaud, X. L. Wang, and M. Ogura. One-dimensional biexcitons in a single quantum wire. *Solid State Communications*, 121(8):401–405, 2002.

[141] H. Akiyama, L. N. Pfeiffer, A. Pinczuk, K. W. West, and M. Yoshita. Observation of large many-body coulomb interaction effects in a doped quantum wire. *Solid State Communications*, 122(3-4):169–173, 2002.

[142] R. Ambigapathy, I. BarJoseph, D. Y. Oberli, S. Haacke, M. J. Brasil, F. Reinhardt, E. Kapon, and B. Deveaud. Coulomb correlation and band gap renormalization at high carrier densities in quantum wires. *Physical Review Letters*, 78(18):3579–3582, 1997.

[143] A. Malko, M. H. Baier, E. Pelucchi, D. Y. Oberli, K. Leifer, D. Chek-al kar, and E. Kapon. Localization of excitons in disordered quantum wires probed by single-photon correlation spectroscopy. *Applied Physics Letters*, 85(23):5715–5717, 2004.

[144] T. Otterburg, D. Y. Oberli, M. A. Dupertuis, N. Moret, E. Pelucchi, B. Dwir, K. Leifer, and E. Kapon. Enhancement of the binding energy of charged excitons in disordered quantum wires. *Physical Review B*, 71(3), 2005.

[145] N. Skold, L. S. Karlsson, M. W. Larsson, M. E. Pistol, W. Seifert, J. Tragardh, and L. Samuelson. Growth and optical properties of strained gaas-gaxin1-xp core-shell nanowires. *Nano Letters*, 5(10):1943–1947, 2005.

[146] M. T. Borgstrom, V. Zwiller, E. Muller, and A. Imamoglu. Optically bright quantum dots in single nanowires. *Nano Letters*, 5(7):1439–1443, 2005.

[147] A. Hartmann, Y. Ducommun, K. Leifer, and E. Kapon. Structure and optical properties of semiconductor quantum nanostructures self-formed in inverted tetrahedral pyramids. *Journal of Physics-Condensed Matter*, 11(31):5901–5915, 1999.

[148] Q. Zhu, E. Pelucchi, S. Dalessi, K. Leifer, M. A. Dupertuis, and E. Kapon. Alloy segregation, quantum confinement, and carrier capture in self-ordered pyramidal quantum wires. *Nano Letters*, 6(5):1036–1041, 2006.

[149] D. Gammon, E. S. Snow, B. V. Shanabrook, D. S. Katzer, and D. Park. Fine structure splitting in the optical spectra of single gaas quantum dots. *Physical Review Letters*, 76(16):3005–3008, 1996.

[150] F. Michelini, M. A. Dupertuis, and E. Kapon. Effects of the one-dimensional quantum barriers in pyramidal quantum dots. *Applied Physics Letters*, 84(20):4086–4088, 2004.

[151] Peter C. Sercel and Kerry J. Vahala. Polarization dependence of optical absorption and emission in quantum wires. *Physical Review B*, 44(11):5681, 1991. Copyright (C) 2008 The American Physical Society Please report any problems to prola@aps.org PRB.

[152] H. Itoh, Y. Hayamizu, M. Yoshita, H. Akiyama, L. N. Pfeiffer, K. W. West, M. H. Szymanska, and P. B. Littlewood. Polarization-dependent photoluminescence-excitation spectra of one-dimensional exciton and continuum states in t-shaped quantum wires. *Applied Physics Letters*, 83(10):2043–2045, 2003.

[153] N. Le Thomas, E. Herz, O. Schops, U. Woggon, and M. V. Artemyev. Exciton fine structure in single cdse nanorods. *Physical Review Letters*, 94(1), 2005.

[154] J. F. Wang, M. S. Gudiksen, X. F. Duan, Y. Cui, and C. M. Lieber. Highly polarized photoluminescence and photodetection from single indium phosphide nanowires. *Science*, 293(5534):1455–1457, 2001.

[155] V. Voliotis, T. Guillet, R. Grousson, M. Menant, J. Bellessa, X. L. Wang, and M. Ogura. Disorder effects on carrier dynamics in a single quantum wire. *Physica Status Solidi a-Applied Research*, 190(3):735–742, 2002.

[156] D. S. Citrin. Radiative lifetimes of excitons in quantum-wells - localization and phase-coherence effects. *Physical Review B*, 47(7):3832–3841, 1993.

[157] M. Lomascolo, R. Cingolani, R. Rinaldi, and F. K. Reinhart. Free versus localized exciton in gaas v-shaped quantum wires. *Physics of Low-Dimensional Structures*, 12:131–136, 1997.

[158] M. Merano, S. Sonderegger, A. Crottini, S. Collin, P. Renucci, E. Pelucchi, A. Malko, M. H. Baier, E. Kapon, B. Deveaud, and J. D. Ganiere. Probing

carrier dynamics in nanostructures by picosecond cathodoluminescence. *Nature*, 438(7067):479–482, 2005.

[159] K. Brunner, G. Abstreiter, G. Böhm, G. Tränkle, and G. Weimann. Sharp-line photoluminescence and two-photon absorption of zero-dimensional biexcitons in a gaas/algaas structure. *Physical Review Letters*, 73(8):1138, 1994.

[160] L. Besombes, K. Kheng, L. Marsal, and H. Mariette. Acoustic phonon broadening mechanism in single quantum dot emission. *Physical Review B*, 63(15):155307, 2001.

[161] E. A. Muljarov and R. Zimmermann. Dephasing in quantum dots: Quadratic coupling to acoustic phonons. *Physical Review Letters*, 93(23):237401, 2004.

[162] G. Burkard, D. Loss, and D. P. DiVincenzo. Coupled quantum dots as quantum gates. *Physical Review B*, 59(3):2070–2078, 1999.

[163] D. P. DiVincenzo, D. Bacon, J. Kempe, G. Burkard, and K. B. Whaley. Universal quantum computation with the exchange interaction. *Nature*, 408(6810):339–342, 2000.

[164] Oliver Gywat, Guido Burkard, and Daniel Loss. Biexcitons in coupled quantum dots as a source of entangled photons. *Physical Review B*, 65(20):205329, 2002. Copyright (C) 2008 The American Physical Society Please report any problems to prola@aps.org PRB.

[165] O. Gywat, G. Burkard, and D. Loss. Quantum computation and the production of entangled photons using coupled quantum dots. *Superlattices and Microstructures*, 31(2-4):127–140, 2002.

[166] A. L. Ivanov and H. Haug. Existence of exciton crystals in quantum wires. *Physical Review Letters*, 71(19):3182, 1993. Copyright (C) 2008 The American Physical Society Please report any problems to prola@aps.org PRL.

[167] C. R. Kagan, C. B. Murray, M. Nirmal, and M. G. Bawendi. Electronic energy transfer in cdse quantum dot solids. *Physical Review Letters*, 76(9):1517, 1996. Copyright (C) 2008 The American Physical Society Please report any problems to prola@aps.org PRL.

[168] G. Ortner, M. Bayer, Y. Lyanda-Geller, T. L. Reinecke, A. Kress, J. P. Reithmaier, and A. Forchel. Control of vertically coupled ingaas/gaas quantum dots with electric fields. *Physical Review Letters*, 94(15), 2005.

[169] A. S. Bracker, M. Scheibner, M. F. Doty, E. A. Stinaff, I. V. Ponomarev, J. C. Kim, L. J. Whitman, T. L. Reinecke, and D. Gammon. Engineering electron and hole tunneling with asymmetric inas quantum dot molecules. *Applied Physics Letters*, 89(23), 2006.

[170] Q. Zhu, K. F. Karlsson, E. Pelucchi, and E. Kapon. Transition from two-dimensional to three-dimensional quantum confinement in semiconductor quantum wires/quantum dots. *Nano Letters*, 7(8):2227–2233, 2007.

[171] K. F. Karlsson, V. Troncale, D. Y. Oberli, A. Malko, E. Pelucchi, A. Rudra, and E. Kapon. Optical polarization anisotropy and hole states in pyramidal quantum dots. *Applied Physics Letters*, 89(25), 2006.

[172] A. Malko, M. H. Baier, K. F. Karlsson, E. Pelucchi, D. Y. Oberli, and E. Kapon. Optimization of the efficiency of single-photon sources based on quantum dots under optical excitation. *Applied Physics Letters*, 88(8), 2006.

[173] J. Y. Marzin and J. M. Gerard. Experimental probing of quantum-well eigenstates. *Physical Review Letters*, 62(18):2172–2175, 1989.

[174] J. M. Gerard and J. Y. Marzin. Direct probing of type-ii band configurations in semiconductor superlattices. *Physical Review B*, 40(9):6450–6453, 1989.

[175] B. S. Song, S. Noda, T. Asano, and Y. Akahane. Ultra-high-q photonic double-heterostructure nanocavity. *Nature Materials*, 4(3):207–210, 2005.

[176] K. Hennessy, A. Badolato, M. Winger, D. Gerace, M. Atature, S. Gulde, S. Falt, E. L. Hu, and A. Imamoglu. Quantum nature of a strongly coupled single quantum dot-cavity system. *Nature*, 445(7130):896–899, 2007.

Publications

Journal papers

Hybridization of Electron and Hole states in Semiconductor Quantum Dot Molecules,
Q. Zhu, K. F. Karlsson, M. Byszewski, A. Rudra, E. Pelucchi, Z. B. He and E. Kapon, submitted.

Quantum Dot Molecules Realized with Modulated Quantum Wire Heterostructures,
Q. Zhu, K. F. Karlsson, A. Rudra, E. Pelucchi and E. Kapon, Physica E, Physica E, **40**, 1815 (2008).

Transition from Two-Dimensional to Three-Dimensional Quantum Confinement in Semiconductor Quantum Wires/Quantum Dots,
Q. Zhu, K. F. Karlsson, E. Pelucchi and E. Kapon, Nano Letters, **7**, 2227 (2007).

Mechanisms of Quantum Dot Energy Engineering by Metalorganic Vapor Phase Epitaxy on Patterned Nonplanar Substrates,
E. Pelucchi, S. Watanabe, K. Leifer, Q. Zhu, B. Dwir, P. De. Los Rios and E. Kapon, Nano Letters, **7**, 1283 (2007).

Alloy segregation, Quantum confinement and Carrier capture in Self-Ordered Pyramidal Quantum Wires,
Q. Zhu, E. Pelucchi, S. Dalessi, K. Leifer, Marc-André. Dupertuis and E. Kapon, Nano Letters, **6**, 1036 (2006).

The perpendicular low-frequency susceptibility of Bi-2223/Ag tape,
D.-X. Chen, E. Pardo, C. Navau, A. Sanchez, J. Fang, Q. Zhu, X. M. Luo, Z.H. Han, Superconductor Science and Technology, **17**, 1477 (2004).

Field dependent critical current of Bi-2223/Ag tapes at different thermo-mechanical stages,
Q. Zhu, D.-X. Chen, Z.H. Han, Superconductor Science and Technology, **17**, 756 (2004).

Conferences

Optical polarization: Features and controllability of site-controlled quantum dots,
K. F. Karlsson, Q. Zhu, V. Troncale, D. Y. Oberli, E. Pelucchi, A. Rudra and E. Kapon, 17th international laser physics workshop, June 30- July 4, 2008, Trondheim, Norway. (submitted, Invited talk)

Hybridization of Electron and Hole States and Wavefunction probing in Semiconductor Quantum Dot Molecules,
Q. Zhu, K. F. Karlsson, M. Byszewski, A. Rudra, E. Pelucchi, Z. B. He and E. Kapon, The 29th International Conference on the Physics of Semiconductors, July 27-Aug 1, 2008, Rio de Janeiro, Brazil. (accepted, Oral talk)

Hybridization of Electron and Hole States in pyramidal Quantum Dot Molecules,
Q. Zhu, K. F. Karlsson, M. Byszewski, A. Rudra, E. Pelucchi, Z. B. He and E. Kapon, The 5th International Conference on Semiconductor Quantum Dots, May 11-16, 2008, Gyeongju, Korea. (contributed, Oral talk)

Site-controlled Pyramidal Quantum Dots,
M. Byszewski, B. Chalupar, Q. Zhu, V. Troncale, K. F. Karlsson, D. Y. Oberli, E. Pelucchi, A. Rudra and E. Kapon, Second Polish-French Workshop on High Magnetic Fields in Semiconductor Physics, Oct. 25-29, 2007, Warsaw, Poland. (contributed, Oral talk)

Quantum Dot Molecules and Superlattices Realized with Modulated Quantum Wire Heterostructures,
Q. Zhu, K. F. Karlsson, A. Rudra, E. Pelucchi, M. Byszewski, P. Gallo and E. Kapon, 13th International Conference on Modulated Semiconductor structures (MSS-13)", July 15-20, 2007, Genova, Italy. (contributed, Oral talk)

Control of Light Polarization using Semiconductor Quantum Dot Molecules,
Q. Zhu, K. F. Karlsson, A. Rudra, E. Pelucchi, M. Byszewski, P. Gallo and E. Kapon, The OSA Topical Conference on Nanophotonics, June 18-21, 2007, Hangzhou, China. (contributed, Oral talk)

Experimental Observation of Transition from 2D to 3D Quantum Confinement in Semiconductor Quantum Wires/Quantum dots,
Q. Zhu, E. Pelucchi, K. F. Karlsson, N. Moret, D. Y. Oberli and E. Kapon, SCOPES Seminar in Moscow, Sept. 11-15, 2006, Moscow, Russia. (contributed, Poster)

Semiconductor Quantum Wires with Controlled Length and Confinement Potential,
Q. Zhu, E. Pelucchi, K. F. Karlsson, S. Dalessi, M.-A. Dupertuis, N. Moret, D. Y. Oberli and E. Kapon, 28th international conference on the physics of semiconductors, July 24-28, 2006, Vienna, Austria. (contributed, Oral talk)

Continuous transition from 2D to 3D quantum confinement realized with pyramidal quantum wires and dots,
Q. Zhu, E. Pelucchi, K. F. Karlsson, N. Moret, D. Y. Oberli and E. Kapon, 4th Inter-

national Conference on Quantum Dots, May 1-5, 2006, Chamonix-Mont Blanc, France. (contributed, Oral talk)

Transition from Quantum Wire to Quantum Dot States in Pyramidal Nanostructures,
Q. Zhu, E. Pelucchi, S. Dalessi, K. Leifer, M.-A. Dupertuis and E. Kapon, International Workshop on Semiconductor quantum dot based devices and applications, Mar. 16-17, 2006, Paris, France. (contributed, Poster)

Alloy Segregation and Carrier Capture in Self-Ordered Pyramidal Quantum Wires,
Q. Zhu, E. Pelucchi, S. Dalessi, K. Leifer, M.-A. Dupertuis and E. Kapon, Annual meeting of the swiss physical society, July 14-15, 2005, Bern, Switzerland. (contributed, Oral talk)

Segregation effects in vertical nanostructures self-formed in inverted pyramids,
Q. Zhu, E. Pelucchi and E. Kapon, 11th European Workshop on Metalorganic Vapour Phase Epitaxy, June 5-8, 2005, Lausanne, Switzerland. (contributed, Poster)

Utilizing surface diffusion processes for quantum confinement control in pyramidal quantum dots grown by MOVPE,
E. Pelucchi, S. Watanabe, K. Leifer, Q. Zhu, B. Dwir, P. De Los Rios and E. Kapon, 11th European Workshop on Metalorganic Vapour Phase Epitaxy, June 5-8, 2005, Lausanne, Switzerland. (contributed, Poster)

OMCVD growth of III-V semiconductor ordered nanostructures in pre-patterned inverted pyramidal recesses,
E. Pelucchi, S. Watanabe, K. Leifer, Q. Zhu, B. Dwir, M. H. Baier, A. Malko and E. Kapon, 19me Journes Surfaces et Interfaces - JSI 2005 Lyon, France. (contributed, Invited talk)

Acknowledgements

I would like to take this opportunity to thank all the people who have made this thesis possible. First and foremost, I would like to thank Prof. Eli Kapon for taking me as his PhD student and supervising my research activity with enthusiastic interest and wise guidance in these four years.

Dr. Shinichi Watanabe has introduced me to our pyramids. He instructed me with great patience in operating most of the equipments that were necessary for my project and also in physics fundamentals related. More important, with his kind help, my fear for the new unfamiliar foreign environment was eliminated.

Dr. Emanuele Pelucchi was indispensable for my project. His super efficient working mode and diligence helped me to promote my research procedure in a unbelievable speed. I greatly enjoyed the time we were working together. I miss very much the "polenta" party and wish to take part in it again in Cork one day!

Dr. Fredrik Karlsson was another indispensable person for my project. I was impressed by his talent modeling skills, deep and wide understanding of solid state physics, together with his research attitude. I also enjoyed our efficient communication method through MSN messenger. I've felt like that you are a full-time online teacher!

I am also grateful to Dr. Marcin Byszewski for fruitful collaboration in the projects and kind aid in the lab. I enjoyed the time spent with his family and his polish friends. Dr. Martin Baier introduced me the big pitch pyramid fabrication and post-growth process. His serious scientific attitude impressed me a lot.

Dr. Alok Rudra contributed a lot in the sample growth and also took care of my project with interest. Dr. Benjamin Dwir gave me a lot of smart advices and instructions in electron beam lithography and AFM. He is also very warmhearted and patient in solving the technical problems of machines, computers and printers. I am very thankful to Dr. Daniel Oberli for the fruitful discussions with him and during the "QD coffee" meeting organized by him. Dr. Jean-Daniel Ganiere helped me in Cathodoluminescence measurement and understanding of microscope working principles.

I further thank Nicolas Moret for his kind help in Optic lab I and his guidance for wonderful Swiss scenery. Dr. Sascha Dalessi and his supervisor Dr. Marc-Andre Dupertuis helped me to get a better understanding of quantum confinement in the QWR. I would also like to thank Dr. Lars Lundeberg for the scientific and non-scientific discussions between us. I also enjoyed discussions with dear Sanna Palmgren, Fabienne Michelini on different types of topics. Thanks also to Kirill Atlasov for exchanging all kind of useful information. Benjamin Chalupar inspired me by his vitality and new ideas. I would like to thank Dr. Zhanbing He for the TEM characterization. Dr. Pascal Gallo helped me in AFM characterization and gave me some good advices on sample growth.

Nicolas Leiser is also a very important for my project. He is doing a wonderful job in taking care of our clean room. Damien Trolliet and Yoan Trolliet also contributed to this job. Thanks also to Dr. Eckard Deichsel and Dr. Andrei Caliman.

Denise Paroz, thank you very much for the continues help you've provided to me during these four years! You are really an angel! I could not imagine the Ph.D life without you. Thanks also to Gabriella Fuchs, Anita Berdoz.

Thanks also to my dear colleagues Tim Otterburg, Gilles Guerrero, Hakon Reichardt, Anton Malko, and Valentina Troncale, Arun Mohan, Marco Felici, Elodie Lamothe, Lukas Mutter, Alessandro Surrente.

Thanks to all my Chinese friends in Lausanne. You made my Ph.D life so enjoyable. And little Mao, thank you. Thank you for being close to me.

Finally, I would like to thank my parents for always supporting my interest and choices. Thanks to my dearest sister Jie Zhu. You make me feel never lonely! Thanks to all the members of my big family, I am so proud for having you around.

Curriculum Vitae

Name:	Zhu Qing		
Address:	Rte. de la Maladière 4, 1022 Chavannes-près-Renens, Switzerland		
Telephone:	+41 21 693 7031	Fax:	+41 21 693 5480
Email:	qing.zhu@epfl.ch	qing.qingzhu@gmail.com	
Nationality:	China		
Date of birth:	16 June 1980		

Education

Mar. 2004 – present:	**PhD student in Physics** **EPFL (Ecole Polytechnique Fédérale de Lausanne).** Thesis: Semiconductor Vertical Quantum Structures self-formed in inverted pyramids
Aug.1998 – Aug.2002:	**Bachelor of Science in Applied Physics** **Tsinghua University , Beijing, China.** Thesis: Field dependent critical current of Bi-2223/Ag tapes at different thermo-mechanical stages

Work Experience

Jan. 2004 – present:	**Laboratory of Physics of Nanostructures (Director: Prof. Eli Kapon),** **Ecole Polytechnique Fédérale de Lausanne (EPFL), Switzerland.** Activity: Research and teaching assistant.
Aug.2002 – Dec.2003:	**Applied Superconductivity Research Center, Tsinghua University, Beijing, China.** Activity: Research assistant.

Languages

English	Reading, writing, speaking fluently. Studying and working in English.
French	Basic knowledge.
Chinese	Mother tongue.

Hobbies

Handcraft, Music, Cooking, Sports(climbing, basketball, long distance race, etc).